NORTHWESTERN UNIVERSITY

Self-Assembly of Supramolecular Biomaterials Across Length Scales; Morphology, Chirality, and Interactions.

A DISSERTATION

SUBMITTED TO THE GRADUATE SCHOOL
IN PARTIAL FULFILLMENT OF THE REQUIREMENTS

for the degree

DOCTOR OF PHILOSOPHY

Field of Biomedical Engineering

By

M. Hussain Sangji

EVANSTON, ILLINOIS

June 2021

Abstract

Soft materials in nature are formed through programmed self-assembly of biomolecules to create complex architectures and optimized physical properties. It is therefore a key challenge in biomaterials science and engineering to understand the principles that govern the structure and properties of such materials, and the interactions between their different components. This work explores the self-assembly of a class of biomimetic molecules, their supramolecular interactions within multi-component systems, and their physical properties across length scales. The materials studied here are Peptide Amphiphiles (PAs), which mimic the self-assembly of peptides and lipids in biological systems to create ordered nanostructures that resemble natural biopolymers. PAs can assemble into various shapes such as twisted ribbons, flat sheets, long cylinders, and micelles, based on the sequence of peptides in the molecule and the charge on the headgroup. High aspect ratio PA nanofibers form networks that can be used as cell scaffolds for regenerative medicine applications. In the first section of this dissertation, nano structures formed by a series of charged hydrophobic PAs were investigated using high resolution atomic force microscopy (AFM). These PAs self-assembled into twisted ribbons of different widths and periodicity. A correlation was observed between the width and pitch lengths of these nanostructures, and a self-assembly model was developed to explain the morphology of the nanostructures based on a balance between the energetically favorable packing of molecules in the center of the nanostructures, the unfavorable packing at the edges, and the deformations due to packing of twisted β-sheets. The morphological polydispersity of PA nanostructures was determined by peptides sequences, and the model indicated that this phenomenon is related to the twisting of their internal β-sheets. There was a change in the supramolecular chirality of the nanostructures as the peptide sequence was systematically modified, even though only amino acids with L configuration were used. The

nanostructures switched from left-handed to right-handed twist as alanines in the sequence were replaced by larger and more hydrophobic valines. In addition, increasing the electrostatic charge on the assemblies changed their morphology from ribbons to cylinders, and then to micelles. Interestingly, a subpopulation of the nanostructures formed a DNA-like double helix structure with alternating major and minor grooves. A physical model was developed by combining known theories of chiral amphiphilic membranes and peptide twist, which established the key role of assembly stiffness in the formation of the double helix. As the stiffness of the assemblies increased, the ribbons become more asymmetric, and shifted towards forming double helices instead of twisted ribbons. When used as cellular scaffolds, the stiffness of these nanostructures also controlled the remodeling capacity of the material. Coatings of flexible fibers primarily deformed during cell spreading and migration, while coatings of rigid fibers primarily degraded. This effect was associated with the presence of more entanglements in flexible fiber networks, which stabilize the coatings. In the second section, multi-component systems of different PAs were investigated using combined fluorescence microscopy and AFM, and both uniformly mixed and self-sorted network architectures were found. The supramolecular organization of the individual components was found to control the final state of the mixtures, where the self-sorting was governed by the complementarity of hydrogen bond orientations in the molecules. This approach was used to study the co-assembly of protein-binding PAs, whose functional activities are known to be modified by the nanostructure. A new approach to create interpenetrating supramolecular networks with sequestered binding epitopes was developed using a combination of self-sorting and uniformly mixing bioactive components. In the third section, the physical properties of PAs were studied from the length scale of molecular organization up to the microscale dynamics of nanofiber networks. Modeling of diffraction patterns showed that the molecules within nanostructures are

arranged in a rectangular lattice, and are tilted in the direction parallel to the hydrogen bonding. The persistence length of PA fibers, a measure of bending stiffness, was comparable to those of natural structural biopolymers like actin and collagen. PA fiber networks also exhibited glassy dynamics at the micron scale, like most fibrous components of the ECM, which supports their use as biomimetic scaffolds. The dynamics of the networks were sensitive to the stiffness of nanofibers only at high concentrations, where the collisions between fibers dominate the properties of the networks. Together, these studies provide a deeper understanding of the nanoarchitectures and physical properties of materials formed by self-assembling peptide-based biomolecules.

Acknowledgments

There are many people without whom I never would have made it this far. I would like to thank Professor Sam Stupp for his guidance during my time in his group. I appreciate the opportunity to have worked in an incredible environment with such a talented group of people, and have the flexibility to study a variety of interesting topics. I would also like to thank my committee members, Professors Evan Scott, Monica Olvera de la Cruz, and Neha Kamat, for their feedback and advice. I am grateful for the numerous discussions with Dr. Liam Palmer, who was always willing to volunteer his time. I am also grateful to Professors Peter Grütter and Paul Wiseman, who introduced me to scientific research at McGill University, and sparked my interest in biophysics and nanoscience.

I am very thankful to have been able to work with incredible collaborators in the group. The numerous discussions with Dr. Hiroaki Sai about the diffraction patterns he measured for me were invaluable to my work. Dr. Stacey Chin, Dr. Ivan Sasseilli, Dr. Jake Carrow, Ruth Lee, and Simon Egner, Ruomeng Qiu, Tom Cotey, and Kristen Wek have all contributed to various aspects of my research, and I thank them for their efforts. Many members of the Stupp group have helped me tremendously over the years with feedback and advice, and I thank them all for their input during biomaterials and self-assembly subgroups. I have also had the pleasure to work with very talented master's and undergraduate students including Melissa Alanis, Matteo Di Bernardo, and Emilien Jung; thank you for teaching me how to be a better mentor. A special thanks to Ruth Lee for continuing with the work that I started and taking it to new directions. None of this would have been possible without the incredible Stupp group support staff, Maura Walsh, Laura Fields, Dan Carstensen, and Todd Linton.

Outside of academic work, I am grateful to call so many members and former members of the Stupp group my friends. There were some incredible times in Evanston, especially in the Cage and the lakefront BBQ spots, with many members of the group. On the downtown campus, it was always great to take breaks to grab coffee and chat with members of the SQI part of the group. It was your friendship and camaraderie that made it possible for me to make it through this journey.

To the BME cohort that started the program with me, thank you for your friendship over the years. Al Hassan, Amy Adkins, Anne Shim, Katherine Rodzak, Sahil Shah, Melisa Alanis, Toni Nepomuceno, Dani van der Merwe, Chris Versteeg, Alejandro Azocar; I am glad I went through this experience with you all. Thank you as well to members of the graduate student groups MGLC, ADCA, and GSA.

Finally, I would like to thank my family for their support and patience during my time in graduate school. My parents and my sisters, Naveen and Sheharbano, taught me the value of hard work and perseverance, and I am eternally grateful.

List of Abbreviations

AFM	Atomic Force Microscopy
BDNF	Brain Derived Neurotrophic Factor
BMP2	Bone Morphogenetic Protein 2
$CaCl_2$	Calcium Chloride
CD	Circular Dichroism
CLSM	Confocal Laser Scanning Microscopy
Cy3	Cyanine-3
Cy5	Cyanine-5
DLS	Dynamic Light Scattering
DMEM	Dulbecco's Modified Eagle Medium
DNA	Deoxyribonucleic acid
DOPC	1,2-dioleoyl-sn-glycero-3-phosphocholine
FAK	Focal Adhesion Kinase
FBS	Fetal Bovine Serum
FFT	Fast Fourier Transform
FGF	Fibroblast Growth Factor

FITC	Fluorescein isothiocyanate
Fmoc	Fluorenylmethoxycarbonyl protecting group
FTIR	Fourier Transform Infrared
HA	Hyaluronic Acid
HFIP	Hexafluoroisopropanol
GAG	Glycosaminoglycan
LC-MS	Liquid Chromatography-Mass Spectrometry
MAXS	Medium Angle X-ray Scattering
MC	Monte Carlo
MD	Molecular Dynamics
MMP	Matrix Metalloproteinase
MSC	Mesenchymal Stem Cell
NaCl	Sodium Chloride
NaOH	Sodium Hydroxide
NHLF	Normal Human Lung Fibroblast
NMR	Nuclear Magnetic Resonance
PA	Peptide Amphiphile
PBS	Phosphate Buffer Saline

PDL	Poly-D-lysine
PFA	Paraformaldehyde
PI	Propidium iodide
SAED	Selected Area Electron Diffraction
SAXS	Small Angle X-ray Scattering
SLB	Supported Lipid Bilayer
SDN	Supramolecular Double Network
SEM	Scanning Electron Microscopy
TAMRA	Tetramethylrhodamine
TEM	Transmission Electron Microscope
TGFβ-1	Transforming Growth Factor β-1
THT	Thioflavin T
WAXS	Wide Angle X-ray Scattering

Table of Contents

List of Figures

List of Tables

1. Introduction

1.1. Self-assembled materials in nature

Materials in nature consists of a hierarchy of structures composed of simpler building blocks.[1] The fundamental classes of building blocks in organisms – peptides, lipids, nucleic acids, and carbohydrates – have been optimized by evolution to create materials with a wide diversity of structural and functional properties.[2] Programmed interactions between these units result in their assembly into large structures with well-defined macroscopic properties. This bottom-up approach contrasts with top-down strategies where bulk materials are fabricated or manufactured into smaller objects (**Figure 1.1**).[3] In bottom-up self-assembly, the design of the larger objects is programmed into the smaller building blocks directly. With these programmed instructions stored in the genetic code, and the cellular machinery required to create the building blocks, organisms can build these materials in a self-contained system.

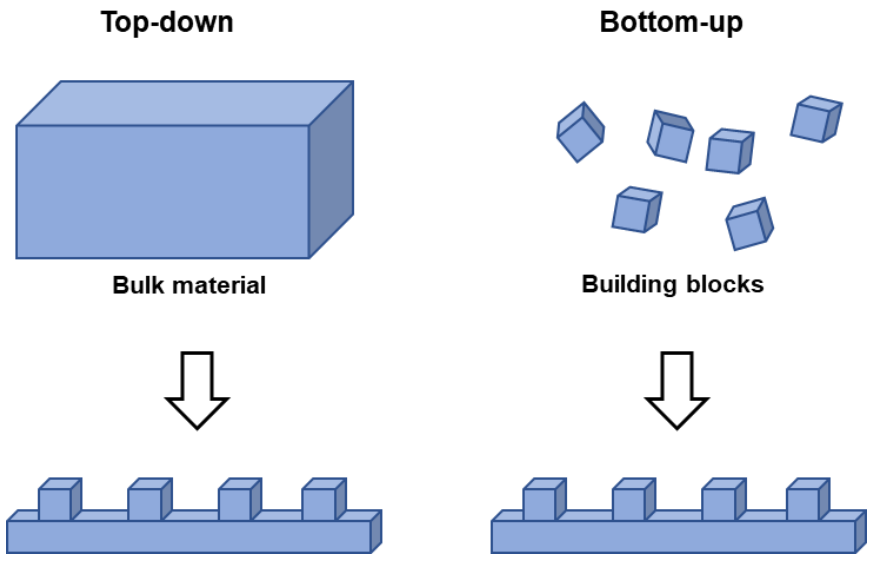

Figure 1.1. Top-down fabrication and bottom-up assembly. In top-down fabrication bulk materials are manufactured into complex objects, while in bottom-up assembly building blocks self-organizing into complex objects.

The programmed interactions in natural materials also allows for controlled complementarity in the self-assembly process, such that materials with multiple components can be formed simultaneously. In eukaryotic cells, the structural integrity and transport of cargo is controlled through the cytoskeleton, a dynamic interconnecting network composed of microtubules and actin filaments, among other components (**Figure 1.2**).[4,5] Microtubules and actin filament networks continuously assemble and disassemble in parallel even as the fundamental building blocks of both types of filaments, the proteins tubulin and G-actin, are synthesized in the same regions simultaneously.[6–9] The programmed complementarity of tubulin and G-actin enables them to form filaments selectively, without interference form the other component, even as they interact with each other in the crowded cellular environment.

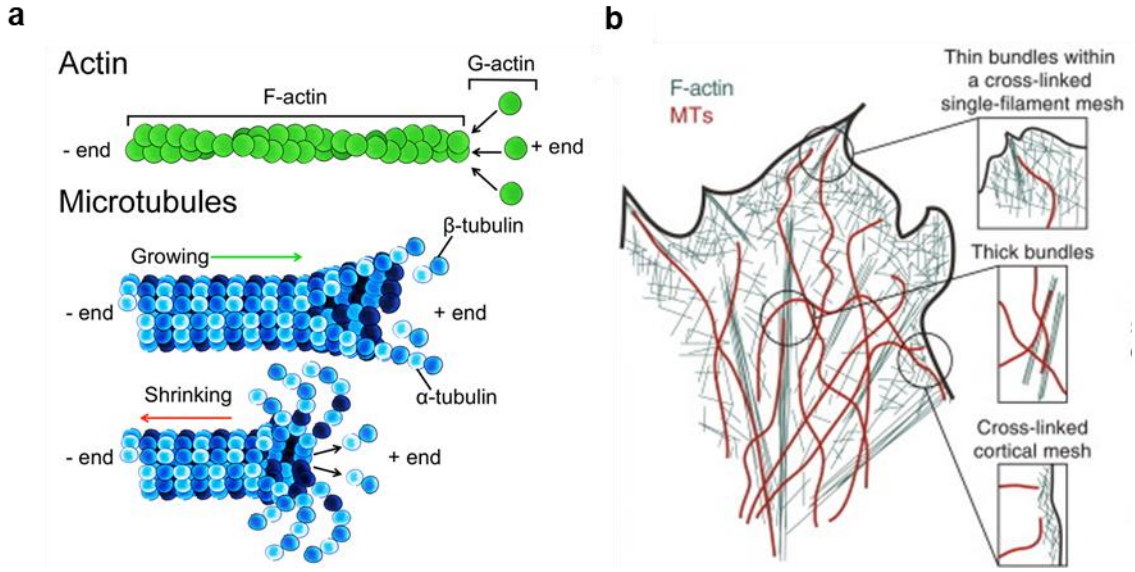

Figure 1.2. Actin and tubulin assembly in the cell cytoskeleton. (a) Actin and microtubule fibers form by intermolecular assembly of monomers. Reproduced from ref.[10] (b) Actin and microtubules form hierarchical interpenetrating networks in the multicomponent cytoskeleton. Reproduced from ref.[9]

The extracellular matrix (ECM) is another multicomponent material composed of a hierarchy of self-assembled units, which provides the structural scaffold for most cells and tissues.[11] The structure and biological properties of the ECM vary based on the tissue type and required function, and the ECM properties in turn can direct cellular behaviour such as migration and stem cell differentiation.[12] Collagen, the most abundant protein in most organisms, is a major component of the ECM, and comes in different forms based on the required functional and physical properties.[13] Collagen I forms large fibrils in order to provide structural integrity to bone, skin, tendon, blood vessels, and other connective tissues that are subject to significant physical forces. (**Figure 1.3**) Collagen II forms thinner fibrils and is found primarily in cartilage tissue, alongside an interpenetrating network of proteoglycans. Other forms include collagen IV which does not form fibers, but rather assembles into two dimensional sheets to support epithelial cells. The fundamental building blocks of fibrous collagen are peptide chains that form a triple helix, called tropocollagen. Tropocollagen, which is about 300 nm long and 1.5 nm in diameter, stacks in parallel in a well-defined orientation to create thick collagen fibrils.[14] In Collagen IV, however, this stacking is disrupted by modification of the peptide sequences, resulting in a less ordered sheet.[15] The formation of ordered fibrils or disordered sheets is therefore programmed into the fundamental amino acid sequence. This architecture controls the physical properties of collagen, which is essential to its function.[16] In addition to its structural properties, the ECM also contains proteins and signalling molecules that direct cellular behaviour. These including proteins that promote interaction between focal adhesions on cells and structural component of the ECM.[17] The ECM also binds and presents growth factors that act as signalling cues to direct cell migration and differentiation into complex tissues.[18,19]

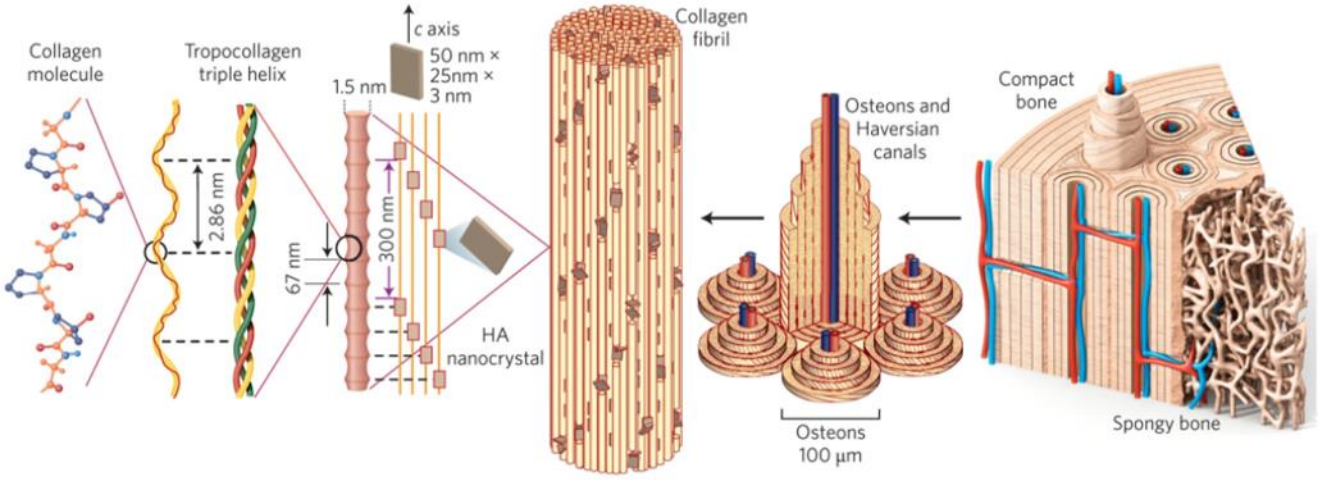

Figure 1.3. Hierarchical assembly of collagen in bone. Collagen peptides assemble into a triple helix tropocollagen through hydrogen bonding. Tropocollagen assembles into stacks to create fibrils, along with crystals of hydroxyapatite. The fibrils arrange in cylindrical, with space for nerves and blood vessels. Reproduced from ref.[20]

1.2. Supramolecular self-assembly

1.2.1. Supramolecular interactions

The role of intermolecular forces was popularized by the physicist Johannes Diderick van der Waals, when he demonstrated that attraction between molecules could account for some of the thermodynamic properties of liquids and gases.[21] The concept of hydrogen bonding in organic compounds emerged in the early twentieth century,[22] and was later followed by the ground-breaking discovery of the structure of the DNA as a double helix formed by the intermolecular interaction of two nucleic acid chains.[23,24] The field of supramolecular chemistry was later formalized by Jean-Marie Lehn in 1978.[25] In modern supramolecular chemistry, the self-assembly of materials is understood to be controlled by the strength and geometry of certain intermolecular interactions, which are both weaker and more dynamic than covalent bonds.[26] The fundamental

interactions in self-assembling systems include; ion-ion interactions between charged species; ion-dipole interactions, such as the organization of water around charged ions; dipole-dipole interactions, especially hydrogen bonds which are essential to the organization of proteins; induced dipole interactions, such as π-π stacking between aromatic groups, which are generally weaker than dipole-dipole interactions; and van der Waals forces, a weak short range attractive interaction between all atoms and molecules. These interactions are ubiquitous in natural and synthetic supramolecular systems.

1.2.2. Self-assembly of amphiphiles

Amphiphiles are molecules composed of a hydrophobic tail and hydrophilic head group, which aggregate in water to create nano and microstructures.[27] The aggregation is driven by the minimization of contact area between water and the lipids, as there is an entropic penalty to arranging water molecules in close proximity to hydrophobic regions. Amphiphilic molecules like phospholipids form supramolecular assemblies such as cell membranes and vesicles that are ubiquitous in organisms.[28] The balance of hydrophobic collapse due to the tail and steric repulsion between headgroups results in various shapes like spherical micelles, cylinders, and flat ribbons. The relation between the geometry of the molecule - the volume, headgroup area, and length- and the resulting structure can be described by the critical packing parameter.[29] As the headgroup area increases, higher curvature structures like spheres become energetically favourable, while increase the tail size promotes the formation of flatter bilayer sheets. (**Figure 1.4**) The packing of chiral amphiphiles is more complex, and is usually described in the continuum limit. Helfrich and Probst developed a theory of chiral amphiphile packing where energetics of the assembled structures can

be described in terms of the curvature of the surface.[30,31] Chiral amphiphiles can assemble into shapes such as twisted ribbons, helical ribbons, and tubes.[32]

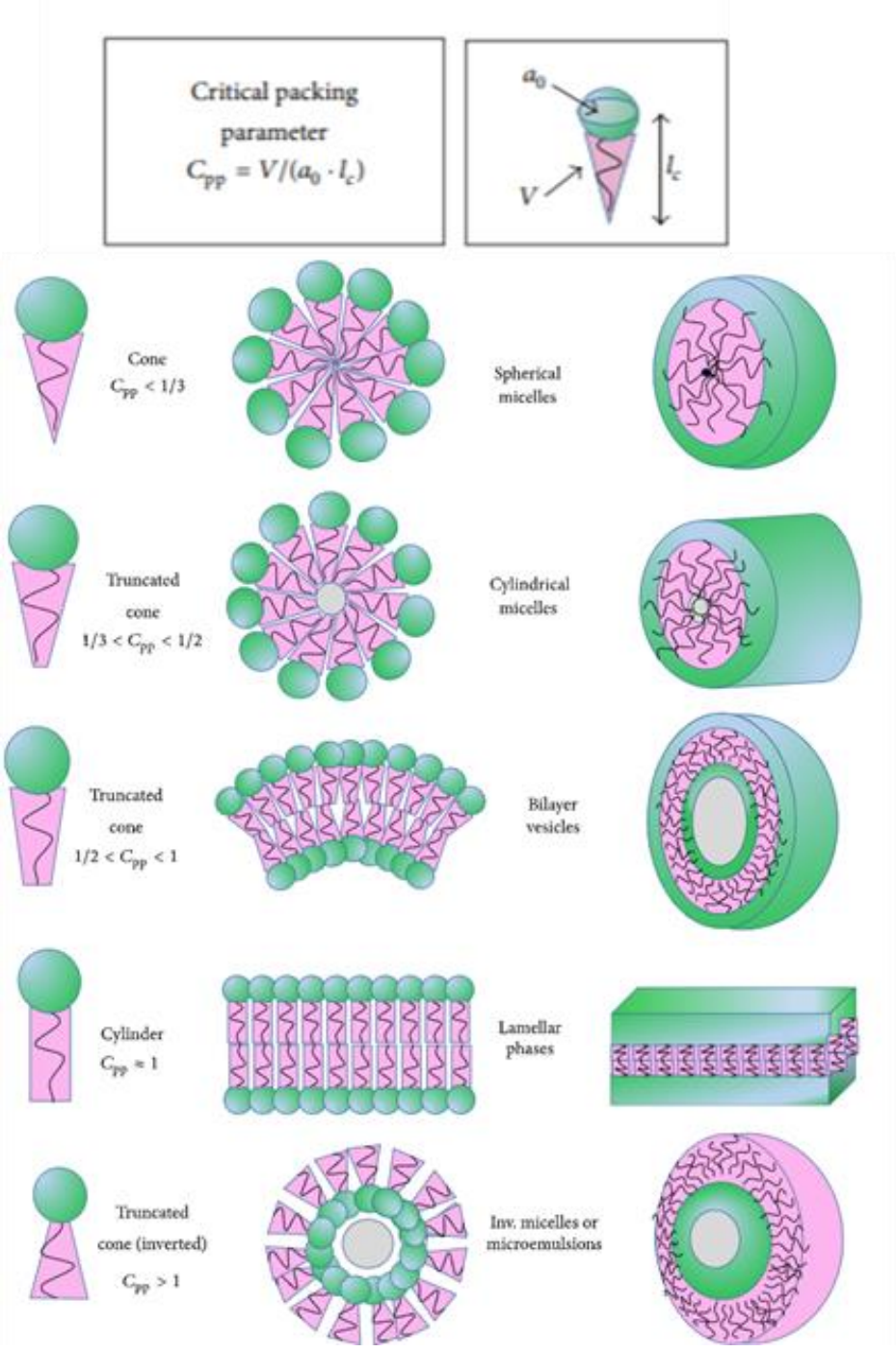

Figure 1.4. Self-assembly of amphiphiles described by the critical packing parameter (CPP) theory of Israelachvili. Reproduced from ref.[33]

The curvature of the two-dimensional surface is described using the curvature tensor, which contains information about the local surface curvature in all directions. Two characteristic curvatures can be calculated form the curvature tensor, the mean curvature H and the Gauss curvature K. A tube or helical ribbon has cylinder-like curvature with $H > 0$ and $K = 0$, while a twisted ribbon has saddle-like curvature with $K < 0$. The Helfrich-Probst has been extended to include a stretching energy in the 2D assemblies.[34–37] The stretching energy penalizes the saddle-like curvature of twisted ribbons, as this requires distortion of the headgroup packing, and results in geometrically frustrated nanostructures in between twisted ribbons and helices. The geometry of the resulting structure is therefore dependent on the hydrophobic collapse, the chiral twist, as well as the stretching stiffness of the assemblies.

1.2.3. Self -assembly of hydrogen bonding peptides

The self-assembly of peptides into complex structures is incredibly complex due to the large phase space of possible peptide confirmations.[38] The 20 amino acids that are genetically encoded in eukaryotes can be included in a peptide chain, and each have side chains of different hydrophobicity, charge, size, and conformational flexibility. Understanding the folding of peptide chains into proteins is one of the grand challenges of biochemistry and biophysics. Peptide chains adopt secondary and tertiary structures through the same intermolecular interactions mentioned previously, either between different regions of the chain or with other peptide chains. (**Figure 1.5**) One common secondary structure is β-sheets, where planar sheets of peptides are formed by hydrogen bonding between chains.[39] In these structures, the amino acid side chains stick out perpendicular to the plane and contribute to further intermolecular interactions that lead to tertiary structures. β-sheets in nature are often twisted due to the orientation of hydrogen bonds and other

intermolecular interactions, as determined by the amino acid side chains and the local environment.[40–42] The arrangement of the peptide chain in proteins has traditional been studied with x-ray crystallography, although recent advances in electron microscopy have enabled the measurement of structures in water.[43,44]

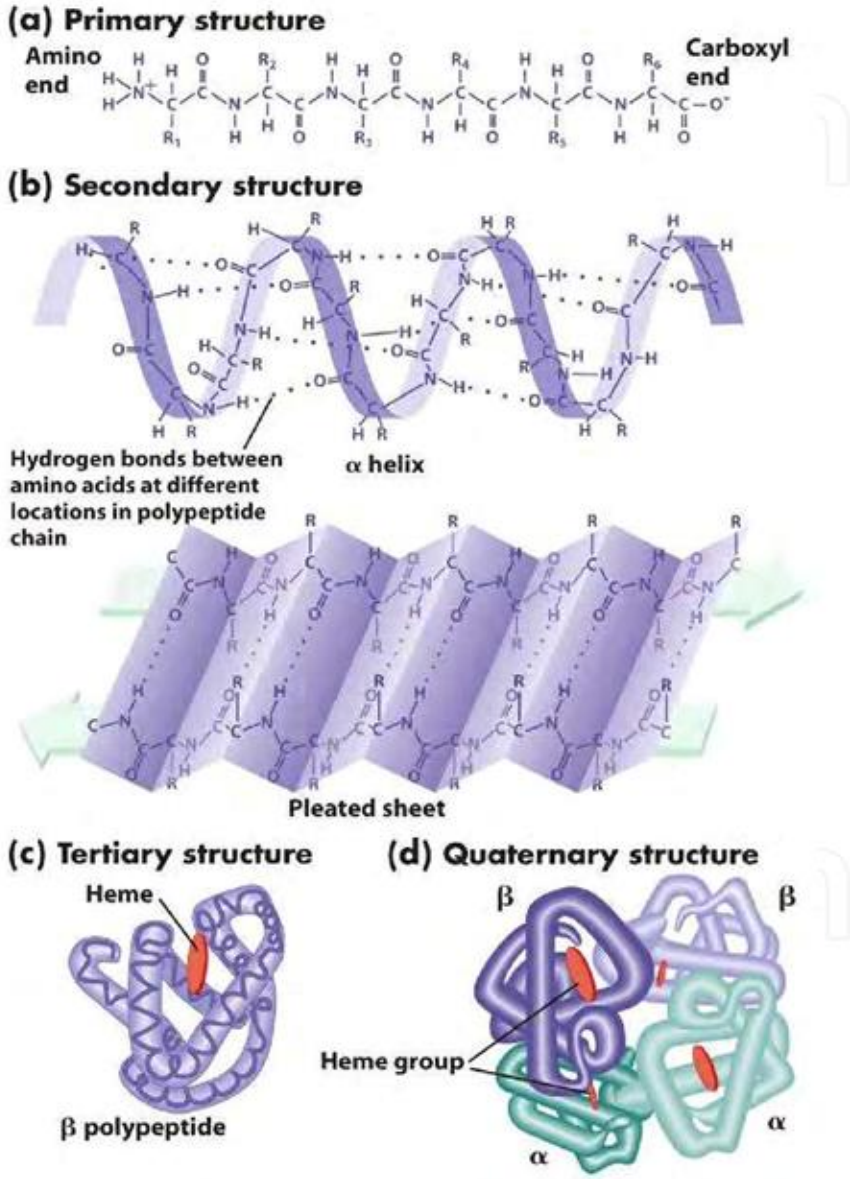

Figure 1.5. Folding of peptides into complex proteins. Amino acid sequences form the primary structure, which fold into secondary structures such as the α-helix and β-sheet through interactions between amino acids. The secondary structure folds further into complex tertiary structures, which can interact with other components to create quaternary structures. Image from public domain.

Long, twisted β-sheets are also found in peptide-based nanostructures such as amyloid fibrils.[45] Here, the planar β-sheets can stack in parallel to create stable fibrils with lengths on the micron scale, driven primarily by hydrophobic packing of the side chains. The formation of fibrils is associated with diseases such as Alzheimer's disease and Parkinson's disease.[46] Amyloid fibrils are typically highly stable due to the hydrogen bonds, and cannot be easily degraded by cells, contributing to their pathogenicity. While amyloid fibrils are associated with misfolded proteins, other β-sheet containing fibrils are essential to certain naturals functions. Spider silk, for example, has remarkable elastic properties and toughness due to highly ordered β-sheet stacking in the fibers.[47] The hierarchical organization of β-sheets in silk results in a semi-crystalline material with tensile strength higher than steel. These natural materials have inspired the design of numerous biomimetic materials fibrous materials that incorporate peptide sequences and hydrogen bonds.[48]

1.2.4. Peptide amphiphiles

The self-assembling properties of amphiphiles and peptides can be combined into single molecules, known as peptide amphiphiles (PAs).[49,50] PAs contain a lipid tail and a charged hydrophilic head group, similar to surfactant amphiphiles, connected by a short peptide sequence that can form β-sheets by hydrogen bonding with other molecules.[51] (**Figure 1.6**) These molecules have been extensive studied by the Stupp group and others. In PAs typically studied by the Stupp group, the lipid tail is12 to 16 carbons long, while the headgroup is composed of 2 to 3 charged amino acids, typically lysine for positively charged PAs and glutamic acids for negatively charged PAs at physiological pH.[52] The connecting peptide sequence contains hydrophobic amino acids such as valines or alanines,[53] or an alternating sequence of hydrophobic and charged residues.[54] These PAs can assembly into high aspect ratio structures like cylinders or ribbons by forming β-

sheets, based on the specific peptide sequence.[55] (**Figure 1.7**) The fibrous architecture of PA nanostructures is mimetic of the ECM, and these materials have received extensive interest for applications as cellular scaffolds in regenerative medicine.[56] Using solid phase peptide synthesis (SPPS), it is straightforward to add bioactive peptide groups to the ends of the molecules, such as sequences that activate cell receptors or bind growth factors.[57] The Tirrell group has investigated PAs where the peptide sequence is composed of therapeutic peptides to activate various cellular pathways.[58,59] These PAs are intended to serve as a delivery vehicle for the bioactive peptide through the cell membrane. They have also investigated therapeutic PAs with different hydrophobic components, such as double chain lipids.[60]

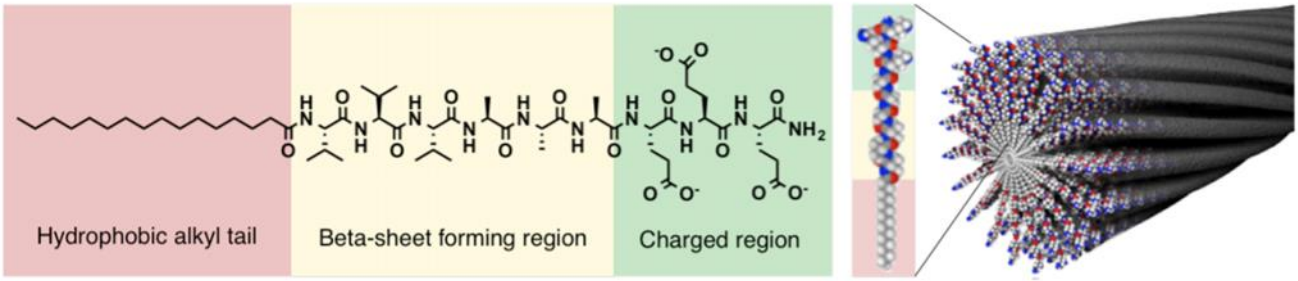

Figure 1.6. Peptide amphiphile structure. PAs are composed of hydrophobic tail and a charged hydrophilic head group, similar to surfactant amphiphiles. These are connected by a short peptide sequence that can form β-sheets through hydrogen bonding, which promotes self-assembly into high aspect ratio nanostructures. Reproduced from ref.[61]

Nanostructures formed by PAs are pathway sensitive, such that the changing the charge, ionic strength, or temperature during assembly modifies the final structure.[52,62] Long PA nanofibers can form liquid crystalline states in solution, which can be shear aligned into anisotropic materials.[63,64] Nanofiber architectures, whether isotropic or aligned, can be fixed with the addition of multivalent ions such Calcium. PAs can also be modified with DNA sequences[65] and host-guest

components[66] to create hierarchical bundles of fibers. The versatility of PAs to create various nanostructures and architectures makes them an excellent candidate for the development biomimetic materials.

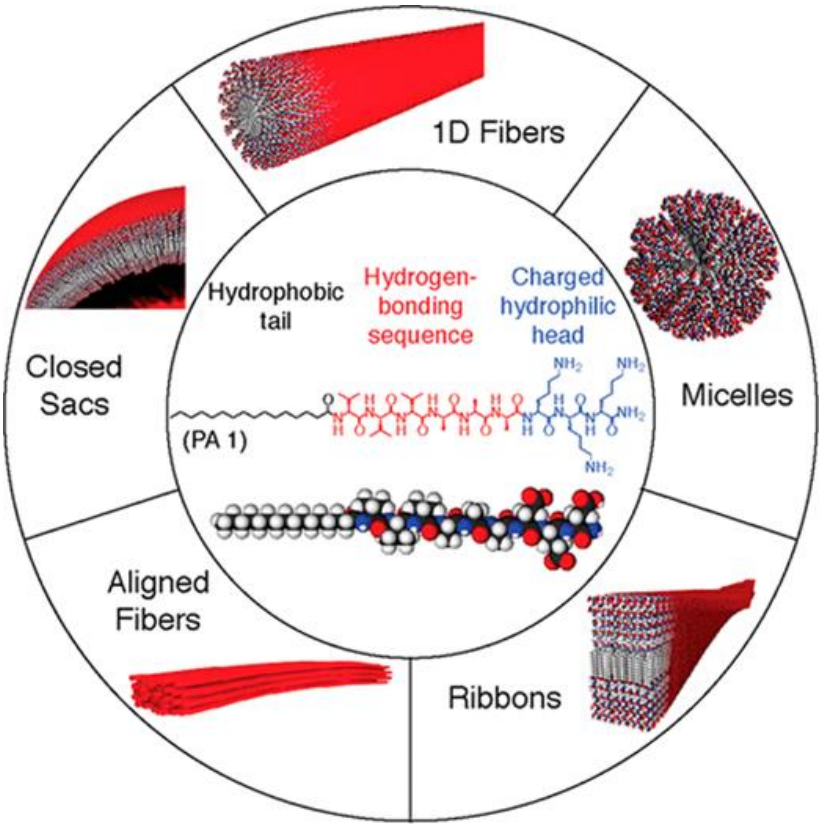

Figure 1.7. Peptide amphiphile assembly into nanostructures. Based on the peptide sequence, PAs can assemble into various shapes such as long cylinders, micelles, twisted ribbons, aligned liquid crystalline materials, and closed sacs. Reproduced from ref.[51]

1.3. Multicomponent supramolecular systems.

The scaffolds formed by PAs can mimic not only the structure of biomaterials such as the ECM, but also the functional properties of natural materials. A common modification is to add ECM mimetic peptides that improve cell adhesion to the ends of the PAs, such as the fibronectin mimetic sequence RGD,[67] or the laminin mimetic IKVAV.[68] Other bioactive peptide sequences

that have been investigated in the Stupp group include epitopes derived from brain derived neurotrophic factor (BDNF),[69] fibroblast growth factor (FGF),[70] and Tenascin-C.[71] In addition, peptide sequences that bind proteins and growth factors have also been explored, including binding sequences for bone morphogenetic protein 2 (BMP2),[72] transforming growth factor β-1 (TGFβ-1),[73] and collagen binding sequences.[74] Bioactive PAs are often co-assembled with bare backbone PAs without a bioactive sequence, in order to minimize crowding and allow the sequence to be accessible to cell receptors and proteins. This similar to the presentation of epitopes in natural materials, such as the distribution of heparin binding groups in collagen 1,[75] or the nanoscale spacing between IKVAV sequences in laminin proteins in the basal lamina.[76]

It is usually presumed that PAs with the same backbone will co-assemble with other, regardless of the bioactive sequence added to the end of the molecule, however, this effect is not well-established. The propensity of two components to mix uniformly within nanostructures is determined by the complementarity of molecular geometry and intermolecular interactions.[77] (**Figure 1.8**) When molecules that assemble via different intermolecular attractions are mixed together, for example a molecule that assembles via hydrogen bonding with one that assembles via π-π stacking, they can self-sort into different assemblies.[78] The complementarity of molecular geometry and size can also lead to self-sorting even when the intermolecular interaction is the same, such as when the orientation of metal coordination complexes does not align between different molecules.[79] In these systems, the enthalpic driving force for like-molecules to interact, or the enthalpic penalty when dislike-molecules interact, overcomes the entropic effect that promotes mixing. This is similar to intermolecular interactions in natural biopolymers, such as the base pairing of complementary DNA strands, or the parallel organization of actin filaments and microtubules in the cell cytoskeleton. Interpenetrating networks of different components are also

essential to proper function of the ECM. The ECM of connective tissues consists of a network of collagen fibrils, surrounded by a fluidic component consisting of various glycosaminoglycans (GAGs) such as hyaluronic acid (HA).[80] (**Figure 1.9**) In these tissues, both collagen and HA play essential roles in directing cell responses. It remains an open challenge to study the role of intermolecular complementarity in the co-assembly and self-sorting of bioactive PA nanofibers.

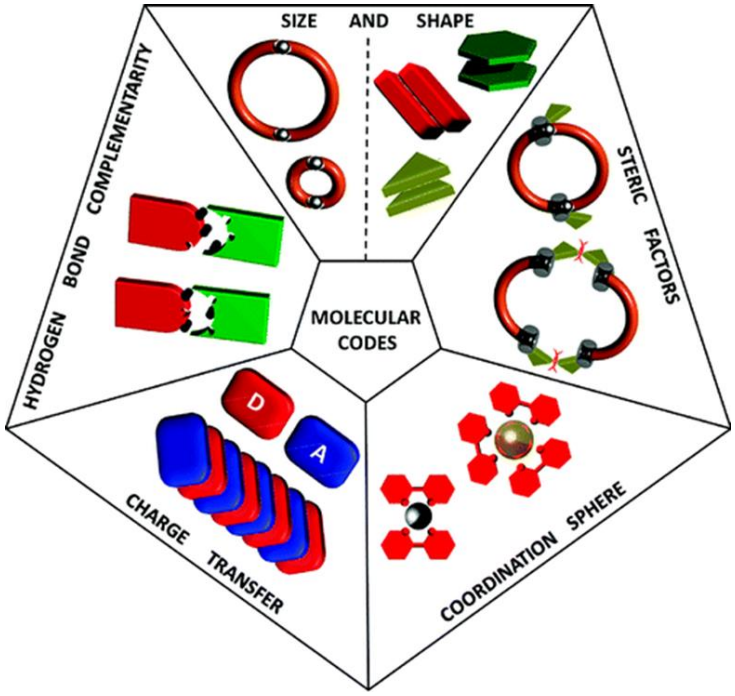

Figure 1.8. Intermolecular complementarity in supramolecular self-sorting. Self-sorting or co-assembly is of multiple components is controlled by complementarity of several factors including size and shape, conformational compatibility, coordination complexes, charge transfer complexes, and hydrogen bond geometry. Reproduced from ref.[77]

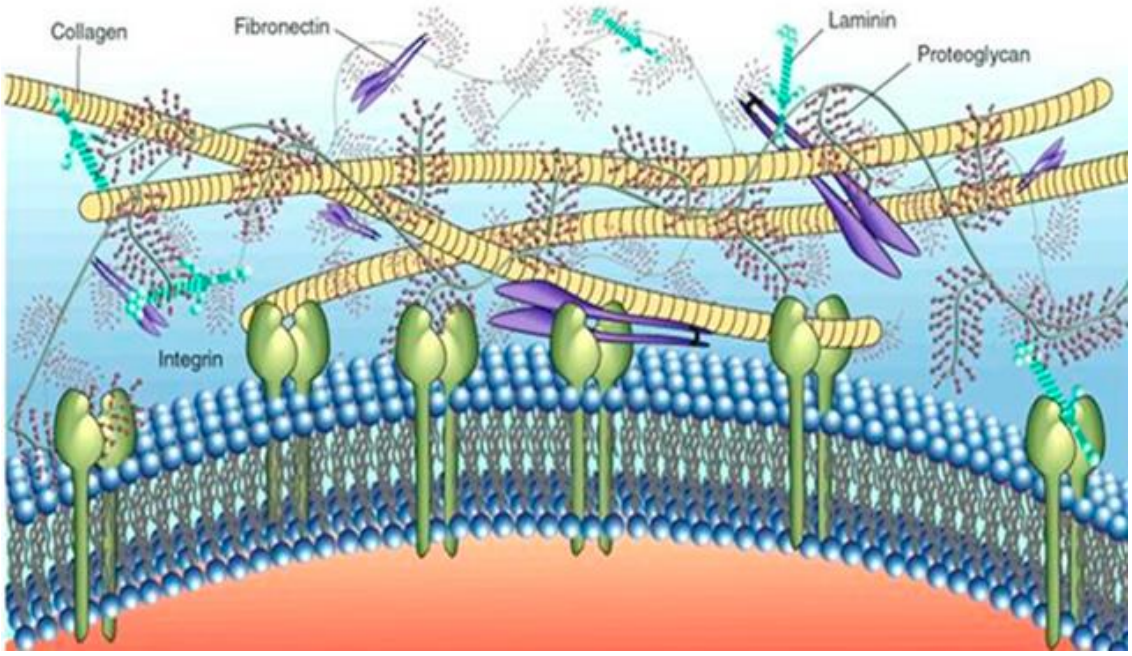

Figure 1.9. Different components of the extracellular matrix. The ECM consists of and interpenetrating network of various fibrous components, such as collagen, hyaluronic acid, and other proteoglycans. Reproduced from ref.[81]

1.4. Biopolymer properties across length scales

The bending stiffness of polymer chains is characterized by their persistence length (l_p), the length separation at which the chain bending fluctuations become decorrelated. (**Figure 1.10**) While polymers typically have persistence lengths of a few nanometers, many biopolymers are much stiffer and have persistence lengths of several microns.[82] When the contour lengths of the fibers are also in the range of several microns, they are called semi-flexible fibers. Semi-flexible fibers include biopolymers such as actin,[83] amyloid fibrils,[84] and even certain filamentous influenza viruses.[85] Actin filaments have a diameter of 7 nms, contour lengths of several microns, and persistence length of about 17 microns. **(Figure 1.11)** The persistence lengths of biopolymers

can be measured either by static imaging of an ensemble of fibers, or by dynamic imaging of a fiber over time. In static imaging, a population of fibers are deposited on a surface and imaged with atomic force microscopy (AFM) or transmission electron microscopy (TEM).[86] In dynamic imaging, fibers are labelled with fluorescent dyes and are measured in solution with fluorescence microscopy.[83] In both methods, the trajectories of the fibers are identified with image analysis algorithms and persistence length is calculated with the semi-flexible fiber theory.

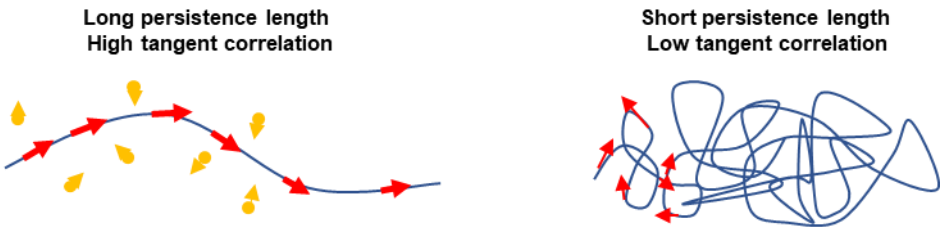

Figure 1.10. Schematic of persistence length of fibers. Long persistence length (left) in a thermal environment corresponds to higher bending stiffness, and higher correlation of tangent vectors. Short persistence length (right) corresponds to lower bending stiffness, and shorter correlation of tangent vectors.

The architecture and physical properties of materials composed of semi-flexible fibers differ drastically from standard polymers. Solutions of semi-flexible biopolymers like collagen fibrils typically exhibit glassy dynamics,[87,88] which results in unusual nonlinear rheological properties like strain-stiffening.[89,90] These mechanical properties have been shown to influence cellular behaviour and stem cell differentiation.[91–93] Scaffold stiffness is well known to control adhesion and spreading of cells through the activation of mechanotransducive pathways.[12] Traction forces produced by cells are transmitted to the scaffold through focal adhesions, and the scaffold deforms based on its elastic properties. Stiff scaffolds enable higher traction forces which promote focal adhesion assembly and activation of the focal adhesion kinase (FAK) signalling

pathways.[94] Stress relaxation, a property of viscoelastic materials, modifies this signalling by allowing the materials to deform without a residual elastic force. Fast relaxing hydrogels, which can be physically remodelled by cellular forces, promotes the cell spreading, focal adhesion formation, and promotes osteogenic differentiation of mesenchymal stem cells (MSCs).[95,96] The microarchitecture and dynamical mechanical properties of biomaterials are therefore of great interest in regenerative medicine applications.

In addition to viscoelastic remodelling, the degradation of the cellular scaffolds in regenerative applications has recently received significant interest. Dynamic remodelling of the ECM is an essential component of natural tissues, as fibroblast cells continuously degrade and reform ECM components.[97] (**Figure 1.12**) ECM components can be degraded by the enzymatic actions of matrix metalloproteinases (MMPs) and reshaped by traction forces.[98] As cells migrate, spread, and differentiate, the properties of the ECM are modified in parallel.[99] Disorders related to disruption of ECM remodelling are responsible for various fibrotic diseases as well as certain cancers.[100] In biomimetic materials, replicating the degradation properties of natural tissue has been shown to play a role controlling 3D tissue organization and in directing the fate of stem cells.[101–103]

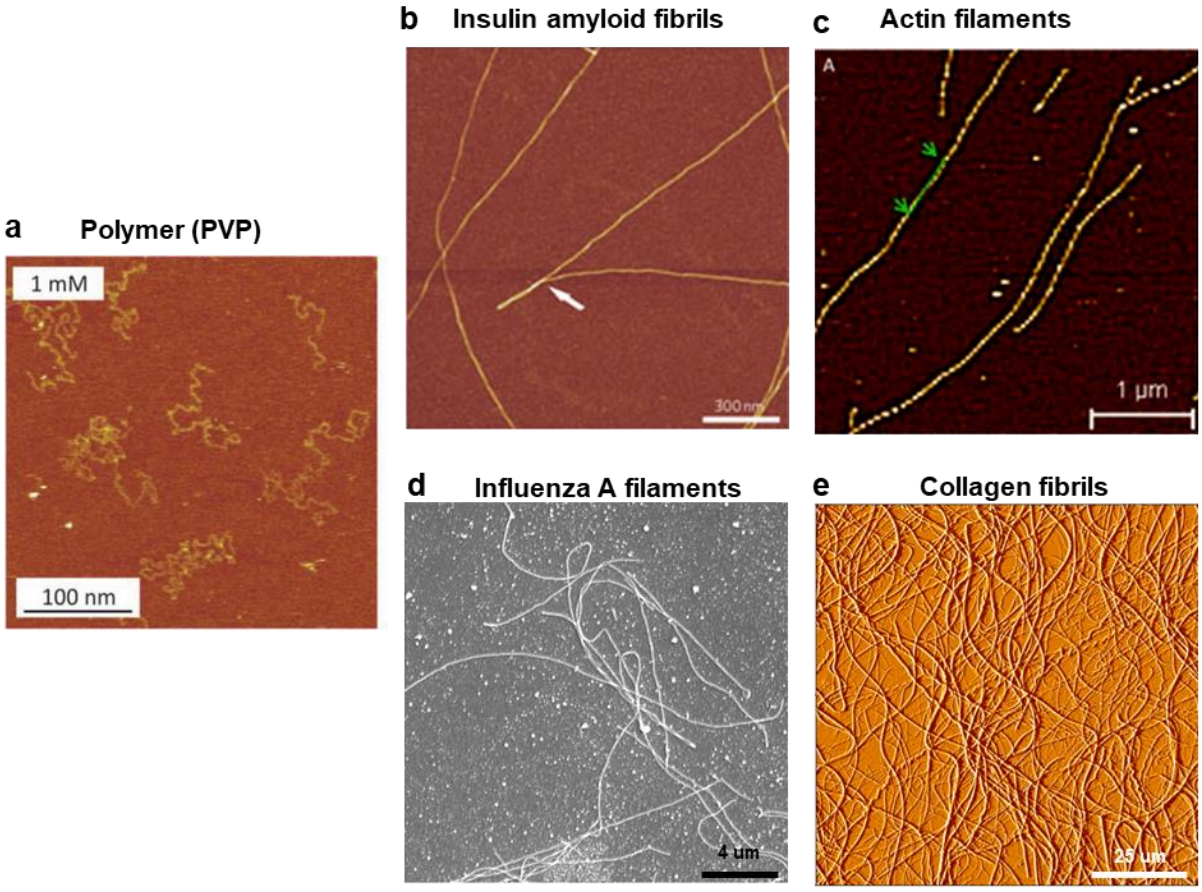

f

Type	Approximate diameter	Persistence length	Contour length
Microtubule	25 nm	~ 1–5 mm	10s of μm
F-actin	7 nm	17 μm	≲ 20 μm
Intermediate filament	9 nm	0.2–1 μm	2–10 μm
DNA	2 nm	50 nm	≲ 1 m
SWNTs	< 1 nm	~ 10 μm	≳ 1 μm

Figure 1.11. Semiflexible biopolymers with long persistence lengths. (a) Chains of Polyvinylpyrrolidone (PVP), a typical polymer has short persistence length of nanometers. Semi-flexible biopolymers have persistence lengths in the micron range, such as (b) insulin amyloid fibrils, (c) Actin filaments, (d) influenza A filaments, and (e) collagen fibrils. (f) A table of common biopolymers and their persistence lengths. Reproduced from refs.[82,84,85,104–106] respectively.

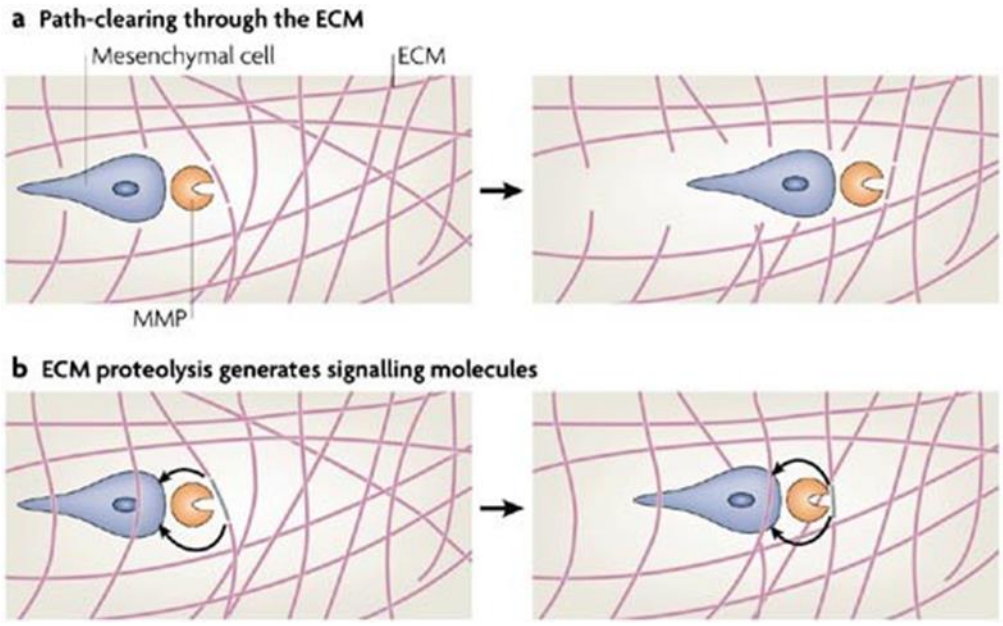

Figure 1.12. Remodeling of the extracellular matrix. The ECM is continuously degraded by cellular forces and MMPs, which generate signals that act in a feedback loop to direct cell behaviour. Reproduced from ref.[98]

1.5. Thesis overview

This thesis aims to uncover the fundamental self-assembly principles of supramolecular nanostructures, and the properties of materials composed of these fibrous materials. Peptide amphiphiles are used to create biomimetic materials and investigate the intermolecularly forces that govern their self-assembly and material properties.

In chapter 2, the twisted ribbon nanostructures formed by class of PAs are investigated by systematically modifying the peptide sequence within the molecule and changing the electrostatic repulsion between the headgroups. These studies show that the supramolecular twist in the β-sheet controls the morphology of the twisted ribbons and can lead to a change in the supramolecular chirality of the nanostructures. A thermodynamic model is developed that explains the formation

of nanostructure in terms of the fundamental intermolecular forces of hydrophobic collapse, hydrogen bonding, and electrostatic repulsion. As charge repulsion between the headgroups is increased, the morphology of the nanostructures changes from ribbons to cylinders, and then to micelles. This study demonstrates the complexity of the interplay between different intermolecular forces and molecular geometry.

Chapter 3 builds on these results to explore a substructure of twisted ribbons which forms double helices. The double helices formed by PAs are shown to have a major and minor groove running on opposite sides of the nanostructure, an unusual geometry that is only found in DNA. The formation of these structures is understood with a theoretical model that combines known theories of amphiphilic self assembly and peptide self-assembly. The stiffness of the assemblies plays an essential role in the formation of the structures. In addition, nanofibers of different stiffnesses are used to create scaffolds for fibroblasts in order to investigate the cellular remodelling of these materials by cells. Networks composed of flexible fibers are more entangled and exhibit viscoelastic deformations, while networks composed of rigids fibers deform and break under cellular traction forces. The degradation and internalization PA nanofibers are also investigated.

Chapter 4 focuses on the multicomponent PA systems, including mixtures of PAs with different peptide sequences, as well as mixtures of PAs with attached protein binding groups. These studies show that PAs with different β-sheet forming sequences can mix or self-sort based on the complementarity of the hydrogen bonding geometry. Supramolecular twist is again found to be an essential parameter that controls the self-sorting behaviour. PAs with the opposite supramolecular chirality self-sort in mixtures to create interpenetrating networks, as the hydrogen bonding orientations are unfavourable to mixing. The self-sorting is studied by incorporating

fluorescent dyes into a subpopulation of the molecules to label each species. This system is then expanded to include a model protein binding PA with biotin tag, which has complementary hydrogen bonding geometry to one of the two components. The biotinylated PA becomes sequestered in the self-sorted nano-assemblies and can selectively bind streptavidin to that component of the interpenetrating network. The co-assembly of a therapeutic PA with a BMP2 binding epitope is also investigated. The inclusion of the BMP2 binding sequence results in hierarchical bundling, which can modify the protein availability and internalization.

In chapter 5, the physical properties of PA assemblies are studied across length scales. The molecular packing of the PAs in nanostructures is investigated by modelling the x-ray and electron diffraction patterns and is found to have a near rectangular lattice with tilted molecules. The mechanical properties of nanofibers at the micron scale are then investigated. These show unusual scaling behaviour at short lengths below ~2 um, corresponding to non-smooth kinks in the fiber shapes. Networks of nanofibers in solution are then studied by labelling a subpopulation of fibers with fluorescent dyes, and imaging with video rate fluorescence microscopy. The correlation functions calculated from these measurements show the networks exhibit sub diffusive glassy dynamics, similar to biopolymers lick actin and collagen. Interestingly, the difference between the dynamics of stiff and rigid fiber networks emerges only at high concentrations as collisions between fibers become increasingly significant.

The thesis closes with chapter 6, where future directions for the study of self-assembling biomaterials are discussed. These included further investigation of the fundamental intermolecular forces in PA self-assembly, and how they can be manipulated to create more complex multicomponent systems. Additional studies to investigate cell-material interactions in PA systems and possible biomaterial applications as cellular scaffolds are proposed.

2. Supramolecular twist controls morphology of self-assembled nanostructures

2.1. Objectives and significance

The relation between the amino acid sequence and the morphology of supramolecular peptide nanostructures is generally difficult to predict due to the complex energy landscape of possible peptide configurations. Here, self-assembling peptide amphiphiles with six amino acid β-sheet forming domains that form twisted nanoribbons in water were investigated, and a self-assembly model that relates the supramolecular twist and the shape of the nanostructures was developed. The ribbon dimensions were found to be determined by a balance between the energetically favourable packing of molecules in the centre of the nanostructures, the unfavourable packing at the edges, and the strain in the β-sheet. Interestingly, a change in the supramolecular chirality of the nanostructures is observed as the peptide sequence is systematically modified. By increasing charge repulsion, it was found that the twisted ribbons change morphology, first to long cylinders, and then to disordered fragments and micelles. These findings provide insight into the self-assembly mechanism of twisted supramolecular peptide assemblies.

2.2. Introduction

Self-assembling peptide based nanostructures have received significant attention for biomedical applications such as extracellular matrix mimetics[45] and drug delivery vehicles.[107] Peptide amphiphiles (PAs) are a class of biomimetic molecules that consist of a hydrophobic lipid tail and a hydrophilic peptide headgroup, and can incorporate a β-sheet forming peptide region to self-assemble into high aspect ratio nanostructures.[50] PAs have been reported to create shapes like flat nanobelts,[54] scroll-like cochleates,[108] twisted ribbons,[109] cylinders,[50] and spherical micelles.[110]

The morphology of PA nanostructures has been associated with changes in functional properties such as the presentation of bioactive signals.[69,74]

Of the range of nanostructures formed by PAs, high aspect-ratio twisted ribbons containing β-sheets are of particular interest due to their potential uses in biomedicine such as scaffolds for regenerative medicine,[56] delivery vehicles for immunotherapeutic epitopes,[111] or for the controlled release of drugs.[112] A relation between the twist of the β-sheet and nanostructure morphology has been demonstrated in several self-assembling peptide systems. Models of β-sheet stacking in amyloid fibrils have incorporated the geometric deformation of twisted β-sheets and an energy penalty of the open face at the edges of ribbon-like fibrils.[113–115] Inclusion of peptides with more hydrophobic side chains has also been observed to increase the dimensions of β-sheet stacks.[116] These models show that the aggregation of β-sheets is controlled by the torsional strain in the β-sheet. As fibrils grow wider, β-sheets further from the centre of the assemblies become increasingly deformed from their ideal configuration, limiting the lateral growth of fibrils. Changes in β-sheet twist can result in nanostructures with shapes such as single sheet tapes, ribbons, helices, and tubes.[117]

The morphology of structures formed by different PAs has been explored empirically, however, it remains an open challenge to understand the mechanistic relation between the peptide sequence in a PA and the resulting nanostructure.[51] In this work, the self-assembly of a set of twisted ribbon PAs, previously developed as scaffolds for regenerative medicine applications,[53] was systematically explored and the role of the peptide sequence and electrostatics was investigated. The molecules are composed of a palmitic acid tail, a charged head group with three glutamic acids, and six hydrophobic amino acids in the middle, consisting of a varying sequence of alanines and valines (**Table 2.1**). Cryogenic transmission electron microscopy (Cryo-TEM)[118]

and liquid atomic force microscopy (AFM)[119] was used to study the nanostructures formed by these PAs, and a model of PA self-assembly appropriate for amphiphilic twisted ribbons was developed. The model includes the twist of β-sheets as well as the three-dimensional geometry of ribbons. The supramolecular chirality of PA nanostructures and its role in controlling morphology is investigated, as well as the role of head group charge in controlling the nanostructure shape.

Table 2.1. Molecular Sequences of **PAs 1-5**.

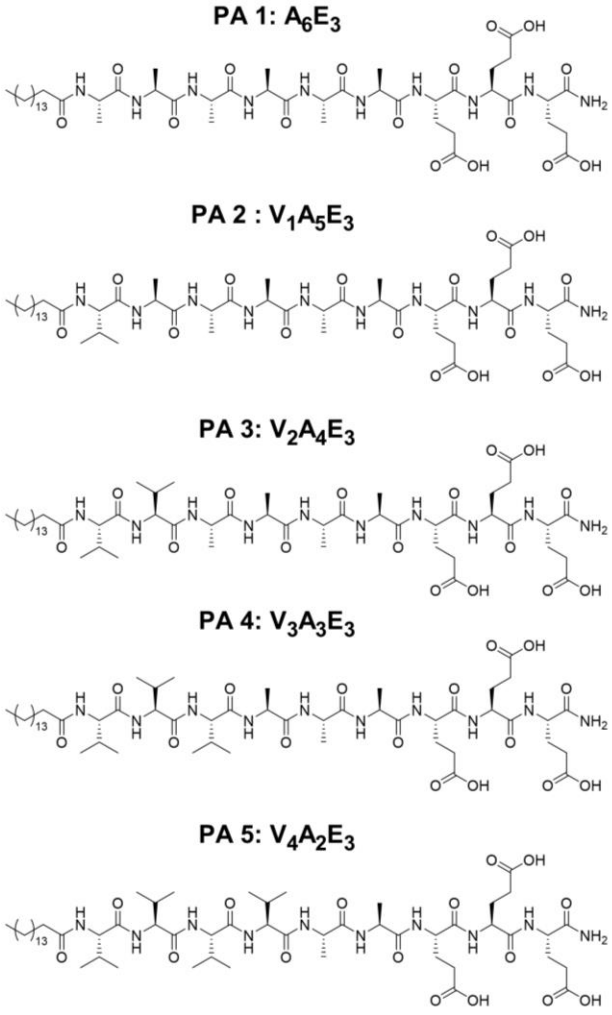

2.3. Results and Discussion

2.3.1. Self-assembly of twisted peptide amphiphile nanostructures

PA 4 (**Figure 2.1a**) has been previously explored by the Stupp group for applications in bone and cartilage regeneration;[72,73] however, its self-assembly behaviour is not fully understood. The samples were by annealing a 10 mM solution of **PA 4** with 20 mM NaOH (pH 8.5) for 30 mins at 80°C, and cooling to room temperature at 1°C/min.[52] This procedure results in high-aspect-ratio nanostructures several microns long (**Figure 2.2**). Liquid AFM images of the PA assemblies show polydisperse structures with a periodically varying height characteristic of twisted ribbons (**Figure 2.1b**). The morphology of twisted ribbons is described by the width and the pitch length (**Figure 2.1c**), where the pitch length is the distance for a full 2π rotation of a helical structure, and a shorter pitch length corresponds to higher rotation angle per unit length. The narrowest structures have a low cross-sectional aspect ratio with a width of 9.5 nm and a thickness of 8 nm, and a pitch length of 120 nm. While the twisted morphology of the narrow structures is clear in the AFM images, it is not always observable in Cryo-TEM (**Figure 2.1d**). When **PA 4** is prepared with 5 mM NaOH (pH 5.5) to reduce the charge on the glutamic acid headgroup, there is an increase in the width of the nanostructures to the point where the twisted ribbon morphology becomes visibly clear in Cryo-TEM (**Figure 2.1e**).

The pitch lengths and ribbon widths of these nanostructures are higher at 5 mM NaOH (pitch length 323 ± 15 nm; width 14.1 ± 0.4 nm) compared to 20 mM NaOH (pitch length 250 ± 17 nm; width 11.8 ± 0.3 nm) (**Figure 2.1f**). Within individual nanostructures both the width and pitch length have high long-range order (**Figure 2.3**), confirming that the variance is due to polydispersity across nanostructures. There is a positive correlation between the pitch length and width (Pearson's correlation coefficient = 0.65), where longer pitch lengths are correlated with

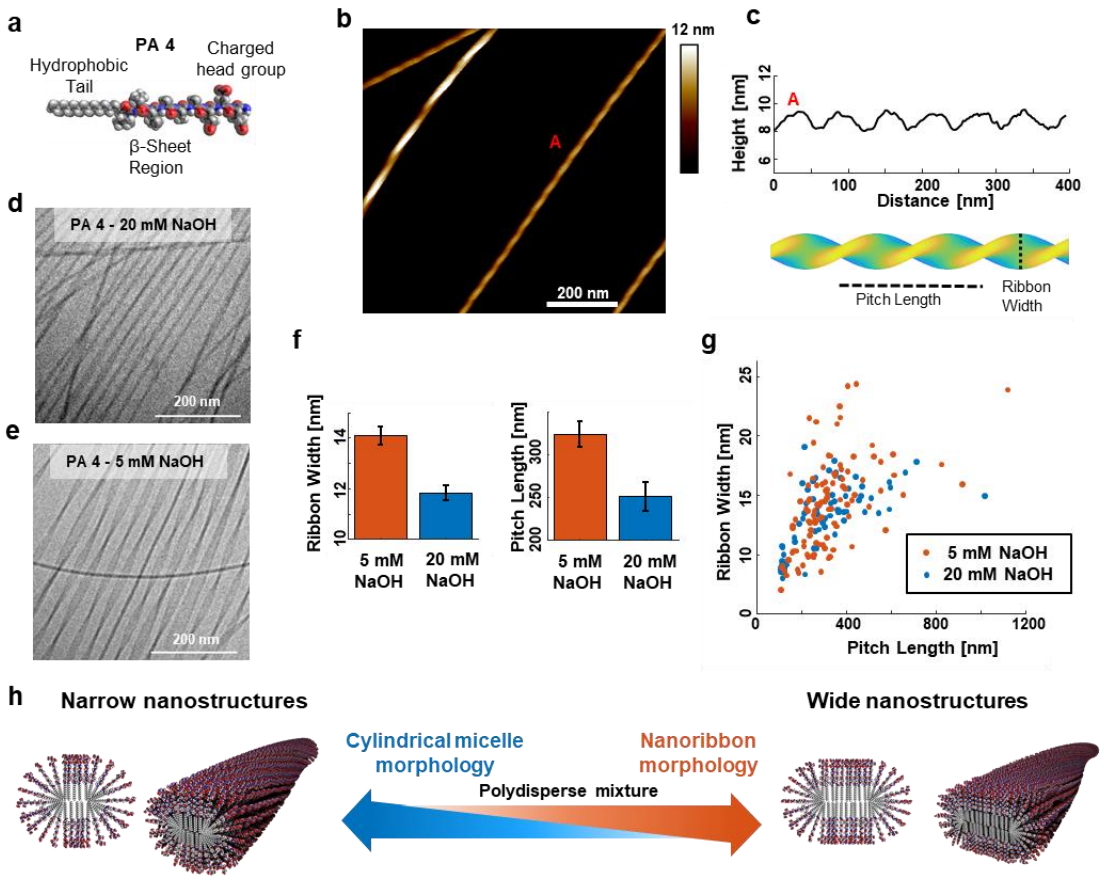

Figure 2.1. Experimental characterization of twisted ribbons formed by **PA 4**. (a) Schematic of peptide amphiphile molecule with a V_3A_3 β-sheet region. (b) Liquid AFM image of high aspect ratio polydisperse nanostructures, and (c) an example height profile showing a characteristic twisted morphology, (d) Cryo-TEM images of PA 4 prepared with 20 mM and (e) 5 mM NaOH. (f) Comparison of ribbon width and pitch length and (g) plot of the relationship between pitch lengths and widths of nanostructures. Pearson's correlation coefficient = 0.65, p-value<10^{-26}, N=211 nanostructures. (h) Schematic polydisperse population of ribbons with different widths.

wider ribbons (**Figure 2.1g**). A schematic of the polydisperse population of ribbons is shown in (**Figure 2.1h**). However, there is no statistically significant effect of pH on the relationship between width and pitch length (**Table 2.2** Linear regression model of pH dependence of PA 4). This suggests that while electrostatic repulsion between molecules can modify the distribution of the polydisperse PA nanostructures, the underlying morphology remains unchanged. This is likely

due to screening effects of bound counterions at the surface. As described by Manning, a nanostructure with a non-zero bare surface charge and dimensions much larger than the Debye length (~1.5-3 nm here) will condense its counterions, greatly reducing the effective surface charge.[120]

Table 2.2 Linear regression model of pH dependence of PA 4

Estimated Coefficients:
Linear regression model: Width ~ 1 + Pitch*pH
Estimated Coefficients:

	Estimate	SE	tStat	pValue
(Intercept)	8.2991	0.59175	14.025	**7.4854e-3**
Pitch	0.017879	0.0020115	8.8885	**3.0593e-16**
pH_2	-0.97187	0.70636	-1.3759	**0.17034**
Pitch:pH_2	4.517e-05	0.002715	0.016633	**0.98675**

Number of observations: 211, Error degrees of freedom: 207
Root Mean Squared Error: 0.156
R-squared: 0.536, Adjusted R-Squared 0.529
F-statistic vs. constant model: 79.7, p-value = 2.52e-34

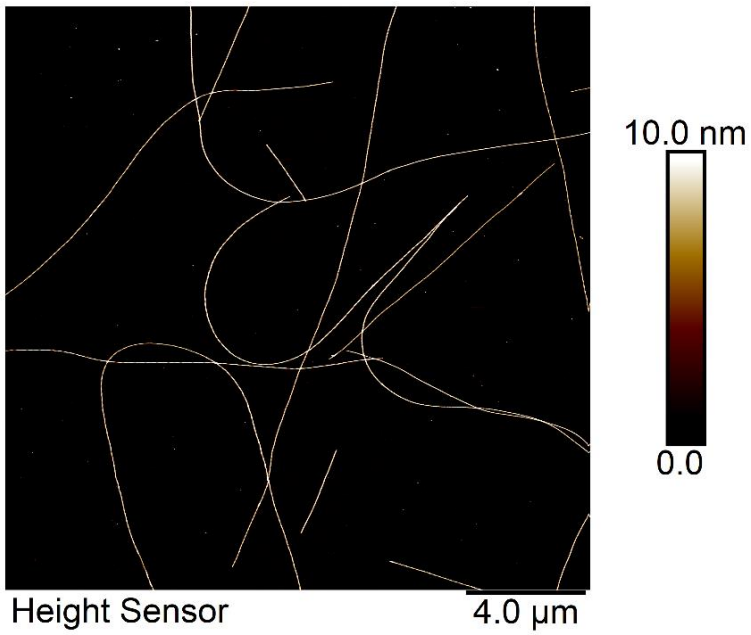

Figure 2.2. Low magnification AFM image of long **PA 4** nanostructures.

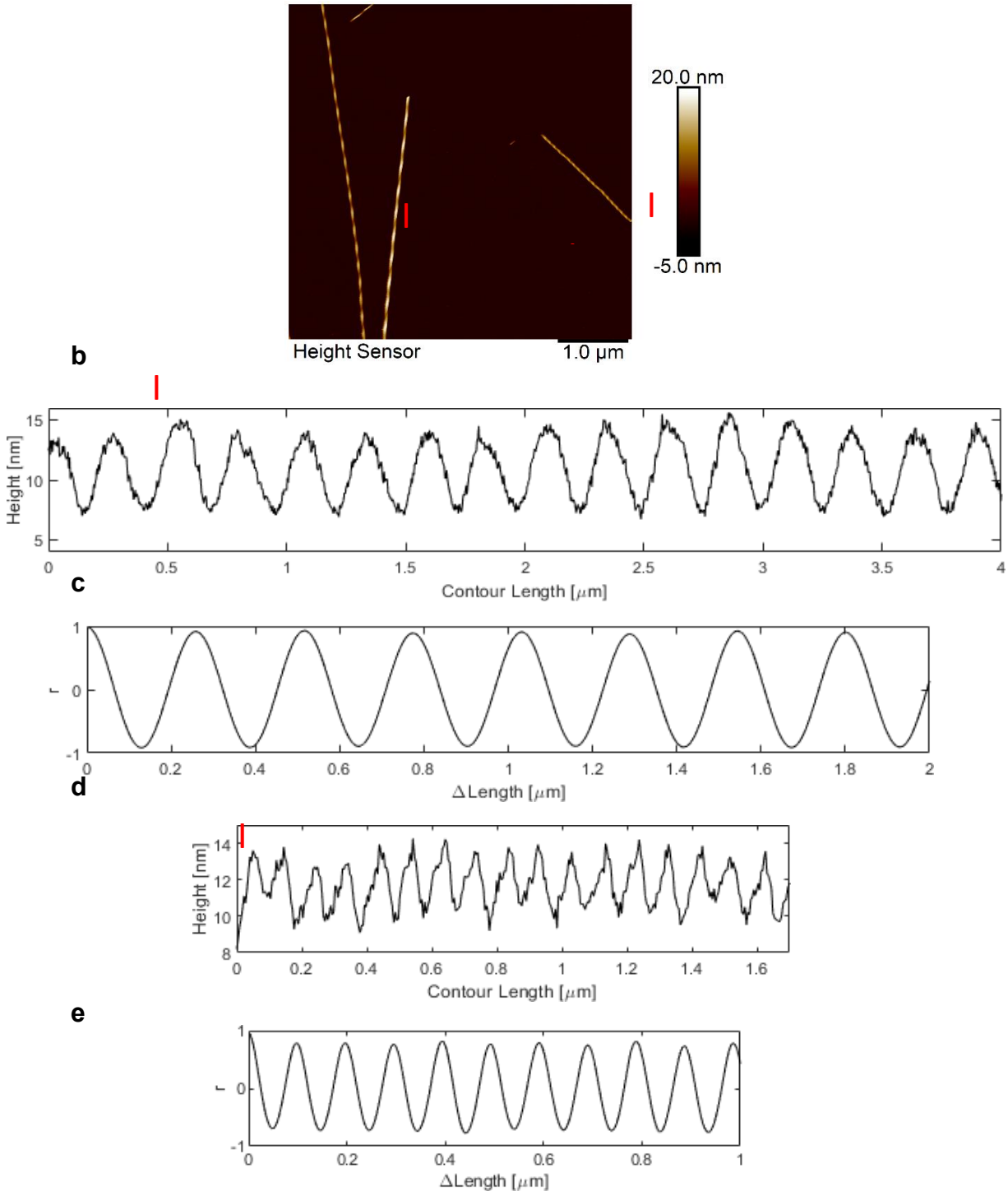

Figure 2.3. Long range order in PA 4 nanostructures. (a) AFM image with labelled nanostructures. (b & d) Height profiles and (c & e) autocorrelation functions of heights of structures I and II, respectively.

To understand this effect, a self-assembly model of twisted ribbons composed of β-sheet forming amphiphiles was developed (**Figure 2.4a**). The twisted ribbons are treated as a rectangularly packed bilayer of molecules in the centre with length L and width W, with cylindrically packed molecules at the edges, and terminal groups at the ends of the nanostructures. This model of rectangular packing is supported by wide angle X-ray scattering (WAXS), which show the characteristic 4.7 Å spacing of molecules along the β-sheets, and a lateral spacing of 9 Å between β-sheets (**Figure 2.5**). The model uses the micelle aggregation theory developed by Tanford, based on a balance of the energy penalty of exposing lipid tails and hydrophobic side chains to water, against the electrostatic repulsion between adjacent charged headgroups.[121,122] The free energy change associated with the transfer of a monomer into an assembly is described with an expression of the form $\frac{\Delta\mu_i^0}{k_BT} = \frac{\Delta\mu_{transfer}^0}{k_BT} + \sigma a_i + K/a_i$. Here, $\Delta\mu_{transfer}^0$ is the constant negative free energy associated with the transfer of the hydrophobic region of the molecule from water to a hydrophobic assembly; σ is the hydrophobic energy per unit area for the residual contact with water at the interface of the assembly; K is the electrostatic coefficient for the headgroup repulsion; and a_i is the effective average headgroup area occupied by a molecule in one of the possible states, either cylindrical, ribbon, or the terminal end.

We describe the packing geometry of the molecules in each state in a manner similar to the packing parameter theory of Israelachvili (**Figure 2.4a**).[26] The cylindrically packed edges with larger headgroup spacing are electrostatically more favourable than the closely packed rectangular regions, but have higher hydrophobic penalty due to the larger residual contact with water. An energy term for the distortions of the twisted β-sheet from its ideal configuration due to steric hindrance from neighbouring sheets is included as an ansatz $f = -H_0 + \epsilon\frac{W}{P}$; where $-H_0$ is the

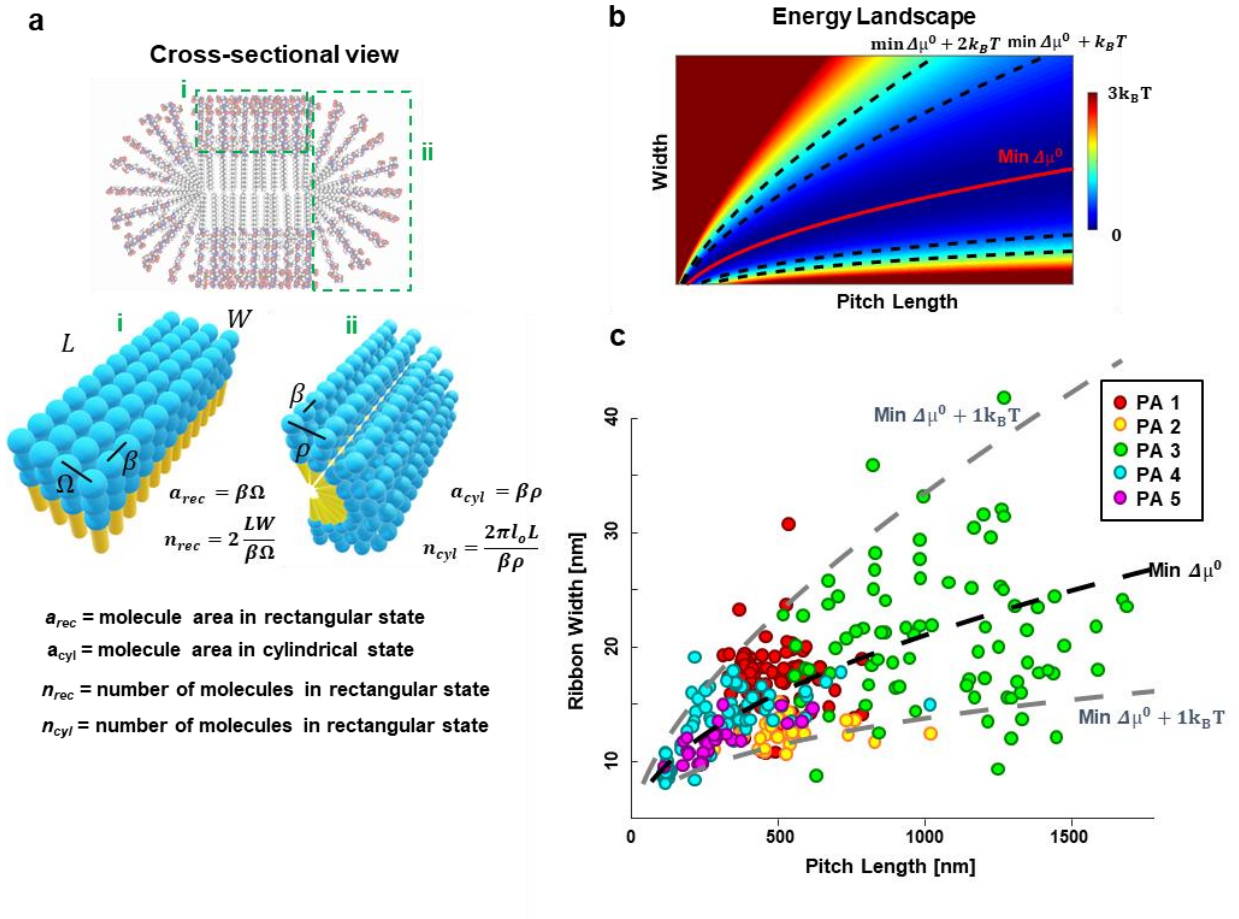

Figure 2.4. PA nanostructure self-assembly model and results. (a) Schematic of self-assembly model of ribbons, consisting of rectangularly packed center and cylindrical edges. Geometrical parameters of molecular spacing (β, Ω, ρ), morphology (*L*, *W*), molecule number (n_i) in each state are indicated. (b) Scaled energy landscape in long nanostructure regime as a function of pitch length and width. Red line indicates the minimum energy condition, and dotted black lines indicate contour lines at a constant energy above the minimum. (c) Plot of the pitch length and width of individual nanostructures for PAs **1-5**, with a fit of the minimum energy curve in red and the curves calculated for the minimum energy $\pm 1k_BT$ curves in black. N=355 nanostructures.

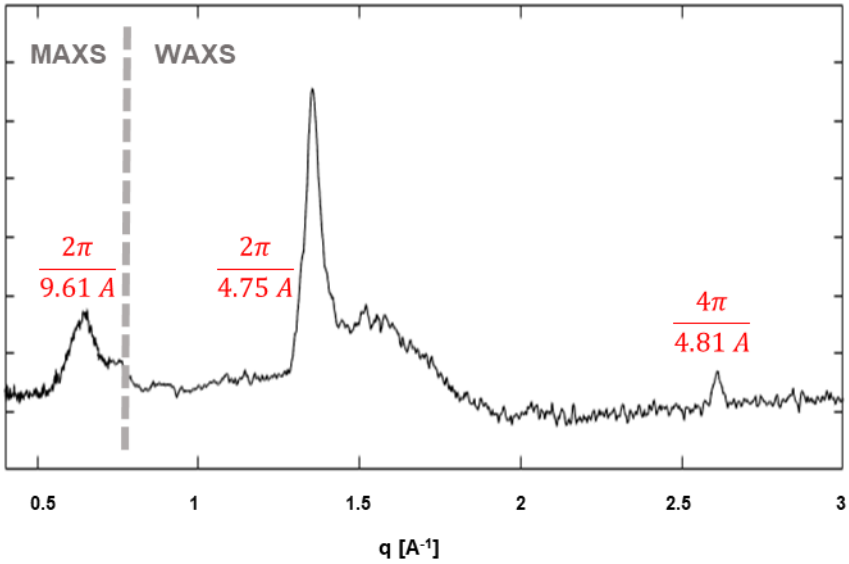

Figure 2.5. X-ray diffraction of PA 4 nanostructures at 20 mM NaOH in MAXS and WAXS regions with peak positions indicated.

negative energy change per molecule due to formation of hydrogen bonds, in units of k_BT; and ϵ is a dimensionless coefficient for the β-sheet strain, related to the pitch length P and width W of the nanostructure. The proportions of molecules in each discrete state are allowed to vary, along with the total particle number. Wider ribbons therefore have more molecules per unit length, but a smaller proportion of molecules are in the cylindrically packed state. The average free energy change per molecule in the complete structure is the sum of the energy change associated with each state, weighted by the proportion of molecules in that state $g_i = \frac{n_i}{N_{Total}}$ as described in **Figure 2.4a**:

$$\frac{\Delta\mu^0}{k_BT} = \frac{\Delta\mu^0_{transfer}}{K_BT} + g_{rib}\left(\sigma a_{rib} + \frac{K}{a_{rib}} + f\right) + g_{cyl}\left(\sigma a_{cyl} + \frac{K}{a_{cyl}} + f\right) + g_{end}\left(\sigma a_{end} + \frac{K}{a_{end}}\right) \qquad (2.1)$$

The equilibrium condition can be found by minimizing the free energy change with respect to the width. This gives an expression for the width of the rectangular region in the regime of long nanostructures, where the contribution of the terminal ends is negligible ($g_{end} \approx 0$).

In the limit of long fibres ($L \gg l_0$) the last term can be dropped as $n_{end} \ll n_{rib} + n_{cyl}$ and so $g_{end} \approx 0$.

$$\frac{\Delta\mu^0}{k_BT} = \frac{\Delta\mu^0_{transfer}}{K_BT} + g_{rib}\left(\sigma a_{rib} + \frac{K}{a_{rib}} + f\right) + g_{cyl}\left(\sigma a_{cyl} + \frac{K}{a_{cyl}} + f\right) \qquad (2.2)$$

The equilibrium condition can be found by minimizing the free energy change with respect to the width. Differentiating (2.1) with respect to W gives:

$$\frac{(\Delta\mu^0)'}{k_BT} = g'_{rib}\left(\frac{K}{a_{rib}} + \sigma a_{rib} + f(W)\right) + g_{rib}f'(W) + g'_{cyl}\left(\frac{K}{a_{cyl}} + \sigma a_{cyl} + f(W)\right) + g_{cyl}f'(W) \quad (2.3)$$

where $g_{rib} = \frac{n_{rib}}{n_{rib}+n_{cyl}}$, and $g_{cyl} = \frac{n_{rib}}{n_{rib}+n_{cyl}}$,

so that $g_{rib} = 1 - g_{cyl}$ and $g'_{rib} = -g'_{cyl}$. (2.4)

and (2.5)

substituting (2.4) and (2.5) into (2.3) gives:

$$\frac{(\Delta\mu^0)'}{k_BT} = -g'_{cyl}\left(\frac{K}{a_{rib}} + \sigma a_{rib} + f(W)\right) + (1 - g_{cyl})f'(W) + g'_{cyl}\left(\frac{K}{a_{cyl}} + \sigma a_{cyl} + f(W)\right) + g_{cyl}f'(W)$$

$$= g'_{cyl}\left(K\left[\frac{1}{a_{cyl}} - \frac{1}{a_{rib}}\right] + \sigma(a_{cyl} - a_{rib})\right) + f'(W) \qquad (2.6)$$

From the model,

$$g_{cyl} = \frac{n_{cyl}}{n_{rib}+n_{cyl}} = \frac{1}{1+\frac{n_{rib}}{n_{cyl}}} = \left(1 + \frac{W a_{cyl}}{\pi l_o a_{rib}}\right)^{-1}$$

And so $$g'_{cyl} = -\left(1 + \frac{Wa_{cyl}}{\pi l_o a_{rib}}\right)^{-2} \frac{a_{cyl}}{\pi l_o a_{rib}} \quad (2.7)$$

Substituting (2.7) into (2.6) gives

$$\frac{(\Delta\mu^0)'}{k_B T} = -\frac{a_{cyl}}{\pi l_o a_{rib}} \frac{1}{\left(1+\frac{Wa_{cyl}}{\pi l_o a_{rib}}\right)^2} \left(K\left[\frac{1}{a_{cyl}} - \frac{1}{a_{rib}}\right] + \sigma(a_{cyl} - a_{rib})\right) + f'(W) \quad (2.8)$$

We use a simple geometric argument to find an appropriate expression for f(W), the elastic energy of deformation. In a system where the twist angle between molecules is $\approx 0^o$ and the pitch length approaches infinity, sheets can stack in parallel with no deformation. At non-zero twist, twisted sheets will deform as they are forced farther from the central axis of rotation, which is given by the width of the nanofiber. The simplest expression which satisfies these two conditions $f(W) \sim -H_0 + \epsilon \frac{W}{P}$ is taken as an ansatz, where the additional constant H_0 is added as the constant energy of hydrogen bond formation. Using $f(W) = -H_0 + \frac{\epsilon}{P} W$, gives

$$f'(W) = \frac{\epsilon}{P} \quad (2.9)$$

Substituting (2.9) into (2.8), and setting $\frac{(\Delta\mu^0)'}{k_B T}$ to 0 leads to a calculation of W_{min}

$$W_{min} = \frac{\pi l_o a_{rib}}{a_{cyl}} \left(\sqrt{\frac{P}{\epsilon} \frac{a_{cyl}}{\pi l_o a_{rib}} \left(K\left[\frac{1}{a_{cyl}} - \frac{1}{a_{rib}}\right] + \sigma(a_{cyl} - a_{rib})\right)} - 1\right)$$

Rewritten in a more convenient form, and using the definitions of the molecular spacing terms a_{rib} and a_{cyl}:

$$W = -\frac{\pi l_o \Omega}{\rho} + \frac{\pi l_o \Omega}{\rho} \sqrt{\frac{1}{\epsilon} \frac{\rho \mathrm{B} \sigma (\rho - \Omega)}{\pi l_o \Omega} \left(1 - \frac{\frac{K}{\sigma}}{\rho \Omega \mathrm{B}^2}\right)} P^{\frac{1}{2}} \quad (2.10)$$

We find that the width grows with the pitch length as $W \sim P^{\frac{1}{2}}$. Here l_0 is the length of the molecules; B is the β-sheet spacing; Ω and ρ are the lateral spacings of the rectangular and cylindrical states, respectively. The model indicates that within the hydrophobic dominated ribbon regime, molecules will stack into the energetically favourable rectangular state until the strain energy penalty of an additional increase in width exceeds the energy cost of a cylindrical edge. The energy landscape calculated numerically from this model (**Figure 2.4b**) shows that the variance of the width is also expected to increase with longer pitch length, as variations in width are less penalized in low twist, long pitch length, nanostructures.

We next measured the morphology of nanostructures formed by five PAs with increasing proportion of valines using AFM (**PA 1**, **PA 2**, **PA 4**, and **PA 5**) and Cryo-TEM (**PA 3**). From the micrographs, there is an excellent agreement of the pitch length-width relationship with the predicted behaviour across the set of molecules (**Figure 2.4c**). Cryo-TEM images were used for **PA 3** as it forms wide twisted ribbons which tend to break during AFM imaging and create artifacts. Additional images for all molecules are provided in **Figure 2.7**-**Figure 2.9**, and the measurements for each PA are shown in **Figure 2.10**. The observed polydispersity of nanostructures likely originates in nucleates early in the self-assembly process, which become trapped in local minima as the structures grow in length. The non-dimensional ϵ is left as a fitting parameter, while the other parameters are calculated from counterion condensation theory as described below,[120] measured from X-ray diffraction **Figure 2.11** and **Table 2.3**, or the AFM imaging. Model fitting and parameter details are provided in the following section, and in **Table 2.4** and **Table 2.5**.

Calculation of electrostatic repulsion parameter K

Since the model has more parameters than fitting coefficients, Manning's theory of counter ion condensation is used to calculate an approximate value of the electrostatic energy term.[120] Manning theory predicts the effective charge per unit area of an object in a dilute electrolyte solution, accounting for the screening effect counterions bound to the surface. Since this is a theory of charged surfaces, it is not expected to be numerically accurate for PA fibers, where charged residues may be located below the surface and not accessible for counterion screening. The electrostatic potential of a charged membrane in electrolyte solution is given by:

$$Uele = \frac{Q^2 \lambda_D}{\epsilon \epsilon_0} \frac{1}{A}$$

$$\frac{Uele}{N_m} = \frac{q^2 \lambda_D}{\epsilon \epsilon_0} \frac{1}{a_{rib}}$$

$$= \frac{e^2 N_{eff}^2 \lambda_D}{\epsilon \epsilon_0} \frac{1}{a_{rib}}$$

$$K = \frac{e^2 N_{eff}^2 \lambda_D}{\epsilon \epsilon_0}$$

For ribbons, the effective charge density is the critical charge density at which counterions condense:

$$\sigma_{crit} = -\frac{e\kappa \ln(\kappa l_B)}{2\pi l_B}$$

$$\frac{N_{eff}}{N} = \frac{\sigma_{crit}}{Ne/a_{rib}}$$

$$N_{eff} = \frac{\kappa \ln(\kappa l_B)}{2\pi l_B} a_{rib}$$

We calculate:

$$q = eN_{eff} \sim 8.1 \times 10^{-21}\ C$$

$$K \sim 2.0 \times 10^{-22}\ J\ nm^2$$

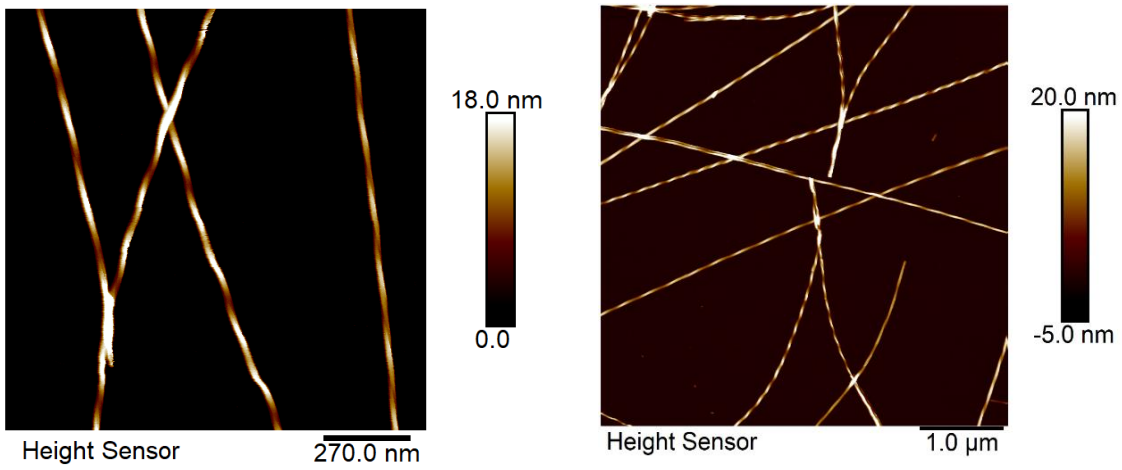

Figure 2.6. Additional AFM images of PA1.

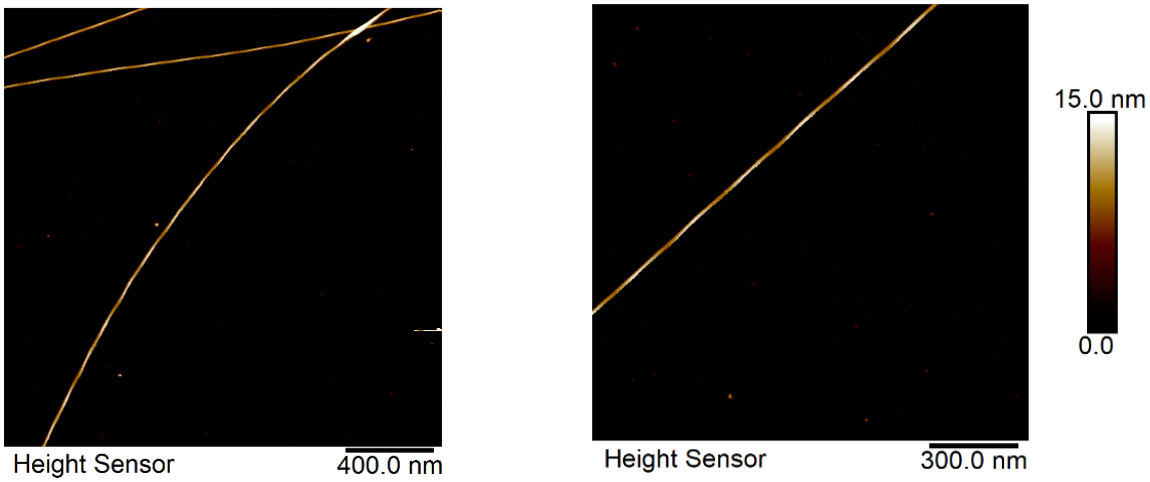

Figure 2.7. Additional AFM images of PA2.

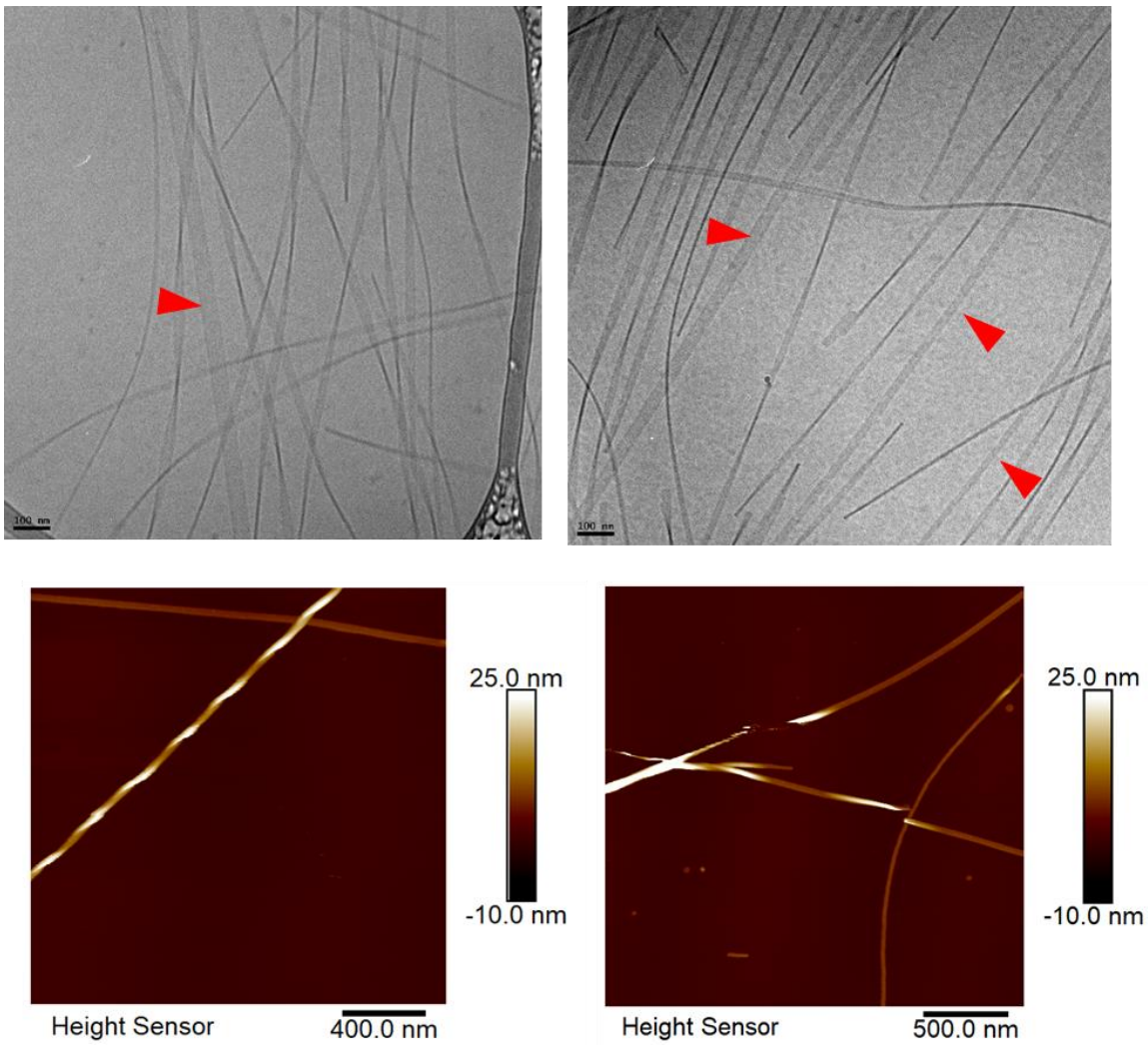

Figure 2.8. Cryo-TEM and AFM images of PA3. Flat untwisted ribbons are indicated with red arrows in cryo-TEM images.

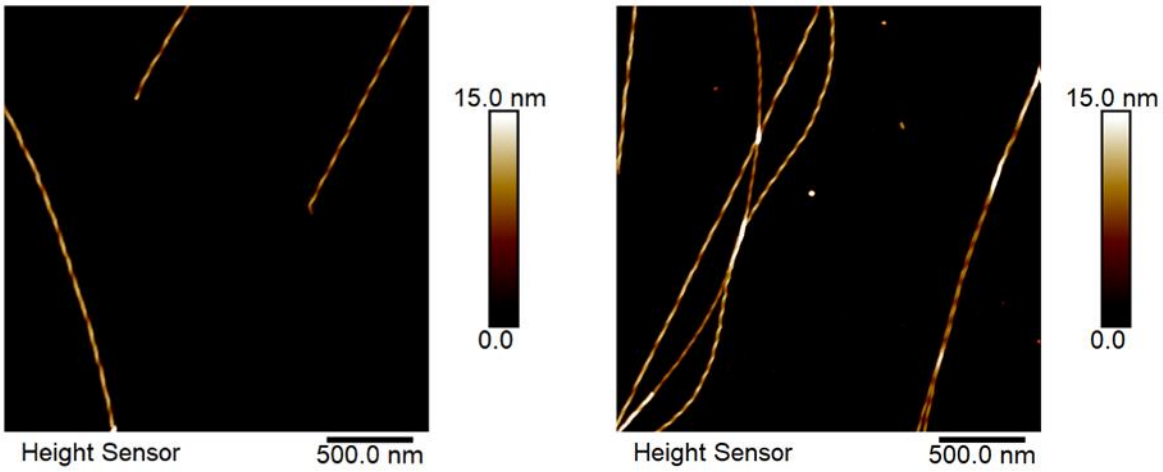

Figure 2.9. Additional AFM images of PA5.

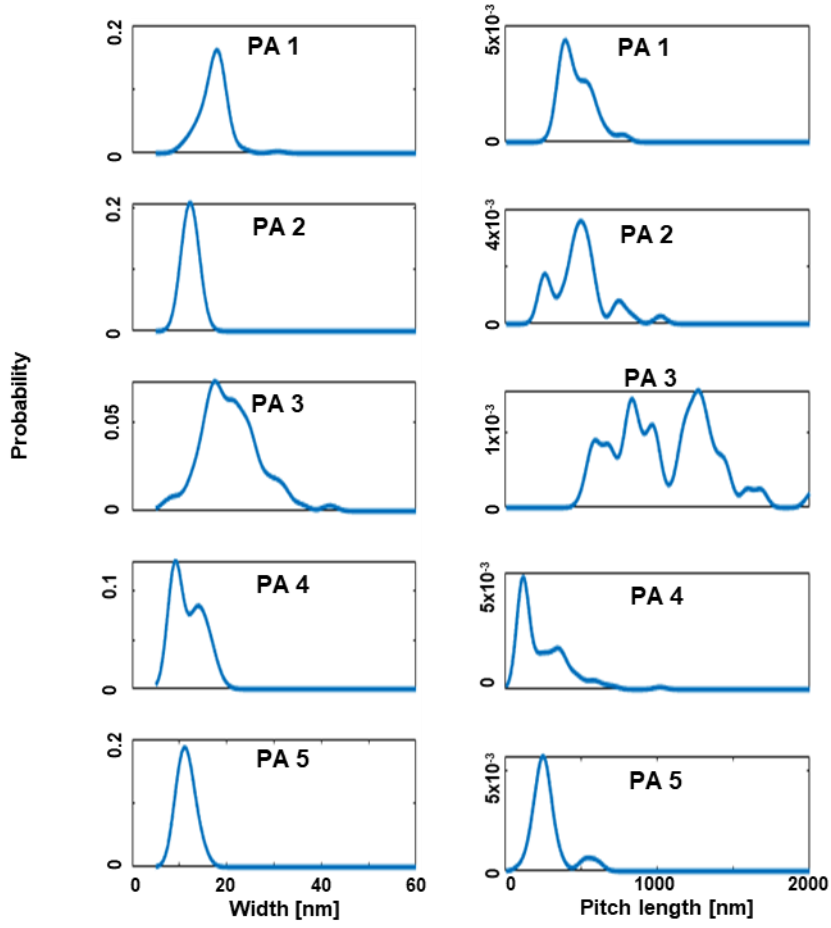

Figure 2.10. The distributions of measured fiber widths and pitch lengths at 20 mM NaOH for all PAs. The distributions are generated using a normal kernel smoothing function with a bandwidth of 1.5nm for widths and 40nm for pitch length.

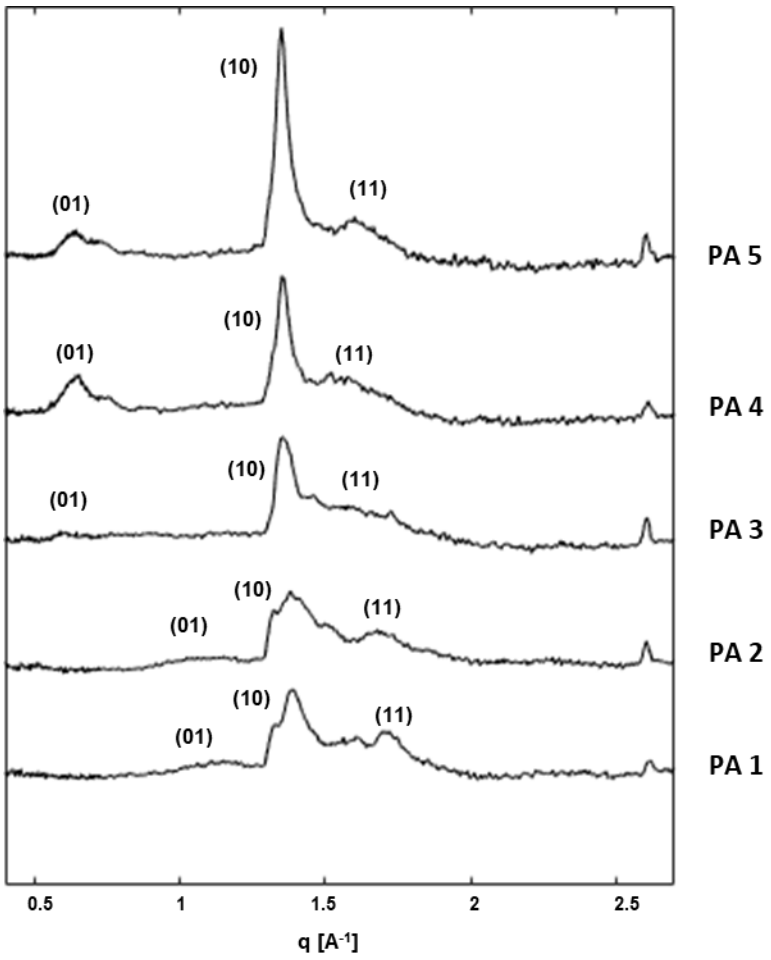

Figure 2.11. WAX of diffraction patterns of PAs 1-5 prepared at 20 mM NaOH. The analysis of peak positions is provided in **Table 2.3.** Lattice calculation from analysis of peak positions from diffraction measurements of PAs 1-5 prepared at 20 mM NaOH..

Table 2.3. Lattice calculation from analysis of peak positions from diffraction measurements of PAs 1-5 prepared at 20 mM NaOH.

PA	$(\mathbf{01})$ [Å^{-1}]	**Ω** [Å]	$(\mathbf{10})$ [Å^{-1}]	**B** [Å]	$(\mathbf{11})$	$\boldsymbol{\theta}$ **(deg)**
PA 1	1.146	5.484	1.391	4.517	1.710	84.8
PA 2	1.098	5.722	1.379	4.556	1.680	84.6
PA 3	0.625	10.053	1.353	4.64	1.455	86.5
PA 4	0.646	9.726	1.349	4.65	1.531	86.5
PA 5	0.645	9.787	1.349	4.65	1.593	80.0

Details of Model Fitting

The constant in equation (2.10) is a purely geometric term, while the coefficient includes both geometric and energy terms. This model has four geometric parameters and three energy parameters, but only two independent parameters can be found from fitting, one of which must be geometric. l_o is found from the SAXS form factor and AFM imaging, B and Ω from WAXS, and leave ρ as the geometric fitting parameter as it cannot be easily found from diffraction measurments. σ is the lipid-water interface energy, an approximate value of K is calculated from counterion condensation theory, and the βsheet twist energy ϵ is left as a fitting parameter. The parameters are summarized in **Table 2.4**. Summary of model parameters., and fitting results are shown in **Table 2.5.** Linear regression of model to all PAs.

Table 2.4. Summary of model parameters.

Parameter	Description	Value	Note
Energy Parameters			
σ	Hydrophobic interaction	$7.2 \times 10^{-2}\, J/m^2$	Ref.[108]
K	Electrostatic interaction	$2.0 \times 10^{-40}\ J\, m^2$	Calculated from counterion condensation theory
$\epsilon\ k_B T$	β-sheet twist energy	$194\ k_B T\ or\ 483 \frac{KJ}{mol}$	Calculated from fit
Geometric parameters			
B	β-sheet spacing	$0.47\ nm$	Ideal β- sheet spacing, confirmed from X-ray scattering
l_o	Length of molecule	$4\ nm$	Measured from AFM, Xray scattering
Ω	Ribbon headgroup spacing	$0.96\ nm$	Measured from X-ray scattering
ρ	Cylinder headgroup spacing	$2.5\ nm$	Calculated from fit

Table 2.5. Linear regression of model to all PAs

	Estimate	SE	tStat	pValue
(Intercept)	3.5177	0.4256	8.2653	2.8559e-15
sqrt_Pitch	0.55163	0.023658	23.317	1.8855e-73

Linear regression model: Width ~ 1 + sqrt_Pitch
Estimated Coefficients:
Number of observations: 355, Error degrees of freedom: 353
Root Mean Squared Error: 0.156
R-squared: 0.606, Adjusted R-Squared 0.605
F-statistic vs. constant model: 544, p-value = 1.89e-73

Consistent with the model, WAXS, Fourier-transform infrared (FTIR) spectroscopy, and circular dichroism (CD) spectra confirm the presence of hydrogen bonding and β-sheet secondary structure for all molecules (**Figure 2.11**-**Figure 2.12**). Interestingly, the position of the peptide sequences along the curve in **Figure 2.4c** does not show a straightforward trend. The initial hypothesis was that the ribbon width would be related to the valine content in the molecule, as an increase in hydrophobicity due to the addition of valines would encourage rectangular-like packing over cylindrical packing, but this is not the case. The high valine-content molecules (**PA 4** and **PA 5**) are on the bottom left of the curve making the narrowest ribbons with short pitch, the intermediate valine molecule (**PA 3**) is on the top right making the widest ribbons with the longest pitch, while the low valine molecules (**PA 1 & PA 2**) are found in the middle of the curve making intermediate ribbons. The lack of a clear trend indicates that the relation between the peptide sequence and the position along the pitch-width curve is not a straightforward function of the peptide hydrophobicity or size.

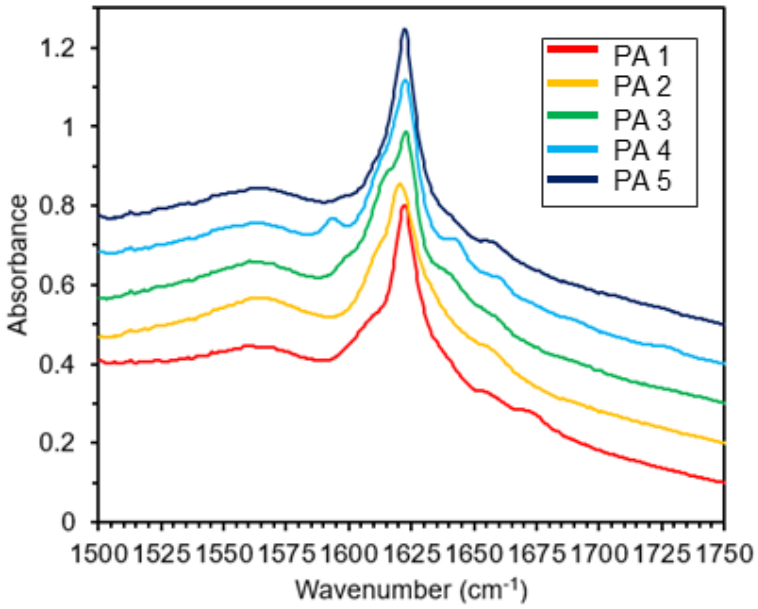

Figure 2.12. FTIR Spectra of PAs 1-5.

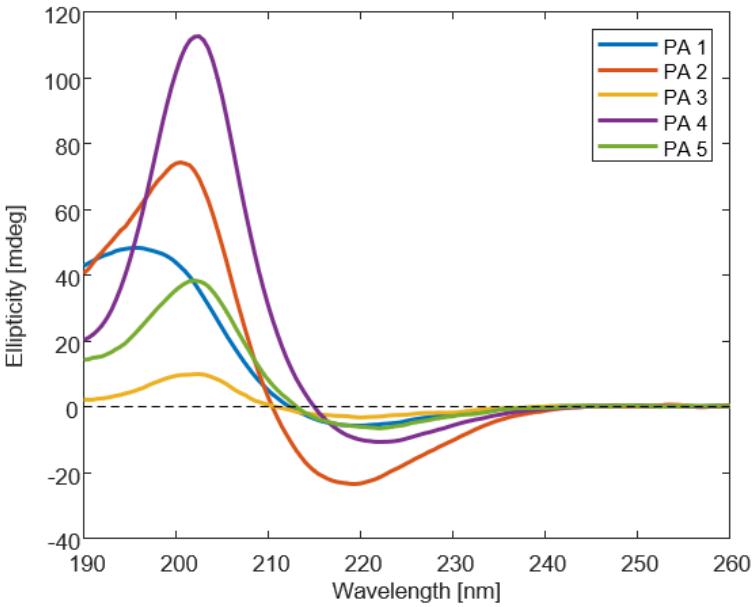

Figure 2.13. CD Spectra of PAs 1-5.

2.3.2. Role of supramolecular chirality in nanostructure morphology

To investigate this phenomenon further, the nanostructure morphologies were assessed by high-magnification liquid AFM. The supramolecular chirality of the nanostructures changes from left-handed to right-handed as the alanines are replaced by valines in the β-sheet region (**Figure 2.14a**). PA 1 and PA 2 nanostructures have a left-handed supramolecular twist; **PA 3** nanostructures can be left-handed, right-handed, or flat with no discernible twist; and **PA 4** and **PA 5** nanostructures are right-handed. Additional images characterizing nanostructure twist are shown in **Figure 2.7**-**Figure 2.9**, and a statistical analysis is provided in **Table 2.6.** Supramolecular chirality statistics from high resolution AFM images **PA 4** and **5** form narrow structures with short pitch lengths as they have high positive twist, **PA 3** forms the widest structures with the longest pitch lengths as it has low twist, and **PA 1 and PA 2** form intermediate structures as they have intermediate negative twist. There is no statistically significant difference between the average pitch lengths of **PA 1** and **PA 2** (473 ± 10 nm and 450 ± 21 nm), or between **PA 4** and **PA 5** (250 ± 17 and 284 ± 18 nm). The change in the handedness of the supramolecular twist explains the unexpected trend, as the pitch length of the ribbons is given by the absolute value of the twist, but the sign of the twist changes with the peptide sequence (**Figure 2.14b**).

Changes in supramolecular chirality are well known in self-assembled systems with different molecular chirality,[123] and have also been observed in certain self-assembling peptide systems with the same molecular chirality, such as modified amyloid forming peptide sequences[43,44,124–126] and insulin protein fibrils.[127] The relationship between the twist direction of β-sheets and the backbone conformation of their constituent peptide chains has been studied extensively in proteins from crystal structures[40–42] and recently in certain tissue-derived pathological amyloid fibrils.[43,44] The twist along the β-sheets can be right or left-handed based on

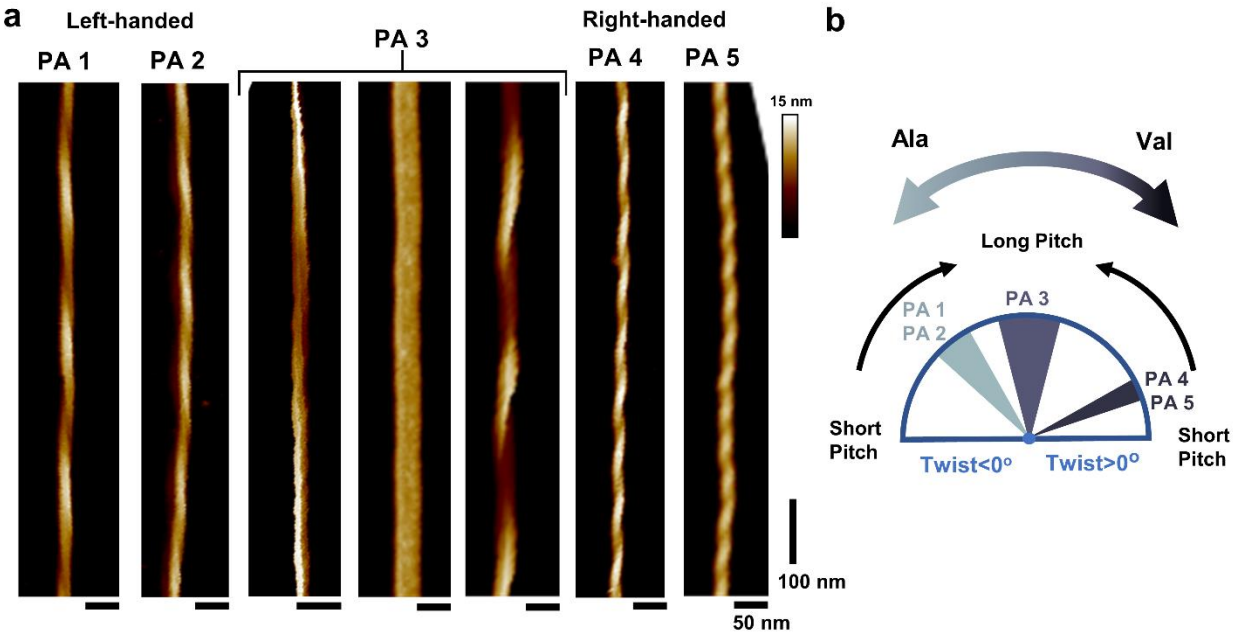

Figure 2.14. PA nanostructure twist and change in handedness. (a) Liquid AFM images illustrating change of supramolecular chirality of nanostructures from left-handed to right-handed with increasing valines. (b) Schematic illustrating the relationship between the supramolecular twist and morphology.

the configuration of dihedral angles in the peptide, although the majority of β-sheets in proteins are left-handed. An examination of the dihedral angle distributions of alanine and valine residues in β-sheets, derived from protein structures in the Protein Data Bank (PDB),[128,129] is consistent with the observation that alanine rich PAs have a higher propensity for left-handed twist than

valine-containing PAs (**Figure 2.15**). CD spectra show a small red shift of the β-sheet signal in

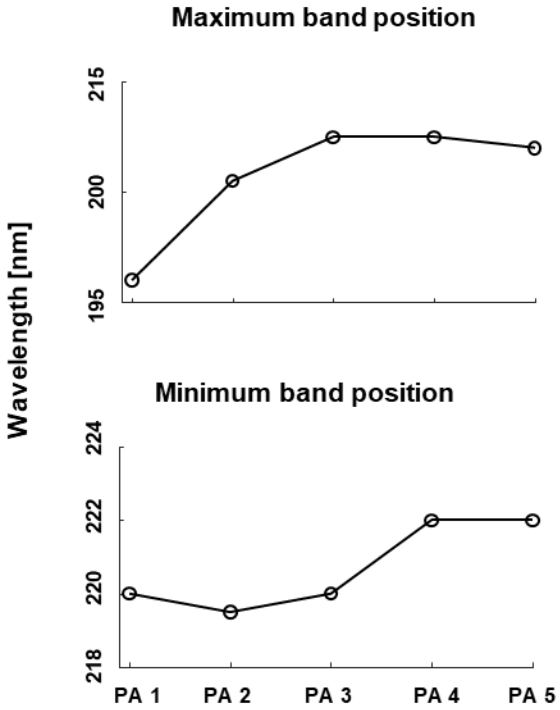

valine-containing PAs (**Figure 2.16**

Figure 2.16) characteristic of increasing left-handed peptide twist,[130] consistent with the observed switch from left- to right-handed nanostructures.

Table 2.6. Supramolecular chirality statistics from high resolution AFM images

	Probability	95% CI	N
PA 1	100% LH	[97%, 100%]	135
PA 2	100% LH	[91%, 100%]	41
PA 3	21% LH 37% F 42% RH	[9%, 37%] [22%, 54%] [26% 59%]	38
PA 4	100% RH	[96%, 100%]	101
PA 5	100% RH	[91%, 100%]	38

(LH = left-handed, RH=right-handed, F=flat)
Confidence Intervals are calculated using the Clopper-Pearson method for binomial distributions.

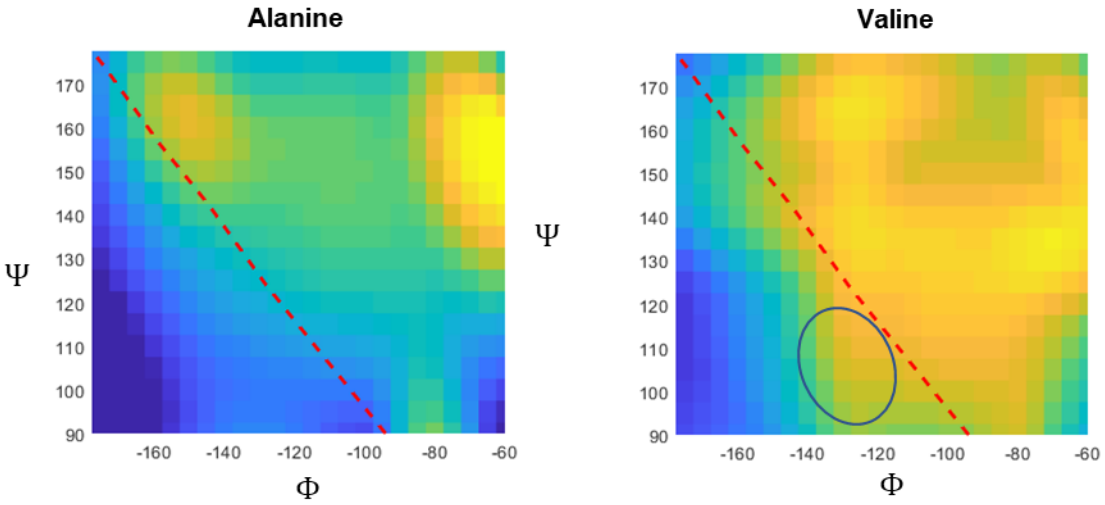

Figure 2.15. Dihedral angle probability density maps. Probability density of alanine and valine residues in the Beta sheet region. Alanines are found primarily in the right-handed portion of the peptide twist map above the dotted line (corresponding to left-handed fibers), while Valines have a significant presence in a section of the left-handed region below the dotted line (corresponding to right-handed fibers). Data source Dunbrack Group.[128,129]

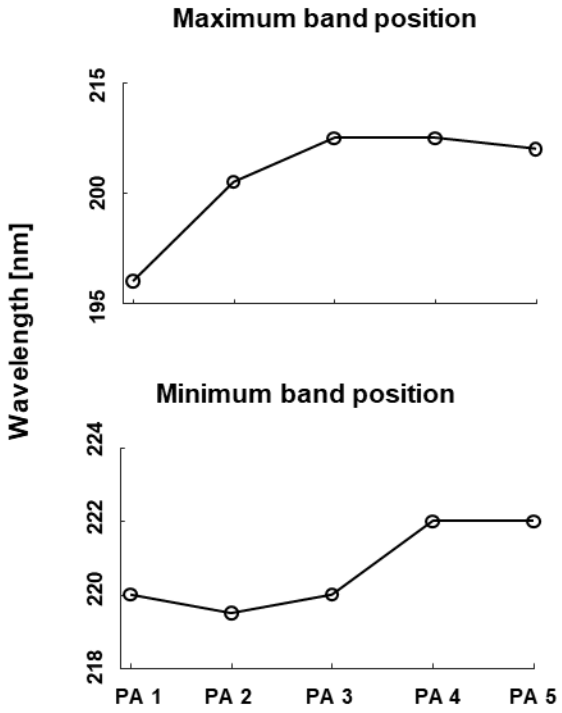

Figure 2.16. Red shift of β-sheet CD band with increasing right-handed twist.

2.3.3. Role of headgroup charge

We next investigated the charge dependence of nanostructure morphology, using the left-handed **PA 1**, the low twist **PA 3**, and the right-handed **PA 4**. The pitch length and width measurements were repeated for the nanostructures prepared at 5 mM NaOH (pH 5.5), and similar to the results shown earlier for **PA 4,** showed that there is no statistically significant difference in the overall relationship between pitch and width (**Figure 2.17** and **Table 2.7.** Linear regression model of pH dependence of PA 1, PA 3, and PA 4.). The nanostructures of the individual PAs do show shifts in the pitch length and width along the curve, however, the effect of reducing charge on **PA 1** and **PA 3** is different from the effect observed on **PA 4** (**Figure 2.18** and **Figure 2.19**).

While the pitch lengths of **PA 4** twisted ribbons showed a statistically significant increase when charge was reduced (250 ± 17 nm to 323 ± 15 nm), the pitch lengths **PA 1** and **PA 3** decreased (473 ± 10 nm to 434 ± 11 nm; and 1078 ± 38 nm to 893 ± 40 nm). The difference in the pitch length response to reduced charge indicates an overall leftward rotation in the supramolecular twist (**Figure 2.18b**). This is consistent with the previous observation that alanine residues, which are closer to the headgroup and likely to be more directly influenced by charge repulsion, impart a left-handed twist to the nanostructure. This suggests that within the ribbon regime, the change in charge alone can affect the molecular conformation of the peptide, but the charges are effectively screened by counterions, leaving the observed nanoscale morphology unchanged.

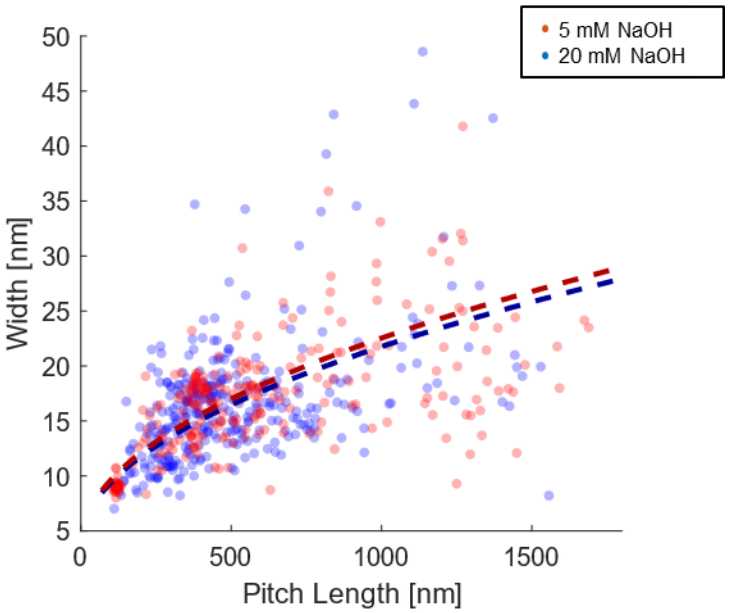

Figure 2.17. pH dependence of PA 1, PA 3, and PA 4 twisted ribbon morphology. All PAs are plotted together.

Table 2.7. Linear regression model of pH dependence of PA 1, PA 3, and PA 4.

	Estimate	SE	tStat	pValue
(Intercept)	3.676	0.44676	8.2281	1.1498e-15
sqrt_Pitch	0.57173	0.025624	22.312	4.0712e-81
sqrt_Pitch:pH_1	0.024657	0.015438	1.5972	0.11074

Linear regression model: Width ~ 1 + sqrt_Pitch + sqrt_Pitch:pH
Estimated Coefficients:
Number of observations: 614, Error degrees of freedom: 611
Root Mean Squared Error: 0.19
R-squared: 0.505, Adjusted R-Squared 0.504
F-statistic vs. constant model: 312, p-value = 4.21e-94

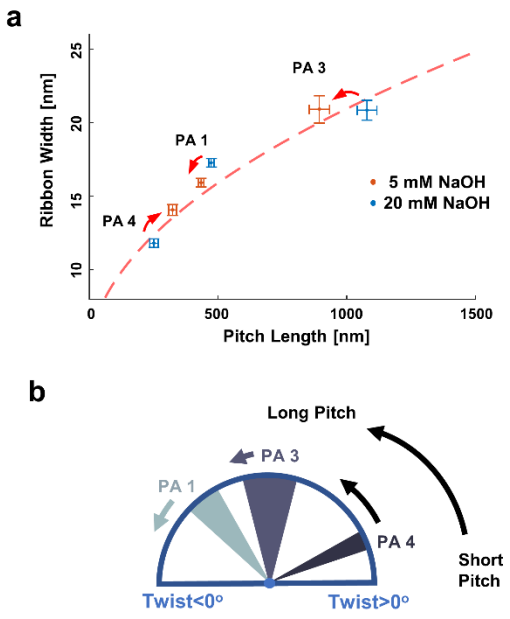

Figure 2.18. Shift in PA nanostructure morphology at lower charge. (a) Shift in the average pitch lengths and widths of PA 1, PA 3, and PA 4. (b) Schematic of the rotation of the supramolecular twist.

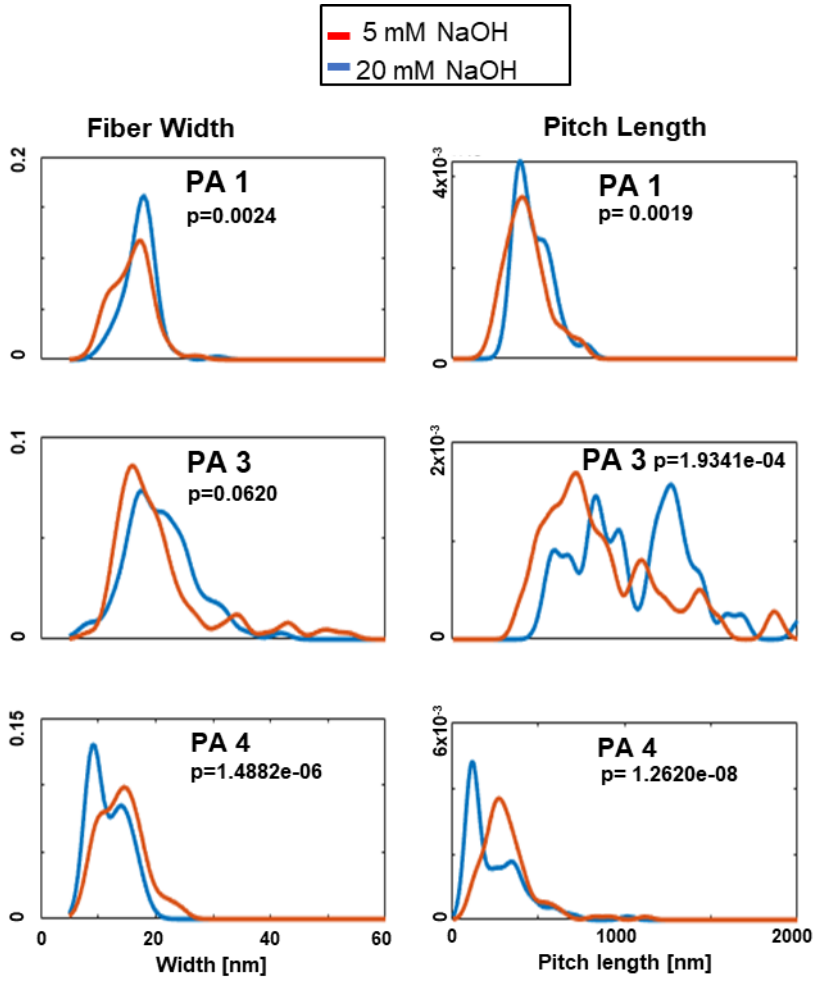

Figure 2.19. The distributions of experimentally measured fiber widths and pitch lengths at 5 mM NaOH and 20 mM NaOH. The distributions are generated using a normal kernel smoothing function with a bandwidth of 1.5nm for widths and 40nm for pitch length. The p-values from two-sample Kolmogorov-Smirnov tests, a non-parametric test for whether two data samples come from the same continuous distribution, are indicated on each graph.

To further investigate the role of charge, a phase diagram of nanostructure morphology was calculate (**Figure 2.20a**).

Derivation of phase boundaries

The ribbon to cylinder transition as a function of Pitch length and electrostatics can be found by identifying the ribbon region, where $W_{min} > 0$.

From (2.10), this occurs when

$$-\frac{\pi l_o \Omega}{\rho} + \frac{\pi l_o \Omega}{\rho}\sqrt{\frac{1}{\epsilon}\frac{\rho \mathrm{B}\sigma(\rho-\Omega)}{\pi l_o \Omega}\left(1-\frac{\frac{K}{\sigma}}{\rho\Omega \mathrm{B}^2}\right)}\sqrt{P} > 0,$$

$$\frac{K}{\sigma} < \rho\Omega \mathrm{B}^2 - \frac{\epsilon}{P}\frac{\pi l_o \Omega^2 \mathrm{B}}{\sigma(\rho-\Omega)} \tag{2.11}$$

Changing the inequality to an equality gives the curve at the boundary of the ribbon-cylinder transition. To identify the micelle region, the g_{end} term that was removed in (2.1) is reintroduced, and instead set g_{rib} and g_{cyl} to 0, which gives $g_{end} = 1$. This gives the energy change for forming micelles or nanostructures with a large portion of terminal ends:

$$\frac{\Delta\mu^0{}_{end}}{k_B T} = \Delta\mu^0_{transfer} + \left(\frac{K}{a_{end}} + \sigma a_{end}\right) \tag{2.12}$$

We similarly solve for the purely cylindrical regime, where $g_{rib} = 0$, $W = 0$, and $g_{cyl} \gg g_{mic}$, such that $g_{cyl} \approx 1$. In addition, $f(W) = -H_0 + \frac{\epsilon}{P}W = -H_0$ when $W = 0$.

This gives the cylinder energy:

$$\frac{\Delta\mu^0{}_{cyl}}{k_B T} = \Delta\mu^0_{transfer} + \left(\frac{K}{a_{cyl}} + \sigma a_{cyl} + f(0)\right) \tag{2.13}$$

The micelle region of the phase diagram is found when $\Delta\mu^0{}_{end} < \Delta\mu^0{}_{cyl}$

$$\Delta\mu^0_{transfer} + \left(\frac{K}{a_{mic}} + \sigma a_{mic}\right) < \Delta\mu^0_{transfer} + \left(\frac{K}{a_{cyl}} + \sigma a_{cyl} - H_0\right)$$

$$\frac{K}{\sigma} > a_{mic}\mathrm{B}\rho + \frac{H_0 a_{mic}\mathrm{B}\rho}{\sigma(a_{mic}-\mathrm{B}\rho)} \quad (2.14)$$

Assuming a spherical micelle at the end, the well-known result from Tanford[122] that the energy of a micelle is a minimum at $a_{mic} = \sqrt{\frac{K}{\sigma}}$ is used. Solving for K gives:

$$\mathrm{K} > \left(a_{cyl}\sqrt{\sigma} + \sqrt{H_0 a_{cyl}}\right)^2 \quad (2.15)$$

Again, changing to an equality gives the curve at the boundary of the cylinder-micelle transition.

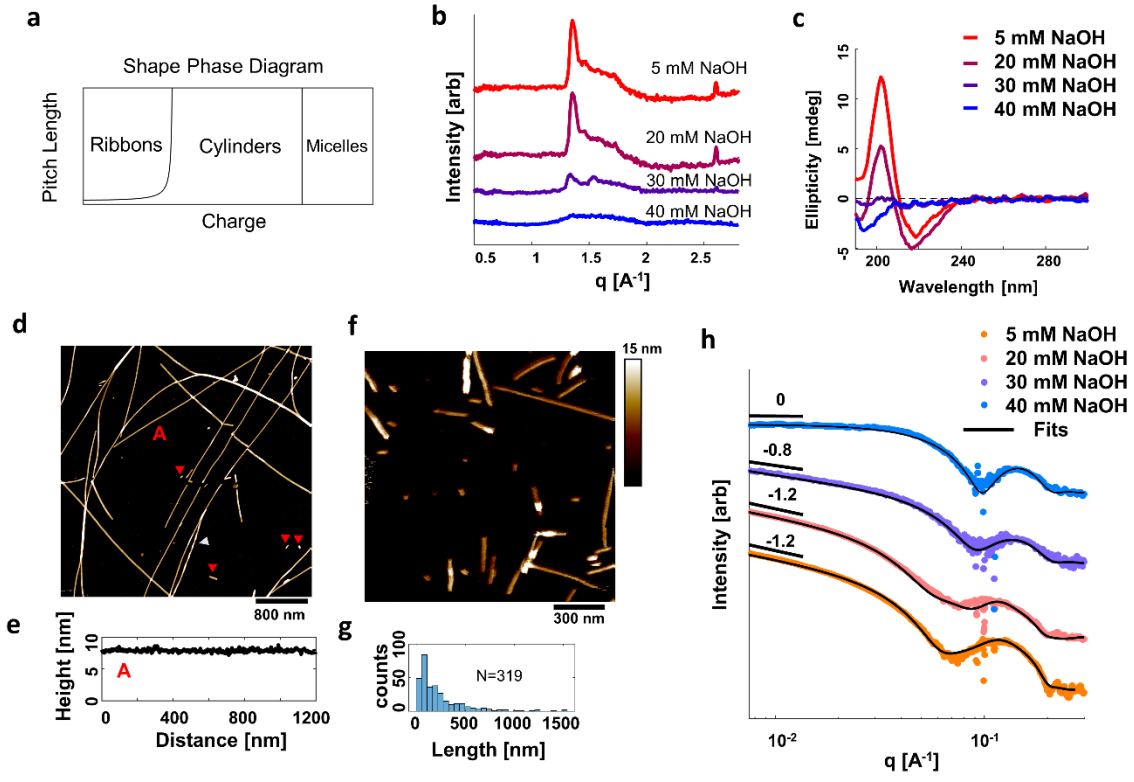

Figure 2.20. Charge dependence of PA assembly. (a) Phase diagram of nanostructure shape from the model as a function of charge and β-sheet pitch length. (b) X-ray diffraction patterns and (c) CD spectra of **PA 3** as a function of NaOH concentration. (d) AFM image of **PA 3** nanostructures at 30 mM NaOH, and (e) a line profile of an example nanostructure showing no measurable twist. (f) AFM images of **PA 3** at 40 mM NaOH and (g) length distribution of short fragments. (h) SAXS data and fits with the form factor models.

The model system forms cylindrical nanostructures at high charge, where the electrostatic penalty of closely packed molecules in the ribbon is larger than the hydrophobic penalty of the edges. As charge repulsion is increased further and overcomes the hydrogen bonding energy, the system forms micelles. This is similar to behaviour that has been previously reported for some other PA assemblies.[109,110,112] To test this behaviour, PA solutions with 30 mM NaOH (pH 9.5) and 40 mM NaOH (pH 11) were prepared. The WAXS diffraction shows reduced crystallinity at higher pH, consistent with a switch from ordered β-sheets to disordered assemblies (**Figure 2.20b** and **Figure 2.21**). The CD spectra also change to a random coil signature (**Figure 2.20c** and **Figure 2.22**). In AFM images of **PA 3** prepared at 30 mM NaOH, microns-long untwisted nanostructures are seen (**Figure 2.20d**). The height profile shows no discernible twist in these narrow nanostructures, consistent with a cylindrical geometry (**Figure 2.20e**). However, the sample is polydisperse and several very short structures (indicated with red arrows) are also observed, along with twisted structures (indicated with grey arrows). When charge is increased further, the molecules form short fragments and micelles (**Figure 2.20f** and **Figure 2.20g**). A similar behaviour is observed for the other PA sequences (**Figure 2.23**). This is confirmed with small-angle x-ray scattering (SAXS), where a slope of ~0 in the Guinier region at 40 mM NaOH is seen, indicating spherical micelles or short fragments, which decreases to -0.8 at 30 mM NaOH, indicating a mixture of long cylinders and short fragments (**Figure 2.20h**).[110] The SAXS measurements at 20 mM NaOH and 5 mM NaOH indicate polydisperse ribbons with a thickness of 8 nm (described below), consistent with the AFM imaging. A similar trend is confirmed for the other PAs (**Figure 2.24**). These results suggest that the effective charge increases significantly when multiple glutamic acid residues are deprotonated, likely because counterions cannot screen charged residues below the surface.

Derivation of ribbon form factor.

The smallest pitch length seen in the system (≈120 nm), is beyond the range measurable in small angle x-ray scattering. An analytical expression for the form factor of the cross section with a rectangular region from -b to b, and the radius of the cylindrical region a, is derived below.

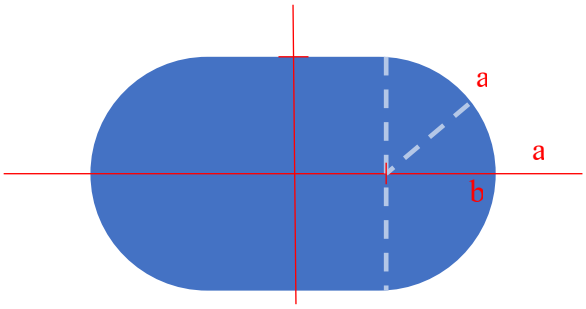

For an object with one dimension much longer than the other two, the scattering intensity can be written as[131]:

$$I(q) = bck + \mathrm{I_z(q)} \int_0^{\pi} \left[A_c(q_x, q_y) \right]^2 d\phi$$

where $|_z(q) \approx \frac{1}{q}$ for the long dimension. The integral over ϕ averages the object over all orientations. The cross-section term A_c is given by:

$$A_c(q_x, q_y) = \int_{-a}^{a} \int_{-b-\sqrt{a^2-x^2}}^{b+\sqrt{a^2-x^2}} e^{i(q_x x + q_y y)}\, dy dx$$

$$= \int_{-a}^{a} e^{iq_x x} \frac{\sin\left(q_y\left(b + \sqrt{a^2 - x^2}\right)\right)}{q_y} dx$$

In polar coordinates, $q_x(q,\phi) = q\,cos(\phi)$ and $q_y(q,\phi) = q\,sin(\phi)$, and the symmetry of the cross section is used to simplify the imaginary terms. This gives the expression:

$$I(q) = bck + \frac{1}{q}\int_0^{\pi}\left[\int_{-a}^{a}\cos\left(q\cos(\phi)\right)\frac{\sin\left(q\sin(\phi)\left(b+\sqrt{a^2-x^2}\right)\right)}{q\sin(\phi)}dx\right]^2 d\phi$$

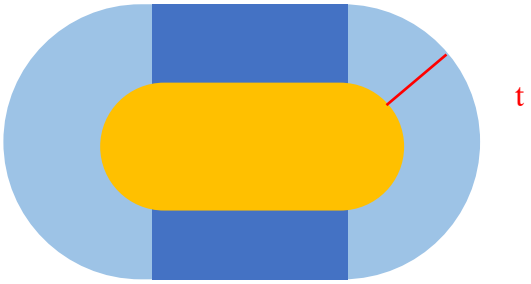

We then extend the model to include a core shell term, where the rectangular packed shell is distinguished from the cylindrically packed shell. The thickness of the shell is t; $(\rho_{cyl} - \rho_{sol})$ is the contrast between the cylindrical shell and the solvent, $(\rho_c - \rho_{cyl})$ is the contrast between the core and the cylindrical shell, and $(\rho_{rib} - \rho_{cyl})$ is the contrast between the rectangularly packed region of the shell and the cylindrical shell.

The final expression is given by:

$$I(q) = bck + \frac{1}{q}\int_0^{\pi}\left[(\rho_{cyl}-\rho_{sol})\int_{-a}^{a}\cos\left(q\cos(\phi)\right)\frac{\sin\left(q\sin(\phi)\left(b+\sqrt{a^2-x^2}\right)\right)}{q\sin(\phi)}dx\right.$$

$$+ (\rho_c - \rho_{cyl})\int_{-(a-t)}^{a-t}\cos\left(q\cos(\phi)\right)\frac{\sin\left(q\sin(\phi)\left(b+\sqrt{(a-t)^2-x^2}\right)\right)}{q\sin(\phi)}dx$$

$$\left.+ (\rho_{rib} - \rho_{cyl})\left[2\frac{\sin\left(qb\sin(\phi)\right)}{q\sin(\phi)}\frac{[\sin(\mathrm{qa}\cos(\phi)) - \sin(\mathrm{q(a-t)}\cos(\phi))]}{\mathrm{q}\cos(\phi)}\right]\right]^2 d\phi$$

Results of SAXS form factor fitting for PA3

PA 3, 40 mM NaOH

Model: Spherical core-shell

$$I_{sphere}(q) = \left[V_{shell-sphere}A_{shell-sphere} + \left(\frac{\rho_{core}-\rho_{shell}}{\rho_{shell}-\rho_{sol}}\right)V_{core-sphere}A_{core-sphere}\right]^2 + Bck$$

$$V_{shell-sphere} = \frac{4\pi R^3}{3} \quad , V_{core-sphere} = \frac{4\pi(R-t)^3}{3}$$

$$A_{shell-sphere} = 3[\sin(qR) - qR\cos(qR)]/(qR)^3$$

$$A_{core-sphere} = 3[\sin(q(R-t)) - q(R-t)\cos(q(R-t))]/(q(R-t))^3$$

Results:

R (Outer radius of sphere/molecule length) = 37.8 A

t (Shell thickness of sphere) = 20.2 A

$\left(\frac{\rho_{core}-\rho_{shell}}{\rho_{shell}-\rho_{sol}}\right)$ (Relative scattering density) = -2.08

Bck (Background) = 0.0160

PA 3, 30 mM NaOH

Model: Spherical core-shell cylindrical core-shell mixture

$$I_{mix} = I_{cyl} + P\, I_{sphere} + Bck$$

$$I_{cyl}(q) = 1/q\left[V_{shell-cyl}A_{shell-cyl} - \left(\frac{\rho_{core}-\rho_{shell}}{\rho_{shell}-\rho_{sol}}\right)V_{core-cyl}A_{core-cyl}\right]^2$$

$$V_{shell-cyl} = 2\pi R^2 \quad , V_{core-cyl} = 2\pi(R-t)^2$$

$$A_{shell-cyl} = 2\,J_1(qR)/(qR) \ , A_{core-cyl} = 2\,J_1(q(R-t))/(q(R-t))$$

Where J_1 is the Bessel function of the First Kind of order 1.

Results:

R (Outer radius of cylinder/molecule length) = 41.9 A

t (Shell thickness of cylinder) = 20.0 A

$\left(\frac{\rho_{core}-\rho_{shell}}{\rho_{shell}-\rho_{sol}}\right)$ (Relative scattering density) = -1.14

P (Proportion of micelles in mixture) = 0.2

Bck (Background) = 0.003

PA 3, 20 mM NaOH

Model: Ribbon
Results:
a (molecule length/radius at edge) = 35.0 A
b (Width of ribbon) =145 A
t (Shell thickness) = 26 A
$(\rho_{rib} - \rho_{cyl})/\ (\rho_{cyl} - \rho_{sol})$ (Relative scattering density) = 0.1
$(\rho_c - \rho_{cyl})/\ (\rho_{cyl} - \rho_{sol})$ = -1.5
Bck (Background) = 0.0002

PA 3, 5 mM NaOH

Model: Ribbon
Results:
a (molecule length/radius at edge) = 34.0 A
b (Width of ribbon) =140 A
t (Shell thickness) = 23 A
$(\rho_{rib} - \rho_{cyl})/\ (\rho_{cyl} - \rho_{sol})$ = 0.4
$(\rho_c - \rho_{cyl})/\ (\rho_{cyl} - \rho_{sol})$ = -1.5
Bck (Background) = 0.0001

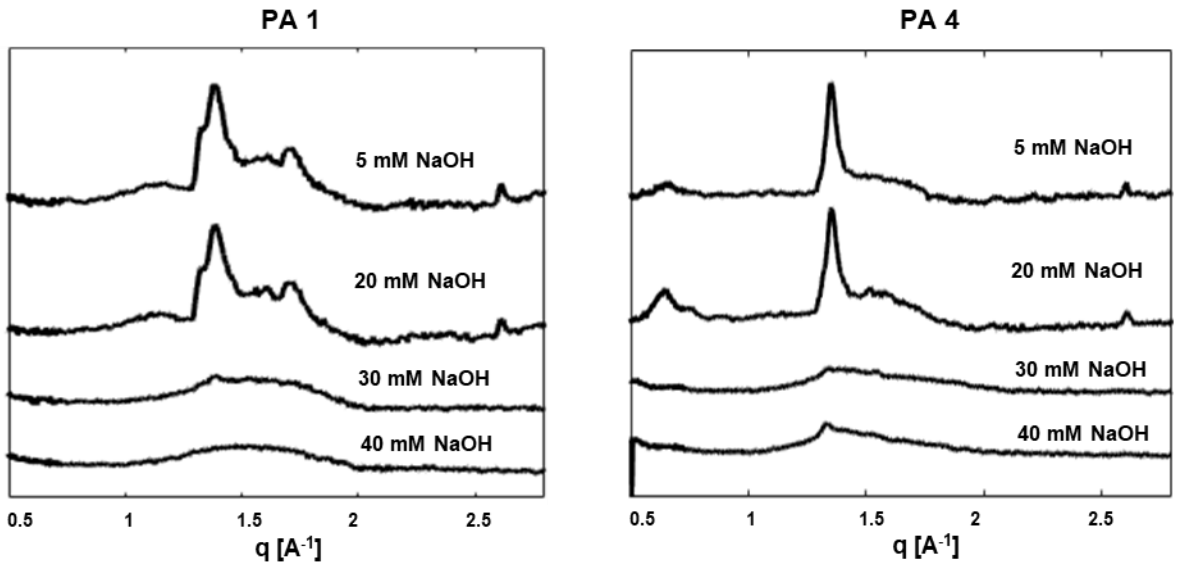

Figure 2.21. MAXS/WAXS diffraction of PA 1 and PA 4 as a function of NaOH concentration.

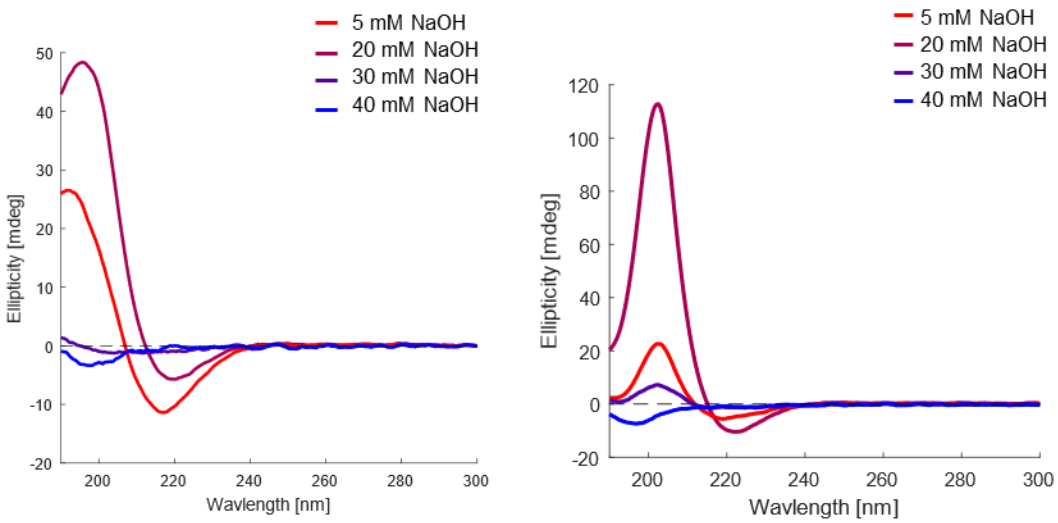

Figure 2.22. CD spectra of a) PA 1 and b) PA 4 as a function of NaOH concentration.

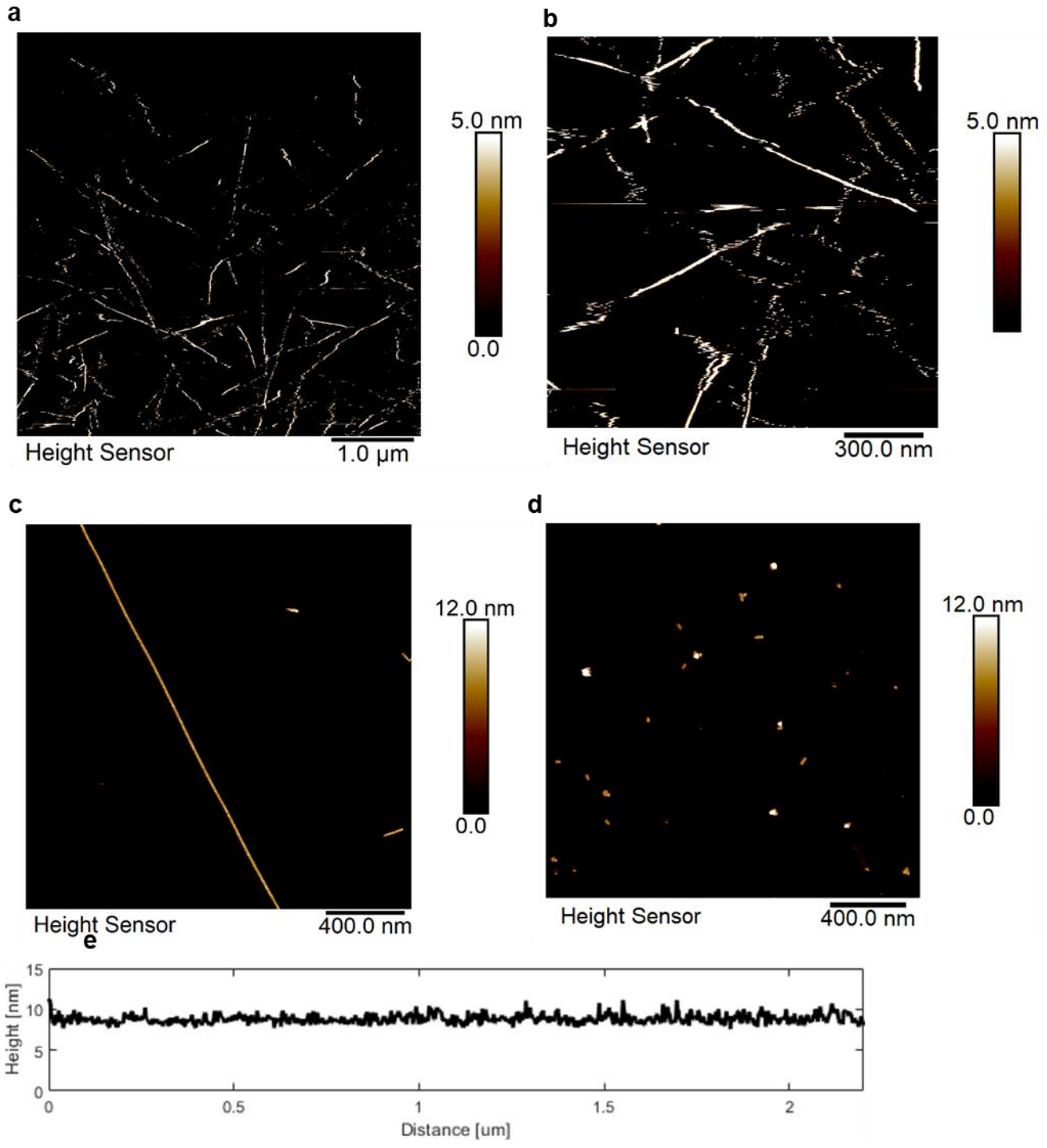

Figure 2.23. AFM images of PA 1 and PA 4 at 30 mM NaOH and 40 mM NaOH. a) PA 1 at 30 mM NaOH and b) at 40 mM NaOH. c) PA 4 at 30 mM NaOH and d) at 40 mM NaOH. e) height profile of cylindrical nanostructure in c)

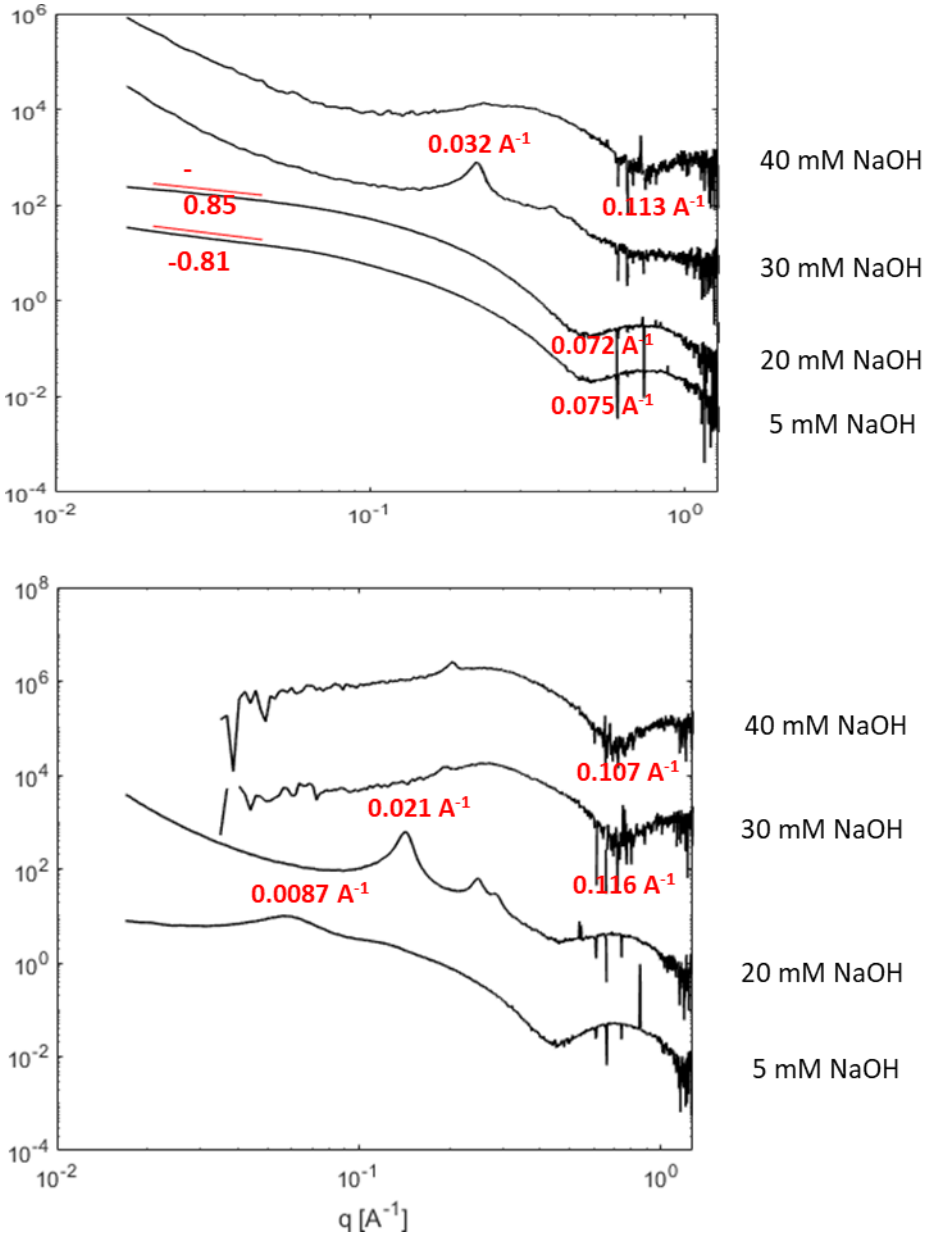

Figure 2.24. SAXS measurements of PA 1 and PA 4. a) At 5 mM NaOH and 20 mM NaOH, PA 1 shows form factors characteristic of high aspect ratio nanostructures with a cross-sectional dimension of 8.3 nm and 8.7 nm respectively, as measured from the position of the first minimum. At 30 mM NaOH PA 1 shows bundling characteristic of hexagonal packing of narrow cylinders with a center-to-center spacing of 19.6 nm. At 40 mM NaOH, PA 1 shows a form factor characteristic of disordered aggregation of micelles or short fragments, with a radius of 5.7 nm measured from the first minimum. b) At 5 mM NaOH and 20 mM NaOH, PA 4 shows bundling characteristics of hexagonal packing of narrow ribbons or cylinders with a center-to-center spacing of 72.2 nm and 29.9 nm, respectively. At 30 mM NaOH and 40 mM NaOH, PA 1 shows a form factor characteristic of aggregated micelles or short fragments with a radius of 5.4 nm and 5.8 nm, respectively.

2.4. Conclusions

In summary, the role of peptide twist in determining the shape of self-assembled peptide amphiphile was investigated. With increasing charge, the structures first transition into long cylinders when the electrostatic repulsion dominates the residual hydrophobic contact, and then into short fragments or micelles. The supramolecular twist of the ribbons also changes chirality based on the peptide sequence in the molecules. The results from this work will guide the design of PA materials in biomedical applications and may be of use to the broader field of peptide self-assembly, such as the study of amyloid-forming peptides. Future work will investigate the interaction of different PAs in mixtures, and the interaction of PA nanostructures with bioactive peptides.

2.5. Materials and Methods

Atomic Force Microscopy (AFM) in liquid

AFM in a liquid environment of soft nanostructures like PA nanofibers has many experimental challenges, which can be overcome with careful sample preparation and good technique. Under idealized conditions, a noise floor of about 1.5 Å can be readily achieved and features as small as single carbon atom wide step edges can resolved, as demonstrated in **Figure 2.25**.

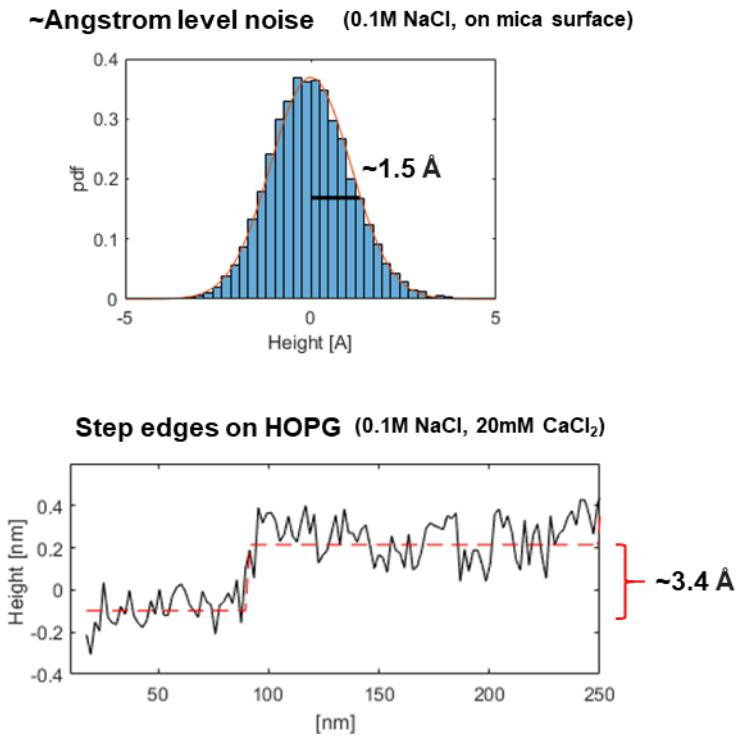

Figure 2.25. Noise and resolution limits of liquid AFM. a) a noise floor of about 1.5 Å can be achieved on a mica surface under ideal conditions. b) HOPG step edges of 3.4 Å, the van der Waals diameter of a carbon atom, can be resolved

A list of observations made during the optimization of liquid AFM experiments, operating in ScanAsyst mode on a Bruker Icon Dimension (Bruker) AFM on PA nanostructures is provided below:

- In order to ensure immobilization and stability of nanostructures on mica, the use of a multivalent cation was necessary. For negatively charged PAs, a 150 mM NaCl 20 mM $CaCl_2$ solution was used in this work. For positively charged PAs, PBS was found to work well. Other methods, like the deposition of a positively charged layer of Poly-D-lysine (PDL) is also possible, but the tip integrity is quickly compromised.

- A Bruker SNL-10A tip, operating at a 50 nm amplitude, was appropriate for all samples. A max force of around 1 nN was usually sufficient.
- For deposition on Mica, a 10-20X dilution of a 10mM solution of PAs (i.e. 1-0.5 mM PA) was often appropriate.
- As PA assemblies are often polydisperse and disordered, there are usually small fragments or micelles in the solution. These can easily stick to the AFM tip and create artifacts. It is essential to rinse the surface several times with NaCl solution, and then again with $CaCl_2$ solution before imaging.
- Taking large images at high scan speeds (e.g. a 10 μm image at 512x512 pixels, at 2 Hz scan speed) quickly degrades the tip quality, as the PA nanofibers break down and fragments can attach to the tip.

PA sample preparation

PA samples were prepared by dissolving lyophilized PA with the noted concentration of NaOH in Milli-Q water, and sonicating for 15 mins. Solutions were annealed in PCR tubes in a thermal cycler (Mastercycler pro, Eppendorf) at 80^{o}C for 30 mins, followed by cooling to 20^{o}C at 1^{o}C/min.

For Atomic Force Microscopy, sample solutions were diluted 10X in 150 mM NaCl and deposited on freshly cleaved mica surfaces for ~1 min, and the excess solution was rinsed with 150 mM NaCl. The samples were then rinsed with 150 mM NaCl 20 mM $CaCl_2$ to immobilize the nanostructures on the mica surface, and measurements were performed in the liquid environment. AFM images were captured in PeakForce tapping mode on a Dimension Icon AFM (Bruker) with

a silicon nitride cantilever (SNL10-A, Bruker) in a liquid cell. Images were flattened to correct sample tilt before analysis.

Cryo-Transmission Electron Microscopy (Cryo-TEM)

Cryo-TEM samples were prepared by plunge freezing using a Vitrobot Mark IV (FEI) vitrification robot at room temperature and 95-100% humidity. 300-mesh copper grids with lacey carbon support (EMS) were glow discharged for 15 s using a PELCO easiGlow Glow Discharge Cleaning System (Ted Pella) and used immediately. 7 μL of sample solution (0.1 w/v%, diluted from 1 w/v% into milliQ immediately before grid preparation) was placed on the copper grid, blotted, and plunge frozen into liquid ethane. Samples were transferred into a liquid nitrogen bath and placed into a Gatan 626 cryo-holder through a cryo-transfer stage. Cryo-TEM was performed using a JEOL 1230 TEM working at 100 kV accelerating voltage. Images were acquired using a Gatan 831 CCD camera.

Image analysis

Image Analysis was performed in MATLAB using the Image Processing toolbox, with custom written codes. AFM images were thresholded and skeletonized to track fiber trajectories, and peaks were identified from the height profiles using a pre-built peak finding algorithm. The distance between peaks and the height of the peaks were averaged for each nanostructure to calculate the pitch length and width. All profiles were assessed by hand, and errant trajectories were removed from the analysis. Regions of interest containing adjacent peaks were identified by hand in Cryo-TEM images, and the peak positions were refined by fitting the peak position to

calculate the pitch length. A line profile was evaluated in the broadest part of each nanostructure, and the edges of the nanostructure were identified by fitting to the minimum to calculate the width of the nanostructures. All statistical analysis and model fitting was performed in MATLAB, using the Statistics and Machine Learning toolbox.

X-ray scattering

X-ray scattering experiments were performed at Beamline 5-ID-D, DND-CAT, Advanced Photon Source at the Argonne National Laboratory. The solution samples were placed in a vacuum flow cell comprising of a 1.5mm quartz capillary connected to a syringe pump. An X-ray energy of 17 keV was selected using a double monochromator, and the scattering patterns for an empty capillary, water-filled capillary and sample-filled capillary were recorded using a set of three charge coupled device (CCD) detectors.[132] The two-dimensional scattering patterns then azimuthally integrated to generate a scattering vector magnitude q vs. intensity plot, where q is defined as $q=4\pi\sin(\theta)/\lambda$ for which θ denotes the half of total scattering angle and λ the X-ray wavelength, 0.7293 Å. 2D to 1D data reduction was performed by GSAS-II software.[133] No attempt was made to determine the absolute scattering intensity.

Fourier Transform Infrared (FTIR) spectroscopy

FTIR spectra were recorded on a Bruker Tensor 37 FTIR Spectrometer. Samples were prepared as described before in deuterated water (D2O) and Sodium deuteroxide (NaOD), and placed between two CaF2 windows with a spacing of 50 μm for the measurements. Spectra are the

result of 25 scans with a resolution of 1 cm^{-1}. Atmospheric CO2 and H2O were background subtracted.

Circular Dichroism (CD)

PA samples were diluted from 10 mM to 50 μm in H_2O immediately before the measurement was taken. All measurements were performed on a JASCO J-815 circular dichroism spectropolarimeter in a quartz cuvette of 0.5 mm optical path length at room temperature. Three spectra collected from 250 nm to 190 nm were averaged and normalized to the final concentration of each sample.

Peptide amphiphile synthesis

PAs were synthesized using a previously reported protocol.[134] Purity was determined by liquid chromatography-mass spectroscopy (LC-MS), as shown below. All PA batches were at least 95% pure.

3. Double helix organization in supramolecular peptide amphiphile assemblies controlled by assembly stiffness

3.1. Objectives and significance

Multi-stranded helical nanostructures are found in several supramolecular systems in nature. Using atomic force microscopy (AFM) in a liquid environment, it was shown that self-assembling peptide amphiphile (PA) nanofibers form polydisperse structures composed of twisted ribbon fibers and double helices. The double helical structures observed here are asymmetric with a major and minor groove running on opposite sides of the structure, similar to the well-known DNA double helix. The abundance of double helices increases in higher stiffness nanostructures. The formation of the double helix is described with a physical model based on optimizing membrane bending curvature against the hydrogen bond stretch and twist in the β-sheets of amphiphilic assemblies. With correlative AFM and confocal laser scanning microscopy (CLSM), the degradation of PA nanofiber coatings by cells is shown to be modified due the stiffness of the nanostructures. Coatings composed of flexible nanofiber networks are primarily deformed by cells, while rigid nanofiber networks are primarily degraded. These findings indicate a pathway of PA self-assembly that combines the known assembly behaviours of lipid amphiphiles and peptides to create new nanostructures, which can be used to control the degradation behaviour of biomaterial scaffolds.

3.2. Introduction

Self-assembling nanomaterials inspired by nature, with tunable supramolecular interactions, can form a vast array of nanostructures. Theoretical and experimental work has demonstrated the relation between the mechanical properties of self-assembling chiral

biomolecules and the resulting nanostructures that they can form.[32,135] The assembly of amphiphilic lipids into structures essential to biology such as bilayer membranes, vesicles, liposomes, and tubules is controlled by the bending moduli and anisotropy of the lipid layers.[30] These mechanical properties can be modified by changing the molecular structure of the amphiphiles, resulting in nanostructures with different characteristic curvatures. In addition, the assembly of biomolecules such as proteins and peptides into fibrils is also an active area of research due to their implication in diseases such as Alzheimer's.[136] Amyloid fibrils, formed by hierarchical packing of individual stacks, can disrupt cellular functions and are resistant to degradation as they create highly stable crystalline structures,[46] in contrast to fluid-like structures formed by amphiphiles. Interestingly, both systems can assembly into morphologically similar twisted ribbons or helical nanostructures, although through different mechanisms.

The hierarchical nature of supramolecular fibrils has motivated advances in high resolution imaging methods like Cryo-TEM, which has enabled the direct observation and high resolution reconstructions of higher order helical nanostructures such as amyloidβ segments,[44,137,138] Tau Paired Helical Filaments (PHF),[139–141] and alpha-synuclein,[142,143] all of which can form double helices from individual fiber strands. Multistranded helical fibrils of certain larger globular proteins have also been reported,[84,144] and certain smaller synthetic molecules have been reported to form double helices in solid state measurements[145,146] and more recently in water.[147] The self-assembly of hierarchical nanomaterials and their mechanical properties are also relevant to components of the extracellular matrix (ECM), such as collagen fibrils. The mechanical properties of ECM scaffolds are well known to affect the behaviour of biological systems, such as the proliferation and differentiation of stem cells,[93] and the migration and invasion of cancerous cells.[148] Recently, the role of dynamic biomaterial microarchitecture and the ability of cells to non-

elastically remodel the ECM and other scaffolds has gained significant interest.[101–103,149] Collagen scaffolds have been shown to stiffen after physical remodeling by cells, which can then lead to a modified biological response.[99,150] Weakening of mechanical properties, such as degradation of hydrogel scaffolds, is also of interest as it has been shown to prolong the stemness of neural progenitor cells.[101] This ability of materials to remodel under biological conditions has emerged as a key parameter in the design of ECM mimetic scaffolds.

Peptide amphiphiles (PAs) are a class of bioinspired molecules that consist of both a hydrophobic lipid tail and a β-sheet forming peptide region which promotes self-assembly into high aspect ratio nanostructures.[50,151] PAs have been reported to create various nanostructures like flat nanobelts, twisted ribbons, and cylinders,[151] which are associated with changes in function such as the presentation of bioactive epitopes.[69,74] PA nanostructures can also assemble into higher order structures due to electrostatic interactions[152] or programmed binding cues.[65] These materials have found extensive use for applications in regenerative medicine, due to their ECM mimetic structure and the ease of manipulating the peptide sequence to add bio-functional groups.[56] Previous work from has shown that PA scaffolds implanted in vivo degrade with a half-life of ~2 weeks.[64] However, the nano and microscale remodeling of PA biomaterials in biological conditions is largely unexplored. In this work, the formation of previously unknown PA nanostructures is investigated with high resolution imaging methods, and a model based on the self-assembly of amphiphilic lipids and their stiffness due to a β -sheet forming peptide sequence is developed. The change in the architecture of these materials due to cellular remodeling in coatings was also investigated as a function of the nanostructure stiffness.

3.3. Results and Discussion

3.3.1. DNA-like double helix

The PA C_{16}-A_6-E_3 (**Figure 3.1a**) has a palmitic acid tail, an internal peptide sequence of six alanines, and a charged hydrophilic head group of three glutamic acids with amide termination. It self-assembles in water into high aspect ratio twisted nanostructures, as seen in liquid environment atomic force microscopy (liquid-AFM) (**Figure 3.1b**) and transmission electron microscopy (TEM) (**Figure 3.2**). The nanostructures are prepared by annealing a 10 mM PA solution with 20 mM NaOH (pH 8.5) at 80°C for 30 minutes followed by cooling to room temperature at 1°C/min, a self-assembly pathway that has been previously shown to create stable states.[52] As indicated in the images, the nanostructures are polydisperse in the pitch length and width, the two parameters that characterize a twisted ribbon structure (**Figure 3.1c**). When the PA solution is prepared with 5 mM NaOH (pH 5.5), such that the glutamic acids have lower charge, a second population of structures becomes more common, consisting of two fibers winding into a double helix (**Figure 3.3a**). The morphology of double helical structures is confirmed with negative stain TEM imaging as well as zero-loss Cryo-TEM imaging with a high coherence emission source, automated focus, and a short defocus length (**Figure 3.3b** and **Figure 3.3c**). The individual strands of the double helix can be seen separating near points where the two strands overlap and lie parallel to the beam direction. Contrast between the two strands is also seen at points where they lie parallel to the image plane, consistent with the AFM results. Occasionally the double helices can be seen fragmenting into their individual strands, likely due to thermal forces or collisions with other structures in solution, which serve as confirmation of the double helical structure (**Figure 3.3d-f**). On average, the width of the double helix is 20 nms, while the two strands are each 10 nms wide (**Figure 3.4**). The distance between the centers of the two strands

is also 10 nms, which indicates that the individual strands have an approximately circular cross-section with a diameter of 10 nms. The individual strands are likely similar in composition to cylindrical PA nanostructures of similar size that have explored previously, composed of ~9 molecules per cross-section.[52]

Surprisingly, the double helix observed here has a distinct morphology remarkably similar to the DNA double helix, with major and minor grooves running on opposite sides of the nanostructure. Large scale liquid AFM images of PA nanostructures show an alternating deep and shallow topography in the assemblies (**Figure 3.5a**). A height profile along the length of the nanostructure shows a deep minimum with a height 7 nms above the surface alternating with a shallow minimum with a height of 15 nms. This indicates that the two strands are wound together asymmetrically, creating the alternating depth between adjacent peaks when imaged topographically with AFM. The deep and shallow grooves running on opposing sides of the nanostructures are observable in high resolution liquid AFM images (**Figure 3.5b**). When imaged in TEM where the top and bottom surface cannot be distinguished, an asymmetry in the outline of the nanostructure when the strands crossover each other is seen instead (**Figure 3.5c**). At cross over points of the double helix, where the two strands stack parallel to the beam direction, one side of the nanostructure has a sharper groove than the other, as indicated with black arrows in the expanded boxes. The orientation of the sharper groove alternates from one cross-over to the other, with a repeat of the helix pitch length, indicative of major and minor on opposing sides of the nanostructure.

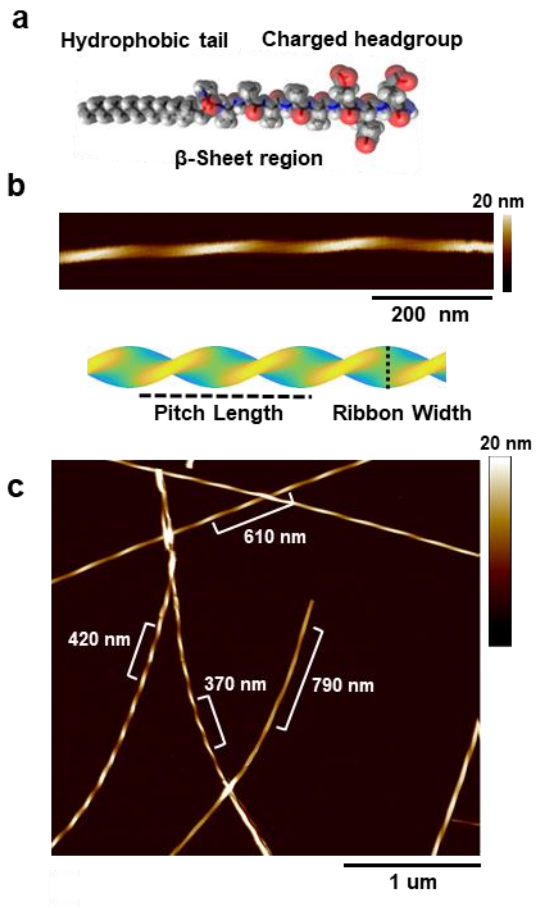

Figure 3.1. Self-assembly of $C_{16}A_6E$ into polydisperse nanostructures at 20 mM NaOH. (a) Molecular structure of the PA. (b) Liquid AFM image of twisted ribbon nanostructure, with characteristic pitch length and ribbon width. (c) Liquid AFM image of polydisperse twisted ribbon nanostructures with pitch lengths indicated.

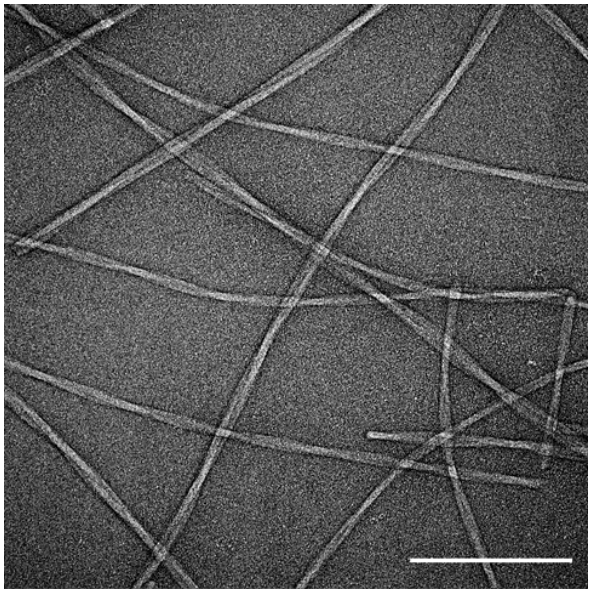

Figure 3.2. TEM image of $C_{16}A_6E_3$ nanofibers. Scale bar = 200nm.

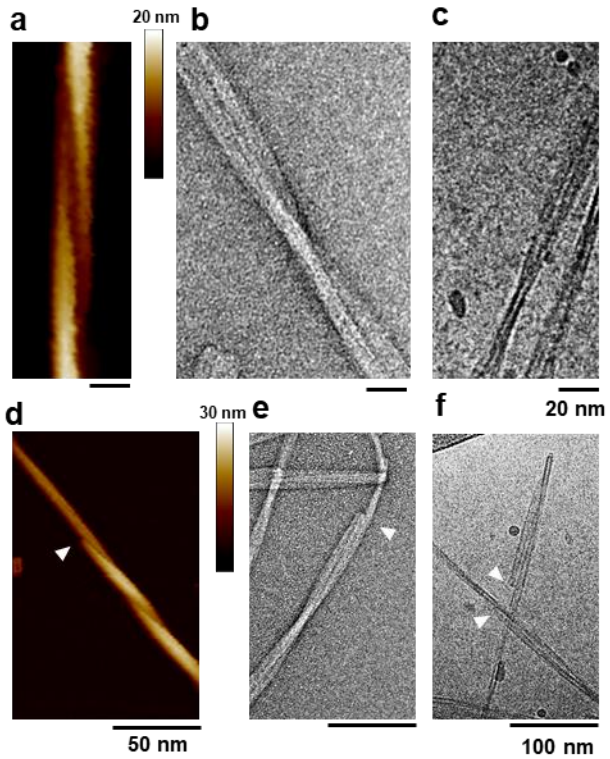

Figure 3.3. Double helical nanostructures formed at 5 mM NaOH (a) Liquid-AFM, (b) negative stain TEM, and (c) Cryo-TEM images of double helical structures. (e) Liquid-AFM, (f) negative stain TEM, and (g) Cryo-TEM images of double helices with one strand breaking off at points indicated with white arrows.

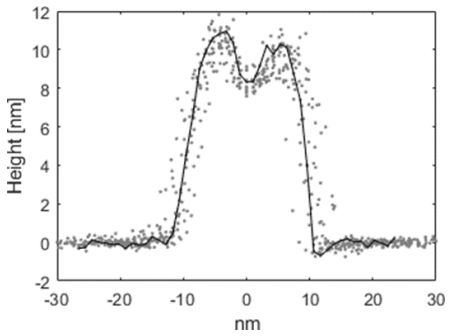

Figure 3.4. Double helix nanostructure cross section height profiles. N=10.

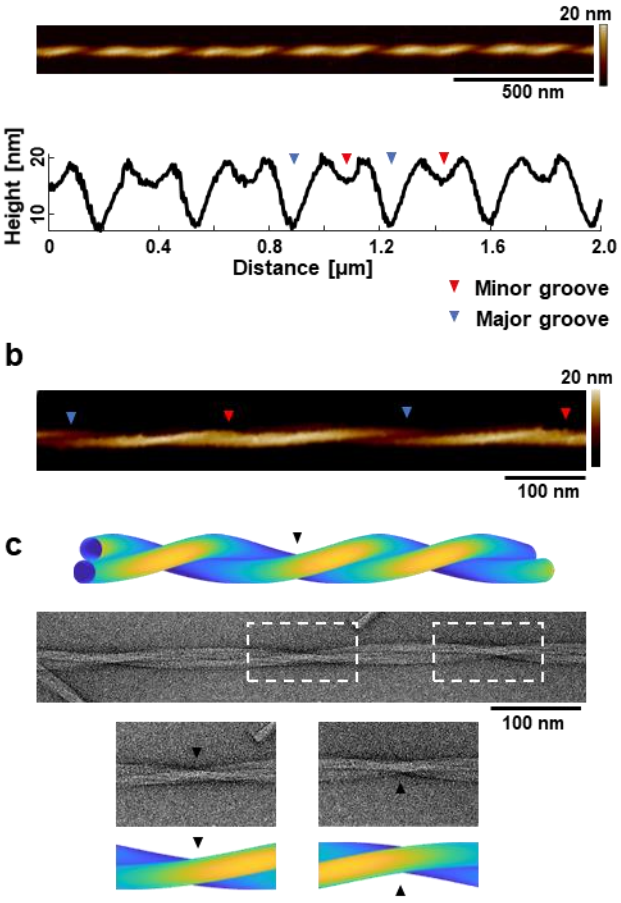

Figure 3.5. Structure of the PA double helix. (a) Liquid-AFM image (top) and height profile (bottom) of a nanostructure with grooves of alternating depth on opposite sides of the double helix. Grooves are labelled as major and minor as indicated by blue and red arrows respectively. (b) High resolution AFM image with the major and minor grooves indicated with arrows. (c) Graphical schematic and stained TEM image of a PA double helix with the strand crossover asymmetry highlighted with black arrows in the expanded boxes.

The long-range order of the nanostructure topography over many microns (**Figure 3.6**) indicates a stable mechanism underlying the formation of major and minor grooves. In the DNA double helix, the offset binding between the two strands is caused by the asymmetric bond angles between the base pairs and the phosphate backbone. While the supramolecular PA structure is morphologically similar to the DNA double helix, it is about 2 orders of magnitude larger in length scale, and there is no obvious source of such an asymmetry between the strands**.** To investigate the origin of this phenomenon, additional properties of the nanostructure populations were measured. It is apparent in large AFM images that the nanostructures prepared at 5 mM NaOH are more rigid than those prepared at 20 mM NaOH (**Figure 3.7a**). The trajectories of nanostructures in large AFM images were tracked using the FiberApp software library[86] and the persistence lengths were calculated using the mean squared mid-point displacement method (**Figure 3.7b**). The persistence length, which is proportional to the bending stiffness in a thermal environment, is longer in the low charge state at 5 mM NaOH (21.5 ± 0.6 um vs 8.4 ± 0.2 um). The relative abundance of single twisted ribbons and double helices between the two charge states was also quantified using both liquid AFM and negative stain TEM images (**Figure 3.7c**). In the low charge population, 60 ± 8% of the structures in the population are double helices, while 33 ± 6% are double helices at high charge. Fourier-transform infrared (FTIR), wide angle x-ray scattering (WAXS), and circular dichroism (CD) spectroscopy show hydrogen bonding and clear β-sheet signatures (**Figure 3.8**), however there is no indication of a significant change in the secondary structure between the two populations in these spectroscopy measurements, which suggests that the difference in structure is due to higher order organization of the β-sheets, rather than within the β-sheets. While the abundance of double helices is lower in the high charge state, there is no difference between the morphology of the double helices formed in the two states (**Figure 3.9**). This suggests that the

change in the stiffness of the assemblies modifies the formation energy of the double helices, but not their geometry.

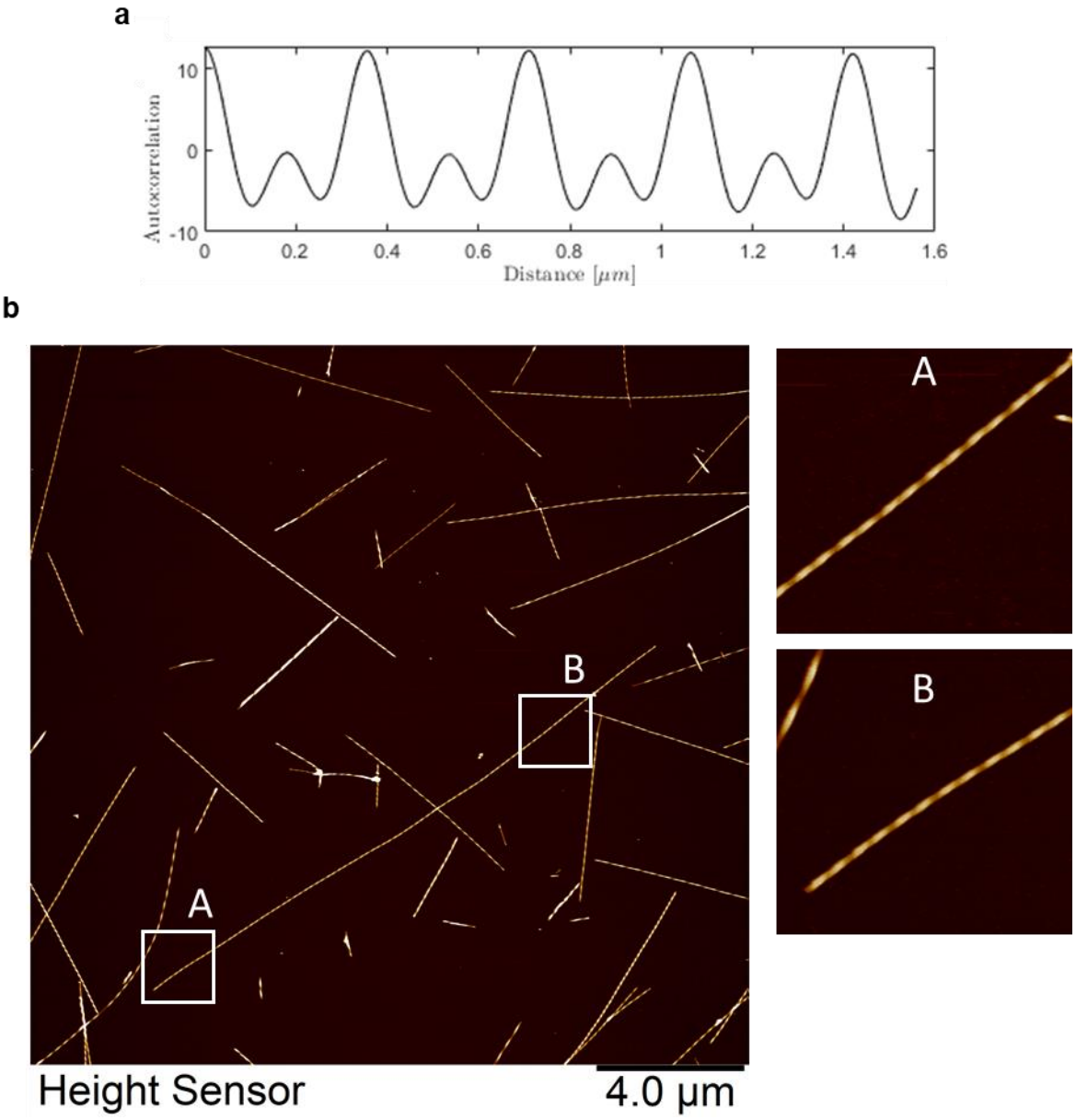

Figure 3.6. Long range order in the double helix. (a) Autocorrelation function of the height profile in **Figure 3.5**, showing little decay on the micron length scale. (b) Regions of long nanostructures separated by ~10 microns show identical nanoscale morphology.

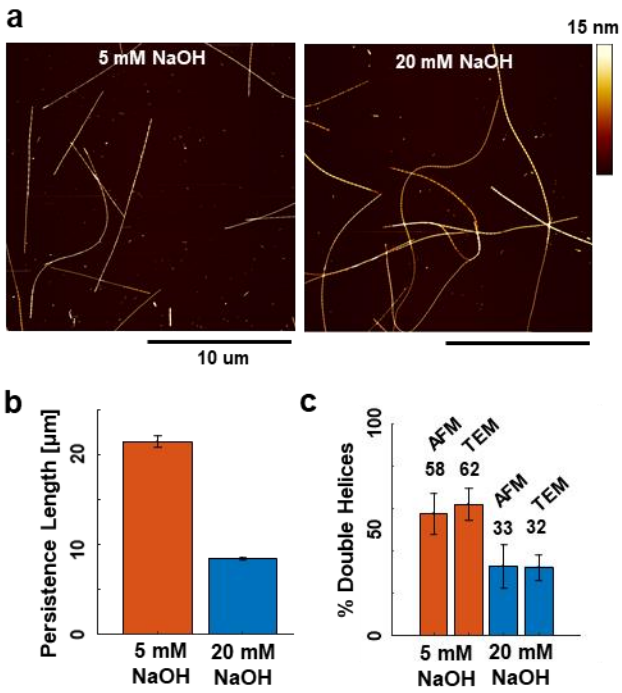

Figure 3.7. Properties of PA nanofibers. (a) Large AFM images and (b) persistence length of PA nanofibers prepared at 5 mM and 20 mM NaOH, measured using the midpoint displacement model. (c) Percentage of nanostructures with a double helix geometry, measured with AFM and TEM. Error bars indicate 95% binomial confidence interval.

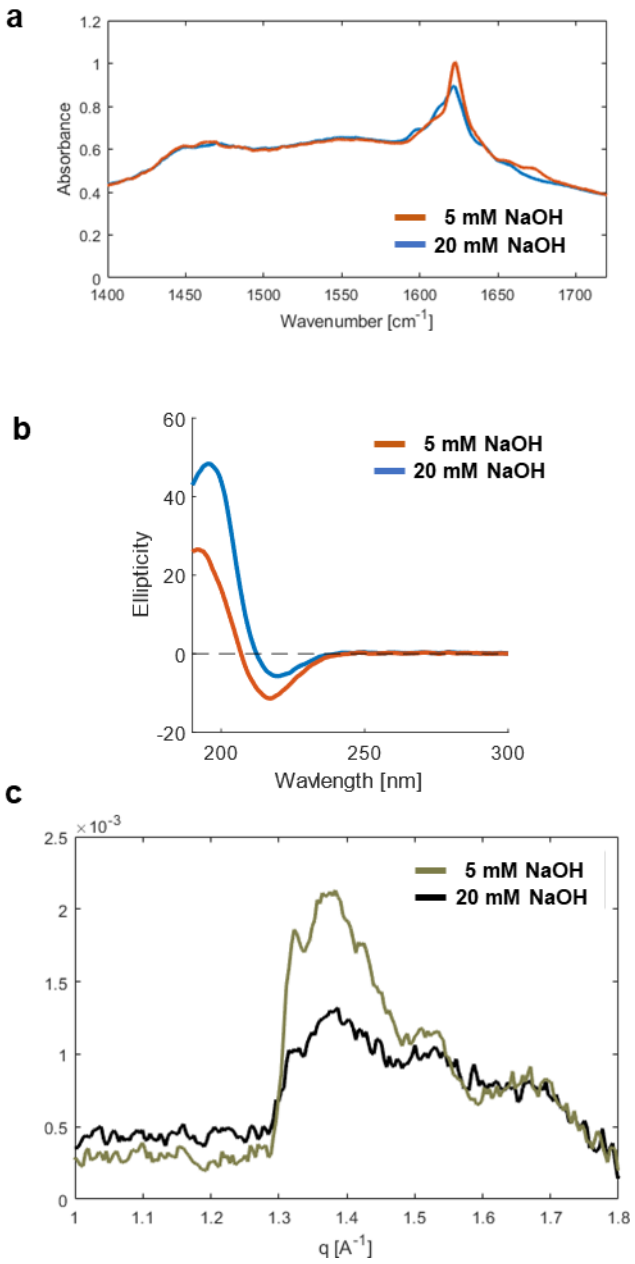

Figure 3.8. Characterization of PA solutions. a) Fourier Transform infrared (FTIR)spectroscopy, b) circular dichroism (CD), and c) wide angle x-ray scattering (WAXS).

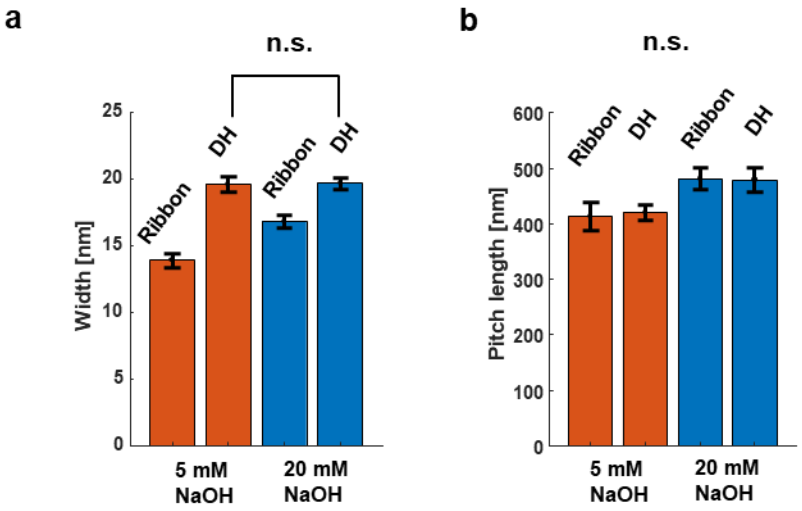

Figure 3.9. Morphology comparison of twisted ribbons and double helices at 5 mM NaOH and 20 mM NaOH. a) Width comparison, and b) pitch length comparison.

3.3.2. Model of double helix formation

We explore the relation between nanostructure stiffness and the propensity to form either twisted ribbons or alternating groove double helices by developing a physical model that can explain the experimentally observed behaviour. In supramolecular peptide double helices that have been studied previously, where the individual strands are composed of a one-dimensional stacks of molecular units such as in Aβ(1-42) fibrils or Tau PHFs, the aggregation has been investigated in terms of the side chain interactions between molecules on each strand. In PA double helices observed here, however, the cross section of the individual strands are multicomponent assemblies, similar to cylindrical micelles. Therefore, an approach built on classical theories of amphiphile self-assembly in the continuum limit is adopted.

We propose that the double helices are formed via an intermediate helical state which splits into two strands as described in the schematic in **Figure 3.10a**, which results in the observed geometry of major and minor grooves, The Stupp group has previously reported that certain PA sequences create both twisted ribbons and helical ribbons or tubes,[153,154] a phenomenon that has been observed and studied theoretically in other self-assembling peptide systems[155,156]. Twisted ribbons and helical ribbons can be described by the Gauss curvature K of the surface in the thin two-dimensional approximation. A twisted ribbon, with a rotational axis along its center, has saddle-like curvature ($K < 0$), while helical ribbons and tubes have the same curvature as the surface of a cylinder ($K = 0$). The relation between the stiffness of twisted ribbon-like nanostructures and their curvature is also well established. Selinger et al. demonstrated with Monte-Carlo (MC) simulations that chiral supramolecular ribbons can form equilibrium states that vary smoothly from a twisted ribbon to a helical ribbon morphology, as a function of the stiffness of the bonds between molecules.[34] Higher stiffness promotes the cylindrical curvature of a helical ribbon over the saddle-like curvature of a twisted ribbon, as saddle-like curvature requires distortion in the molecule spacing. Ribbons in-between the helical and twisted states, where $K < 0$ but the axis of rotation is not in the center of the ribbon, are found at intermediate stiffness. The Sharon group has developed an analytical theory of similar nanostructures in continuum limit using the theory of incompatible elasticity.[34,35] They extend the classical Helfrich-Probst theory of membrane assembly,[31] which describes the self-assembly of amphiphilic chiral molecules in terms of surface curvatures, to include the effects of membrane stretching. The stretching of the membrane penalizes the saddle-like curvature of twisted ribbons, resulting in geometrically frustrated structures in between twisted ribbons and helices.

As described in Chapter 2, the twist of the β-sheet plays a significant role in determining the shape of PA nanostructures, in a manner similar to stacking of amyloid fibrils[113]. Here, a simpler form of the geometric frustration model is used where only the hydrogen bonds in the β-sheet contribute to the stretching energy, in addition to the hydrophobic region of the molecule which contributes to the classical membrane bending energy. A two-step model in the continuum limit is adopted; in the first step the shape of the ribbon in terms of its bending moduli and the anisotropic β-sheet stretch is solved, and in the second step the ribbons are allowed to split into a double helix by optimizing the β-sheet twist and the interaction between strands. To describe these terms, an analytical model of the geometry of the nanostructures is developed, and then the curvatures and torsions on the surface are calculated. The cross-section of a nanostructure can be defined in a local coordinate system by a curve of the form $\overrightarrow{P_c}(p) = \{r(p)\cos(p), r(p)\sin(p), 0\}$, which is transformed along a helical path $\vec{X}(t) = \{R\cos(\omega_0 t), R\sin(\omega_0 t), \frac{C\omega_0 t}{2\pi}\}$ as shown in **Figure 3.10b**. Here, R is the radius of the helical path, C is the pitch length of the helix, and $\omega_0 = \pm 1$ defines the handedness. The surface of the nanostructure can be parametrized as:

$$\vec{P}(t,p) = \vec{X}(t) + \begin{bmatrix} cos(\omega_0 t) & -cos(\alpha)\,sin(\omega_0 t) & sin(\alpha)\,sin(\omega_0 t) \\ sin(\omega_0 t) & cos(\alpha)\,cos(\omega_0 t) & sin(\alpha)\,cos(\omega_0 t) \\ 0 & -sin(\alpha) & cos(\alpha) \end{bmatrix} \overrightarrow{P_c}(p) \quad (1)$$

Where the coordinate transformation described by Crick is used to translate a local coordinate system along a helix.[157] Here, α is the pitch angle of the helix, given by $\tan(\alpha) = \frac{2\pi R}{C}$, and the helix radius R corresponds to the offset of the center of the nanostructure from the axis of rotation. For the first step the cross-section is assumed to be that of a thin bilayer ribbon, and for the second step the cross section of either a thick ribbon $r_{rib}(p)$ or a strand of the double helix

$r_{DH}(p)$ is used, as shown in **Figure 3.10c**. Each strand of the double helix can be described as a circle of radius l with its edge lying on the central axis, offset in the x-direction by a distance $\pm l$:

$$\overrightarrow{P_c}(p)_{DH} = \{\pm l \mp \sqrt{l^2 - p^2}, p, 0\} \text{ where } p \in [-l, l]$$

The central section of a ribbon can be described simply by two parallel lines, one a distance l above the central axis, and another a distance l below the central axis, where l is the length of a molecule. That is, for a ribbon:

$$\overrightarrow{P_c}(p)_{Rib} = \{p, \pm l, 0\} \text{ where } p \in [-l, l]$$

This describes the central portion of the ribbon, which is compared to the central portion of the double helix. The geometry described in equation (1) is confirmed to be a good approximation to experimentally measured nanostructures by including the effect of AFM tip convolution (**Figure 3.11**).

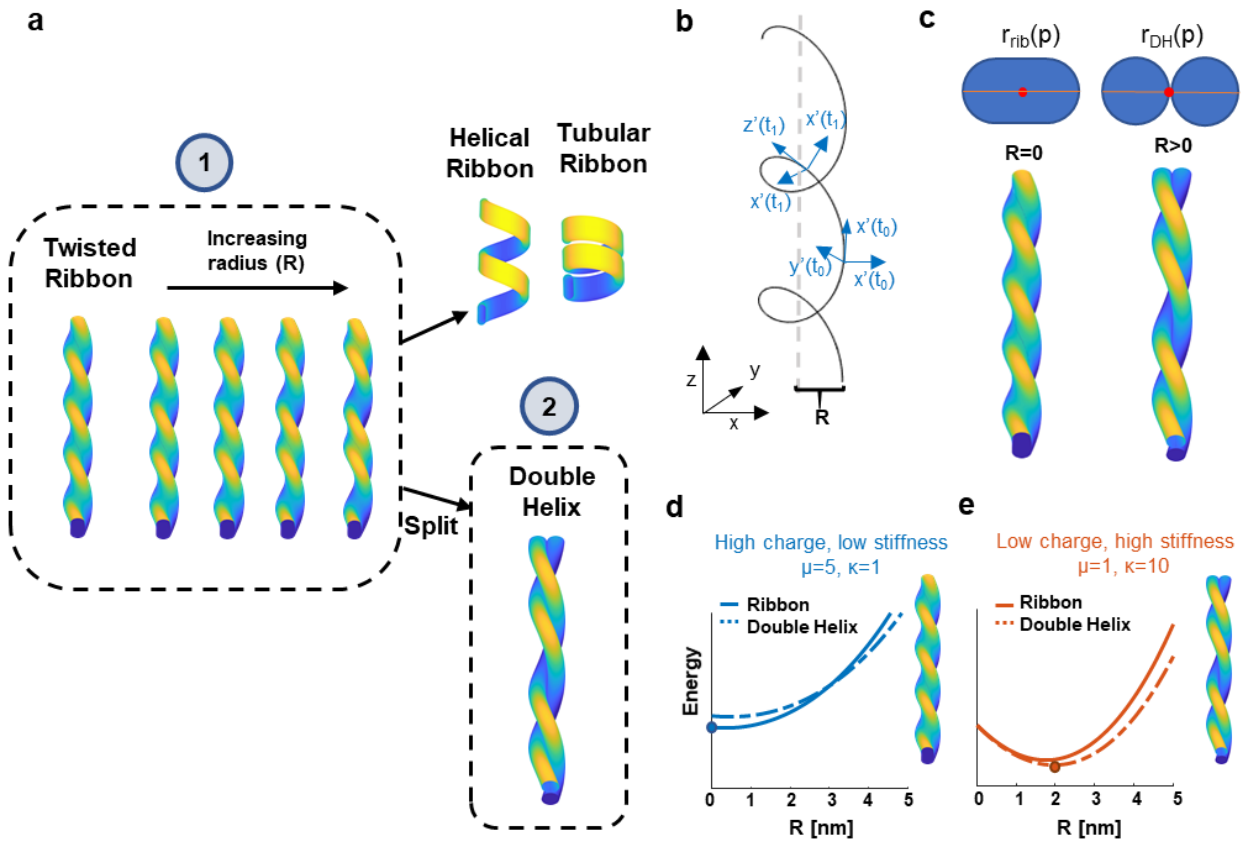

Figure 3.10. Model of double helix formation. (a) Schematic indicating the morphology of twisted ribbons and helical ribbons, and a pathway to create double helices with major and minor grooves from geometrically frustrated ribbons. (b) The coordinate transformation used to describe the geometry of the nanostructures. (c) Cross-section of a twist ribbon and double helix. (d) & (e) Results for numerical analysis of the model, indicating the energy minimum for twisted ribbon and double helix formation.

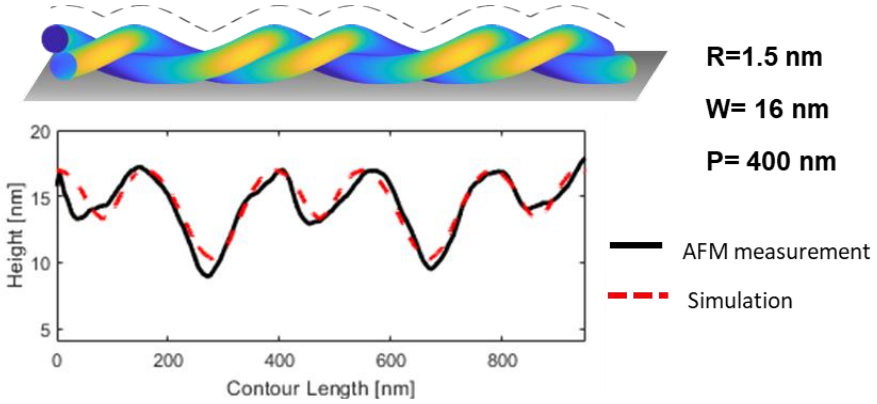

Figure 3.11. Comparison of measured double helix AFM topography with modelled geometry.

The bending energy of the ribbons is calculated using the classical Helfrich-Probst energy. Previous work has demonstrated that PA molecules without a hydrogen bonding peptide sequence create flat sheets.[110] The Helfrich-Probst bending energy per unit area of such bilayer ribbons without spontaneous curvature is given by [ref] $E_{HP} = \frac{1}{2}k_H H^2 + k_K K$, where H and K the mean and Gauss curvature respectively, with moduli k_H and k_K. The stretch energy of the surface due to the peptide can be expressed as $E_s = \frac{1}{2}k_\beta\left(C_\beta - C_o\right)^2$, where C_β is the curvature of the surface in the direction parallel to the helical axis, and C_o is the curvature of an ideal β-sheet. The curvatures H, K, and C_β can be calculated numerically from equation (1) as a function of the nanostructure shape.

The energy of the internal torsional deformation of the twisted β-sheets is described as the torsion of the surface along the helical axis, a continuum approximation of twist of discrete β-sheets. The torsion parallel to the helical axis on surface is given by $\tau(p) = \frac{r'(p)}{r'(p)^2 + C^2}$, where r' is the distance from the axis of rotation to the point on the surface, and can calculated numerically from equation (1). The torsion energy arises from the strain in the β-sheet due to a change in twist from its ideal state τ_o. The torsional energy per unit area over the surface is described as a torsional spring: $E_\tau = \frac{1}{2}k_\tau(\tau(p) - \tau_o)^2$, where k_τ is the torsional modulus.

E_{HP}, E_S, and E_τ can be numerically integrated to calculate the total energy of the structure. Due to the translational symmetry, all three terms are independent of the parameter t, and the integration only needs to be performed over the cross-section. As expected, the $\int E_{HP}$ and $\int E_S$ terms drive the transition from a twisted ribbon to a helical ribbon as the k_β modulus is increased (**Figure 3.12**). The $\int E_\tau$ term is also lower in a double helix state as compared to a twisted

ribbon (**Figure 3.13**), as β-sheets become more strained further from the center in ribbons, while in double helices where each strand is similar to a cylinder, the β-sheets are more uniform and closer to their ideal state.

In the continuum approximation used here, the discreteness of the charged molecules and their bound counterions has been removed, which is appropriate for a ribbon or for each individual strand of the double helix. Within a complete double helix, however, the interaction of two strands is expected to contribute an additional net energy penalty, primarily due to electrostatic repulsion. The interaction at the interface between strands is treated as a constant energy per unit length $E_{inter} = \epsilon > 0$.

The final energy per unit length of nanostructures is:

$$E_{ribbon} = \int E_{HP}[r_{rib}] + \int E_S[r_{rib}] + \int E_\tau\,[r_{rib}] \tag{2}$$

$$E_{DH} = \int E_{HP}[r_{DH}] + \int E_S[r_{DH}] + \int E_\tau\,[r_{DH}] + \epsilon \tag{3}$$

where the integration is over the cross-section of a nanostructure. A numerical analysis of the model shows that twisted ribbons have lower energy than double helices when the membrane bending modulus is low and the charge repulsion is high, as the minimum energy state is a twisted ribbon with $R = 0$ (**Figure 3.10d**). When the bending modulus is high and the charge is low, however, the double helices have lower energy with $R = 0$, resulting in a double helix with major and minor grooves (**Figure 3.10e**). The parameters for the numerical calculations were chosen to provide qualitatively similar behaviour to experimental observations, and a complete phase diagram is shown in **Figure 3.14**. The results indicate that the major and minor grooves originate from the transition from a twisted ribbon to a helical ribbon intermediate, driven by an increase in the stretch stiffness. The change in the state from the helical intermediate to a double helix is driven

by the reduction of the β-sheet strain and is opposed by the electrostatic penalty at the interface of the strands. This emergent supramolecular behaviour contrasts with the peptide based double helices reported previously, where the aggregation of two individual one-dimensional strands is controlled by the interaction of side chains at their interface.

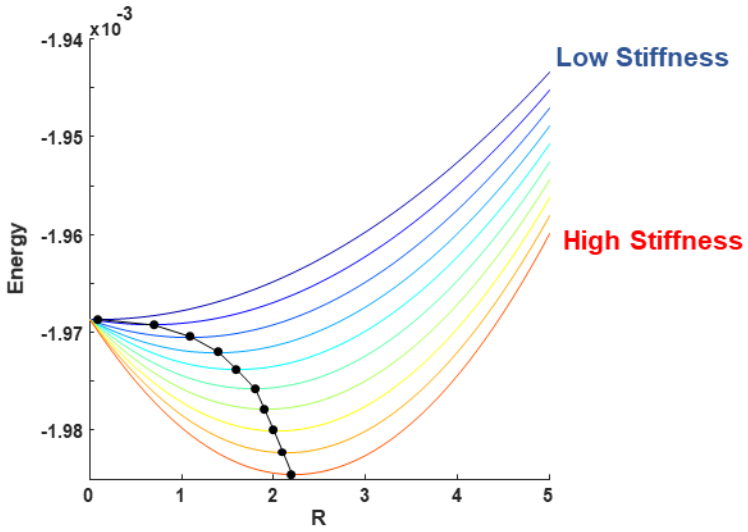

Figure 3.12. Ribbon curvature and stretch energies as a function of asymmetry parameter R, for different values of stiffness. Dots indicate R value that minimizes energy.

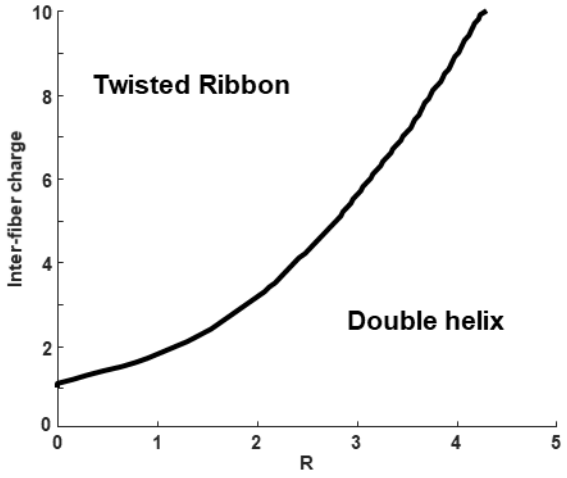

Figure 3.13. Phase boundary of the torsional energy component between twisted ribbon and double helix regime as function asymmetry R and inter-fiber charge.

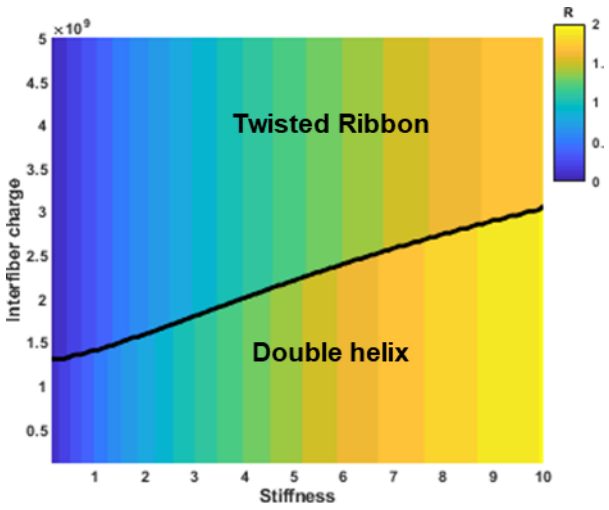

Figure 3.14. Phase diagram of the complete model.

3.3.3. Nanomechanical measurements of PA nanofibers

In addition to measuring the persistence length of nanofibers, direct measurements of the stiffness of the nanostructures were attempted with AFM indentation experiments. For these measurements, the Quantitative Nano mechanics (QNM) system developed by Bruker was used,

where the AFM tip is oscillated at a sub-resonant frequency during imaging and the force curves are recorded simultaneously.[158,159] This method provides high resolution stiffness maps, which are essential to observe the stiffness of small nanostructures like PA nanofibers. An unusual phenomenon is observed in these experiments, where the measured stiffness has an unexpected dependence on the morphology of the nanostructure, as shown in **Figure 3.15**. For twisted ribbons, the peaks in the height correspond to stiff regions, while the troughs correspond to soft regions. On the other hand, in double helices the major groove corresponds to stiffest regions, the peaks correspond to regions of intermediate stiffness, while the minor groove corresponds to softest regions. Rather than a real change in the stiffness of the nanostructures, it is hypothesized that this effect is an artifact of the three-dimensional arrangement of the nanostructure above the mica substrate. This is tested by calculating the distance between the bottom of the nanostructures and the substrate, using the geometry developed previously. The apparent stiffness is first assumed to be directly proportional to the distance between the bottom of nanostructure and the substrate, and the result is compared to the measured stiffness. As described in **Figure 3.6**, there is an excellent agreement between the simulations and experiments for both twisted ribbons and double helices. This confirms the hypothesis that the stiffness measured using QNM is not related to the modulus of nano assembly but is instead an artifact of the morphology.

Previous work by Sweers et. al. has also shown that QNM measurements on charged nanostructures are highly sensitive to the salt content in the solution.[160] At high salt, the measured modulus of nanostructures can appear to be higher than the underlying substrate, which contradicts the assumptions made when measuring the modulus itself. This likely due to a change in the short-range electrostatic repulsion near the surface of charged objects due to screening by salts. The AFM tip during QNM measurement is likely deflecting due to the electrostatic double layer

repulsion before the nanostructure is physically deformed, leading to an incorrect interpretation of the elastic modulus. These results, combined with the measurements shown here, suggest that QNM is not a reliable method to measure the stiffness or elastic modulus of charged nanostructures with complex morphologies. Therefore, only the persistence length is used as a measure of nanofiber stiffness.

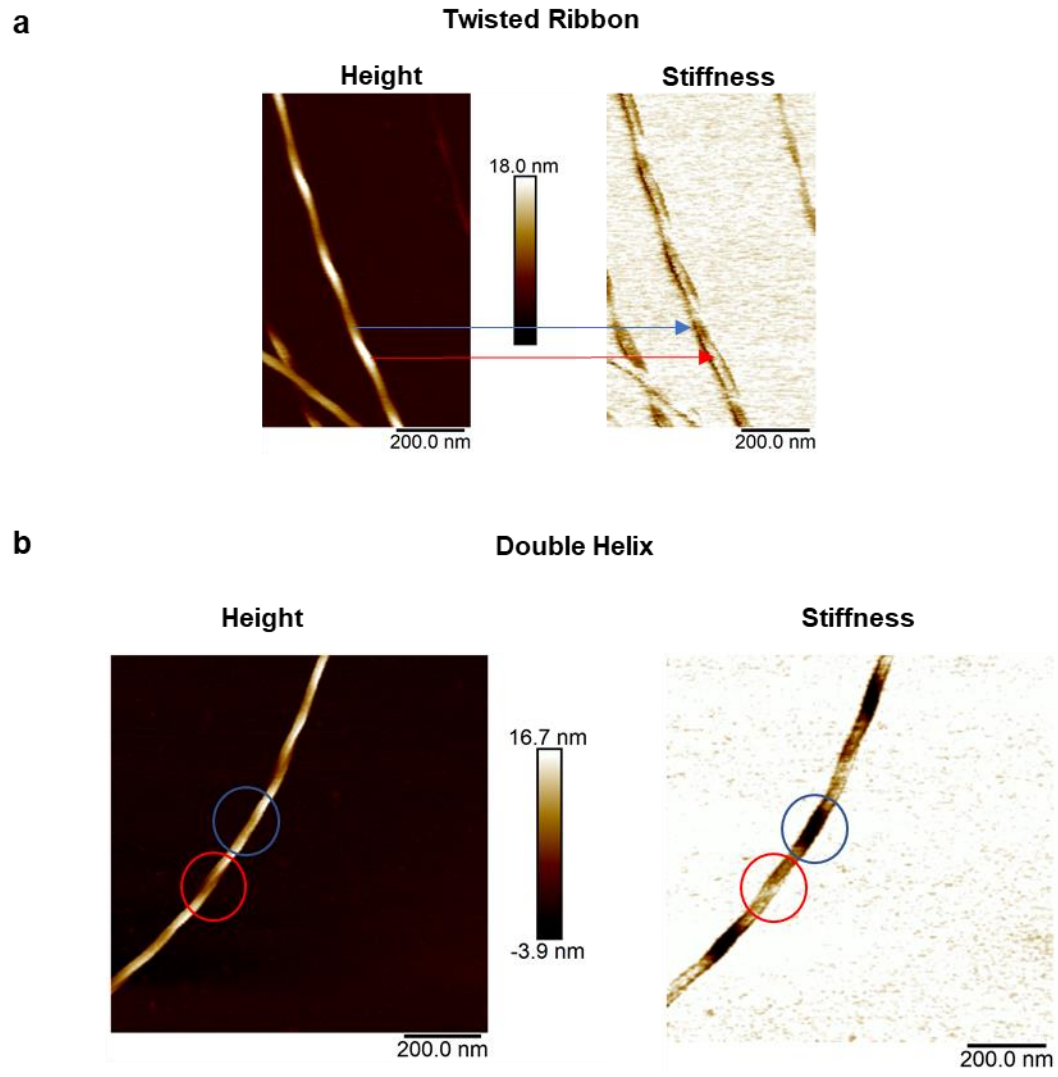

Figure 3.15. Relation between nanostructure height and stiffness measured with QNM. Measurements for (a) twisted ribbons and (b) double helices.

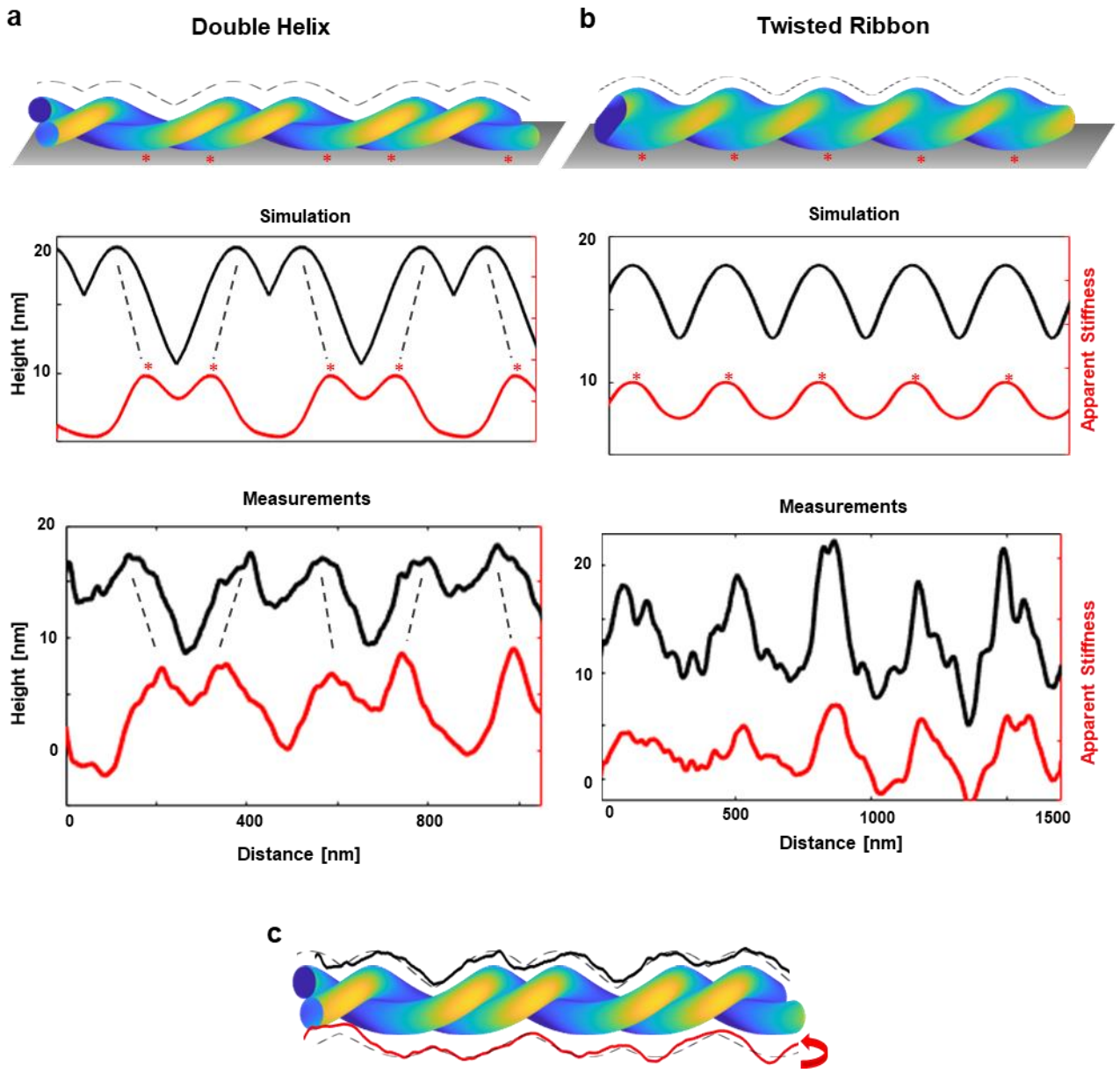

Figure 3.16. Simulations and measurements of PA nanomechanics. Comparison of the simulated and measured height and stiffness of (a) double helices and (b) twisted ribbons, with the assumption that the apparent stiffness is entirely an artifact of the geometry. (c) A comparison illustrates that the apparent stiffness (red line) is highly correlated to the distance between the bottom of the nanostructure and the substrate.

3.3.4. Remodeling of nanofiber biomimetic scaffolds

The persistence lengths of the PA nanostructures observed here of the same order of magnitude as those of extracellular matrix (ECM) components such as collagen fibrils (Pl ~ 10-100 ums). Therefore, the applicability of these nanostructures with different persistence lengths as biomaterial scaffolds was investigated. While PA scaffolds have been shown to degrade in vivo, changes in PA network architecture in biological environments has not been investigated. For biological experiments, PA solutions were deposited onto coatings to immobilize the network architecture formed by fibers of the different persistence lengths. To visualize changes in the micro-architecture of the coatings, the PA nanostructures were doped with a fluorescent dye labelled version of the molecule. Coatings were formed by diluting the labelled PA solutions to 0.1 mM in phosphate buffer saline (PBS), and drop casting onto poly-D-lysine (PDL) coated glass bottom petri dishes. The excess solution was washed off, and the coatings were equilibrated in PBS before plating normal Human Lung Fibroblasts (NHLF). AFM imaging shows that the coatings are thin monolayer networks of fibers, and confocal laser scanning microscopy (CLSM) confirms that the coatings are uniform across length scales of 100s of microns, much larger than the size of the cells (**Figure 3.17**).

Imaging the coatings 24 hours after cell plating shows that the microstructure of the nanofiber networks is significantly modified by the cells (**Figure 3.18a**). There are large areas in the vicinity of the cells that are cleared of fluorescence, while some small regions, indicated with white arrows, show an increase in fluorescence intensity, suggestive of bundling and aggregation of fibers. To examine these microarchitecture changes in more detail, correlative CLSM-AFM imaging was used, where the same regions of the sample are imaged with both CLSM and AFM. The correlative imaging confirms that the fiber network is physically degraded and deformed by

the cells in the areas with decreased fluorescence (**Figure 3.18b** and **Figure 3.18c**). These regions are interpreted as locations that were occupied by the cells during the incubation and were modified by cellular traction forces. In addition, fibers are seen to aggregate at higher density at the edges of the deformed areas, which correlates directly with local increases in fluorescence intensity, as indicated with arrows. Although the resolution of optical microscopy is much lower than size of individual nanostructures, these measurements confirm that the fluorescence intensity of the coating can be used as a measure of the local network architecture.

In addition to the regions of localized high intensity around the periphery of the cell, internalization of the fluorescent molecules is also observed. PA nanostructures have previously been shown to be readily internalized by a variety of mammalian cell lines, and the endocytosis behaviour is determined primarily by the lipid tail.[60,161] Three-dimensional z-stacks in CLSM confirm that the PA coatings used here are also internalized by the cells, as fluorescence intensity can be seen localized inside the cell body (**Figure 3.19**). Labelling the cells with lysotracker (Sigma), a pH sensitive cell permeant dye, also confirms that the internalized PA is present in lysosomes within the cell body (**Figure 3.20**). The deformation, degradation, and internalization of the PA coating by the cells observed here is indicative of significant material remodeling.

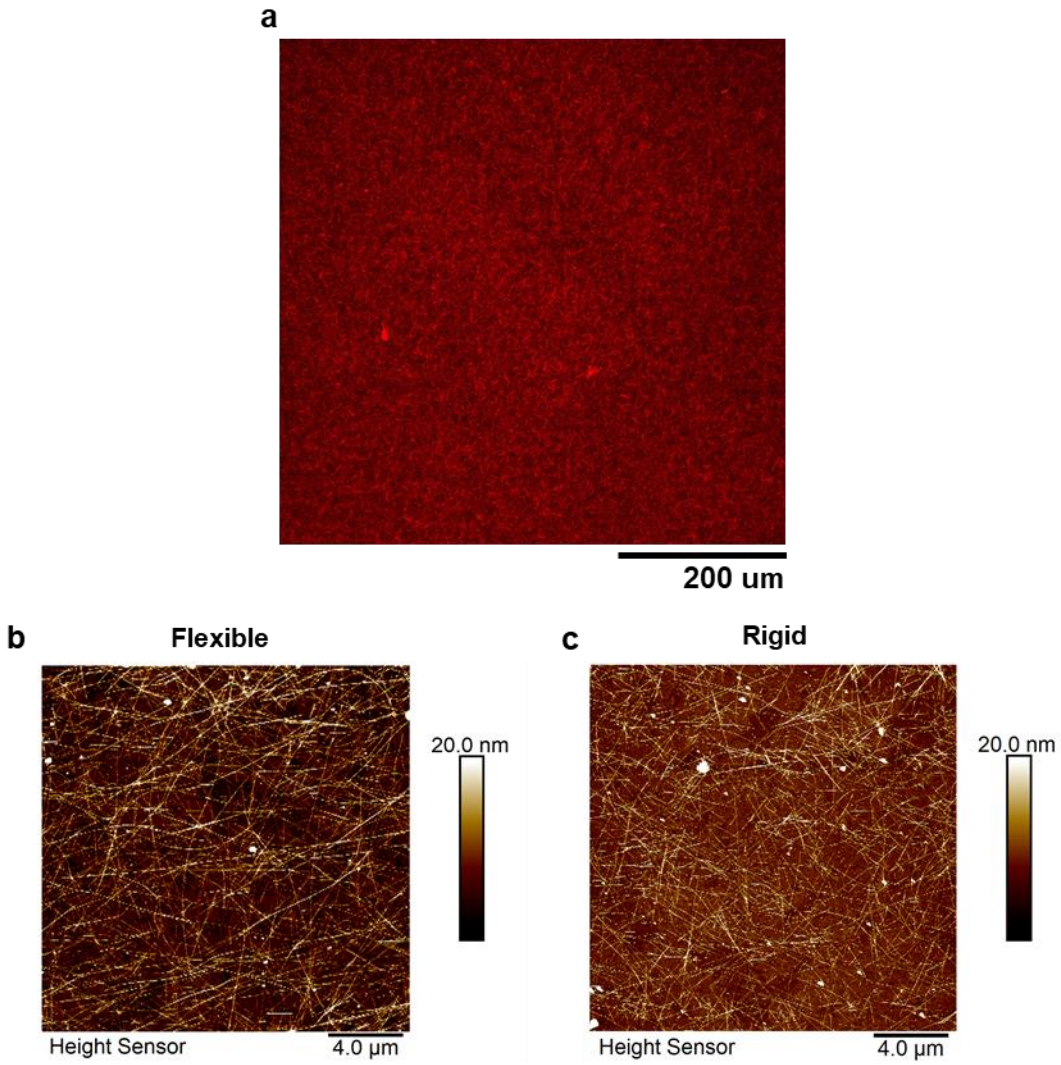

Figure 3.17. PA Coating uniformity measured with CLSM and AFM. a) CLSM max intensity projection of a stitched composite image, of a flexible fiber coating. AFM images of a b) flexible fiber coating and c) rigid fiber coating.

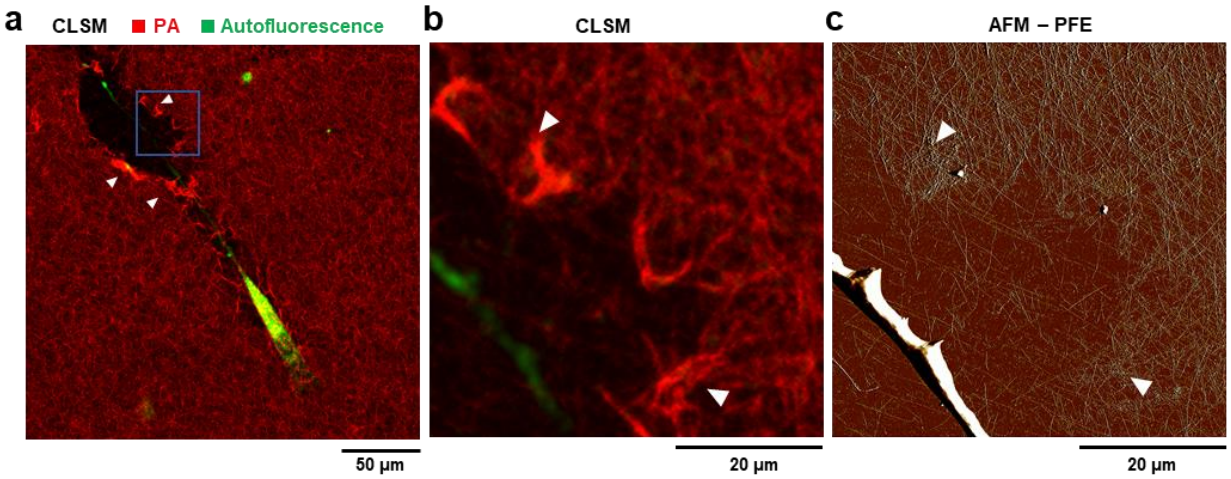

Figure 3.18. Remodeling of PA nanostructure coatings by cells. (a) CLSM image of a PA coating (red) with fibroblasts (green) plated for 24 hours. Dark regions correspond to areas where PA has been removed from the surface, and white arrows indicate regions of high fluorescence intensity. (b) and (c) Correlative CLSM-AFM of the boxed region in (a), where the fluorescence signal from PA nanostructures in (a) correlates with density of nanostructures on the coating observed in the AFM image in (b). White arrows indicate regions of higher fiber density.

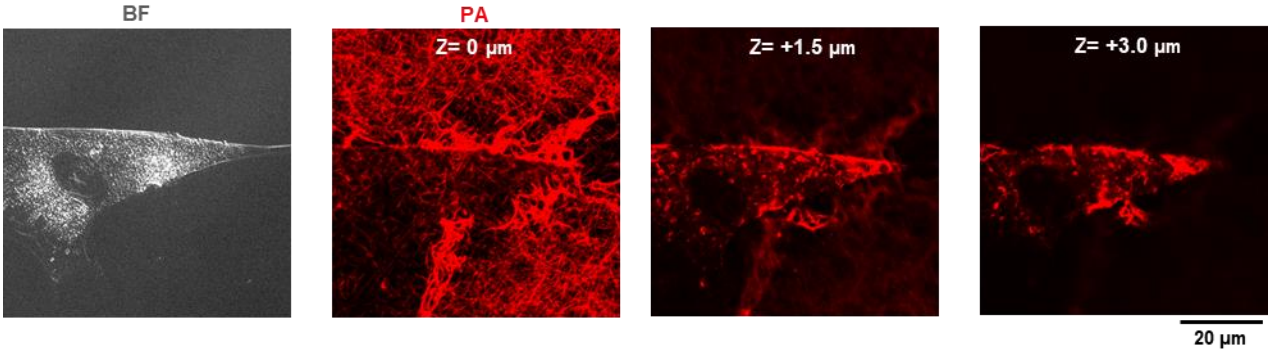

Figure 3.19. Z-stack CLSM images of internalization of fluorescent PA by into the cell body.

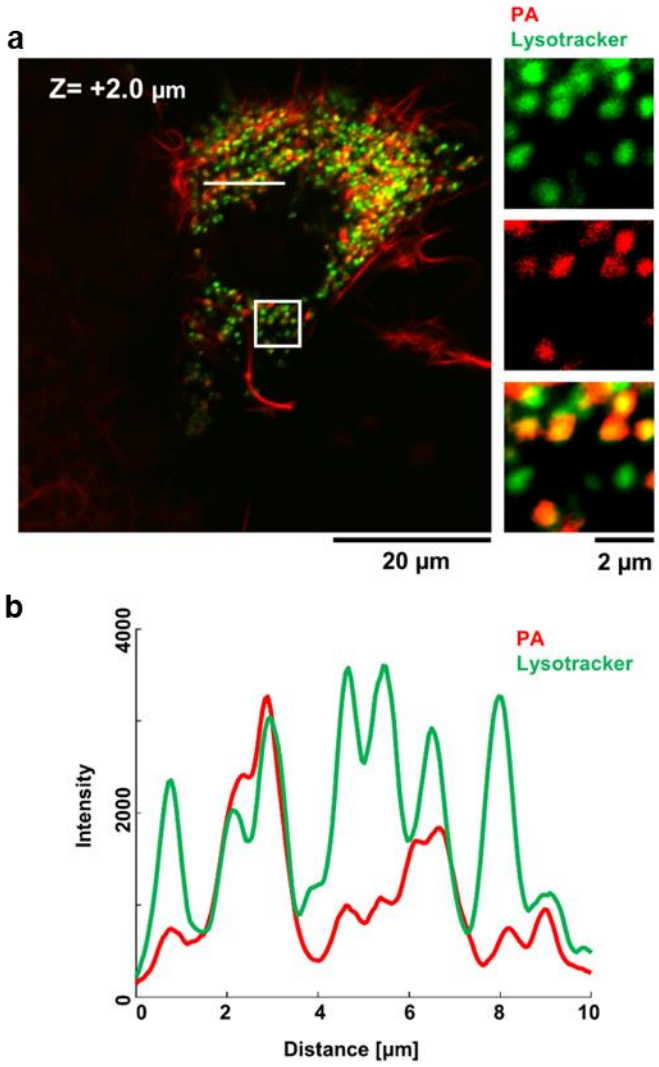

Figure 3.20. Trafficking of internalized PA to lysosomes.

While previous work has established that PA nanofibers are internalized via a clathirin mediated pathway, it is unclear how the PA nanofibers disintegrate before internalization. While the PAs could be degraded by proteases at the cell surface, the mechanism may be more general as a variety of different peptide sequences have shown to internalized. Missirlis et. al. demonstrated that a bioactive PA maintained its bioactivity once internalized, which suggests the

PA is internalized without cleavage of the peptide sequence.[59] The possibility that the biophysical interaction between PAs and amphiphilic phospholipids on the cell membrane could cause the assemblies to disintegrate, similar to a detergent effect, is also investigated. To test this idea, supported lipid bilayers (SLB) of 1,2-dioleoyl-sn-glycero-3-phosphocholine (DOPC), a common phospholipid in cell membranes, were prepared using published protocols.[162] Briefly, lyophilized DOPC (Sigma) is dissolved in chloroform, aliquoted, and the chloroform is evaporated off under nitrogen flow to create a film of DOPC. The DOPC is dissolved in deoxygenated milliQ water at a concentration of 0.5 mg/ml, stirred for 1 hour with a magnetic stir bar, and then sonicated for 10 minutes. This results in a clear solution composed of nanoscale vesicles. The solution is deposited onto cleaved mica substrates for 20 minutes, and then rinsed with PBS. The formation of an SLB is confirmed by de-wetting the surface to observe the disintegration of the bilayer (**Figure 3.21**). PA nanofibers were added to the SLB at a concentration of 0.1 mM, and rinsed off after 10 mins. AFM imaging shows that the nanofibers break apart into smaller fragments on the surface (**Figure 3.22**). In addition, the breakdown of fluorescently labelled PA nanofibers on SLBs was measured with CLSM. The CLSM images showed rapid disintegration of nanofibers into small fragments after 2 hours of contact with lipid bilayer (**Figure 3.23**). These results confirm that a non-specific biophysical interaction of PA nanofibers with amphiphilic phospholipids is sufficient to explain the disintegration observed in cell experiments.

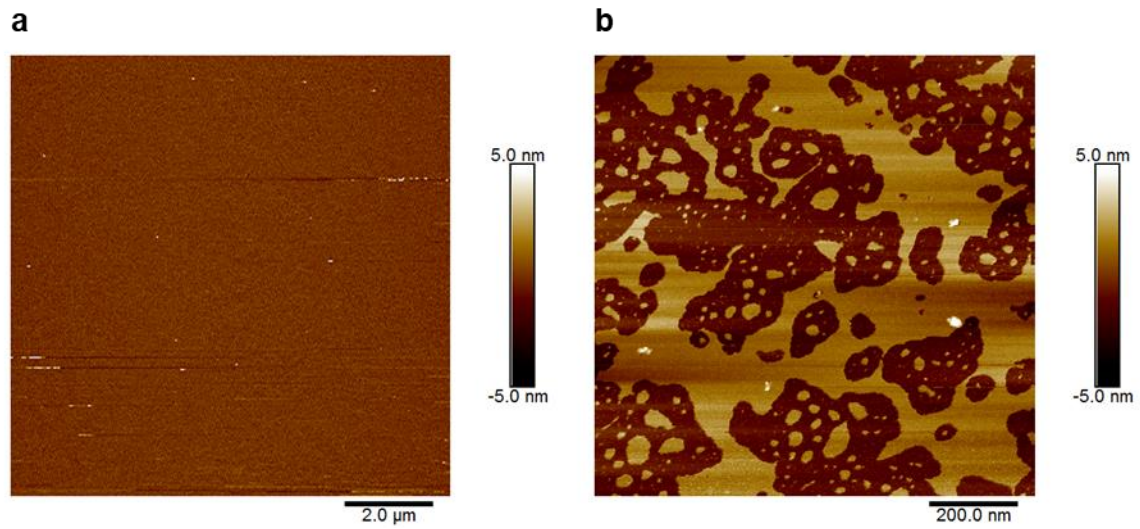

Figure 3.21. DOPC supported bilayers on mica substrates. DOPC bilayers on mica image (a) before and (b) after de-wetting.

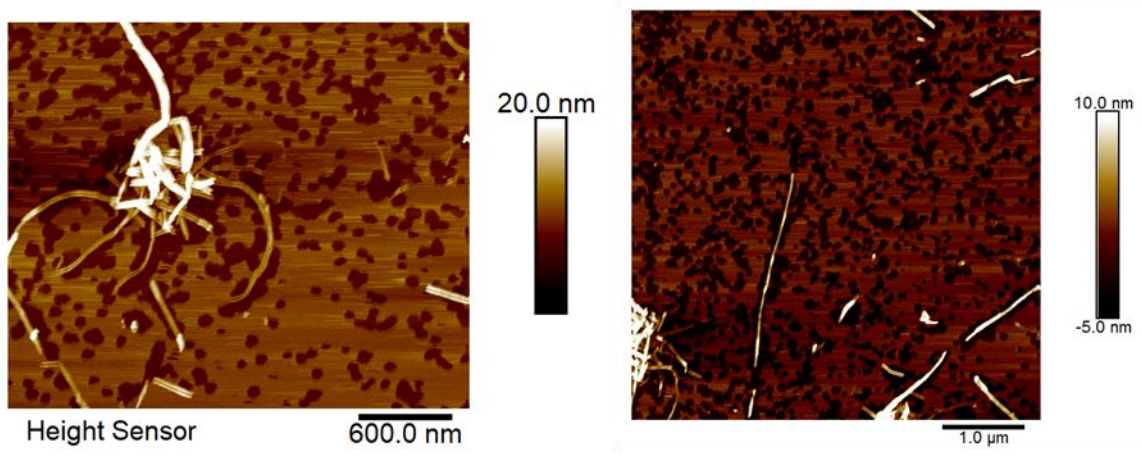

Figure 3.22. AFM images of disintegration of PA nanofibers on DOPC bilayers. Example AFM images of PAs deposited on DOPC biolayers, imaged after de-wetting, with small fragments and bundles visible.

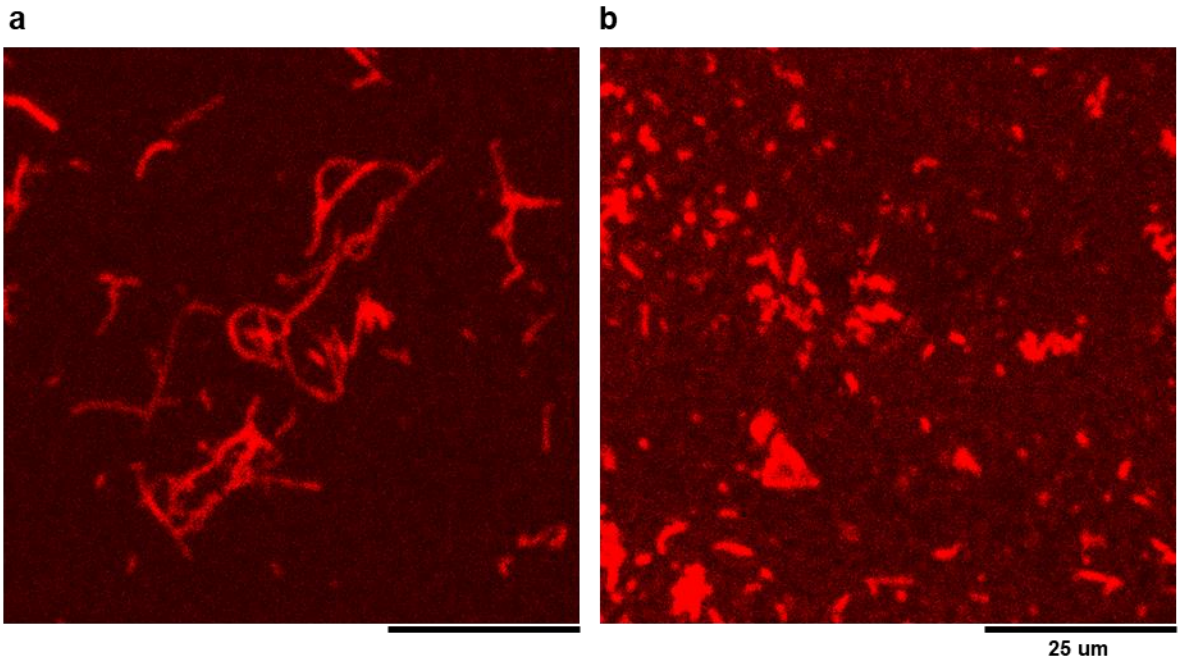

Figure 3.23. CLSM images of disintegration of PA nanofibers on DOPC bilayers. (a) Control image of fluorescent PA nanofibers on mica substrate. (b) Image of fluorescent PA nanofibers deposited on DOPC biolayer after 2 hours of incubation.

We next compared the cell mediated degradation of PA coatings composed of rigid fibers with those composed of flexible fibers. Maximum intensity projections were calculated from z-stack CLSM images (**Figure 3.24a** and **Figure 3.24d**) and the total degraded surface area in the vicinity of each cell was measured (**Figure 3.24b** and **Figure 3.24e)**. The uniformity of the degraded region around the boundary of the cells was also measured, as a percentage of the area overlapping between the immediate vicinity of the cell boundary and the degraded region of the coating (**Figure 3.24c** and **Figure 3.24f**). The measurement shows that the rigid coatings are degraded over a significantly larger area than flexible coatings (**Figure 3.24g**). In addition, the rigid coatings are degraded more uniformly around the boundary of the cells, while cells on

flexible coatings overlap with regions where nanofiber microarchitecture has not been degraded (**Figure 3.24h**). To understand this difference, the interaction of cells with the fiber network was assessed at the edges of the cellular lamellipodia, where traction forces are highest during cell spreading and migration.[163] The average intensity profile of the PA coating across the lamellipodia edges shows a large drop in intensity in the rigid fiber compared to the flexible coatings, indicating more removal of material from the local environment of the lamellipodia (**Figure 3.24i**). This suggests that the difference in coating degradation is due to a modified material response to the traction forces exerted near the cell edges as the cells spread on the coating.

The deformation of the PA network around the lamellipodia was investigated using Z-stack 3D CLSM images and AFM. Cells were imaged in brightfield (**Figure 3.25a**), and approximate cell outlines were identified from the autofluorescence signal (**Figure 3.25b**). The fluorescence z-stacks were converted to depth coded intensity images, and the three-dimensional position of the nanofibers over the cell lamellipodia were compared (**Figure 3.25c**). On rigid fiber coatings the nanofibers are mostly cleared around the lamellipodia, and some material is found on top of the cell body farther from the edge, as expected. In contrast, on the coatings of flexible fibers the fibers overlapping the lamellipodia lie on top of the cell rather than underneath, which implies that the cells migrate between the substrate and the coating, and displace the network out of the plane of the substrate without significant degradation. As confirmation, regions near the cell lamellipodia on flexible fiber coatings that were imaged in brightfield and z-stack CLSM imaging (**Figure 3.25d** and **Figure 3.25e**) were also measured in correlative AFM (**Figure 3.25f**). Nanofibers can be observed crossing across the top of the cells in the correlative images, as indicated with arrows in **Figure 3.25g**, which confirms that the cellular extensions at the lamellipodia edges bury

underneath the coating. In contrast, the rigid fibers seen in AFM-CLSM appear to be removed entirely from the vicinity of the cells, as expected from the previous results (**Figure 3.26**). Although it initially appeared that the cells were spreading over the flexible PA network, these results show that cells can deform the flexible coatings without degrading them during spreading. This also suggests that under these experiments the cell behaviour is likely dominated by interactions with the underlying substrate. Interestingly, there is no statistically significant difference in the cell morphology, cytotoxicity, or oxidative stress between either of the PA coatings or the blank control (**Figure 3.27**). This confirms that the difference in the coating response is due to the physical properties of the material itself, rather than a change in biological behaviour of the cells. The conclusion is that the cells degrade the coatings to adhere to the attractive PDL substrate after plating, and then flexible fiber coatings are primarily deformed by traction forces rather than degraded further.

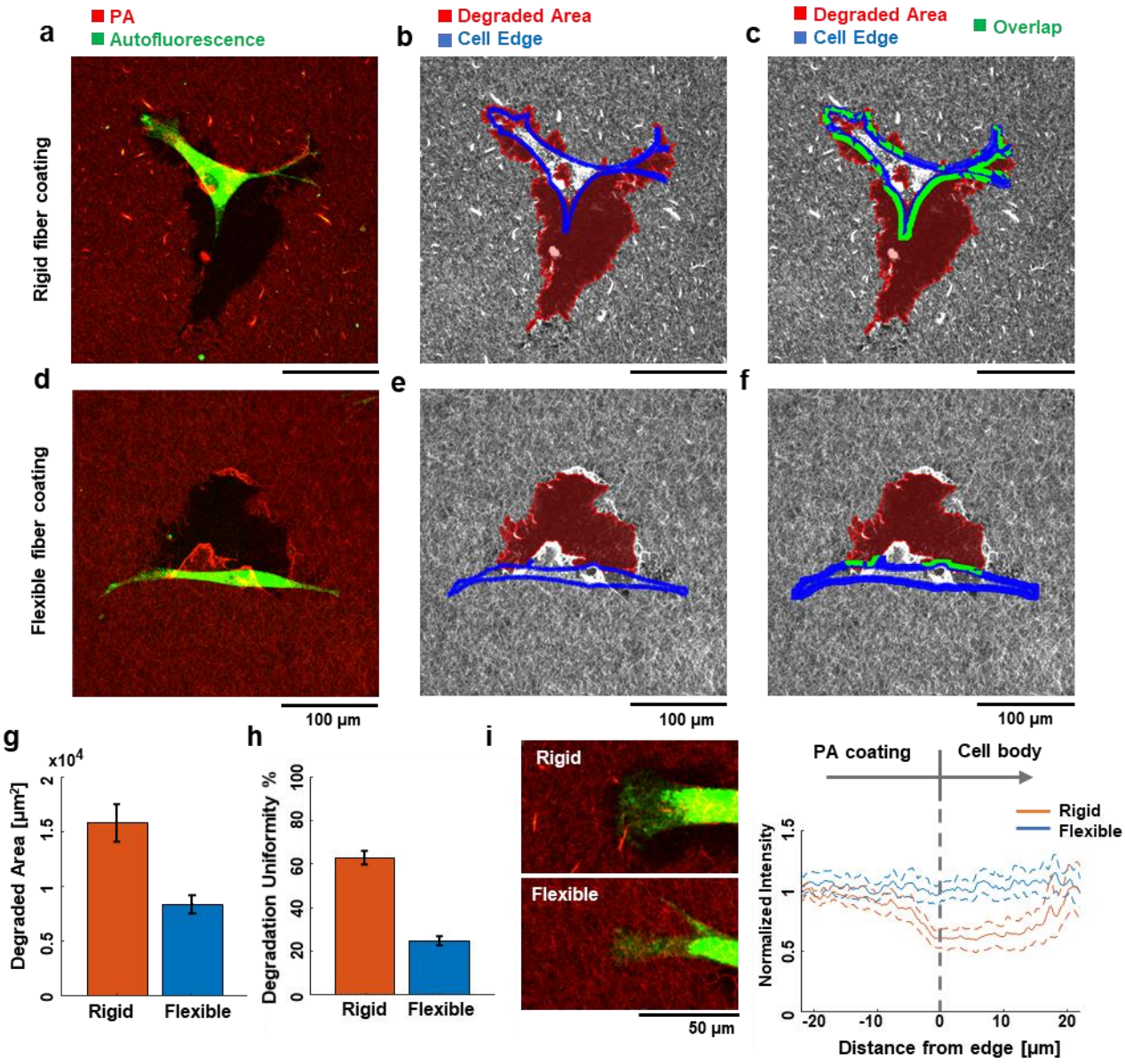

Figure 3.24. Remodeling of PA coatings as a function of fiber stiffness. (a) CLSM of a coating of rigid fibers plated with NHLF cells for 24 hours. (b) Measurement of degraded area per cell and (c) uniformity of degradation around the boundary of the cell. Green regions indicate overlapping areas between the cell edge and the degraded region. (d-f) Corresponding image and analysis for flexible fiber coating. (g) Degraded area and (h) degradation uniformity comparison between rigid and flexible coatings. (p-val=1.3×10^{-4} and p-val=1×10^{-15}, N=35). (i) The average fluorescence intensity profile across the lamellipodial edges of cells. Dotted lines indicate the 95% confidence interval (n= 40).

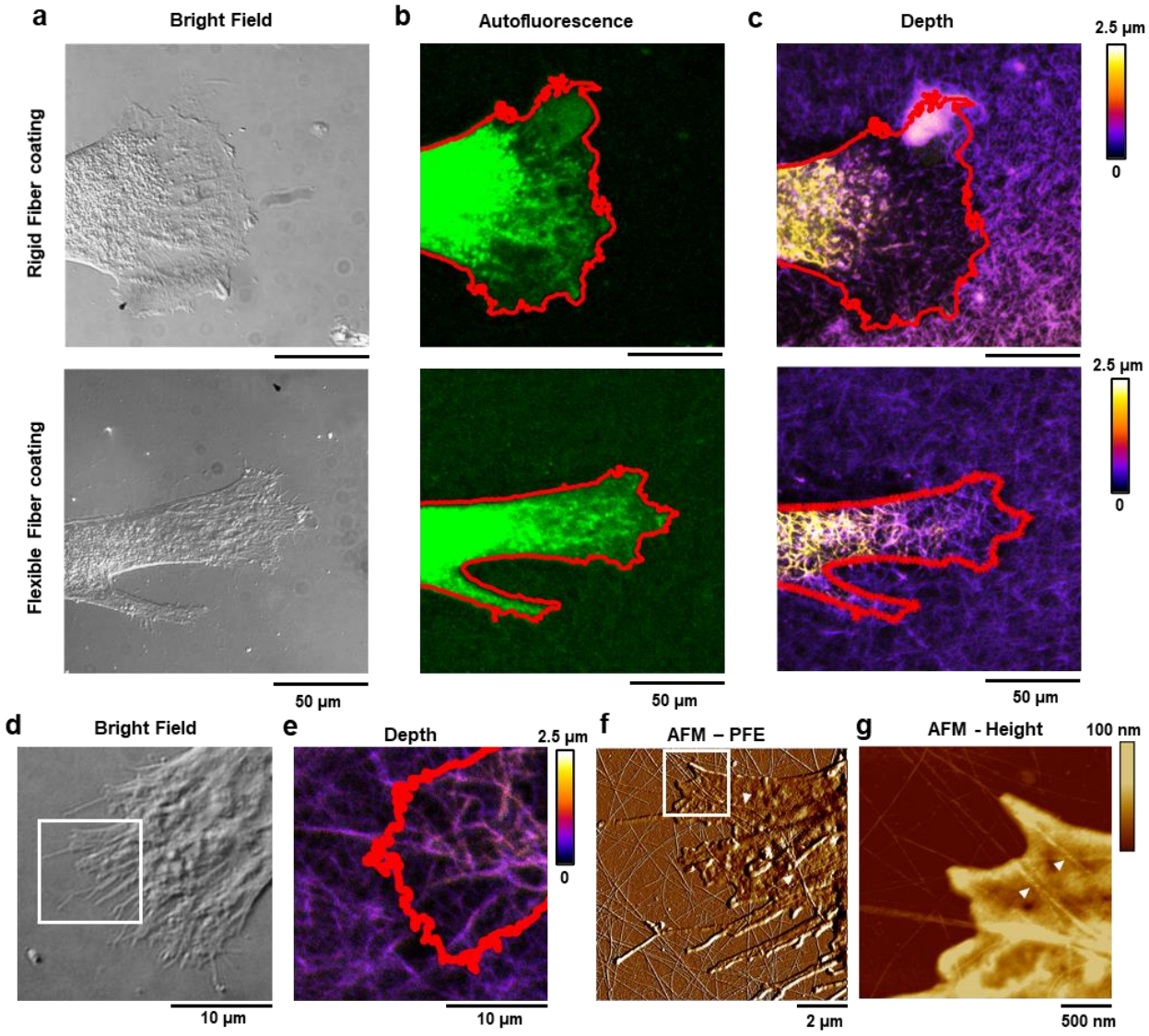

Figure 3.25. Out of plane deformation of PA coatings. (a) Bright field image of a cell on a flexible fiber coating, (b) autofluorescence image of cell with approximate cell edge highlighted, and (c) depth coded z-stack of nanofibers on rigid (top) and flexible (bottom) fiber coatings. (d) Bright field and (e) depth coded image of nanofibers on the cell, (f) correlative AFM image of the same region, and (g) zoomed topographic image of the boxed area in (f). White arrows indicate nanofibers that pass on top of the cell.

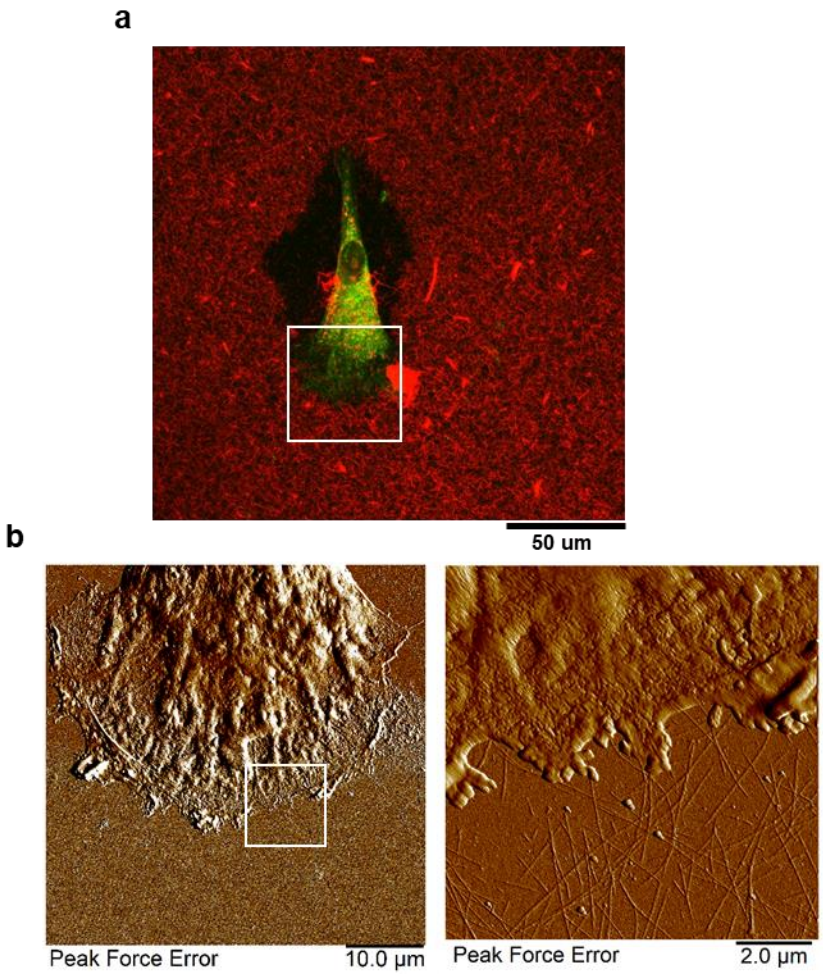

Figure 3.26. Correlative AFM for Rigid coatings. a) CLSM image of a cell and coating, and b) AFM image of the same cell in the vicinity of the lamellipodia.

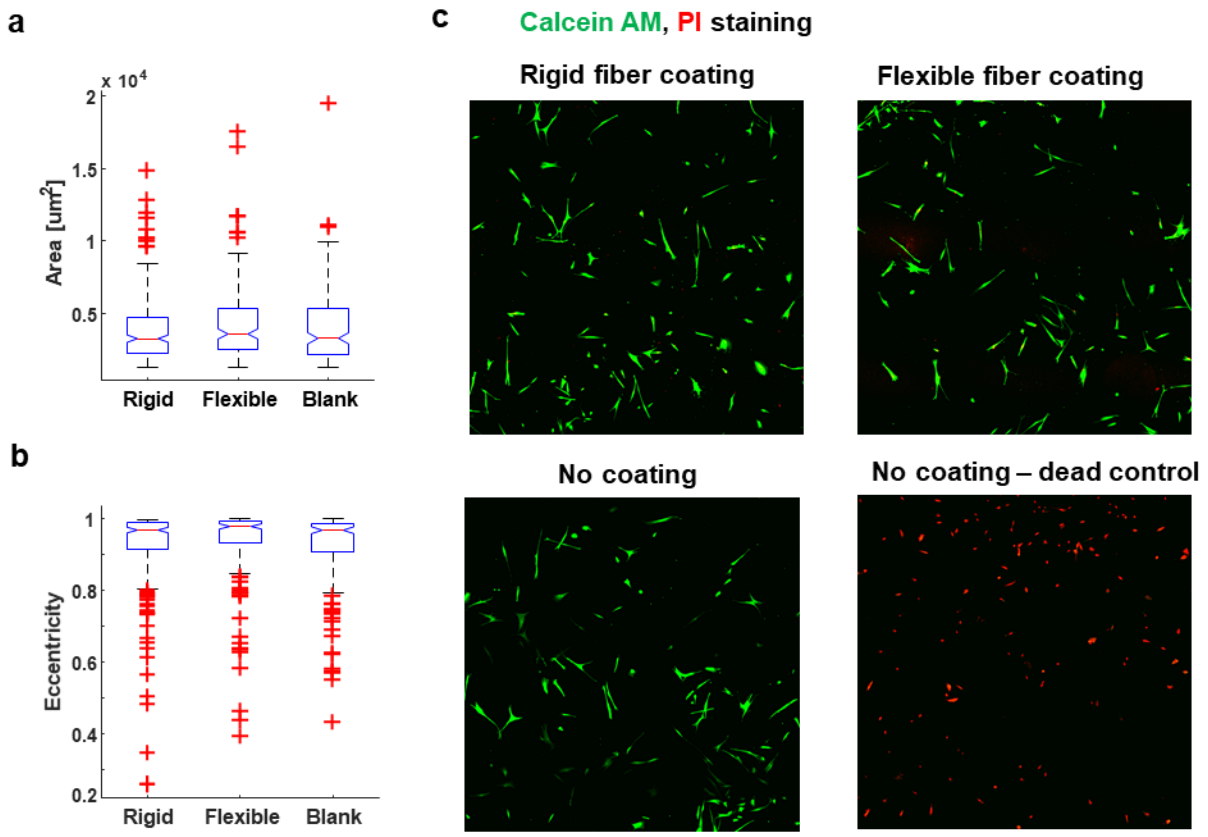

Figure 3.27. Characterization of cell behaviour. (a) Measurements of cell area and (b) cell eccentricity. (c) Example representative cell viability assessments on coatings, with comparison to dead cell control, shows no changes in cytotoxicity.

This effect can also be seen in certain images where the cells deform the network and leave behind bundled tracks along the direction of spreading, as indicated with arrows in **Figure 3.28a**. In rigid coatings, however, primarily micron sized pieces of material broken off from the network are seen, as indicated with arrows. It is hypothesized that the flexible fiber coating is more resistant to degradation due to a more entangled network topology, while the rigid fibers are less entangled resulting in networks that are more easily deformed and degraded by traction forces. To test this hypothesis, networks of fibers with different persistence lengths are modelled using a Monte-Carlo scheme. Each fiber of length L consists of segments of length ds, where the angles between

adjacent segments are drawn from a normal distribution with a mean of zero and a variance of $\sigma^2 = ds/l_p$. The origin point of each fiber is assigned a random location within the 2D simulation box, and the initial angle of the first segment is drawn from a uniform distribution between $[0, 2\pi]$. Fibers pairs in the network are identified as either overlapping or entangled, as shown in the schematic in **Figure 3.28b**. To assess crossover points in the network, each pair of fibers is compared sequentially. If the two fibers do not intersect, there is no cross over. If the two fibers intersect once, that is considered an overlapping pair. If the two fibers intersect more than once, then the fibers are randomly assigned as either lying on the top or bottom with equal probability. If the individual fibers have at least one crossover on top and one on the bottom, the intersections are treated as an entanglement. Otherwise the intersection is treated as overlapping. Overlapping fibers are expected to slip past each other, while entangled fibers should create more stable networks. Simulation snapshots confirm that low persistence length flexible fibers have more entanglements in the networks, while high persistence length rigid fibers primarily overlap without entanglement. This effect increases logarithmically with the persistence length of the fibers in the network (**Figure 3.28c**). Shear rheology measurements show that upon calcium cross-linking, the flexible fibers prepared at 20 mM NaOH form a hydrogel with a higher storage modulus (G'= 76.1 ± 0.8 kPa, G"=9.1 ± 0.2 kPa) than the stiff fibers prepared at 5 mM NaOH (G'= 4.8 ± 0.1 kPa, G"=0.83 ± 0.02 kPa) and more viscous behaviour (**Figure 3.28d**). In these bulk hydrogels, the calcium crosslinking is expected to immobilize the network in a manner analogous to the coatings of fibers deposited on a substrate.[63] The rheological measurements confirm that a highly entangled network of flexible fibers is more elastic than a network of rigid fibers with fewer entanglements, and is therefore more stable under shear stress.

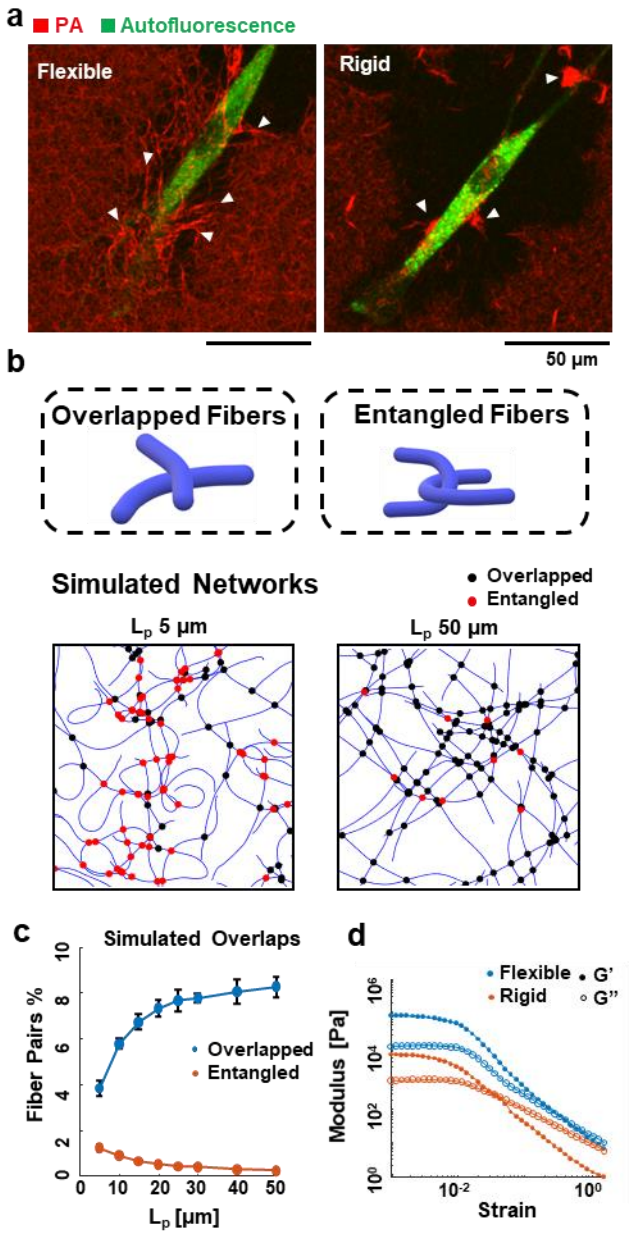

Figure 3.28. Deformation of entangled and overlapping PA networks by cells. (a) Deformation of a flexible coating with bundled tracks indicated with white arrows (left) and removal of material from rigid coating, indicated with white arrows (right). (b) Monte-Carlo simulation of fiber networks of low and high persistence length, with overlapping and entangled points indicated. (c) Percentage of fiber pairs with overlaps and entanglements as a function of persistence length. (d) Shear rheology of PA hydrogels.

3.4. Conclusions

In this work, a new high aspect ratio nanostructure formed by a self-assembling peptide amphiphile that is similar in morphology to the structure of the DNA double helix is reported, with major and minor grooves running on opposite sides of the nanostructure. It is proposed that this structure is formed by geometrically frustrated twisted ribbons splitting into two strands to optimize the twist in the β-sheets. With correlative fluorescence and AFM imaging, the microarchitecture formed by these nanomaterials is shown to respond differently to cellular forces, with rigid fiber networks degrading more than the flexible fiber networks. The nanostructure preparation pathways investigated here may be used to modulate the scaffold remodeling response in applications in regenerative medicine. Scaffolds composed of flexible twisted ribbons area likely more suitable for applications where implantable scaffolds are required to support cellular growth over the long term, while the rigid structures may be preferred when faster remodeling and degradation are required.

3.5. Materials and Methods

PA solution preparation

PA samples were prepared by dissolving lyophilized PA with the noted concentration of NaOH in Milli-Q water, and sonicating for 15 mins. For fluorescently labelled PA solutions, PAs were mixed with 5 mol % TAMRA labelled PA in HFIP in Eppendorf tubes. The samples were left under vacuum overnight, and then dissolved in NaOH solution and sonicated. Solutions were annealed in PCR tubes in a thermal cycler (Mastercycler pro, Eppendorf) at 80^{o}C for 30 mins, followed by cooling to 20^{o}C at 1^{o}C/min.

Atomic Force Microscopy (AFM)

Sample solutions were diluted 10X in 150 mM NaCl and deposited on freshly cleaved mica surfaces for ~1 min, and the excess solution was rinsed with 150 mM NaCl. The samples were then rinsed with 150 mM NaCl 20 mM $CaCl_2$ to immobilize the nanostructures on the mica surface, and measurements were performed in the liquid environment. AFM images were captured in PeakForce tapping mode on a Dimension Icon AFM (Bruker) with a silicon nitride cantilever (SNL10-A, Bruker) in a liquid cell. Images were flattened to correct sample tilt before analysis. Persistence lengths were measured by tracking fiber trajectories from large images (20x20 um) using the FiberApp plugin, with the mid-point displacement method.

High resolution Cryogenic transmission electron microscopy (TEM)

For cryo-TEM, samples were diluted 10-fold and was plunge-frozen onto glow-discharged lacey carbon grids (LC-300-Cu, Electron Microscopy Sciences) using a Gatan Vitrobot Mark IV instrument. High resolution cryo-TEM was obtained on a JEOL 3200FS microscope operated at 300 kV acceleration voltage, equipped with an in-column energy filter and a Gatan K2 Summit direct electron detector. The image acquisition was controlled by Leginon software[164] with a defocus of 2 um.

Negative Stain TEM

Samples were diluted to ~1mM concentration with water immediately prior to sample preparation. Carbon coated TEM grids (CF300-Cu-UL, Electron Microscopy Sciences) were glow discharged using a PELCO Easi-Glow instrument with 15 mA current for 30 s. 5 uL of diluted sample was applied on a grid and the excess solution wicked with a filter paper after 30s. 5 uL of 1 wt% uranyl acetate solution, filtered with a 200 nm PTFE syringe filter before use, was applied on the grid. After 10s, the excess staining solution was wicked with a filter paper, and the sample was allowed to dry. TEM images were obtained using a JEOL ARM300F microscope operated at 300 kV acceleration voltage. The images were recorded with a Gatan OneView IS detector in imaging mode, with real-time drift correction.

PA Coating preparation

Glass bottom petri dishes (Mattek) were incubated with 0.01 mg/ml PDL for 3 hours, rinsed three times with water, and allowed to dry in a sterile biosafety cabinet. PA solutions were prepared as previously described at a concentration of 10 mM, diluted to 0.1 mM in PBS, and drop cast onto the PDL coated glass wells. The dishes were rinsed with PBS three times after 1 minute of incubation, and kept covered with PBS until ready for cell plating.

Cell experiments

Normal human lung fibroblasts (NHLF) cells were cultured in Dulbecco`s Modified Eagle Media (DMEM, Gibco), with 10% fetal bovine serum (FBS, Gibco), and 1% penicillin-

streptomycin, and passaged every three to four days. For measurements of coating deformation and degradation, cells were plated onto PA coated dishes at low concentration of 1000 cells/ml, to ensure minimal overlapping between cells. The cells were kept in a cell incubator at 37^{o}C at 5% CO_2 for the required time of the experiment, then rinsed with PBS and fixed with 4% paraformaldehyde (PFA). Live-dead staining was preformed using a Calcein-Propidium Iodide assay. Samples were incubated in the Calcien-PI solution for 20 mins in a cell incubator, and then imaged using a 20X air objective. Lysosomes were labelled with Lysotracker-Green (Thermofisher) by incubating cells at 50 nM for 30 mins in PBS, followed by confocal imaging.

Confocal Laser Scanning Microscopy (CLSM)

Fluorescence microscopy was performed on a Nikon-A1R confocal microscope. For analysis of degradation area and coating deformations, z-stacks of fixed dimensions were measured with a 20X air objective (Nikon), and maximum intensity projections were calculated for further analysis. The 488 nm laser line was used to image cellular autofluorescence. Image analysis was performed using custom written Matlab codes using the Image Processing toolbox.

Correlative AFM-Fluorescence imaging on cells was performed by removing the glass coverslip from the petri dish with razor blade, and mounting the coverslip on the AFM stage. The region of interest with a cell was identified using the digital camera mounted to the AFM head, as illustrated in

Figure 3.29. AFM images were captured in PeakForce tapping mode on a Dimension Icon AFM (Bruker) with a silicon nitride cantilever (SNL10-A, Bruker).

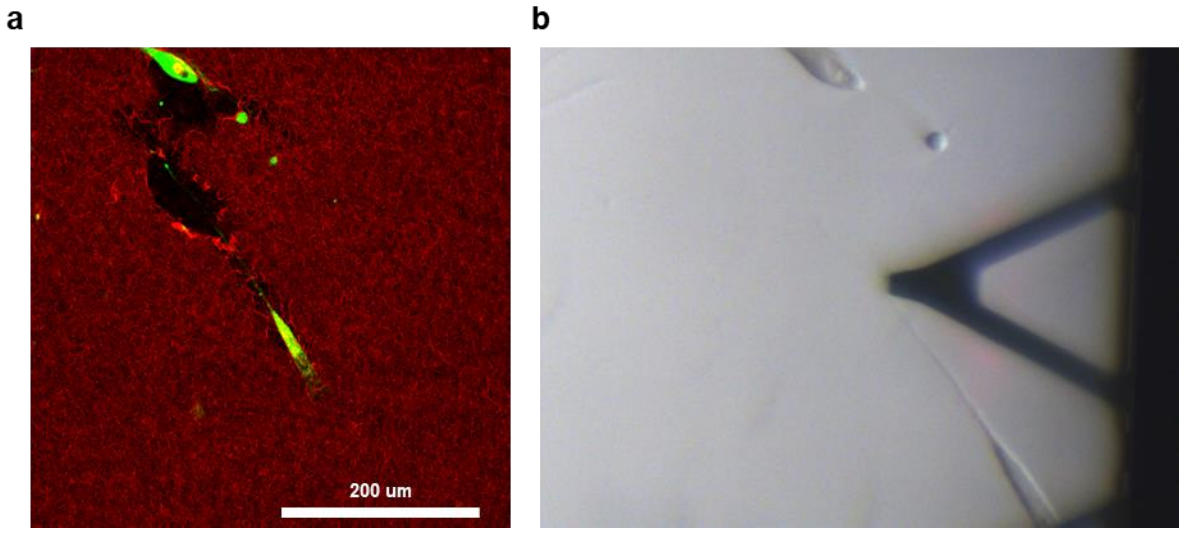

Figure 3.29. Correlative AFM-CLSM of cells on PA coatings. (a) CLSM image of cell and (b) image taken through the digital camera mounted on the AFM. The two can be compared to identify correlating regions.

Supported lipid bilayers (SLB)

DOPC SLBs were prepared as described by Attwood et al.[162] Lyophilized 1,2-dioleoyl-sn-glycero-3-phosphocholine (DOPC, Sigma) was dissolved in chloroform, aliquoted, and evaporated off under nitrogen flow. The DOPC was dissolved in deoxygenated milliQ water at a concentration of 0.5mg/ml, stirred for 1 hour with a magnetic stir bar, and then sonicated for 10 minutes. The solution was stored at 4^{o}C, and was sonicated again before use. The solution was deposited onto cleaved mica substrates, which were glued onto glass slides, for 20 minutes and then rinsed with PBS, without allowing the surface to de-wet. AFM imaging was performed as previously described. For CLSM, a glass coverslip was placed on top of the mica to create a wet mount.

Rheological measurements

An Anton Paar MCR302 Rheometer with a 25 mm cone plate was used for rheological testing. $CaCl^2$ was used to gel PA solutions, which were prepared as described previously. The final concentration for the measurements was 7.81 mM PA and 50.1 mM CaCl2. The samples were initially equilibrated at 0.1% strain and 10 rad/s, followed by a frequency sweep from 1 - 150 rad/s at 0.1 % strain, an amplitude sweep at 10 rad/s from 0.1 to 150 % strain.

4. Supramolecular co-assembly of peptide amphiphiles

4.1. Objectives and significance

Soft materials in nature like the extracellular matrix (ECM) and the cell cytoskeleton are composed of mixtures of molecules with different functions that self-assemble into multicomponent networks through supramolecular interactions. It is therefore an important challenge to create biomimetic materials with multiple components that can self-sort into individual populations. Here, it is demonstrated that peptide amphiphiles (PAs) with different hydrogen bonding sequences can be designed to co-assemble within nanostructures or self-sort, by tuning the amino acid sequence. Fluorescent dyes are used to monitor the self-sorting within nanostructures with fluorescence imaging, and atomic force microscopy (AFM) is used to measure the nanomorphology of the assemblies. Unlike previously reported self-sorting networks which are controlled by the chemical similarity, the driving force for the self-sorting reported here is determined by the supramolecular twisting in the PA nanostructures. It is demonstrated that the self-sorted networks can be designed to selectively sequester biofunctional PAs within either of the components, by including biotinylated PAs as a model protein binding group. Finally, the addition of a bone morphogenetic protein 2 (BMP2) binding PA sequence is found to change the supramolecular nanostructure into fiber bundles, which slows the degradation and internationalization of the bioactive component.

4.2. Introduction

Biomaterials in nature have complex architectures composed of multiple types of fibrous networks in coexistence. These networks can form by programmed supramolecular interactions, which impart robust architecture and biological function to materials. Actin and Microtubules, for

example, assemble into coexisting fibrous networks in the complex environment of cell cytoplasm, and each plays a different structural role in the cellular cytoskeleton.[6,7] The ECM of connective tissues consists of a network of collagen fibrils, surrounded by a fluidic component consisting of various glycosaminoglycans (GAGs) such as hyaluronic acid (HA). In these tissues, both collagen and HA play essential roles in directing cell responses.[80] The growth of these fibers is precisely controlled through programmed interactions between monomers and various enzymes. The different components in fibrous biomaterials can impart different biological functions, such as presenting biochemical cues, binding protein, or controlling scaffold stiffness.[165] In order to mimic the formation of these materials, supramolecular interactions between synthetic molecules must be designed to enable them to self-sort into independent populations. In order to self-sort, the interactions between individual components must have a sufficient enthalpic penalty overcome the entropic driving force towards uniform mixing.[166,167] This can be achieved by incorporating different supramolecular interactions into the components, such that they interact favourable only with similar molecules.[77] Shigemitsu et. al. developed a self-sorting supramolecular hydrogel where one component assembles due to peptide-like hydrogen bonding, while the other assembles due to lipid-like hydrophobic collapse.[78] The response of supramolecular double network (SDN) to stimuli could be tuned by targeting either of the two component sequentially.

Self-sorting can be readily achieved by manipulating different intermolecular interactions, or combining components with significantly different molecular geometries, thereby increasing the enthalpic penalty of mixing.[168,169] However, self-sorting networks from geometrically similar components using the same type of supramolecular interaction are more challenging to create.[170,171] Peptide Amphiphiles (PAs), a class of self-assembling biomolecules composed of lipid tails attached to peptide sequences, which form high aspect ratio nanofibers in water through

hydrophobic collapse and hydrogen bonding between peptides.[51] These materials are of great interest due to their potential use as scaffolds for regenerative medicine and delivery vehicles for proteins.[56] PAs modified with bioactive groups have been co-assembled with bare PAs to create scaffolds with functional properties, such as controlling the fate of stem cells or guiding neural regeneration.[69,72,172] PAs can be modified with standard solid phase synthesis to present bioactive peptide epitopes or protein binding sequences. In previous chapters, it was demonstrated that the hydrogen bonding interactions of PA molecules within assemblies are highly complex due to large phase space of possible peptide conformations, however the hydrogen bonding complementarity of different peptide sequences within PA mixtures is largely unexplored.

Previous work by the Stupp group has also demonstrated that nanostructures formed with the co-assembly of biofunctionalized PAs with backbone PAs are highly effective at cell signaling and growth factor binding and release.[56] One biofunctional PA system of particular interest is a PA with a peptide binding sequence for Bone morphogenetic protein 2 (BMP2).[72] The BMP2-binding PA has shown great promise for applications in bone regeneration, due to its ability to promote osteogenesis with much lower concentrations of BMP2 than standard treatments.[173] This PA has the highest efficacy in vitro when it is co-assembled with a backbone PA without a bioactive group. The mechanism underlying this increase in efficacy with the addition of a non-functional PA is unknown, although it is likely related to the creating of more stable nanostructures. In addition, it has not been conclusively demonstrated whether a mixture of bioactive PA and backbone PA are uniformly co-assembled within individual assemblies, due to a lack of an experimental method to directly measure this effect. Direct observation of co-assembly or self-sorting of supramolecular nanostructures remains experimentally challenging in disorders systems like PAs. One approach that has been used successfully for supramolecular self-sorting

materials is to use a fluorescent probe which is similar to the individual components in the interacting portion, such that it can selectively label assemblies that are rich in that particular component.[174] In Chapter 3, it was the viability of this approach to study the microscale properties of nanofiber materials was demonstrated. Previously, the Stupp group has also attached fluorescent dyes to the ends of PA molecules to investigate the kinetics of self-assembly and mixing within single component nanostructures.[175] In this work, it is demonstrated that multicomponent PA mixtures can be designed to self-sort into SDNs by tuning the amino acid sequence within the molecules, even as all components assemble due to β-sheet forming hydrogen bonds. PAs are labelled with fluorescent tags to monitor their location within assemblies, and the nanostructures are imaged with confocal laser scanning microscopy (CLSM) and atomic force microscopy (AFM). The relation between amino acid sequence, the supramolecular nanostructure, and the resulting co-assembly or self-sorting behaviour of the molecules in mixtures is investigate. The effect of bio-functional epitopes on the formation of PA nanostructures, and the effect of nanostructure morphology on the bioactivity of the BMP2-binding PA, is also studied.

4.3. Results and Discussion

4.3.1. Self-sorting and co-assembly of PA mixtures

The PA with sequence $C_{16}A_6E_3$ (**PA1**) forms long, high aspect ratio twisted ribbons in water, as described in Chapter 2 (**Figure 4.1a**). Previously, the Stupp group has investigated the kinetic mixing of monomers between nanofibers using super-resolution microscopy, by incorporating fluorescent dye-labelled molecules into the system.[175] To visualize the co-assembly or self-sorting of PAs, fluorescent dyes are attached to the terminal ends of the molecules via a tri-glycine linker (**Figure 4.1b**). The dyes used in this work are Cy3 (e.g. **PA1-Cy3**), Cy5 (e.g. **PA1-Cy3**), TAMRA (e.g. **PA1-Tamra**), or FITC (e.g. **PA1-FITC**). To prepare the assemblies, 2 mol%

each of **PA1-Cy3** and **PA1-Cy5** are mixed with 96 mol% PA1. The mixture is made in Hexafluoroisopropanol (HFIP), which disrupts hydrogen bonding and results in PA monomers uniformly dissolved in solution.[62] HFIP is removed under vacuum, and the deposited film is resuspended in 20 mM NaOH to a final concentration of 10 mM total PA. The solution is annealed at 80°C for 30 minutes, then cooled by 1°C per minute to room temperature.[52] The fluorescently labelled PA solutions are diluted by 200X in PBS, deposited onto freshly cleaved mica disks, and rinsed with PBS after approximately one minute. The disks are then rinsed with a 20 mM $CaCl_2$ 150 mM NaCl solution, a coverslip is placed on top, and the samples are imaged with confocal laser scanning microscopy (CLSM). In the images in this work, the colours representing each the cyanine dyes are blue-shifted by a channel for easier visualization, therefore the far red emission signal of Cy5 is shown in red, while the red emission signal of Cy3 is shown in green.

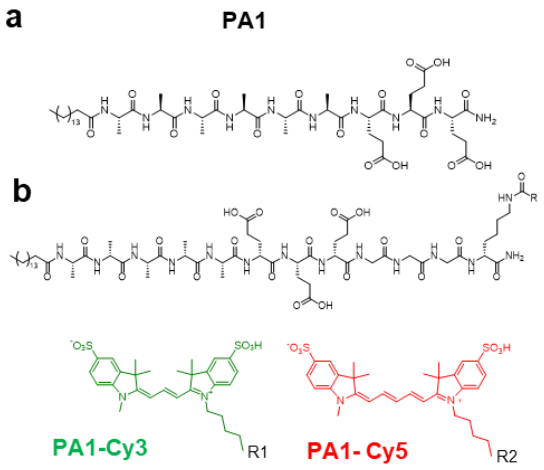

Figure 4.1. Molecular structure and assembly of PA1. a) Structure of the backbone PA and b) structure of the fluorescent dye functionalized PA.

The mixture of **PA1-Cy3** and **PA1-Cy5** with PA1 filler shows high colocalization of the fluorescent signals when imaged with CLSM (**Figure 4.2a** and **Figure 4.2b**), where the nanofibers on the surface appear yellow. This is expected as both dye populations are attached to the same backbone PA. In contrast, when PA1/PA1-Cy3 and PA1/PA1-Cy5 mixtures are

prepared separately, and then deposited on the same surface, two clear populations can be seen (**Figure 4.2d** and **Figure 4.2e**). This can be quantitatively measured using object-based correlation, where the centers of nanofibers are identified using an image skeletonization procedure, and their intensity in both imaging channels is compared (**Figure 4.3**). The intensities co-assembled networks have a high positive correlation (ρ=0.44), while the negative control, separated networks have a negative correlation (ρ=-0.45) (**Figure 4.2c** and **Figure 4.2f**).

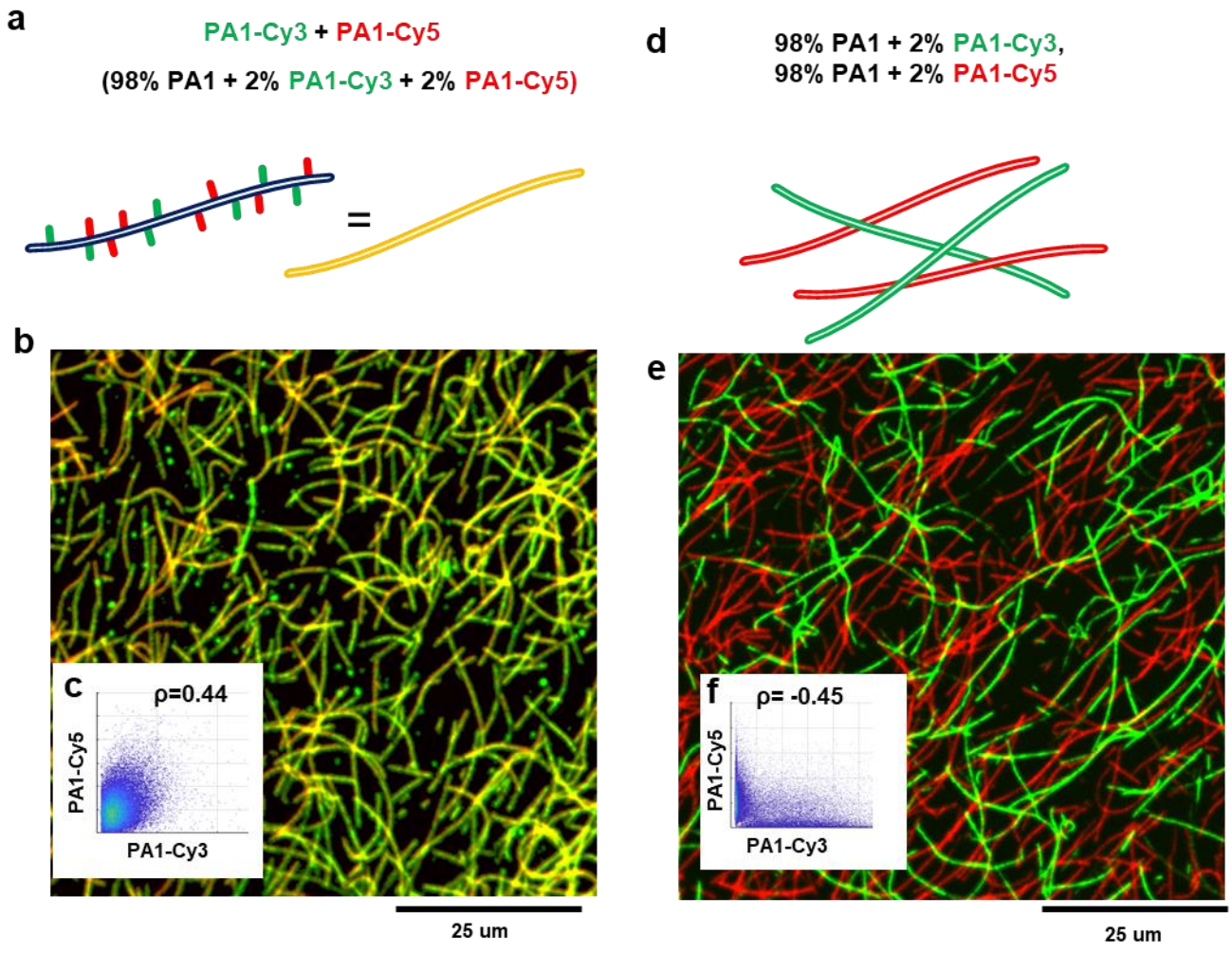

Figure 4.2. Co-assembly of dye labelled PA1. a) Schematic of the core assembly of dye label PAs, and b) CLSM image of co-assembled fibers deposited on a mica surface. c) Plot of object-based pixel intensities of the nanofibers showing correlation between the two channels. d) Schematic of the mixture of two separate PA populations, e) a CLSM image of the mixture deposited on the mica surface. f) Corresponding histogram of the non-co-assembled PAs.

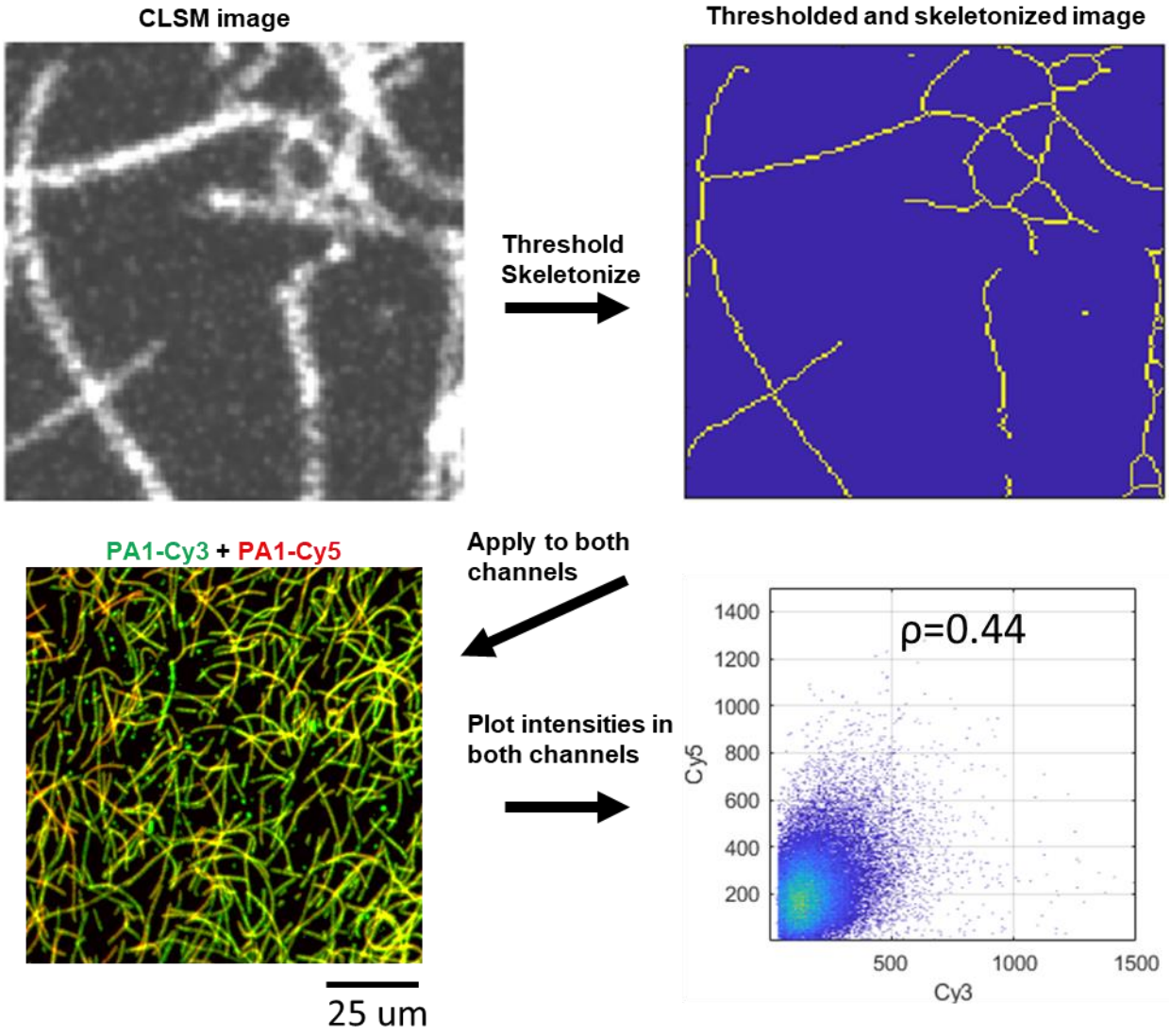

Figure 4.3. Analysis of co-assembly in CSLM images of PA nanofibers. Threshold and skeletonize CLSM images and combine into one composite. Plot the intensity for the skeletonized pixels in both channels. Calculate correlation between the two channels.

Next, similar dye labelled molecules were prepared with a second PA backbone, $C_{16}V_3A_3E_3$ (**PA 2**) as shown in **Figure 4.4a**. In Chapter 2 it was shown that PA 1 and PA2 both form twisted ribbons, but with opposite supramolecular chirality. PA1 forms left-handed ribbons, while PA 2 forms right-handed ribbons, which is related to twist of the peptide sequence and steric restrictions within the assemblies (**Figure 4.4b**). When PA1 and PA2 are co-assembled in HFIP at 1:1 ratio and annealed, the system has both left and right handed fibers (**Figure 4.4c**). This could either be due to a majority-rules behaviour where molecules within nanofibers are mixed but with majority controlling the nanostructure, or due to self-sorting.[176] PA1/PA1-Cy5 and PA2/PA2-Cy3 are co-assembled, again with 2 mol% of each dye labelled component. The PAs are imaged immediately after dissolving in water (**Figure 4.5a**), before the assemblies can form into long nanostructures, and it is confirmed that PA1-Cy5 and PA2-Cy3 are initially colocalized. Upon annealing, the fibers are separated into two populations rather than colocalized, which indicates a self-sorting effect (**Figure 4.5b**). The colocalization intensity plots confirm a negative correlation (ρ=-0.33), as expected (**Figure 4.5c**). Together, these measurements confirm that the mixtures begins as a co-assembly and then self-sort into separate populations, as described in **Figure 4.5d**.

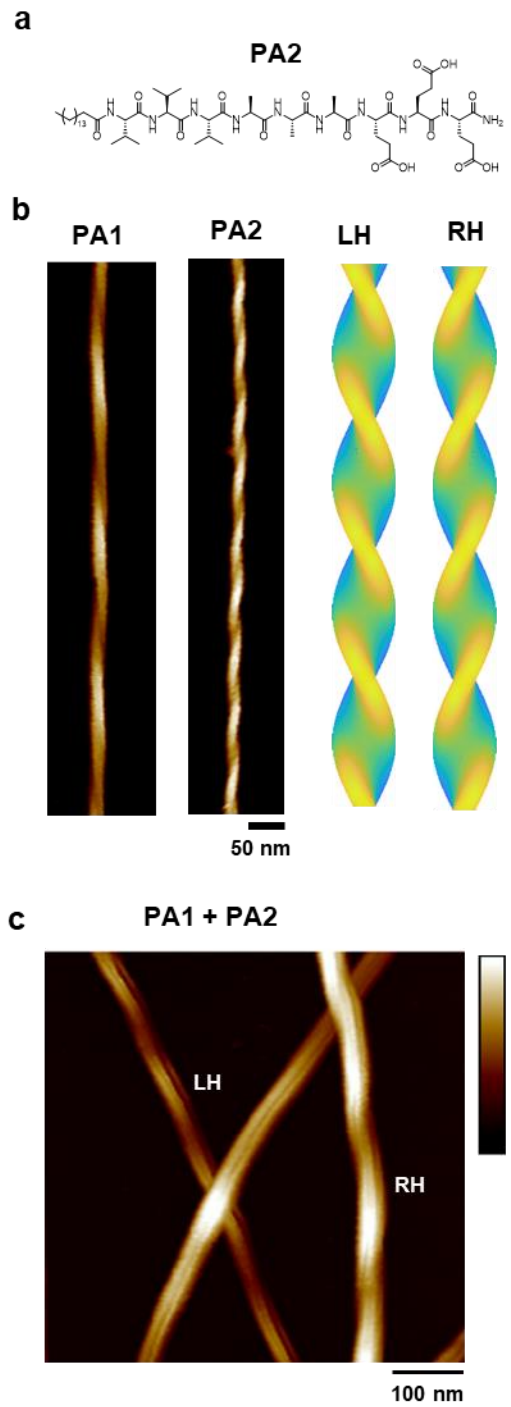

Figure 4.4. Molecular structure and co-assembly of PA1 and PA2. a) Structure of the backbone PA 2. b) opposite Supramolecular chirality of PA 1 PA 2. c) AFM image of the co-assembly of PA 1 and PA 2 with left and right-handed fibers indicated.

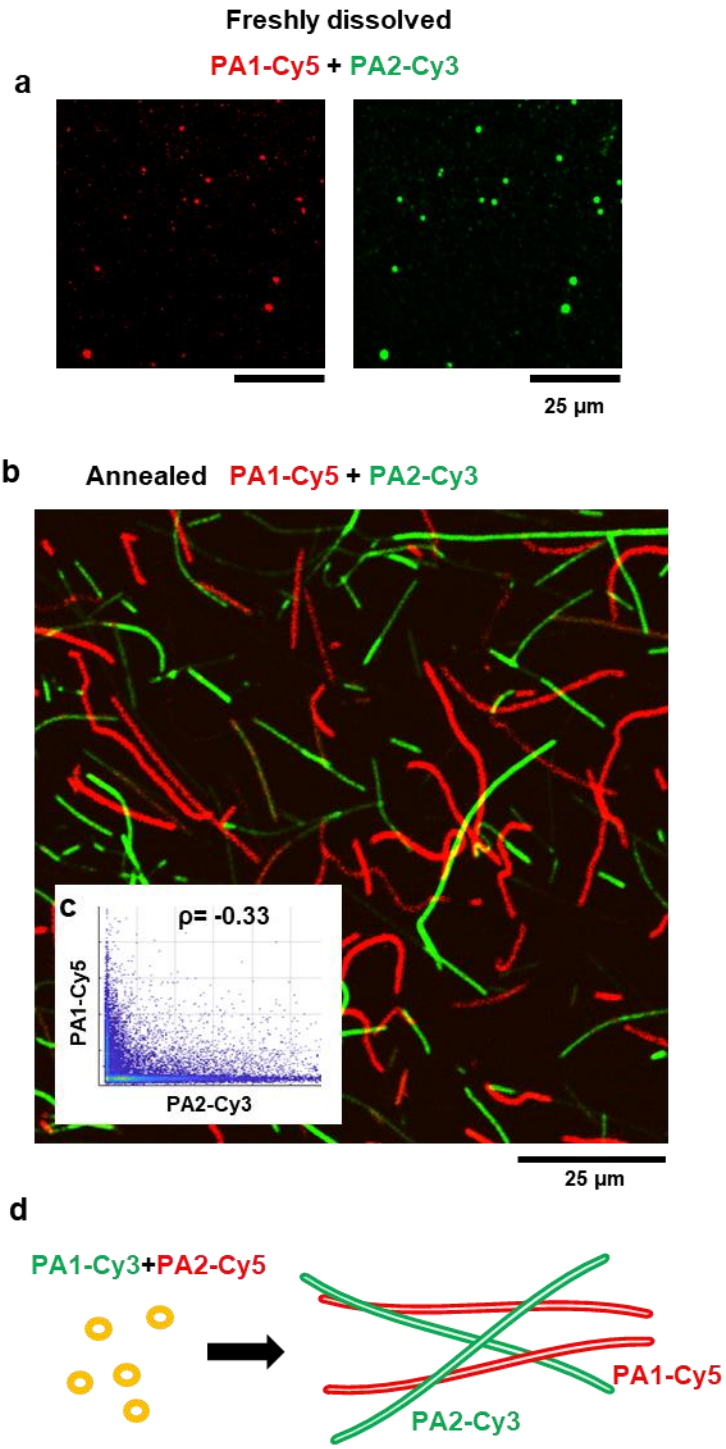

Figure 4.5. Co-assembly of fluorescent dye labelled PA1 and PA2. a) CLSM image mixture of PA 1-Cy5 and PA 2-Cy3 freshly dissolved into solution, and b) after annealing, deposited on a mica surface. c) Histogram of intensities calculated from the non-co-assembled image. d) Schematic illustrating these self-sorting behaviours off PA 1 and PA 2.

4.3.2. Correlative AFM-Fluorescence imaging of single nanofibers

While left-handed PA1 and right-handed PA2 self-sort into different populations, it is unlikely that these individual nanostructures are entirely pure. This raises the question of whether the supramolecular chirality behaviour of the individual components is preserved in the self-sorted nanostructure. To investigate this, correlative AFM-CLSM is used, where the same regions of the sample are imaged in CLSM and in AFM. Example images are shown in **Figure 4.6**, where the ability to measure nanoscale features of the assemblies is compared alongside CLSM images, which can be used to label the chemical identity of each species. The procedure is described in **Figure 4.7**. First, the mica surface is marked with a scratch, the PA sample is deposited, and the surface is imaged in CLSM. The coverslip is then removed, and the sample is transferred to the AFM stage. Using a digital camera that is attached to the AFM head, the same approximate region of the sample is identified and imaged. Distinctive features such as bending or crossing nanofibers are identified in the CLSM and AFM images, and are then used to align the two images as shown in **Figure 4.8**.

Correlative AFM-CLSM images of the co-assembled PA1/PA1-Cy5 and PA2/PA2-Cy3 system confirm the ability to identify fibers labelled with a particular dye, and measure their nanostructure (**Figure 4.9**). Imaging confirms that nanofibers rich in PA1-Cy5 are left-handed, and those rich in PA2-Cy3 are right-handed **Figure 4.10**. These measurements are repeated with the alternate dye labelled system, PA1-FITC and PA2-TAMRA, in order to rule out effects of the dyes. This system also shows self-sorting behaviour, and correlative AFM-CLSM confirms that the sorted fibers maintain the supramolecular chirality of their pure populations **Figure 4.11**. Beyond the use of this experimental method to study the self-sorting of PA nanofibers, this approach can be used to answer other questions about PA self-assembly. Correlative AFM-CLSM

may be used, for example, to study the presentation of bioactive epitopes on nanostructures, measure protein binding, or be used with the (thioflavin T) THT assay to monitor aggregation behaviour of different nanostructure morphologies in a polydisperse system.

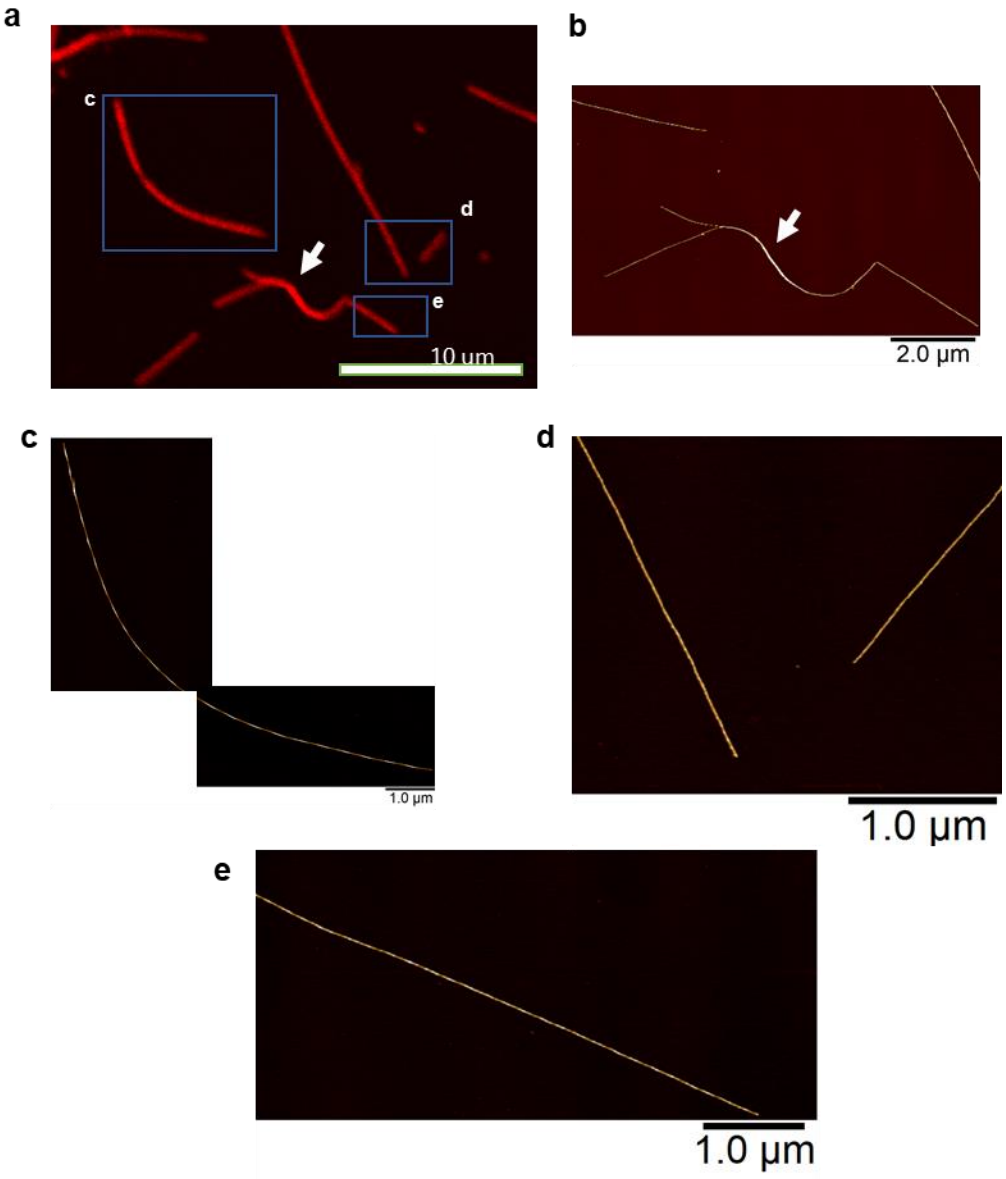

Figure 4.6. Demonstration of Correlative AFM- CLSM on PA1-TAMRA. a) CLSM image of PA1-TAMRA deposited on a mica surface, and b) AFM image of the same region, with distinctive crossing fibers indicated with white arrows. c), d) and e) high resolution AFM images of the corresponding boxed regions in a).

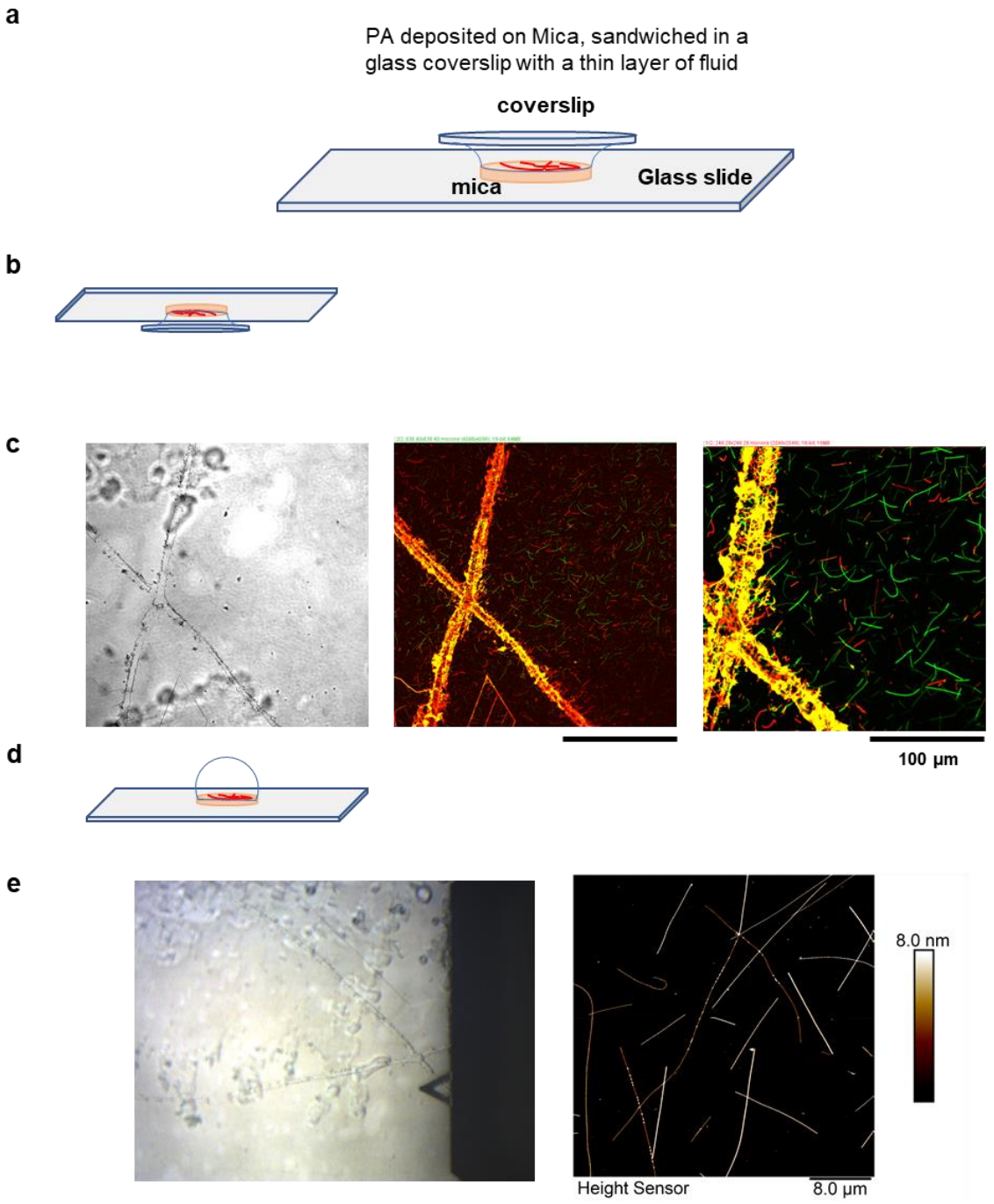

Figure 4.7. Description of the procedure to measure correlative AFM-CLSM images of PA nanostructures. a) schematic of the prepared sample. b) The sample is first imaged in the confocal microscope through the cover glass, in the vicinity of the marked region shown in c). d) The scratches on the mica show brightly as nanofibers aggregate at the high energy step edges. Signal in the fluorescent channels and e) the zoom in image of the region adjacent to the cross. f) Schematic of the sample after removal of the coverslip and transfer to the AFM stage. g) The same region of the sample is identified through the digital camera attached to the AFM head and, f) images are captured.

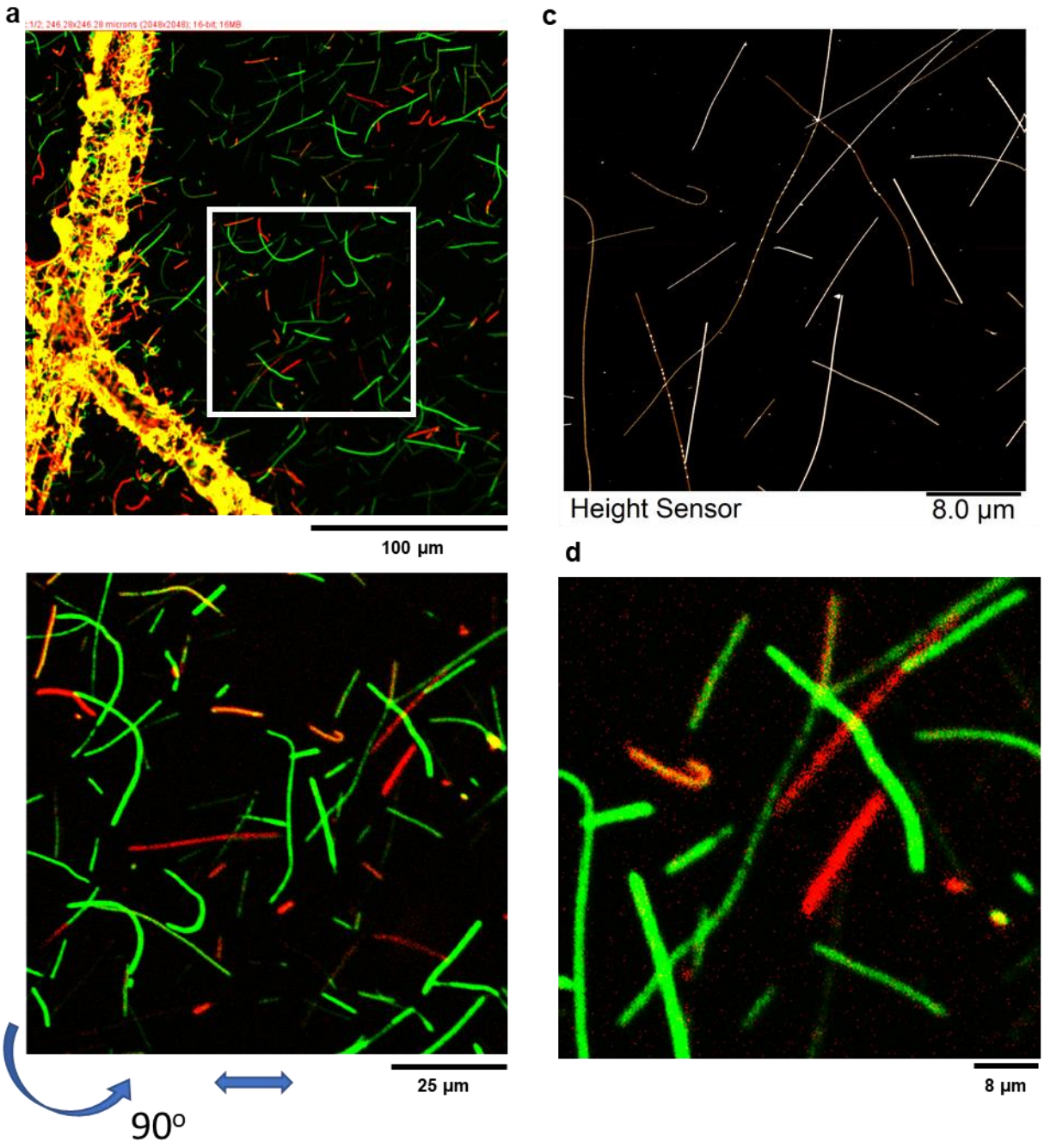

Figure 4.8. Procedure to align and compare AFM and CLSM images of PA mano fibers. . a) Large CLSM image taken in the vicinity off the marked mica, and b) an AFM image taken within that region. c) The CLSM image is rotated 90 degrees to align with the AFM setup and distinctive corresponding features are identified, as shown in the boxed regions. d) Finally, the identified region can be directly aligned with the AFM image.

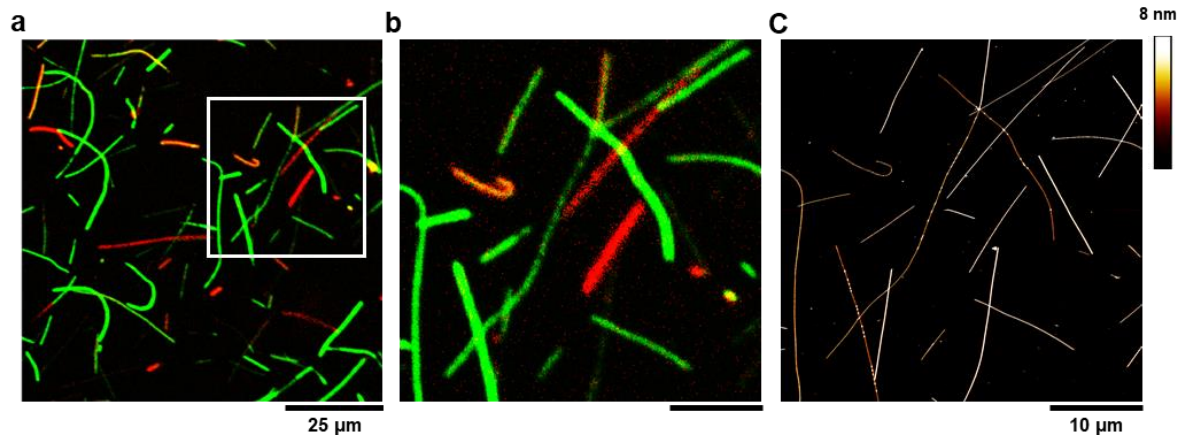

Figure 4.9. Correlative AFM- CLSM images of PAs. a) CLSM image of PA1-Cy5 and PA 2-Cy3 deposited on a mica surface, and b) zoomed in image of the boxed region. c) AFM image of the corresponding region with the same fibers visible.

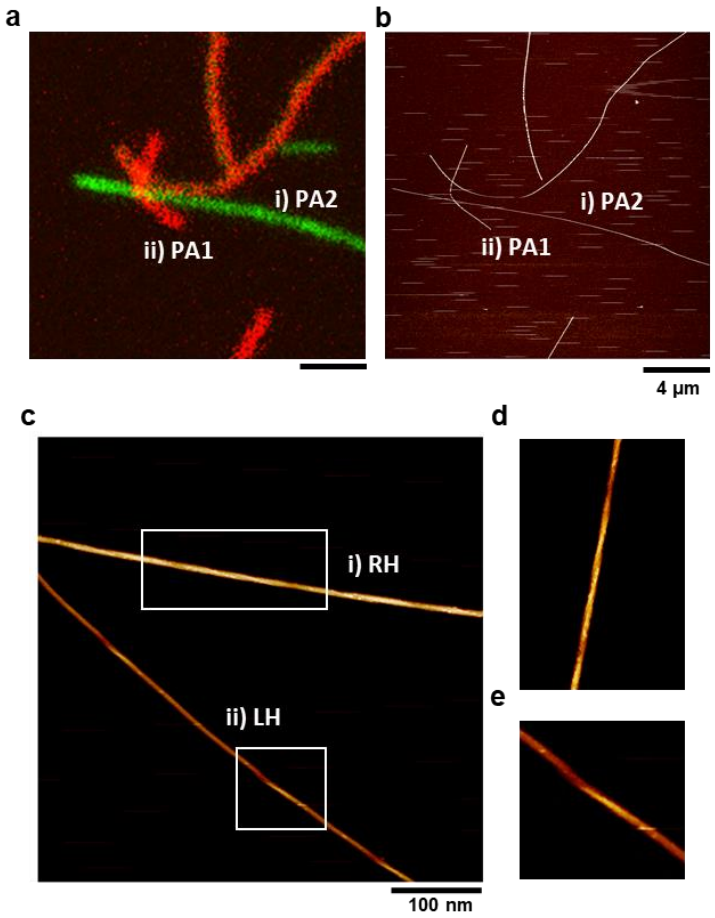

Figure 4.10. Chirality of PA nanofibers measured in Correlative AFM-CLSM images. a) CLSM image of PA1-Cy5 and PA 2-Cy3 deposited on a mica surface, and b) AFM image of the corresponding region with the same fibers. c) Higher resolution AFM image of the indicated fibers. d) and e) magnification of the boxed fibers showing the supramolecular twist direction.

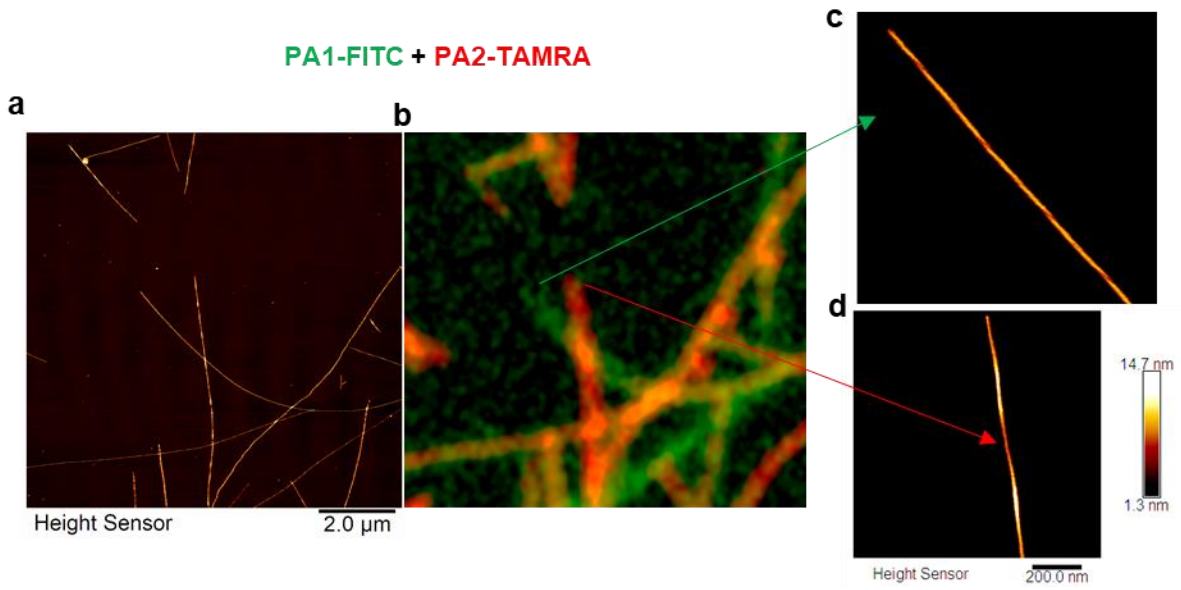

Figure 4.11. Additional images PA nanofibers measured in Correlative AFM-CLSM. a) AFM image of PA1-FITC and PA2-TAMRA deposited on a mica surface, and b) CLSM image of the corresponding region with the same fibers. c) and d) Higher resolution AFM images of the indicated fibers showing the supramolecular twist direction.

4.3.3. Influence of supramolecular chirality on self-sorting of PAs

Next, PA3 is incorporated into the co-assembly system (**Figure 4.12a**). PA3 forms a mixture of right-handed, flat, and left-handed nanostructures (**Figure 4.12b**), as described in Chapter 2. It is therefore expected that it may be able to co-assemble with PA1 and PA2. The combination of PA1/PA1-Cy5 and PA3/PA3-Cy3 results in colocalized fibers (**Figure 4.12c**), and the object-based intensity histograms show a positive correlation (ρ=0.64, **Figure 4.12d**) . In contrast, the combination of PA2/PA2-Cy5 and PA3/PA3-Cy3 results in a mixture of red, green, and yellow fibers in colocalization composite images (**Figure 4.12e**), as well as an intermediate correlation value (ρ=0.03, **Figure 4.12f**). This suggests that the mixture is kinetically trapped with local minimums near the co-assembled state. A summary the PA molecular sequences the phase diagram of the mixtures shown in **Figure 4.13**. If the PAs mixtures in water are treated as regular

ternary solutions composed of two molecules and water, the co-assembled pair can be interpreted to have free energy of mixing $\Delta_{mix}G < 0$, the self-sorted pair to have $\Delta_{mix}G > 0$, and the intermediate pair to have $\Delta_{mix}G \approx 0$ although the structures are trapped in local minima. All pairs will have the same entropy of mixing, as their respective mole fractions are the same. Interestingly, the that degree of co-assembly between two components is not directly a function of the chemical similarity of the molecules, as the most miscible pair (PA1 and PA3) is chemically less similar than the intermediate pair (PA2 and PA3). It is also not a directly related to the expected confirmational flexibility of the peptide sequence, as PA1 with only alanines would be expected to be the most miscible with the other molecules. Instead, the self-sorting is determined by supramolecular twist of the individual components. **Figure 4.13c** shows a schematic of the amount of twist, measured as the average pitch length in Chapter 2, of each molecule. PA1 is left-handed with negative twist, PA 2 has close to zero twist, and PA 3 has high positive twist. There is a direct correlation between the difference between the twist of the pairs and their ability to co-assemble. PA1 and PA2 are the farthest apart in twist, and therefore have the strongest drive to self-sort. PA1 and PA3 are the closest pair, and therefore have the lowest self-sorting, while PA2 and PA3 are intermediate. Finally, AFM imaging confirms that the mixture of PA1 and PA3 has only left-handed fibers while the mixture of PA2 and PA3 has only right-handed fibers, as would be expected if PA3 was the most flexible PA (**Figure 4.14**). From this result, it can be concluded that the supramolecular twist of the peptide amphiphile assemblies is preserved in these mixtures, and is the source of the enthalpic energy penalty that determines whether two PAs from this class of sequences mix or self-sort.

Next, a three-component system consisting of PA1-Cy3, PA2-Cy5, and PA3 (unlabeled) was investigate. If PA3 is miscible with both PA1 and PA2, it may serve to bridge the interactions

in a manner that results in a co-assembled state. However, if the supramolecular chirality of PA3 is flexible and can match either PA1 or PA2, and the supramolecular twist is the driving force for self-sorting, then the mixture would also be self-sorted. It is observed that a mixture of 25 mol% PA1-Cy3, 25 mol% PA2-Cy5, and 50 mol% PA3 results in a self-sorted nanostructure, as shown in **Figure 4.15**.

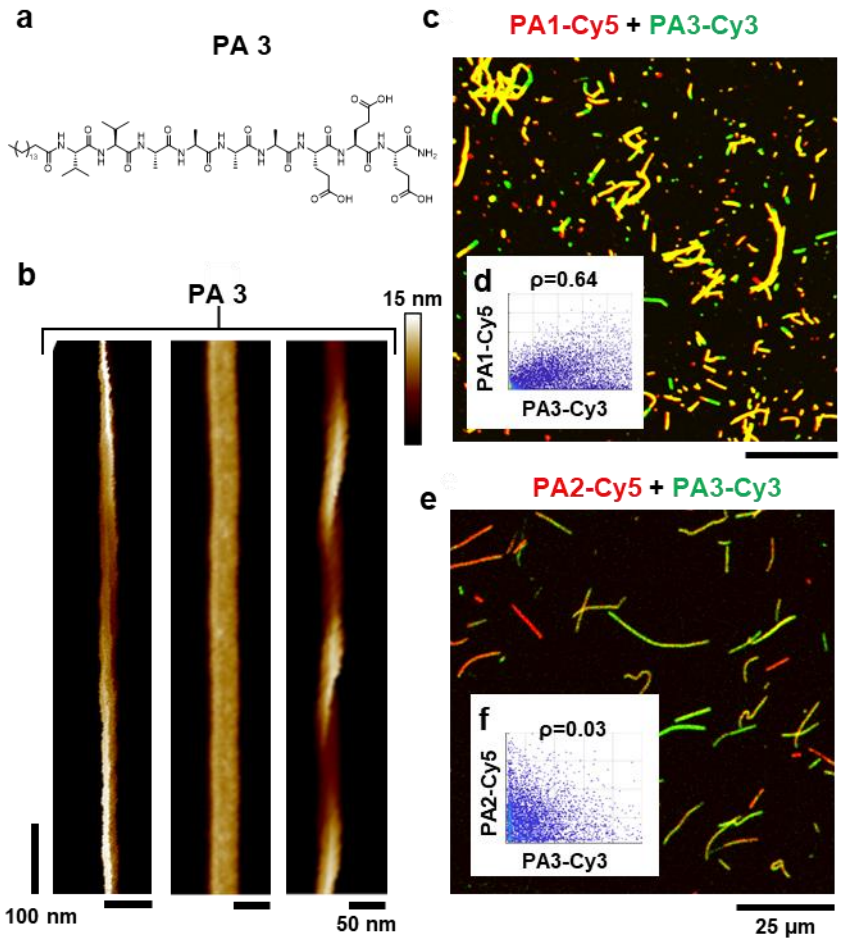

Figure 4.12. Molecular structure and co-assembly of PA3. a) Structure of the backbone PA 3, and b) nanostructures with mixed supramolecular chirality. c) CLSM image of co-assembled PA1-Cy5 and PA3-Cy3 fibers deposited on a mica surface, and d) histogram of pixel intensities of the nanofibers showing positive correlation between the two channels. e) CLSM image of co-assembled PA2-Cy5 and PA3-Cy3 fibers deposited on a mica surface, and f) histogram of pixel intensities of the nanofibers showing no correlation between the two channels.

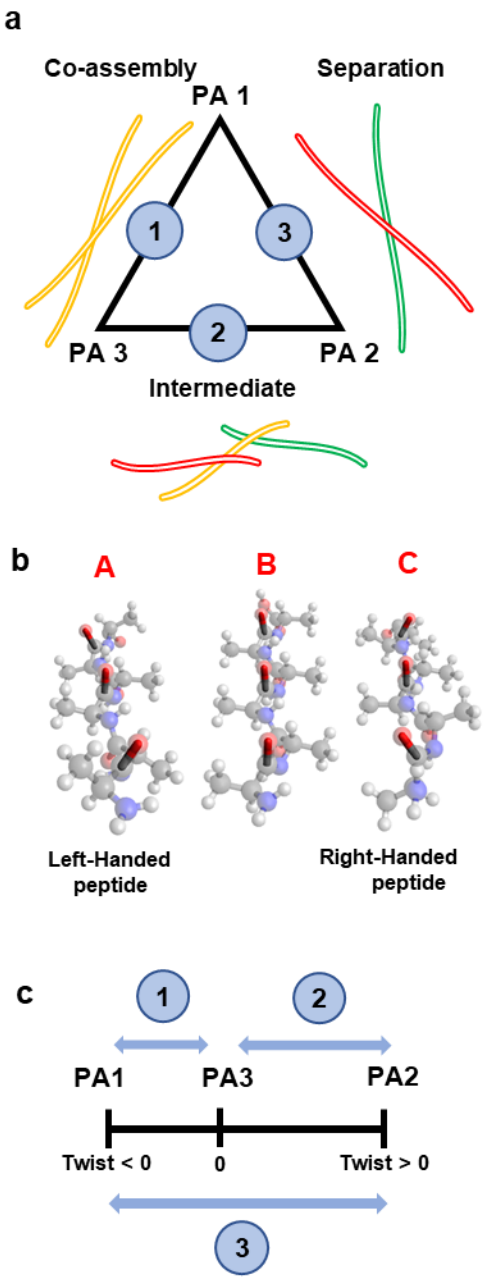

Figure 4.13. Dependence of PA co-assembly on supramolecular twist. a) Schematic of the phase diagram of PA co-assemblies. b) Interpretation of the source of enthalpic pick energy penalty due to peptide twist in co-assemblies. c) Interpretation of the propensity to co-assemble based on the distance between the PA supramolecular twists.

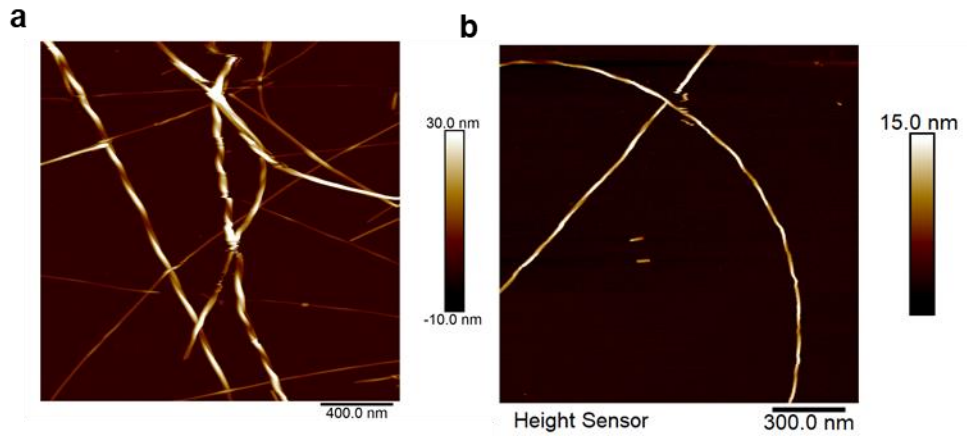

Figure 4.14. AFM images of PA 3 co-assemblies. a) Co-assemblies of PA1 and PA3 showing all left-handed fibers. b) Co-assemblies of PA 2 and P A3 showing all right-handed fibers.

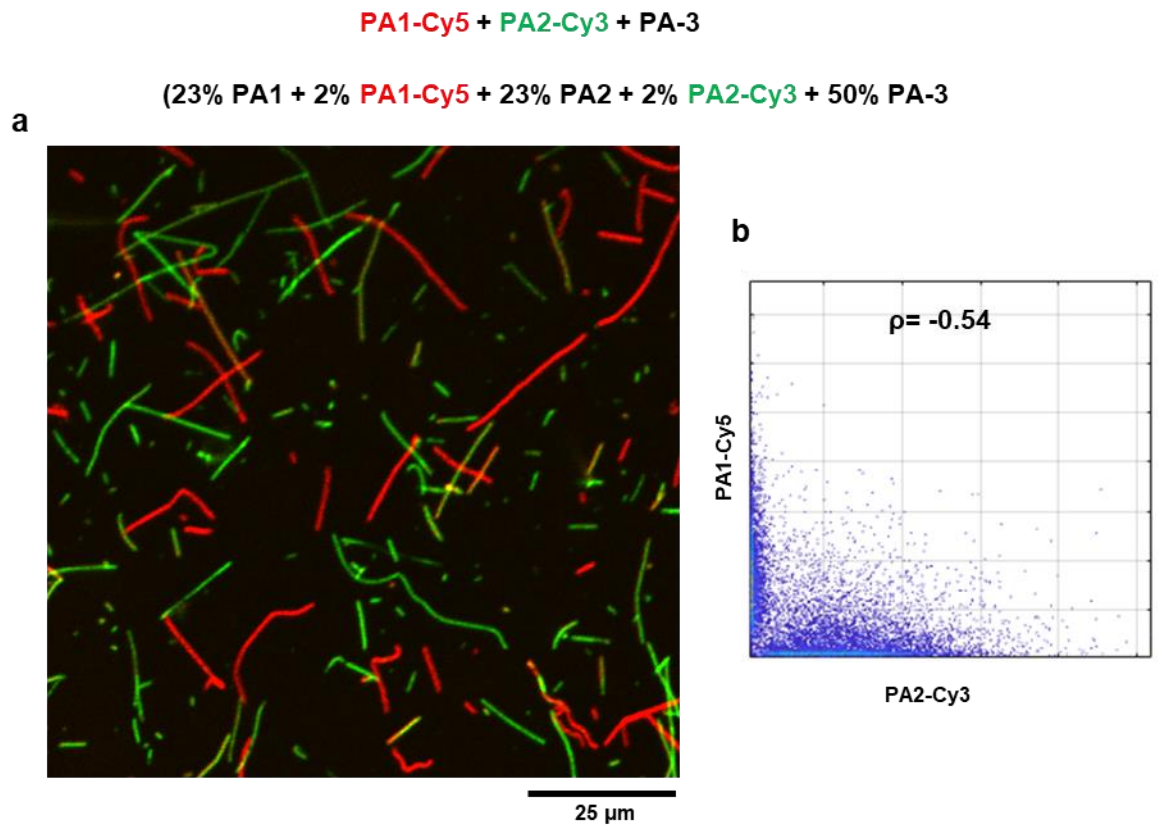

Figure 4.15. Co-assembly of PA1, PA2, and PA3. a) CLSM image of co-assembled PA1-Cy5, PA2-Cy3, and PA-3 fibers deposited on a mica surface, and b) histogram of pixel intensities of the nanofibers showing negative correlation between the two channels.

Finally, the concentration dependence of the self-sorting was studied. In these experiments, the mole fraction of the dye labelled PA1-Cy5 and PA2-Cy3 is kept at 2 mol% each, while the mol fraction of the filler PAs is varied. The final mol fractions of the PA1/PA1-Cy5 component vary from 90% to 10%. At high mole fractions of PA1/PA1-Cy5 at 75mol% and 90 mol%, a similar self-sorting behaviour as the initial experiment at 50 mol% is seen, as shown in **Figure 4.16**. At low concentrations of 25 mol% and 10 mol%, the PA1-Cy5 fluorescent signal is instead no longer found in long fibers, but rather in short fragments or micelles. As PA1 should form fibers at 25 mol% this unexpected behaviour is likely due to the dye labelled component not completely assembling with the unlabelled component. It is possible that PA1 is in fact co-assembled with PA2 nanofibers, but the PA1-Cy5 component is not able to enter those nanofibers at high enough concentration, limiting the colocalization signal. To test this hypothesis, a mixture of PA1/PA1-Cy3 at 10 mol% with 90 mol% of unlabelled PA2 was prepared. A strong PA1-Cy3 fluorescence signal was found in micelles, but also a weaker signal in nanofibers (**Figure 4.17**). This suggests that PA1 at low concentrations is co-assembled with PA2. These results suggest that PA2 has a high driving force to self-sort as it forms an independent population at low concentrations, while the driving force is weaker with. This can be interpreted as resulting from the increased number of valines in the PA2 sequence which create a more conformationally restricted peptide.

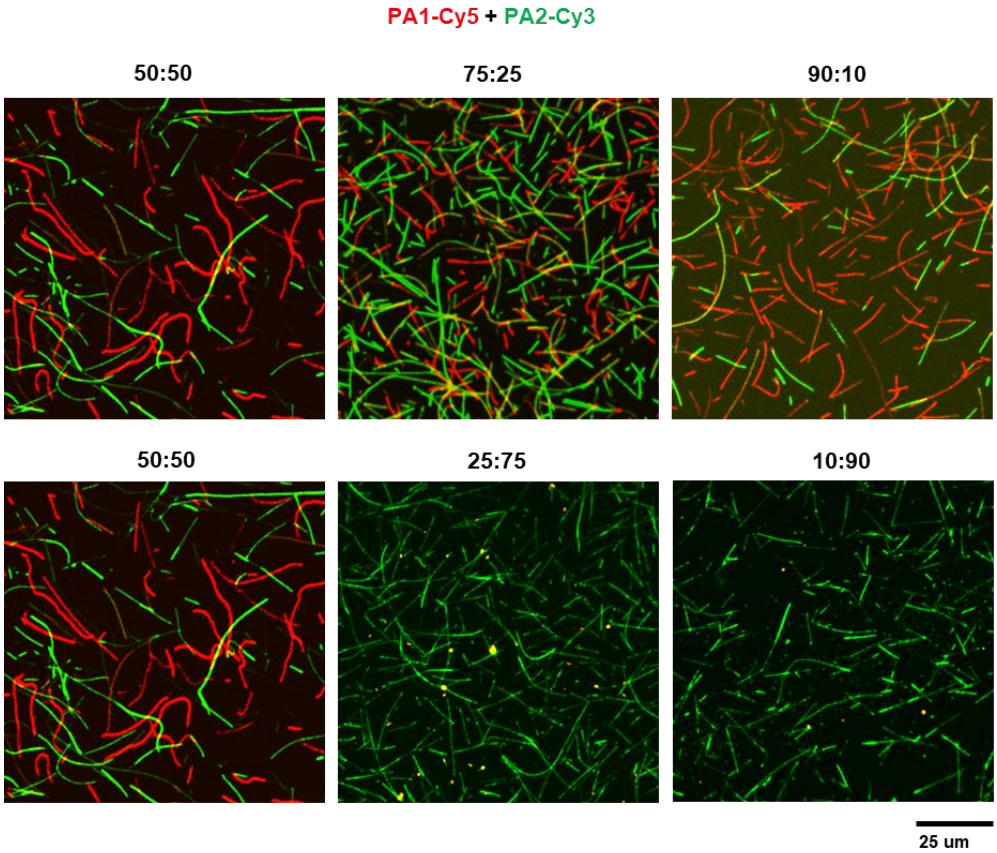

Figure 4.16. Concentration dependence of PA 1 and PA 2 co-assembly.

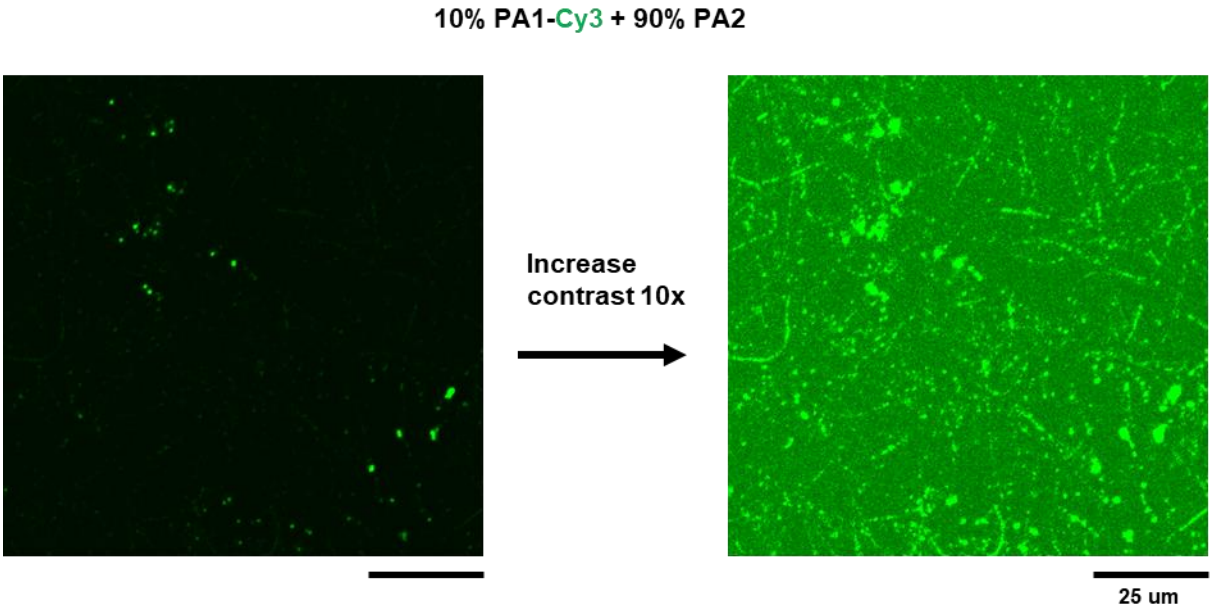

Figure 4.17. Incomplete co-assembly at low PA 1 concentrations.

4.3.4. Supramolecular composite networks with sequestered bioactive groups.

Since PAs with fluorescent dyes clearly have the ability to sequester within a mixture of two PAs into the PA assemblies consisting of the molecule with the matching backbone, it is next explored if this effect can be used to sequester bioactive groups. In the proposed scheme (**Figure 4.18**), two different bioactive ligands are attached to two different self-sorting PA backbones, like PA1 and PA2. The system will then be expected to self-assemble from a homogenous mixture into a supramolecular double network (SDN) with different bioactive groups on each component, mimetic of natural materials like the ECM.

This approach is tested by adding an additional component, a biotinylated-PA with the same backbone as the filler PAs (**Figure 4.19a**).[177] In these experiments the fluorescent PAs are kept in the mixtures as well, in order to visualize the nanostructures in CLSM. The biotin group is used as a model epitope, as it strongly binds to the streptavidin protein. Streptavidin conjugated to the Alexa-488 fluorescent dye is used order to measure the binding of the protein.[178] In the following images, the Alexa-488 signal is shown with blue colour. The specificity of streptavidin binding to PA nanostructures is measured by co-assembly PA1 with 10 mol% PA1-Biotin, without any fluorescent labels. The solution is diluted by 100X in PBS, then deposited onto a mica disk as described previously. The streptavidin-A488 solution is added at 10ng/ml in PBS for 10 mins. The process is repeated for a pure PA1 solution, to act as a control for non-specific binding of streptavidin. CLSM confirms the binding of streptavidin-A488 onto the fibrous network on the surface (**Figure 4.19b** and **Figure 4.19c**). Some non-specific binding to the nanofibers is also seen, but the signal is much lower in intensity, as expected.

Next, PA1-biotin is added to the mixture of PA1 and PA2. Here, 38 mol% PA1, 2 mol% PA1-Cy3, 10 mol% PA1-biotin, 48 mol% PA2, and 2 mol% PA2-Cy5 is used. The mixture is

prepared and deposited on the surface as before, and streptavidin-A488 is added to the solution. CLSM imaging confirms that the streptavidin-A488 binds to fibers containing PA1-Cy3, and not to fibers containing PA2-Cy5 (**Figure 4.20a**). This confirms that the biotin PA also sequesters into nanostructures with the same backbone in a mixture of PA1 and PA2. When the backbone of the biotin PA is switched, i.e. in the mixture with 10 mol% PA2-biotin and no PA1-biotin, the streptavidin-A488 signal binds primarily to fibers containing PA2-Cy5 instead (**Figure 4.20b**). However, there are also several fibers in both systems that appear to be unlabeled by the fluorescent dye. These fibers only have a signal corresponding to streptavidin-A488, which suggests they contain only the biotin PAs. Taken together, these results confirm that a protein binding group can be sequestered into either population in a system of self-sorting PAs by choice of the backbone of the binding PA, and can effectively bind the target protein in solution.

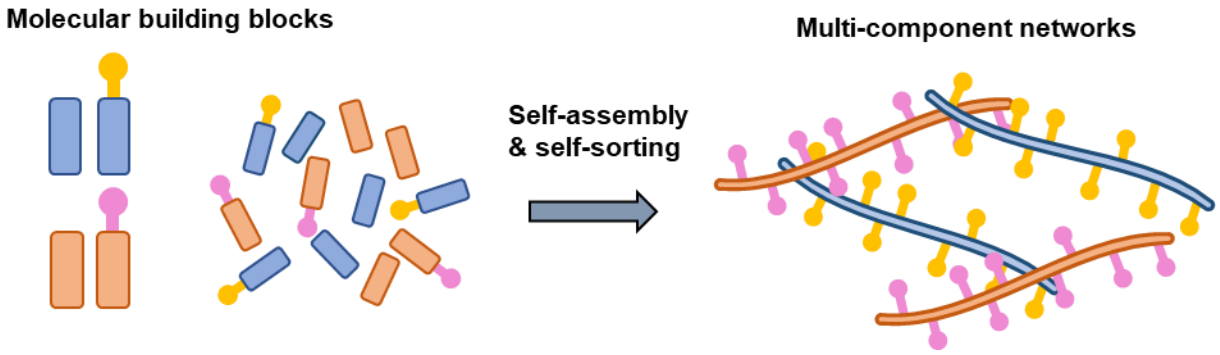

Figure 4.18. Multicomponent PA networks with sequestered bioactive groups. Schematic of the self-sorting of two PA backbones each with a subpopulation of bioactive groups attached.

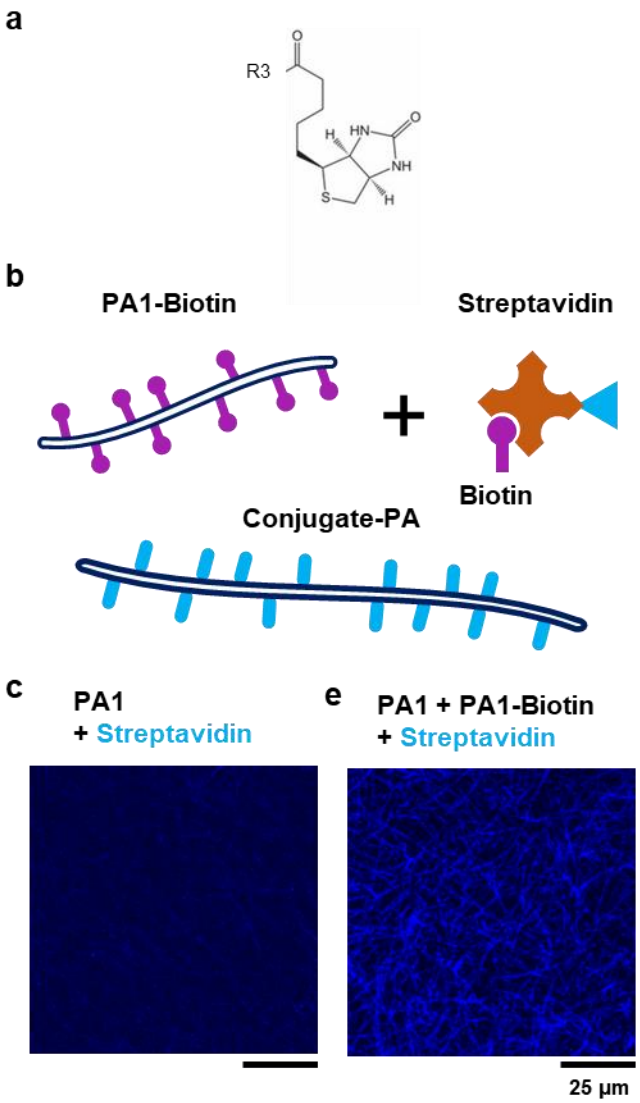

Figure 4.19. Biotinylation of PA nanofibers. a) Structure of the biotin functionalized PA1. b) Schematic of the proposed test system with fluorescently labeled streptavidin binding to biotinylated PA fibers.

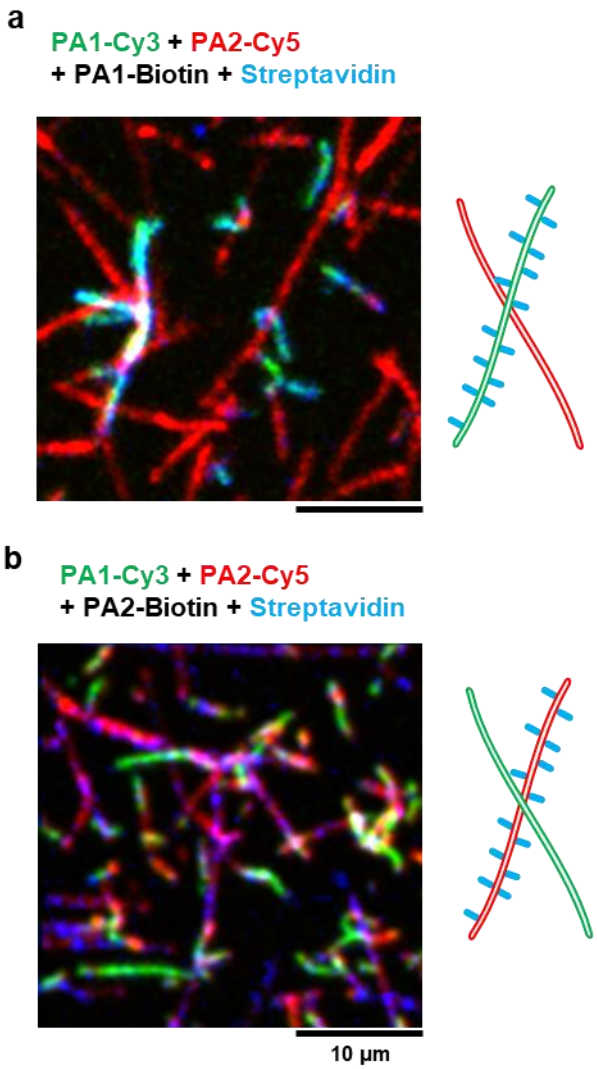

Figure 4.20. Sequestration of biotinylated PAs within multicomponent PAs. A mixture of PA1 and PA2 demonstrating the sequestration a) the PA1-Biotin into PA1 nanofibers, and b) the PA2-Biotin into PA2 nanofibers, as labeled by fluorescent streptavidin binding.

4.3.5. Supramolecular structures of protein binding PAs.

A protein-binding PA of particular interest is the PA with a peptide sequence that binds to bone morphogenetic protein 2 (BMP2). This PA has shown promise in applications for regeneration of bone tissue, particularly in spinal cord fusion studies. Interestingly, in vitro work shows that the PA must be co-assembled with a backbone PA in order to be efficacious.[72] In these experiments the PA solutions were added to plated C2C12 cells with 50 ng/ml of BMP2 protein. As shown in **Figure 4.21**, the pure BMP2-binding PA and the negative control backbone PA show a similar osteogenic effect as measured with an alkaline phosphatase (ALP) assay. However, the co-assembly of the BMP2-binding PA and the backbone shows a significantly higher efficacy then portion by itself. The mechanism of this unusual synergy has not yet been identified, and it is likely that the protein binding and release behaviour of the co-assembly differs significantly from that of the pure BMP2-binding PA.

AFM measurements on the PA systems show a significant change in the nanostructure of the systems (**Figure 4.22**). While the backbone PA assembles into long nanofibers, as expected, the BMP2-binding PA only forms short fragments and micelles. On the other hand, the co-assembly of the two results in large bundles ~100 nm in diameter, as well as some isolated fibers and smaller micelles. It is confirmed that the backbone PA and the BMP2-binding PA are co-assembled in fibers using the CLSM, by labelling 2 mol% of each population with a dye labelled version of the molecules (**Figure 4.23**). These large nanostructures likely form due to the interactions of bioactive headgroup between individual fibers in the co-assembly, where the interactions are blocked due to crowding in the pure BMP2-binding system. In Chapter 2, it was shown that PA nanofibers are readily internalized by cells. In addition, studies on BMP2 have

shown that the protein is internalized by cells and degraded, which reduces its effectiveness in activating the BMP receptors on the cell surface.[179] Based on the nanostructure change, it is hypothesized that the internalization of the protein is modified by complexing with the PA nanostructures (**Figure 4.24**). Since the BMP2-binding PA forms short fragments, its complex with BMP2 protein would be internalized quickly. However, the large nanostructures and bundles in the co-assembly would slow down the internalization of BMP2-protein, thereby extending its half-life and effective dose.

This hypothesis is tested by first measuring the internalization of PA and PA co-assemblies by C2C12 cells in flow cytometry, where 5 mol% of the molecules in each system are labelled with fluorescent dye (TAMRA). In these experiments, the PA solutions were added to plated cells for a fixed amount of time, and the cells were fixed and processed for flow cytometry. Preliminary results confirm that the large bundles in the co-assembly are internalized at a slower rate than the individual components by themselves (**Figure 4.25**). This effect is observable at both 4 and 24 hours of PA incubation time. Next, BMP2 protein is labelled with fluorescent dye (Alexa 488) to visualize it CLSM and flow cytometry. The fluorescent protein is confirmed to bind to the BMP2-binding PA co-assemblies as shown in **Figure 4.26**. In future work, the internalization of the BMP2 protein will be directly measured in these PA systems.

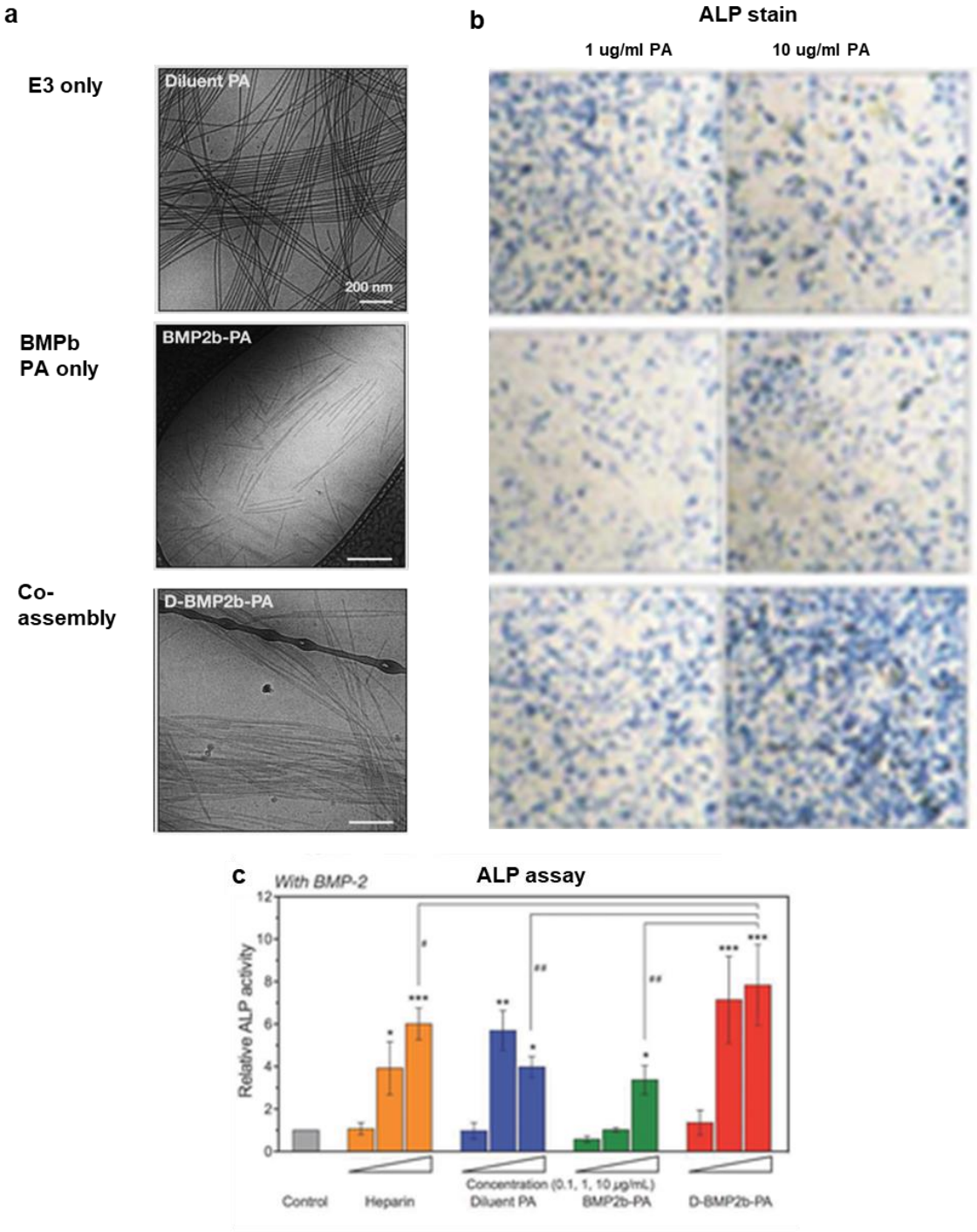

Figure 4.21. In vitro efficacy of BMPb-PA co-assemblies. a) Cryo-TEM images of E_3 PA, BMPb-PA, and co-assembly. b) ALP stain of cells with 1 ug/ml and 10 ug/ml of PA in solution, with 50 ng.ml of BMP2 protein. c) ALP assay of E_3 PA, BMPb-PA, and co-assembly. Reproduced from ref.[72]

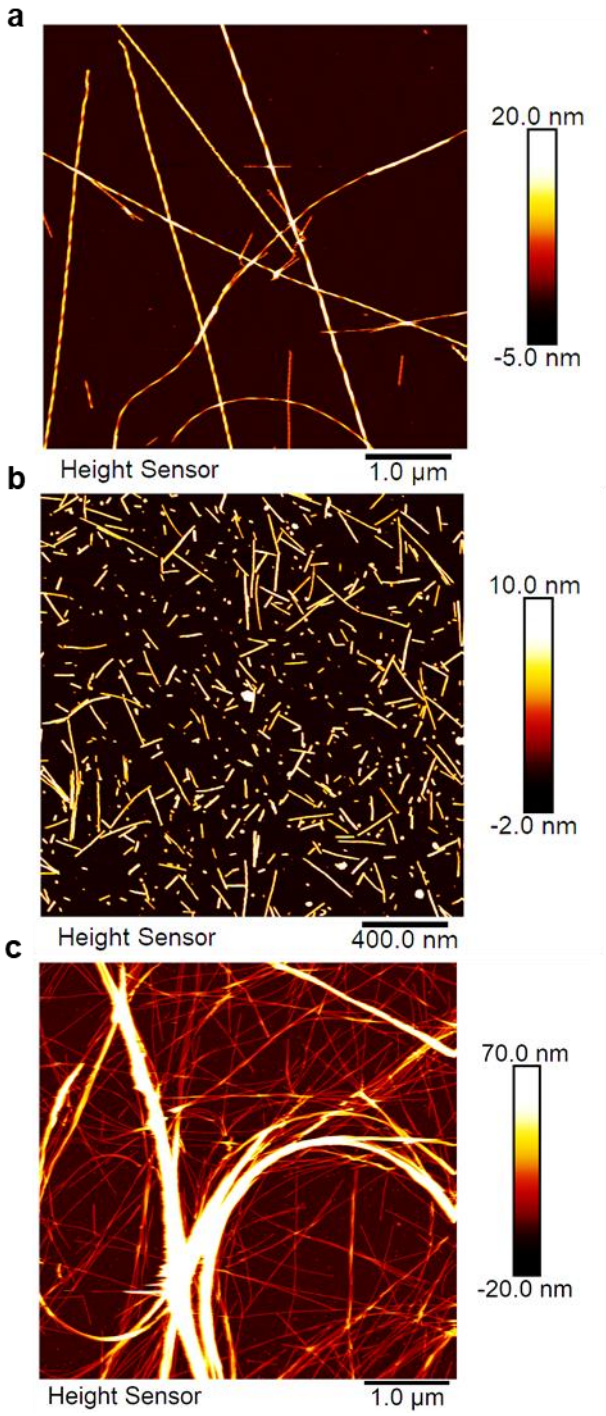

Figure 4.22. Superstructure bundling of BMPb PA. AFM images of a) E_3 PA alone, b) BMPb PA alone, and c) 50 wt% co-assembly of E_3 PA and BMPb PA. Material preparation by Dr. Wei Ji.

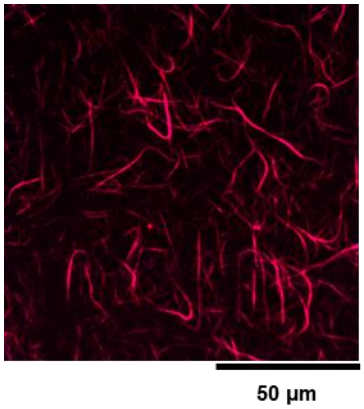

Figure 4.23. Co-assembly of $C_{16}V_3A_3E_3$ with BMPb-PA. CLSM images show high colocalization between the signals of fluorescently labeled $C_{16}V_3A_3E_3$ and BMP2b-PA. Samples prepared by Ruomeng Qui.

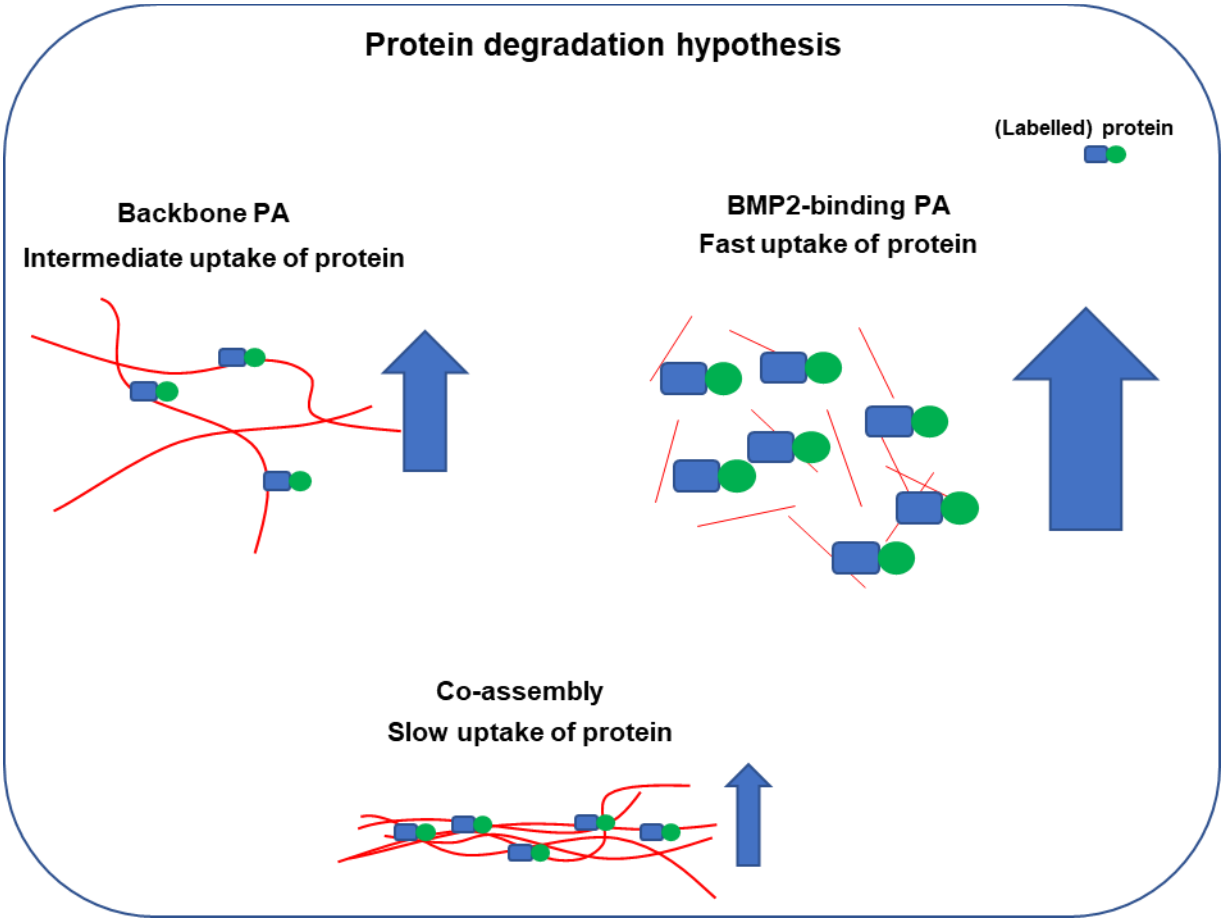

Figure 4.24. Schematic of the hypothesis of the cellular degradation of BMP2 PA-protein complex.

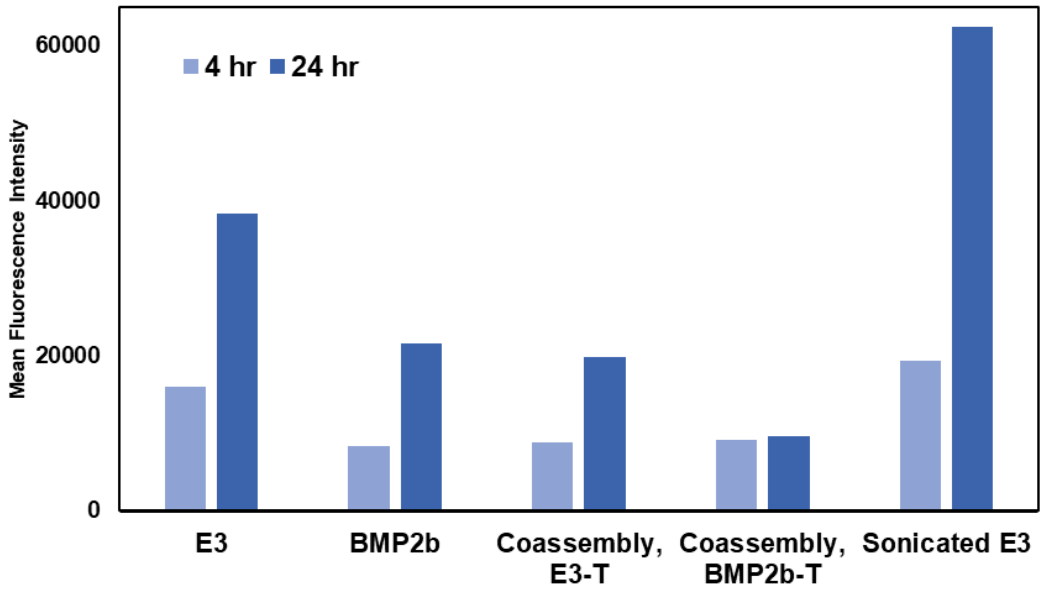

Figure 4.25. Flow cytometry measurements of cellular uptake of BMPb-PA co-assemblies. Experiment performed by Ruth Lee.

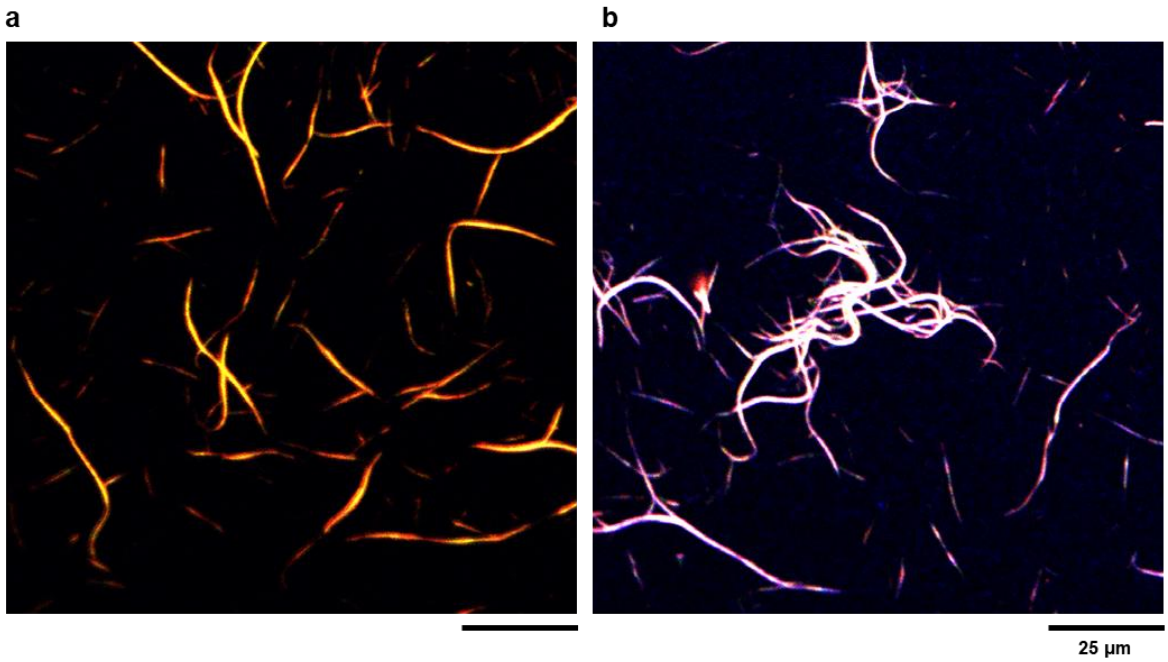

Figure 4.26. BMP2-Alexa488 binding to BMPb-PA co-assembly. CLSM images of a) co-localization of E_3 PA and BMPb-PA and b) co-localization of BMP2-A488 with the PA co-assembly. Samples prepared by Ruth Lee.

4.4. Conclusions

In summary, it was shown the multicomponent PA mixtures can co-assemble or self-sort based on the supramolecular twist of the assemblies. When molecules that form left-handed nanostructures are mixed with molecules that form right-handed nanostructures, the two components self-sort. This is likely due to the enthalpic penalty of the torsion required to change the twist of a peptide in a β-sheet. However, a PA that forms both left- and right-handed nanostructures can co-assembly with either PA to different extents. Correlative AFM-CLSM confirms that in these situations, the nanostructures adopt the supramolecular twist of the homochiral component. This self-sorting behaviour is controlled by the internal hydrogen bonding sequence, and so bioactive groups can be attached to the ends of the PAs, and can be selectively sequestered into either component. The addition of BMP2-binding PA also causes the formation of large bundles when mixed with a backbone PA, although the BMP2-binding PA forms short fragments in a pure population. The bundles slow down the cellular uptake of the PA system, likely prolonging the half-life of bound BMP2, and resulting in higher efficacy.

4.5. Materials and Methods

Atomic Force Microscopy (AFM)

Sample solutions were diluted 10X in 150 mM NaCl and deposited on freshly cleaved mica surfaces for ~1 min, and the excess solution was rinsed with 150 mM NaCl. The samples were then rinsed with 150 mM NaCl 20 mM $CaCl_2$ to immobilize the nanostructures on the mica surface, and measurements were performed in the liquid environment. AFM images were captured in PeakForce tapping mode on a Dimension Icon AFM (Bruker) with a silicon nitride cantilever (SNL10-A, Bruker) in a liquid cell. Images were flattened to correct sample tilt.

Confocal Laser Scanning Microscopy (CLSM) and analysis

Fluorescence microscopy of PA nanofibers was performed on a Nikon-A1R confocal microscope. 10 mM PA solutions were diluted to 0.05 mM in PBS, deposited on freshly cleaved mica surfaces glued onto glass slides, for ~1 min, and the excess solution was rinsed with PBS. The samples were then rinsed with 150 mM NaCl 20 mM $CaCl_2$ to immobilize the nanostructures on the mica surface. A glass coverslip was placed on top to create a wet mount, and the images were captured with a 20X air objective (Nikon). Object based correlation histograms were calculated using custom Matlab codes utilizing the Image analysis toolbox.

For streptavidin binding experiments, the PAs were deposited onto mica substrates, and a 10 ng/ml solution of streptavidin-Alexa 488 (Sigma) was added for 1 min. The solution was rinsed off with PBS, and then with 150 mM NaCl 20 mM $CaCl_2$. A glass coverslip was placed on top, and imaging was performed as before.

5. Physical properties of PA assemblies across length scales

5.1. Objectives and significance

Many soft materials in nature are composed of molecular building blocks which assemble into nanofibers, which then interact to create networks. The design of biomimetic materials requires an understand of analogous properties across multiple length scales. In this work, the molecular organization of peptide amphiphiles within nanostructures, the properties of nanofibers, and the dynamics of nanofiber networks in solution are investigated. By modelling diffraction patterns, it is found that stacked PA β-sheets are organized in a rectangular lattice, and the molecules are shown to be tilted along the direction parallel to the hydrogen bonding by angle between 16^o and 19^o. At the length scale below 2 ums, the nanofibers exhibit anonymous compressed exponential scaling in the tangent correlation function due to sharp kinks in the trajectories, but exhibit standard semi-flexible behaviour at larger length scales. Fluorescence imaging and image correlation analysis are used to investigate the dynamics of nanofiber networks as a function of persistence length, and find concentration dependent glassy dynamics. The network dynamics are independent of persistence length at low concentrations, but show a significant change at high concentrations, where high persistence length corresponds to slower decorrelation of the network. Together, these experiments provide fundamentally new insights into the behaviour of PA materials across length scales.

5.2. Introduction

Biomaterials found in nature are inherently hierarchical with drastically different properties across length scales. Materials such as collagen scaffolds in the extracellular matrix or actin and microtubule networks in the cell cytoskeleton are composed of proteins with well-defined tertiary

structure, which assemble into high aspect ratio supramolecular fibers with diameters in the nanoscale and lengths on the micro scale.[6,7,14] The fibers in turn interact with each other as well as with other components of the system to create macroscale materials. The approach to understanding these materials also changes at each length scale. At the small length scale, the structure of proteins are studied with x-ray scattering from crystalized proteins[180] and with electron microscopy reconstruction.[43,138,143,181] Proteins are studied extensively with analytical chemistry methods such as infrared spectroscopy,[182] circular dichroism (CD),[130,183] and nuclear magnetic resonance (NMR) spectroscopy.[184] At the intermediate length scale, the properties of interest of supramolecular fibers are primarily related to their mechanical properties, such as the persistence length, extensional stiffness, and stability. These properties are typically studied with imaging methods like atomic force microscopy (AFM) and transmission electron microscopy (TEM),[119] and fluorescence imaging.[83] At the microscale, the physical properties of networks of fibers are with imaging methods to measure network density or pore size,[185] as well as with bulk measurements like rheology.[89,90] Biomaterials composed of semi-flexible fibers have been studied extensible with computer simulations and analytical modelling, which has shown that these fibrous materials exhibit glassy dynamics in solution.[82,87,88] Glassy behaviour is essential for the unique rheological properties of biomaterials such as strain stiffening and visco-plasticity.[186] In order to create biomimetic materials, it is important to investigate material properties at similar length scales and understand the design principles control their structure and function.

Peptide amphiphiles (PAs) are a class of biomimetic materials that show great promise for their potential applications as scaffolds for regenerative medicine.[45] PAs are composed of a lipid tail and hydrophilic charged head group that promotes hydrophobic collapse, as well as an internal hydrogen bonding sequence which forms β-sheets. As shown in previous chapters, PAs assemble

into high aspect ratio twisted nanofibers which interact to create networks and scaffolds. Previous work has shown that diffraction patterns of PA assemblies with hydrogen bonding amino acids exhibit a peak corresponding to a 4.7 Å spacing, associated with the formation of β-sheets.[187] Analysis of diffraction patterns from PAs that form 2D crystalline sheets has been used to establish the lattice type and describe the orientation of the molecules within the unit cell.[110,188] However, this approach has not yet been applicable to PA nanofibers due to limited crystalline order and complex cylindrical symmetry. In chapter 3, the mechanical properties of PA nanofibers were investigated by measuring their persistence lengths under the assumption that they behave like semi-flexible fibers, but the length scale at which this assumption becomes valid was not established. The biological response to static 2D scaffolds was also studied as a function of fiber persistence length, but the formation of networks in solution and their dynamics were not explored.

In this work the molecular organization of PAs within twisted ribbons is investigated with x-ray scattering and electron diffraction, combined with analytical modelling. The lattice spacing is identified, as well as the orientation of molecules within the unit cell by modelling the diffraction in fiber geometry. The tangent correlation functions of nanofibers from AFM images are then investigated, and used to identify the semi-flexible regime, as well as anomalous scaling behaviour. This is combined with confocal laser scanning microscopy (CLSM) of nanofibers to measure their persistence length with dynamic imaging. Finally, CLSM is used to measure the dynamic properties of PA nanofiber networks in solution.

5.3. Results and Discussion

5.3.1. X-ray and electron diffraction of PA assemblies

WAXS diffraction from solutions of $C_{16}A_6E_3$ nanofibers show a large peak corresponding to 4.53 Å, which has previously been associated with the β-sheet spacing (**Figure 5.1a**). However, several other discernible peaks are also observed in the vicinity of this peak. Notably, a shoulder at slightly lower q than the largest peak corresponds to 4.76 Å, closer to expected position of a β-sheet peak. Due to the disorder in the PA assemblies in solution, the peaks are not sharp, making peak assignment difficult. Therefore, selected area electron diffraction (SAED) measurements were performed on aligned PA fibers, from which 2D fiber diffraction patterns were measured (**Figure 5.1b**). Comparing the peaks in the solution WAXS to the those in the electron diffraction allows one to assign peak positions, as the angle of the peak positions can be clearly identified. Interestingly, it is observed that the shoulder corresponds to the direction parallel to the fiber alignment, marked as 'B' in **Figure 5.1**, while the largest peak is offset, marked as 'A'. Additional peaks are identified in the diffraction pattern which are associated with the lateral packing of β-sheets (01) at 5.48 Å, as well as the (11), (02), (20), and (03) peaks. The 5.48 Å lateral spacing peak is the expected spacing of two sheets composed of alanines. All peaks identified in the electron diffraction pattern correspond to a standard 2D lattice, with the surprising exception of the largest peak. The shoulder at lower q is concluded to be the (10) β-sheet, and an explanation for the origin of the largest peak corresponding to a spacing of 4.53 Å is explored. This peak is found on the same position along the y-axis as the (10) β-sheet peak, but is off-set along the x axis. While peaks in crystal diffraction patterns are associated with spacings between Bragg planes, diffraction patterns from fibers with cylindrical or helical symmetries commonly can exhibit additional peaks, such as the famous cross 'X' pattern of the DNA double helix.[23,189] These peaks

come from the interference pattern of the Bessel functions which describe crystals with cylindrical symmetry. For helical chains of molecules, like DNA, peaks on a 2D diffraction pattern appear on layer lines along the y-axis, similar to what is observed for the large 'A' peak in the PA diffraction pattern. As layer lines originate from the 1D nature of a chain of molecules, it is considered that this peak may have a similar origin in the 1D geometry of the β-sheets. Specifically, if a straight 1D chain has a spacing of d_β between molecules, its reciprocal lattice will consist of layer lines separated by a spacing of $2\pi/d_\beta$. The diffraction pattern will then be given by the intensity of the Fourier transform of the scattering density within the unit cell, the basis, that lies along the layer lines. The scattering from an aligned sample of fibers can be calculated by integrating the intensity over all orientations. The diffraction patterns can therefore be calculated numerically by modeling the lattice and the scattering density within the unit cell.

The scattered intensity can be written in spherical coordinates as:

$$I(\vec{q}) \sim \sum_i \int_0^{2\pi} \int_0^{\pi} e^{-\left(\frac{1}{2\sigma_i^2}\right)\left(\vec{q}-\overrightarrow{G_i}\right)^2} |F(\vec{q})|^2 \sin(\phi)\, d\phi\, d\theta \qquad (5.1)$$

Where F is the form factor of the basis, and the summation is over the reciprocal lattice vectors $\overrightarrow{G_i}$. σ_i is the characteristic spread of the of the Gaussian approximation of the scattering intensity, inversely proportional to the coherence length of crystalline order. As the coherence length increases the Gaussian approximation approaches a delta function, as expected for large crystals. The calculation of x-ray diffraction patterns requires the lattice vectors, which can be found from the measured diffraction patterns, as well as the form factor of the basis, which must be approximated.

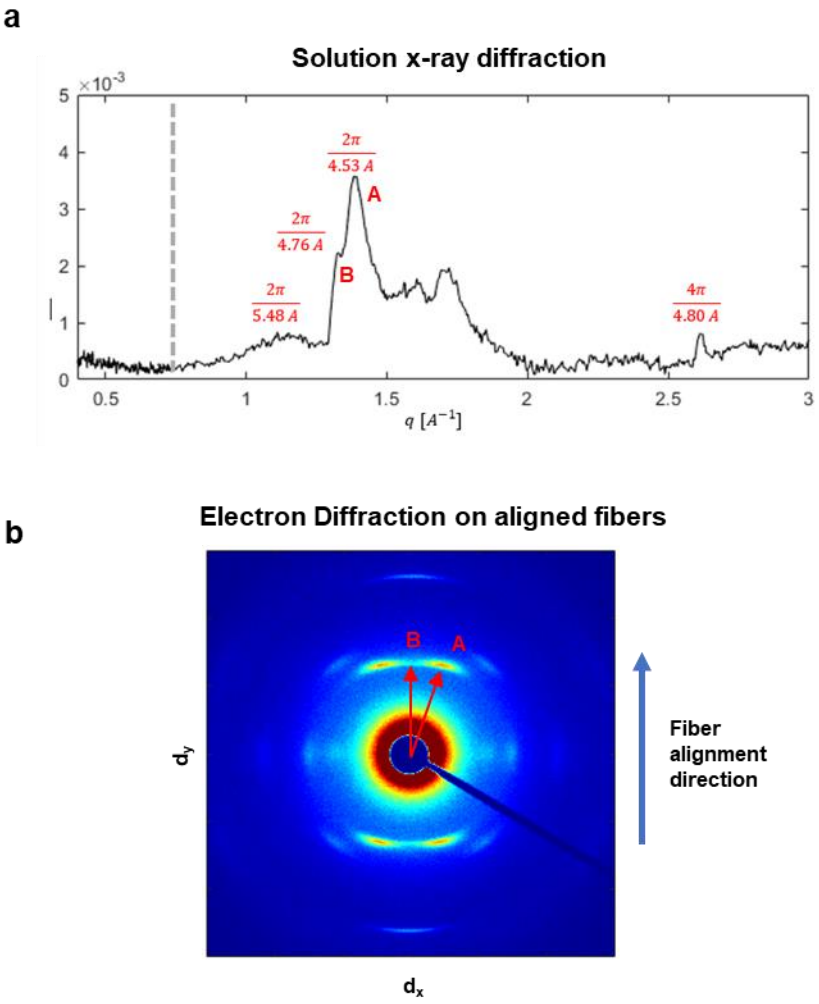

Figure 5.1. Diffraction patterns of $C_{16}A_6E_3$ nanofibers. (a) MAXS and WAXS diffraction from PA solutions. (b) Electron diffraction form aligned nanofibers.

The resolution at which the molecular electron density distribution can be measured is determined by the order in the crystal. Since the diffraction patterns measured from PAs do not show sharp peaks, a coarse-grained approximation for the molecule's electron density distribution is used. Similar to previous work, the PA molecules are approximated as cuboid slabs of constant electron density with the three sides of length $a, b,$ and c.[110] The form factor of a cuboid is given by its Fourier transform:[131]

$$f(\vec{q}) \sim sinc\left(\frac{q_x a}{2}\right) sinc\left(\frac{q_y b}{2}\right) sinc\left(\frac{q_y c}{2}\right) \quad (5.2)$$

A simple expression can be found for the scattering from a 2D sheet of cuboid molecules, appropriate to describe the flat portion of a twisted ribbon corresponding to $\theta = 0^o$, as shown in **Figure 5.2a**. In the 2D projection of this the molecules are arranged in a rectangular lattice for illustration purposes. Since PA nanofibers have pitch lengths much longer than the spacing between molecules, the lattice can be treated as a 2D Bravais lattice without twist. Here, expression 5.1 describes the product of the reciprocal rectangular lattice with the form factor of the basis. Around each reciprocal lattice point given by $\overrightarrow{G_l}$, the intensity is described by a Gaussian with width σ, represented by circles in **Figure 5.2a**. Multiplication with the cuboid form factor results in a diffraction pattern similar to the schematic, with the highest intensity spot in the middle.

Scattering from the narrow portion of the twisted ribbon, corresponding to $\theta = 90^o$ can be found in a similar way, as shown in **Figure 5.2b**. Along this projection, the molecules appear as a 1D chain rather than a 2D sheet. The resulting representation of expression 5.1 is a series of reciprocal space lines with width given by σ, multiplied by the form factor of the molecule. If the cuboid was strictly parallel or perpendicular to the fiber alignment direction, the highest intensity peak would lie along the x- or y-axis, respectively. Since the highest peak lies along the first layer line, but offset along the x-direction by an angle α, it is treated as a tilted cuboid instead. The tilt can be included by rotating the y and z-axis of the molecules coordinate system:[110,190]

$q_y' = q_y \cos(\alpha) - q_z \sin(\alpha)$,

$q_z' = q_y \sin(\alpha) + q_z \cos(\alpha)$, and

$$F(\vec{q}) \sim sinc\left(\frac{q_x a}{2}\right) sinc\left(\frac{q_y' b}{2}\right) sinc\left(\frac{q_y' c}{2}\right) \quad (5.3)$$

The contribution of the $\theta = 90^o$ orientation therefore results in the additional 'A' peak that does not correspond to a Bragg plane. Instead, this peak originates from the tilt of the molecule in a 1D fiber diffraction geometry. The total scattering intensity can be found by integrating over all angles θ. These results are summarized in **Figure 5.3**. A direct comparison of the peaks in the WAXS patterns and the electron diffraction patterns confirms that the largest peak in WAXS corresponds to the rotated peak from the molecular tilt, while the lower intensity shoulder peak corresponds to the β-sheet spacing. This can be described by tilting the molecules in a 2D sheet by the angle measured in the electron diffraction pattern, and approximating the molecules as cuboid slabs of electron density. Calculating the full scattering density for (10) peak using expression 5.1 shows an excellent agreement with the measured WAXS pattern. The β-sheet spacing appears to split into two peaks, with the lower intensity shoulder corresponding to the spacing of 4.76 Å, and the higher intensity peak corresponding to a tilt angle of 19.7°.

These measurements were repeated for the PA $C_{16}V_3A_3E_3$, and similar results were found (**Figure 5.4**). The tilt angle measured from electron diffraction is lower at 16.1°, and therefore there is less separation between the peak and shoulder measured in WAXS. The calculated pattern shows a β-sheet spacing of 4.75 Å, while a naïve interpretation of the main peak would correspond to a spacing of 4.64 Å. For this molecule, the lateral (01) spacing between β-sheets is larger at 9.61 Å, consistent with the larger size of the valine side chains.

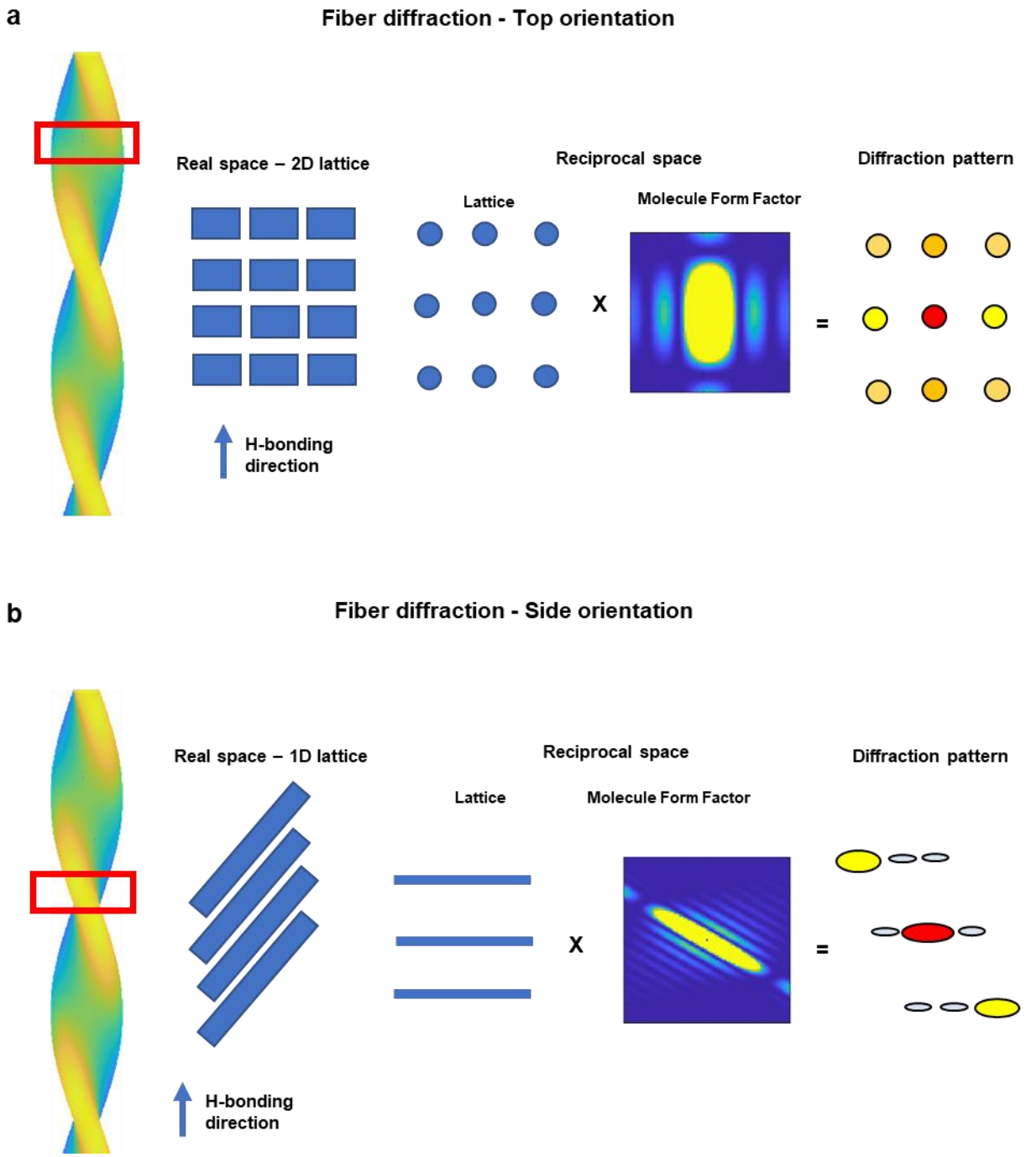

Figure 5.2. Explanation of peak positions in PA nanofiber diffraction. Diffraction patterns from the projection of the (a) top orientation of the flat portion of the ribbons and (b) from the side orientation of the narrow portion of the ribbon.

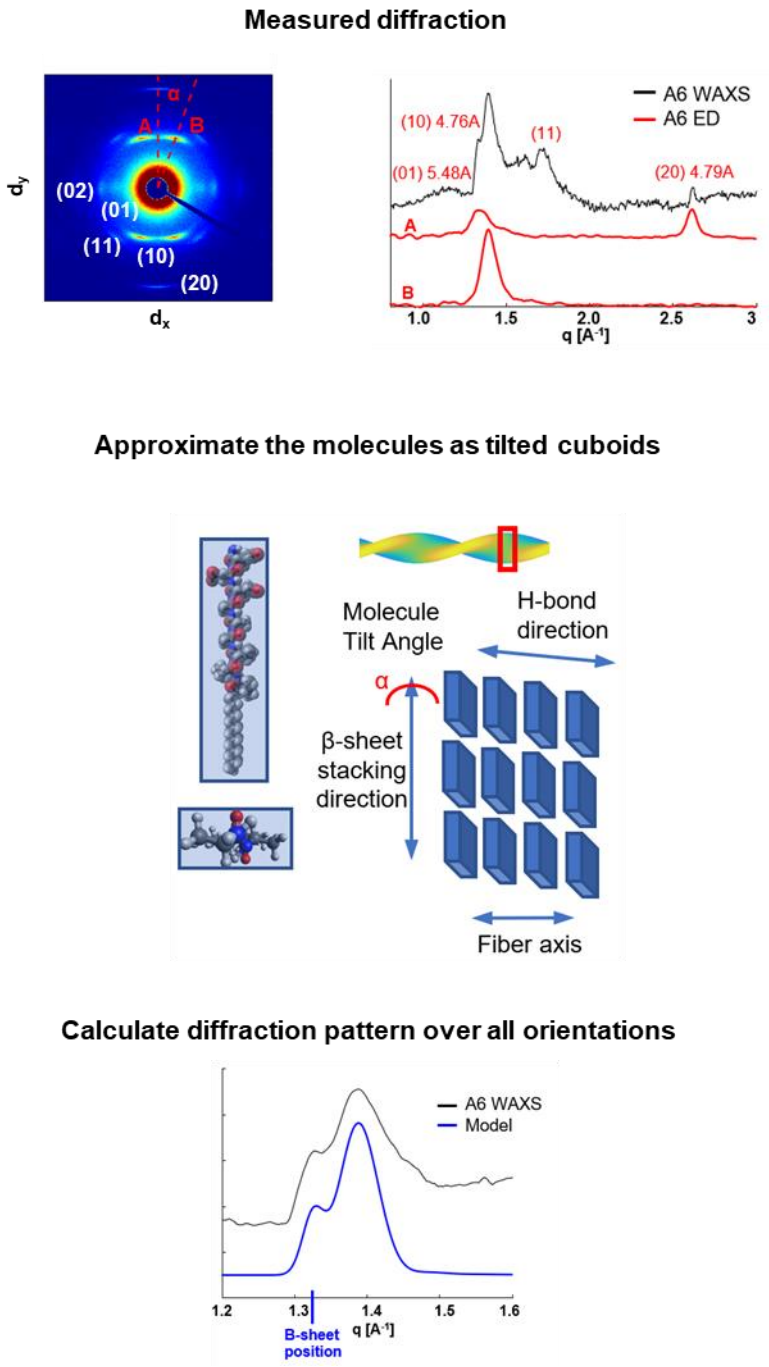

Figure 5.3. Summary of the diffraction calculation procedure for twisted nanoribbons.

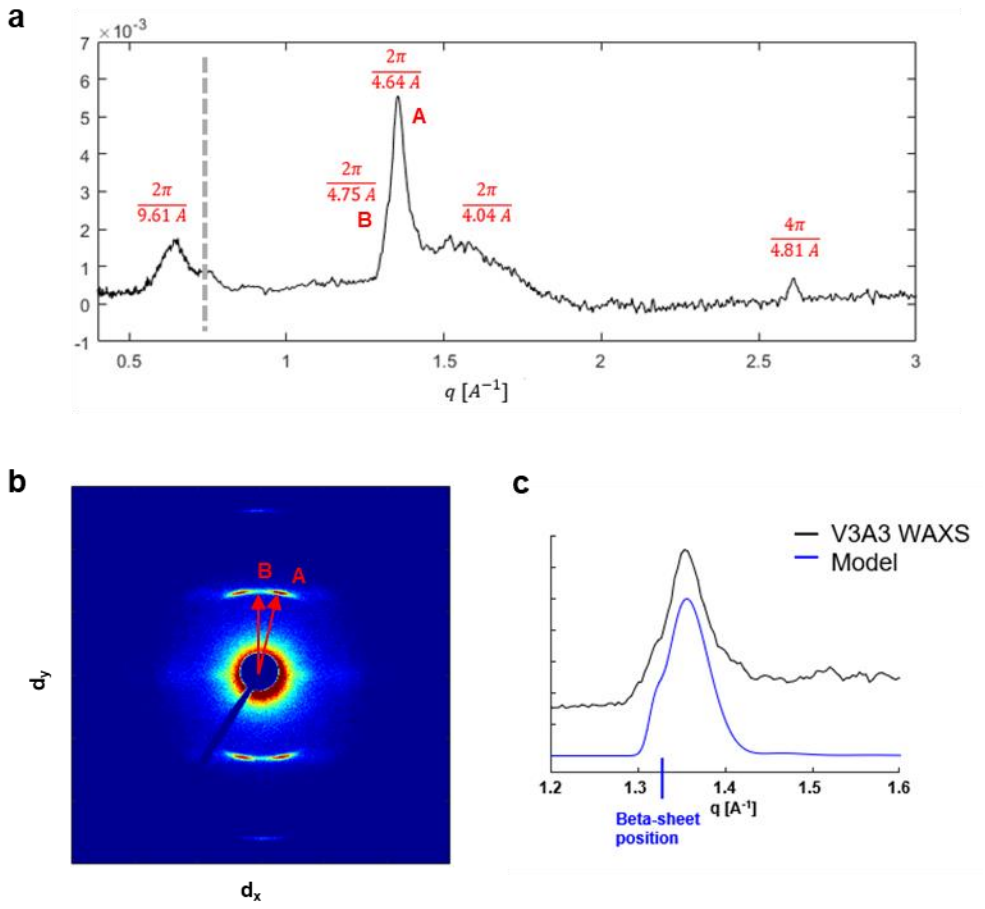

Figure 5.4. Diffraction patterns of $C_{16}V_3A_3E_3$ nanofibers. (a) MAXS and WAXS diffraction from PA solutions, (b) electron diffraction form aligned nanofibers, and (c) comparison with calculated diffraction pattern.

5.3.2. Persistence length and the tangent correlation function

We next investigate the behaviour of the $C_{16}A_6E_3$ nanofibers at the microscale. PA nanofibers are deposited on mica surfaces as described previously. The tangent correlation function of nanofibers, which contains information about the bending stiffness or persistence length, is calculated by tracking fiber trajectories in large AFM images (**Figure 5.5**). The fibers are tracked using an open source MATLAB plugin FiberApp,[86] developed by the Mezzenga group.

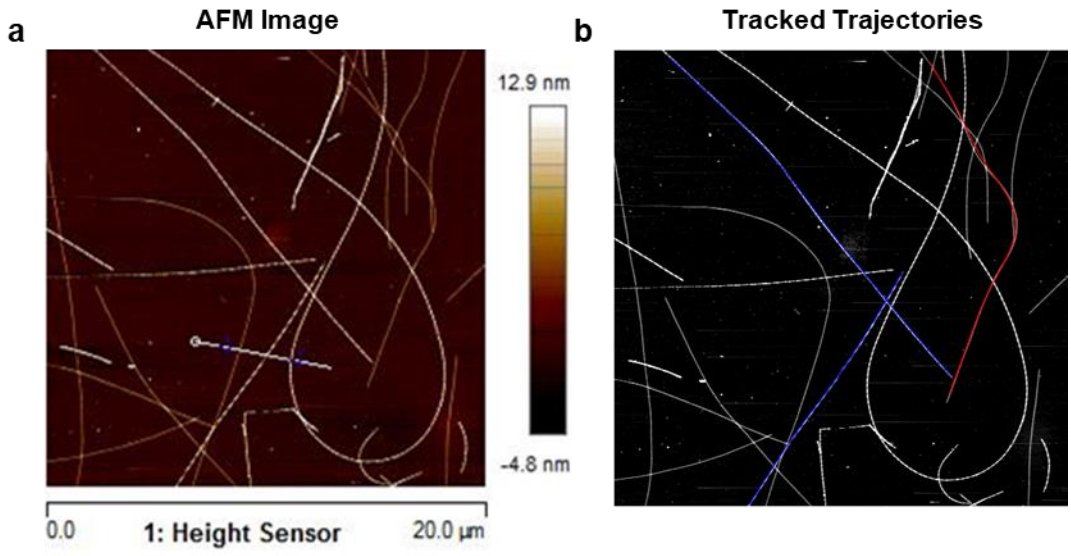

Figure 5.5. Tracking nanofiber trajectories from AFM images. (a) Large AFM image of $C_{16}A_6E_3$ nanofibers and (b) trajectories tracked with FiberApp.

The tangent correlation function is calculated from the ensemble of discretized fiber trajectories, with appropriate weighting for the number of data points at each length scale. The AFM images used for this calculation are 20x20 microns, long enough to capture the bending behaviour of the fibers. For an ensemble of semi-flexible fibers on a 2D surface, the tangent correlation functions is expected to exhibit an exponential decay of the form $g(r) = e^{-\frac{r}{2l_p}}$, where r is the distance along the fibers, and l_p is the persistence length. It is more convenient to look at the logarithm of the correlation function, given by $\log\big(g(r)\big) = -\frac{r}{2l_p}$, as it forms a straight line of constant slope.

This expected behaviour can be seen by simulating an ensemble of semi-flexible fibers with persistence length similar to contour length, the relevant regime for PA nanofibers, as shown in **Figure 5.6**. The simulated fibers are generated using the procedure described in Chapter 3.

Interestingly, the log correlation of $C_{16}A_6E_3$ nanofibers prepared at 20 mM NaOH shows a deviates from this behaviour at short lengths scales, where the early part of the curve is not exponential, and the expected exponential decay begins at a length of ~2 um (**Figure 5.7**). A similar behaviour is observed for nanofibers prepared at 5 mM NaOH, but with a slower overall decay as the nanofibers are stiffer. The tangent correlation function can be generalized to the form $g(r) = e^{-\left(\frac{r}{\lambda}\right)^{\beta}}$, where $\beta = 1$ corresponds to the usual scaling, $\beta < 1$ corresponds to stretched exponential decay, and $\beta > 1$ corresponds to a compressed exponential decay. The logarithm of the correlation function is given by a power law with exponent β, $\log\big(g(r)\big) = -\left(\frac{r}{\lambda}\right)^{\beta}$. As shown in **Figure 5.8**, the slope of the curve on a log-log plot corresponds to the scaling exponent. At longer length scales, it is observed that $\beta = 1$, as expected, while $\beta \approx 1.33$ at length scales below 2 um. A second linear region in the portion below 300nm is also observed, however this is likely too short of a length scale to be experimentally meaningful. A similar compressed exponential scaling is observed for the system at 5 mM NaOH, which reverts to $\beta = 1$ scaling at the micron scale. Compressed exponential scaling in correlation functions is rare, but has been observed in some glassy systems.[191] It corresponds to an avalanche like change in order, where a jammed system suddenly changes order. Examinations of the nanofiber images shows occasional kinks in the fiber trajectory, where the fiber direction changes rapidly over a short distance (**Figure 5.9**). These kinks in the nanofibers likely arise due to localized disorder in the assembly, and may be responsible for the compressed exponential scaling in the tangent correlation function. A similar scaling of the tangent correlation function in $C_{16}V_3A_3E_3$ PA nanofibers is confirmed (**Figure 5.10**), with an initial compressed exponential regime with exponent $\beta = 1.9$, followed by a semi-flexible regime corresponding to a persistence length of 11 um.

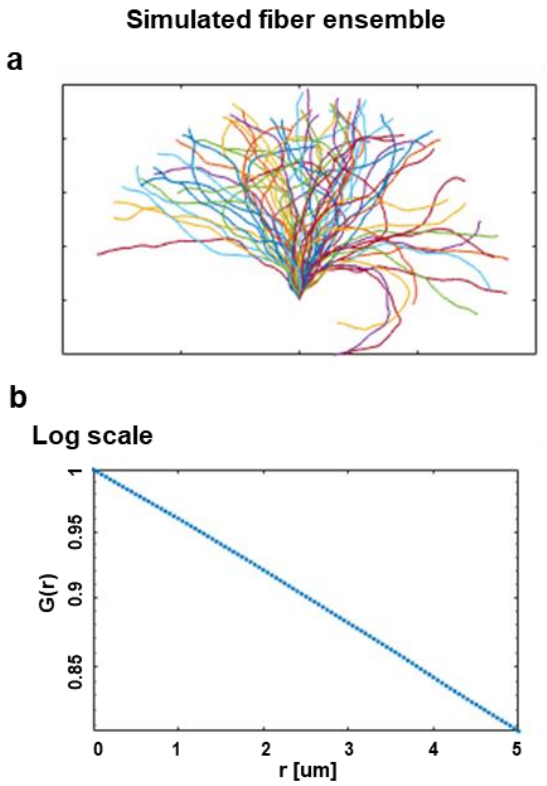

Figure 5.6. Tangent correlation function of simulated semiflexible fibers. (a) Simulated ensemble of semiflexible fibers and (b) the tangent correlation function on a log scale, showing a straight line.

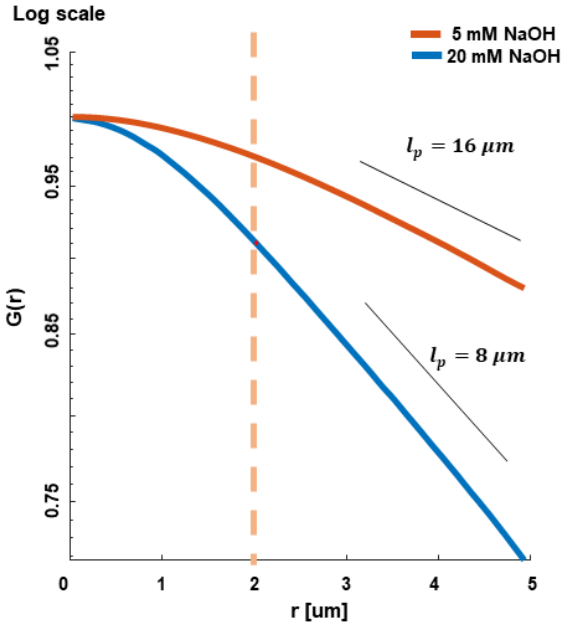

Figure 5.7. Tangent correlation function of $C_{16}A_6E_3$ PA nanofibers. Persistence length is calculated form the linear regime at long distances.

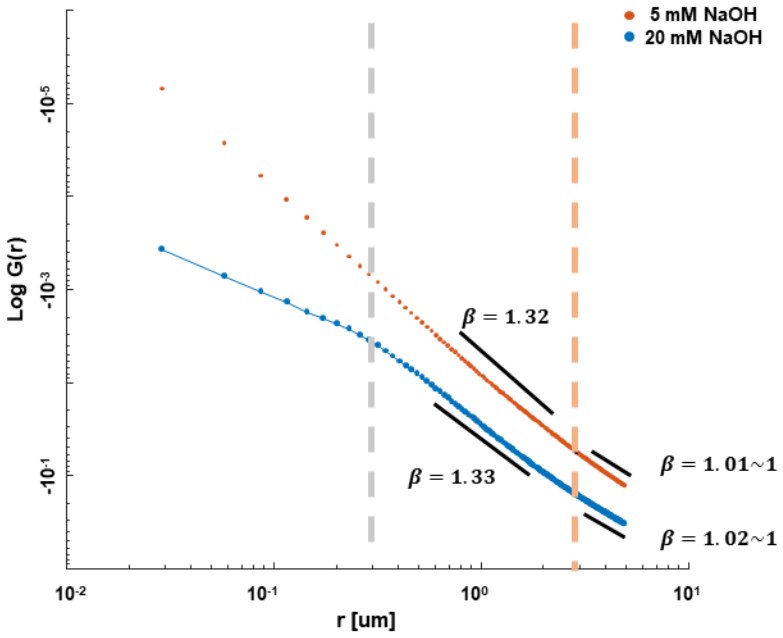

Figure 5.8. Log of the tangent correlation function of $C_{16}A_6E_3$ PA nanofibers. Curves show an initial compressed exponential regime followed by a standard semi-flexible regime.

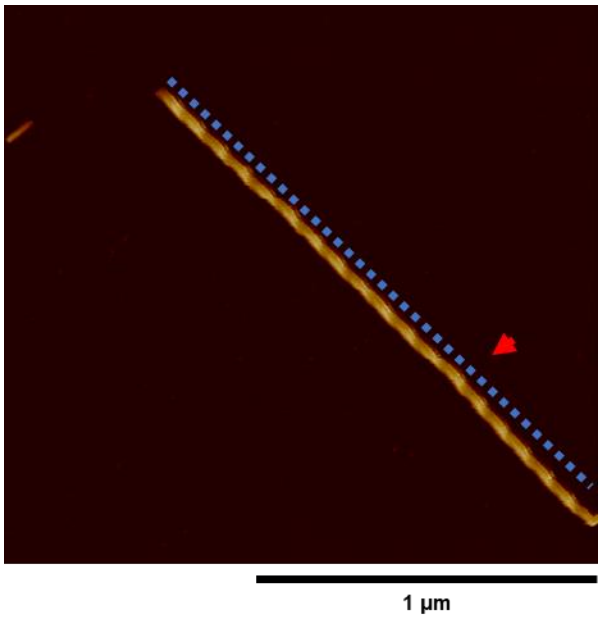

Figure 5.9. Kinks in nanofiber trajectories. Red arrow indicates point of deviation.

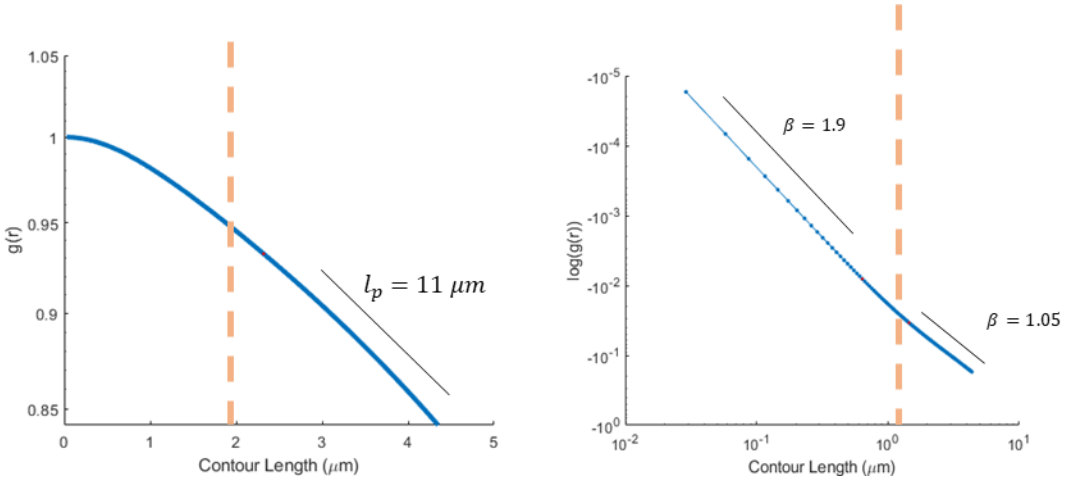

Figure 5.10. Tangent correlation functions of $C_{16}V_3A_3E_3$. Curves show an initial compressed exponential regime followed by a standard semi-flexible regime.

Nest, the temporal dynamics of single nanofibers were measured by dynamic light scattering (DLS),[192] as well as by tracking fiber trajectories in fluorescence microscopy. The dynamic correlation function of dilute semiflexible fibers fluctuating in a thermal environment are expected to follow a stretched exponential decay of the form $g(\tau) \sim e^{-(\tau \backslash T)^{\frac{3}{4}}}$.[82] The PA solutions were diluted to 50 uM and measured in a Zetasizer light scattering instrument (Malvern). The resulting correlation function is well described by the expected $\tau^{3/4}$ stretched exponential scaling (**Figure 5.11**). This confirms that PA nanofibers obey semiflexible fiber dynamics. $C_{16}A_6E_3$ was then co-assembled with 5 mol% of a TAMRA labelled version of the PA, in order to visualize the assemblies in fluorescence microscopy. The solutions were imaged in CLSM at video rates using the resonant scanning mode. In these videos, individual nanofibers can be seen, and their bending fluctuations can be observed in real time. Using a modified version of the FiberApp MATLAB code, the trajectories of the nanofibers were tracked over the course of a video, as described in **Figure 5.12**. The trajectories can then be used to calculate the persistence of the fibers.[83] The tangent angles along the discretized fiber trajectory $\theta(s)$ are calculated and expressed as a sum of

cosine Fourier modes $\theta(s) = \sqrt{2\pi \backslash L}\ \sum_{n=0}^{\infty} a_n \cos(qs)$, where L is the length of the trajectory, and a_n is the amplitude of the n[th] Fourier mode. The amplitudes of the bending modes contain information about the dynamics of the fiber at different length scales. Specifically, the variance of the amplitudes measured at different time points is given by $Var(a_n) = \left(\frac{L}{n\pi}\right)^2 \frac{1}{l_p}$. The expression for the variance of the measured trajectories, including the effects of noise, is given by:[83]

$$Var(a_n)^{measured} = \left(\frac{L}{n\pi}\right)^2 \frac{1}{l_p} + \frac{4}{L} < \epsilon_k^2 > \left[1 + (N-1)\sin^2\left(\frac{n\pi}{2N}\right)\right], \tag{5.4}$$

where $< \epsilon_k^2 >$ is the measurement noise which is left as a fitting parameter.

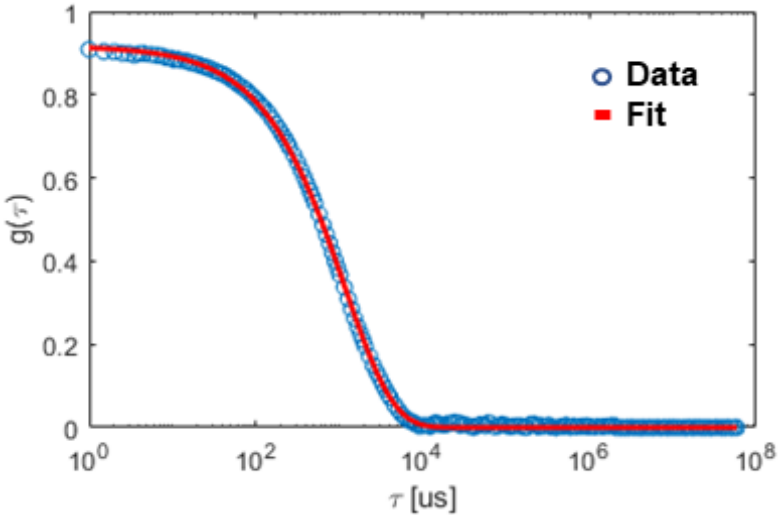

Figure 5.11. Dynamic correlation function measured from DLS. The red line is a fit to stretched exponential function.

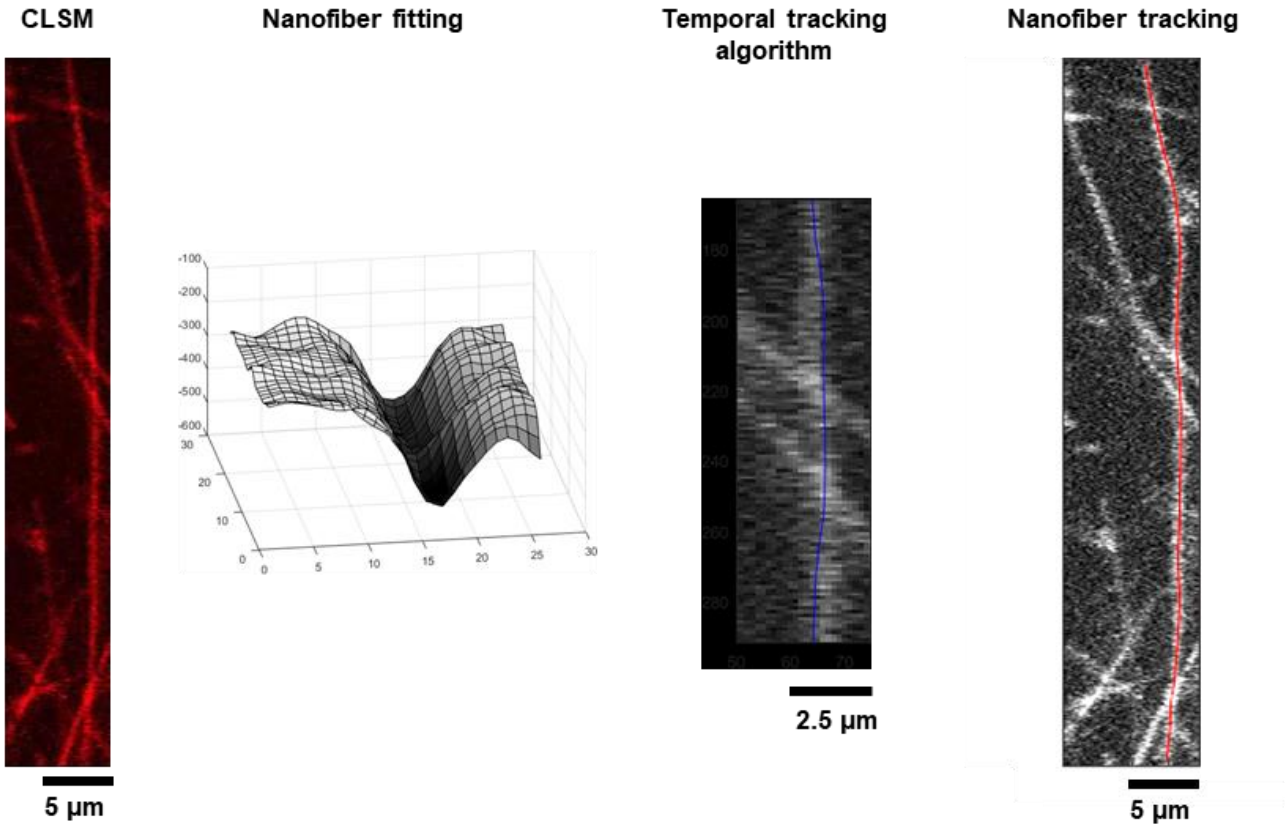

Figure 5.12. Nanofiber tracking procedure in CLSM videos.

The variance of the Fourier amplitudes measured experimentally for several fibers are fit to expression 5.4, as shown in **Figure 5.13**. The measured variances follow the expected semi-flexible behaviour closely, as the smallest length scales observable with fluorescence microscopy correspond to ~1 um, around the length scale where the tangent correlation function adopts semi-flexible scaling behaviour. The measure persistence lengths vary from 20-50 um, although this experimental method cannot be easily scaled to large numbers of measurements. This method has been used to report the persistence lengths of biopolymers like actin and microtubules. In particular, the persistence lengths of PA nanofibers are quite similar to those of actin (~10 um).[82]

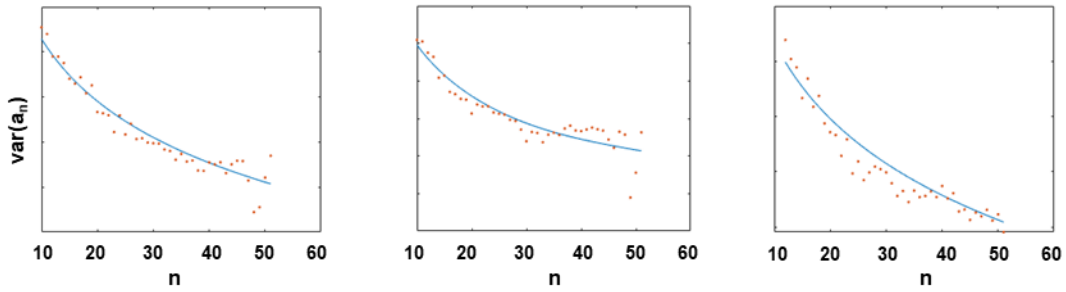

Figure 5.13. Variance of Fourier amplitudes from nanofiber trajectory videos. Results are shown for three fiber trajectories.

5.3.3. PA nanofiber network dynamics

As the concentration of PA nanofibers in solution increases, collisions between nanofibers begin to dominate the behaviour of the system. Networks of semiflexible fibers are expected to show glassy dynamics at length scales longer than or comparable to the fiber interaction spacing.[82,165] PA nanofiber networks can be observed in CLSM similar to the previous section, but the concentration at which fibers can be resolved is limited by the diffraction limit of light of ~500 nm. Therefore, an approach to measuring the dynamics of high concentrations of fibers was developed, by labelling only a subset of the nanofibers with a fluorescent dye. This is done by mixing the fluorescent dye labeled nanofibers with a solution of unlabelled nanofibers, as described in the schematic in **Figure 5.14**. Here, the concentration of the labelled PA solution is kept constant at 10 uM, while the concentration of the total PA can be varied. Droplets of the mixed PA solutions are deposited on glass bottom petri dishes and imaged in CLSM using a resonant scanner for video rate imaging. The sample is allowed to equilibrate after deposition to minimize flow or drift within the solution, and images are taken ~50 um above the glass surface at a frame rate of 15 Hz, for a total of 50 seconds. Snapshots of the videos at different

concentrations are shown in **Figure 5.15**, where fluorescent fibers are resolvable within a high concentration PA solution.

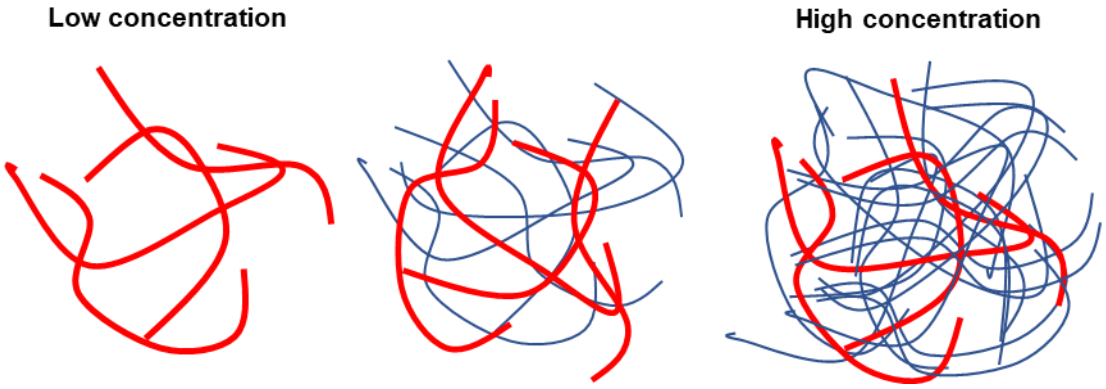

Figure 5.14. Schematic of the fluorescent labelling of PA nanofiber solutions.

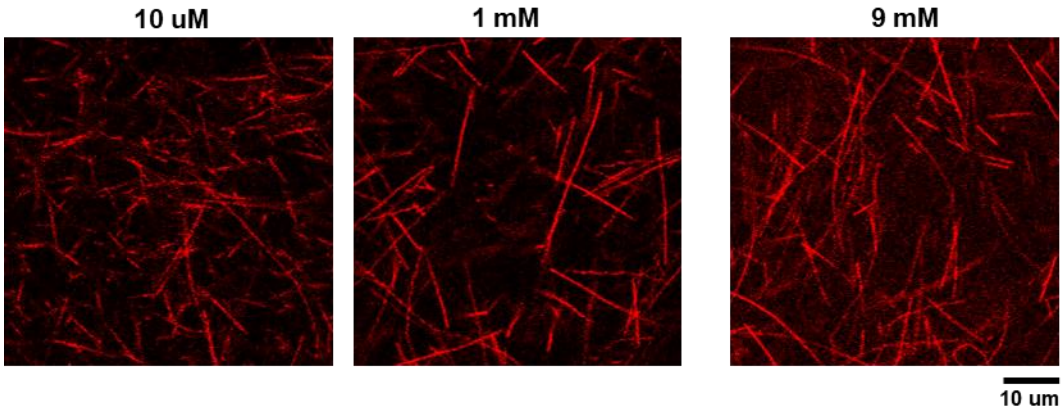

Figure 5.15. Snapshot of labelled nanofiber solutions at different concentrations. Individual nanofibers are clearly observable even at high concentrations.

We use temporal image correlation analysis to analyze the dynamics of the nanofibers, as described in **Figure 5.16**.[193] In this method, each image in a series, given by the function $I(x, y, t)$, is converted to Fourier space $\tilde{I}(k_x, k_y, t)$ using a fast Fourier transform (FFT). The temporal autocorrelation function is calculated for the amplitude of each Fourier mode, given by

$g(k_x, k_y, \tau) =< \tilde{I}(k_x, k_y, t)\tilde{I}(k_x, k_y, t+\tau) >_t$, where the angular brackets indicate average over all values of t. As the system is isotropic, the correlation function $g(k_x, k_y, \tau)$ is radially average over values of $|\vec{k}| = \sqrt{k_x^2 + k_y^2}$, giving the final temporal correlation function $G(k, \tau)$. $G(k, \tau)$ is the 2D equivalent to the correlation function measured in DLS. However, this method enables the measurement of the dynamics of PA networks at higher concentrations than is usually accessible in DLS. In addition, the correlation functions for different lengths is measured simultaneously, as opposed to DLS where most instruments only measure scattering at a fixed q vector. Together, this approach is used to study the concentration dependent dynamics of PA networks.

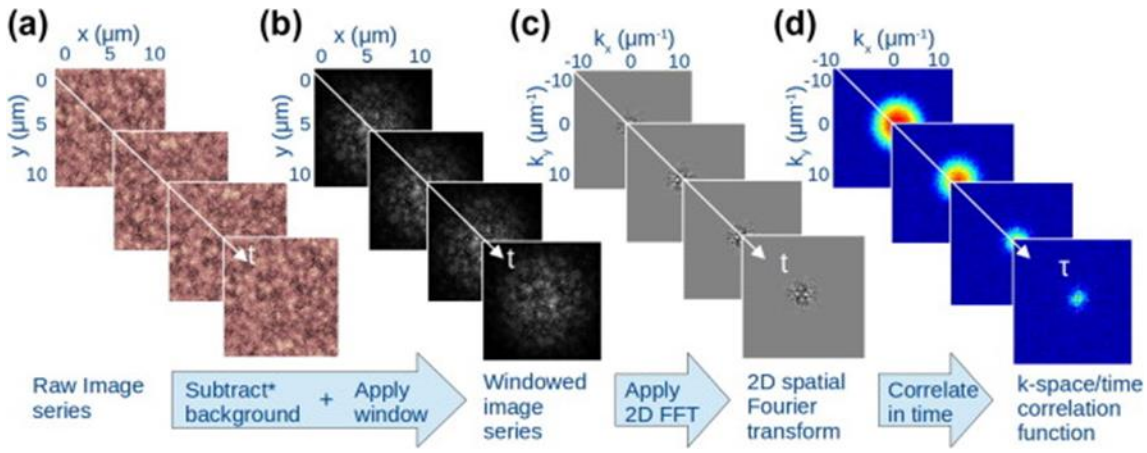

Figure 5.16. Explanation of the image temporal correlation algorithm. Reproduced from ref.[193]

First, the temporal correlation functions measured from solutions of flexible PA nanofibers, prepared at 20 mM NaOH, exhibit an initial fast exponential decay followed by power law decay at long time scales (**Figure 5.17**). Both the plateau and the scaling exponent decrease as the concentration increases, indicating the emergence of glassy dynamics at high concentrations. The curves can be compared to the measurement of a static network of fibers, measured on the glass

surface, which includes only the contribution of photophysical dynamics and noise. Next, the initial decay rate for the different concentrations is measured as a function of the spatial k-vector, which describes the decorrelation time at different length scales. The initial decay is approximated as an exponential $G(k,\tau) = e^{-\tau/\lambda_k}$, where λ_k is the characteristic decorrelation time. In a diffusive system, a ballistic scaling of the form $\lambda_k \sim k^2$ is expected. The scaling coefficient is close to $k^{3/2}$ for all concentrations, indicative of glassy dynamics over all spatial scales (**Figure 5.18**). These PA networks are compared to networks of fibers with higher stiffness, prepared at 5 mM NaOH. While the temporal correlation curves in the dilute systems at 10 uM and 100 uM are nearly identical, a significant difference in the plateau and scaling at the higher concentrations of 9 mM is observed (**Figure 5.19**). As described in Chapter 3, this decrease in dynamics corresponds to reduction the storage modulus of hydrogels upon calcium cross linking, and an increase in viscosity (**Figure 3.28**). This is likely due to fewer entanglements when the material is sheared, where the stiffer nanofibers are able flow past each other. On the other hand, the correlation decay time follows a similar $\sim k^{3/2}$ sub-diffusive power law scaling over spatial scales (**Figure 5.20**), with similar behaviour at all concentrations. This suggests that the change in nanofiber persistence length effects the network dynamics only at high concentrations, where the fiber fluctuations become significantly reduced by the surrounding fibers in the solution. However, this effect does not change the spatial length scale dependence of the power law scaling in the decorrelation time.

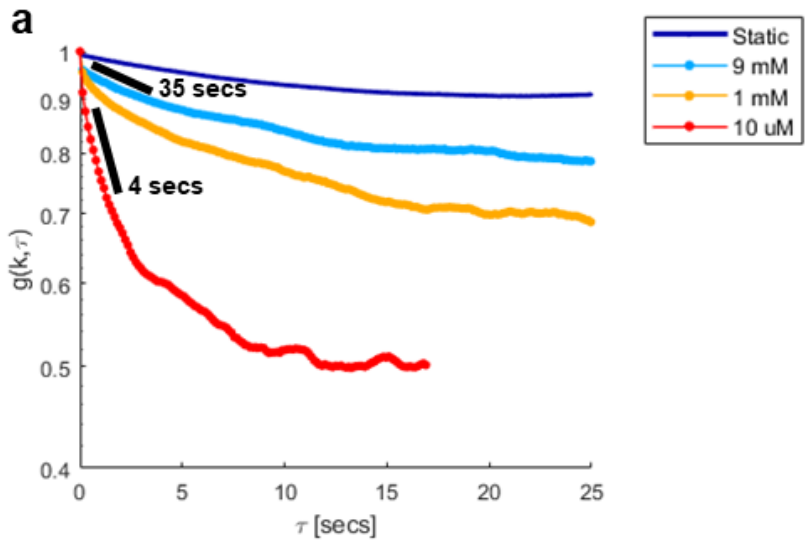

Figure 5.17. Temporal correlation function of PA nanofibers prepared at 20 mM NaOH. The curves exhibit an initial concentration dependent fast decay, followed by a power law decay at long timescales.

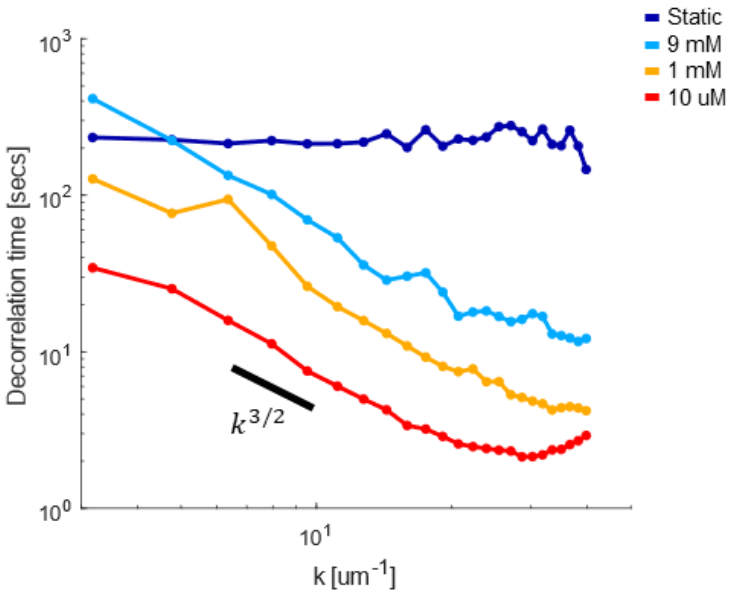

Figure 5.18. Scaling of network decorrelation time over spatial scales. The black line indicates a scaling of $k^{3/2}$. The dark blue lien is a static control system.

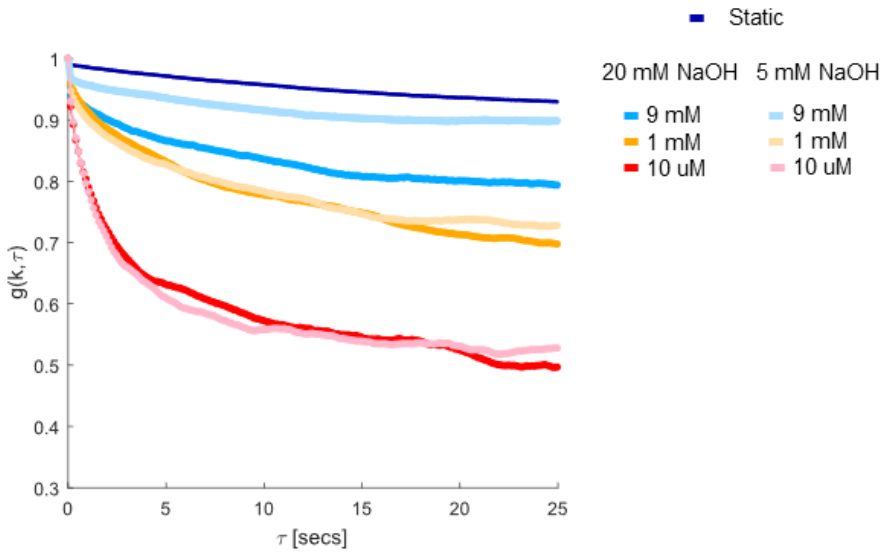

Figure 5.19. Temporal correlation function of PA nanofibers with different stiffness. The dynamics are only significantly different at the highest concentration.

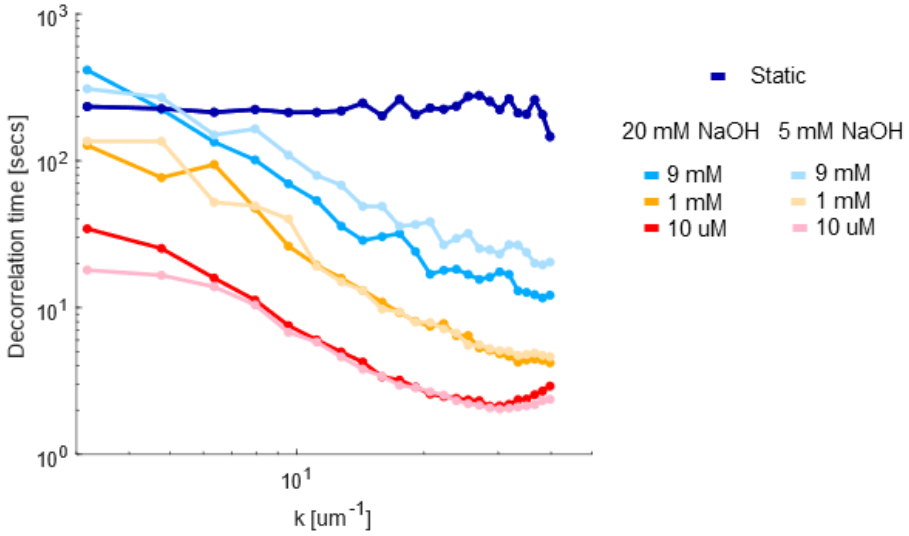

Figure 5.20. Stiffness dependence of the scaling of network decorrelation time over spatial scales.

5.4. Conclusions

Together, these results combine different experimental and modelling approaches to investigate the properties of PA nanostructures from the Angstrom scale organization of molecules in the nanostructures to the microscale dynamics of the nanofiber solutions. Although the PA nanostructures are not highly ordered crystals, the lattice structure as well as coarse grained distribution of the electron density distribution within the unit cell have been identified, which suggests that the molecules area tilted in the plane of the nanoribbons parallel to the β-sheet. Without this complete analysis using electron diffraction and simulations, the peak assignments in the x-ray diffraction pattern would be incorrect. The low coherence in the assemblies is also seen at the micron scale, where sharp kinks in the nanofiber trajectories results in tangent correlation functions with anomalous compressed exponential behaviour. However, the measurements confirm that PA behave as semi-flexible fibers at length scales above a few microns. The interactions of nanofibers create glassy networks in solution, with sub-diffusive dynamics at long time scales, similar to biopolymers such as actin and collagen.

5.5. Materials and Methods

X-ray scattering

X-ray scattering experiments were performed at Beamline 5-ID-D, DND-CAT, Advanced Photon Source at the Argonne National Laboratory. The solution samples were placed in a vacuum flow cell comprising of a 1.5mm quartz capillary connected to a syringe pump. An X-ray energy of 17 keV was selected using a double monochromator, and the scattering patterns for an empty capillary, water-filled capillary and sample-filled capillary were recorded using a set of three charge coupled device (CCD) detectors.[132] The two-dimensional scattering patterns then

azimuthally integrated to generate a scattering vector magnitude q vs. intensity plot, where q is defined as $q=4\pi\sin(\theta)/\lambda$ for which θ denotes the half of total scattering angle and λ the X-ray wavelength, 0.7293 Å. 2D to 1D data reduction was performed by GSAS-II software.[133] No attempt was made to determine the absolute scattering intensity.

Selected area electron diffraction (SAED)

For SAED acquisition, dried TEM samples with a high density of aligned nanostructures were produced by applying 5 uL of the 10 mM samples on glow-discharged carbon coated TEM grids, followed by wicking with a filter paper from a corner of the grid and subsequently drying the grid. The JEOL ARM300F was used with the emission current reduced to 5 uA, and the sample was searched in diffraction mode with a selected area aperture inserted to identify and quickly obtain the fiber diffraction patterns. The sample was then imaged in bright field mode to confirm the correspondence between the diffraction pattern and the real space images.

Atomic Force Microscopy (AFM)

Sample solutions were diluted 10X in 150 mM NaCl and deposited on freshly cleaved mica surfaces for ~1 min, and the excess solution was rinsed with 150 mM NaCl. The samples were then rinsed with 150 mM NaCl 20 mM $CaCl_2$ to immobilize the nanostructures on the mica surface, and measurements were performed in the liquid environment. AFM images were captured in PeakForce tapping mode on a Dimension Icon AFM (Bruker) with a silicon nitride cantilever (SNL10-A, Bruker) in a liquid cell. Images were flattened to correct sample tilt before analysis. Tangent correlation functions were measured by tracking fiber trajectories from large images (20x20 um) using the FiberApp plugin.[86]

Dynamic Light Scattering (DLS)

DLS Measurements were performed on a Malvern Zetasizer Nano ZSP light scattering spectrometer. The PA solution was diluted to 50 uM in milliQ water and measured for 10 seconds at 173o backscatter mode. Measurements were averaged over 5 runs. Default automatic settings were used of the attenuator.

Confocal Laser Scanning Microscopy (CLSM)

Fluorescence microscopy of PA nanofiber solutions was performed on a Nikon-A1R confocal microscope. 20 uL droplets of PA solutions were deposited on glass bottom petri-dishes, and the images were captured with a 20X air objective (Nikon), using the resonant scanner for video rate imaging. Image series analysis was performed using custom written Matlab codes, and a modified version of the FiberApp software.

6. Summary and Future Directions

Together, these studies demonstrate the importance of designed intermolecular interactions in formation of peptide based biomimetic nanomaterials. This work investigated the organization of supramolecular materials from the sub-nanometer scale of molecular packing up to the microscopic scale of cellular scaffolds. Intermolecular complementarity of hydrogen bonding was manipulated to create multi-component systems with sequestered bioactive groups. This thesis lays the groundwork for future investigations of supramolecular biomaterials across length scales.

6.1. Fundamental principles of peptide amphiphile self-assembly

The relation between the amino acid sequence and the morphology of peptide nanostructures developed in chapter 2 demonstrates the role of supramolecular twisting in the self-assembly process. The role of headgroup charge repulsion was also studied, and it was shown that as charge is increased the structures first transition into long cylinders and then into short fragments or micelles. The supramolecular twist of the ribbons also changes chirality based on the peptide sequence in the molecules, which is intrinsically linked to the morphology of the structures. While the peptide sequences used in this work were relatively simple, consisting only of valines and alanines, there is a large number of interesting sequences that can be explored. The larger size of the valine side chain is clearly an important factor in determining the morphology of the nanostructures as it increases the spacing between β-sheet stacking and modifies the peptide twist. This can be extended to investigate larger side hydrophobic side chains such as leucine and isoleucine. In addition, including amino acids with polar uncharged side chains such as serine in the peptide sequence may lead to new fundamental insights into the self-assembly process.

The discovery of a new nanostructure in chapter 3, a double helix with major and minor grooves, illustrates the complexity of PA self-assembly that remains to be explored. While hierarchical PA superstructures have been created using designed interactions between fibers,[65,66] this work demonstrates the emergence of complex structures from fundamental intermolecular forces and simple building blocks. Different self-assembly pathways, in this case the charge state of the molecules during assembly, can control the morphology of the nanostructures. Other pathway parameters of interest that can be investigated include the ionic strength of the solutions, the temperature, concentration, and pressure. The role counterions in particular would be of significant interest, as recent work has shown that charge screening by counterions can modify the curvature and twist of PA assemblies.[108]

In the course of these studies, a significant improvement in the quality of nanoscale imaging was developed which allowed access to these new structures. Improvement in high resolution atomic force microscopy (AFM) in a liquid environment was crucial to measure the supramolecular chirality of the nanostructures. While the same molecules have been studied by the Stupp group in the past, the nanostructures were characterized primarily by transmission electron microscopy (TEM) methods, where information about chirality is lost as there is no in-plane mirror symmetry when electrons pass through the entire nanostructure. The relation between peptide sequence and nanostructure morphology found in chapter 2 can only be understood if the supramolecular chirality is included. This raises the possibility that other PAs studied by the Stupp have similar changes in chirality which have gone unnoticed, but may be essential to understanding the self-assembly.

6.2. Multicomponent PA systems

Chapter 4 reports on multicomponent mixtures of different PAs, which were found to self-sort into different populations when the β-sheet twist orientation did not match between molecules. Including a biotin group on one of the two components resulted in sequestration of the biotinylated PA into one of the self-sorted components, and this was used to demonstrate selective binding of a model protein. The imaging methods developed in this work, especially single nanofiber fluorescence microscopy, holds great promise for further investigation of multicomponent systems. This imaging method enabled direct observation of the locations of specific molecules in the system, and when combined with correlative AFM, provided information about the nanostructure as well. Although different PAs are often mixed together in biological studies, the self-sorting or co-assembly of different PAs is a largely unexplored area. It is presumed that the PAs co-assemble when they have the same internal peptide sequence, but this effect can now be tested directly. This approach can also be extended to study the binding of proteins or peptides to PA nanofibers, an active area of research in the Stupp lab.

The sequestration of bioactive groups in interpenetrating networks can be used to create better ECM mimetics. Different signalling epitopes and protein binding groups could be added to the different network components. For example, separating a BMP2 binding sequence on one component and a TGFβ1 binding sequence on the other may lead to improved osteogenic effects as both BMP2 and TGFβ1 work through similar pathways,[194,195] and separating the signals spatially may prevent interference. Alternatively, a cell adhesion promoting sequence like RGD could be sequestered on one component, while the other binds and presents a growth factor like BMP2.

6.3. Physical and biological properties of PA materials

Chapter 5, as well as the second half of chapter 2, explores the properties of PA nanomaterials across length scales. The molecular packing of PAs within assemblies was found to create a near rectangular lattice with tilted molecules. The model developed to derive the structure from x-ray and electron diffraction pattern is applicable to PA nanofibers more generally, and can be used to investigate the packing and orientation of many PAs studied in the Stupp group. The persistence length of the PA nanofibers, a measure of their bending stiffness, was shown to increase when the charge repulsion between molecules is reduced. This effect will be of interest to the study of charged bioactive PAs such as those presenting IKVAV epitopes. The change in persistence length also modified the properties of nanofiber networks, both in solution and on coatings. Solutions of PA nanofibers exhibit concentration dependent glassy dynamics similar to biopolymers. Further studies can use this approach to investigate the interaction of PA nanofibers with proteins or crosslinking agents.

When used as 2D scaffolds, PA nanofiber networks were found to be deformed and degraded by fibroblasts. The change in the scaffold microarchitecture was directly observed using fluorescence microscopy. Networks composed of flexible fibers were primarily deformed by cells, while networks composed of rigid fibers were primarily broken and degraded. This is likely due to an increase in fiber entanglement in the flexible nanofiber networks. The degradation of the PA coatings was accompanied by internalization of the PA nanostructures by cells. Experiments on phospholipid bilayers suggest that the biophysical interactions of PAs with lipid amphiphiles can lead to disintegration of the nanostructures. However, PA nanofibers may also be degraded by MMPs excreted by cells, and the role of MMPs in PA degradation is currently unknown and

represents a rich area to be explored. Understanding the various mechanisms of PA degradation may be essential for applications where PAs are implanted in vivo. In addition, the Stupp lab has published several studies in variety of cell types showing significant cell-material interactions on PA scaffolds - such as adhesion, migration, and mechanostransduction - in systems where there no adhesion epitopes like RGD or IKVAV.[64,65,69,134] This raises the question of how focal adhesions on cells bind to the PA scaffold and transmit traction forces. This adhesion likely occurs due to non-specific binding of PA nanofibers to an excreted ECM component like fibronectin, but may also involve the cell glycocalyx, or regions of the cell membrane with different lipid or cholesterol composition. An extensive study of the mechanism of cell-PA attachment, in the absence of adhesion promoting sequences, is required to understand this effect.

References

(1) Elemans, J. A. A. W.; Rowan, A. E.; Nolte, R. J. M. Mastering Molecular Matter. Supramolecular Architectures by Hierarchical Self-Assembly. In *Journal of Materials Chemistry*; 2003. https://doi.org/10.1039/b304972h.

(2) Mendes, A. C.; Baran, E. T.; Reis, R. L.; Azevedo, H. S. Self-Assembly in Nature: Using the Principles of Nature to Create Complex Nanobiomaterials. *Wiley Interdiscip. Rev. Nanomedicine Nanobiotechnology* **2013**. https://doi.org/10.1002/wnan.1238.

(3) Cademartiri, L.; Bishop, K. J. M. Programmable Self-Assembly. *Nature Materials*. 2015. https://doi.org/10.1038/nmat4184.

(4) Fletcher, D. A.; Mullins, R. D. Cell Mechanics and the Cytoskeleton. *Nature*. 2010. https://doi.org/10.1038/nature08908.

(5) Huber, F.; Schnauß, J.; Rönicke, S.; Rauch, P.; Müller, K.; Fütterer, C.; Käs, J. Emergent Complexity of the Cytoskeleton: From Single Filaments to Tissue. *Advances in Physics*. 2013. https://doi.org/10.1080/00018732.2013.771509.

(6) Dominguez, R.; Holmes, K. C. Actin Structure and Function. *Annu. Rev. Biophys.* **2011**. https://doi.org/10.1146/annurev-biophys-042910-155359.

(7) Brouhard, G. J.; Rice, L. M. Microtubule Dynamics: An Interplay of Biochemistry and Mechanics. *Nature Reviews Molecular Cell Biology*. 2018. https://doi.org/10.1038/s41580-018-0009-y.

(8) Dogterom, M.; Koenderink, G. H. Actin–Microtubule Crosstalk in Cell Biology. *Nature Reviews Molecular Cell Biology*. 2019. https://doi.org/10.1038/s41580-018-0067-1.

(9) Preciado López, M.; Huber, F.; Grigoriev, I.; Steinmetz, M. O.; Akhmanova, A.; Dogterom, M.; Koenderink, G. H. In Vitro Reconstitution of Dynamic Microtubules Interacting with Actin Filament Networks. In *Methods in Enzymology*; 2014. https://doi.org/10.1016/B978-0-12-397924-7.00017-0.

(10) Monastyrska, I.; Rieter, E.; Klionsky, D. J.; Reggiori, F. Multiple Roles of the Cytoskeleton in Autophagy. *Biological Reviews*. 2009. https://doi.org/10.1111/j.1469-185X.2009.00082.x.

(11) Mouw, J. K.; Ou, G.; Weaver, V. M. Extracellular Matrix Assembly: A Multiscale Deconstruction. *Nature Reviews Molecular Cell Biology*. 2014. https://doi.org/10.1038/nrm3902.

(12) Humphrey, J. D.; Dufresne, E. R.; Schwartz, M. A. Mechanotransduction and Extracellular Matrix Homeostasis. *Nature Reviews Molecular Cell Biology*. 2014. https://doi.org/10.1038/nrm3896.

(13) Ricard-Blum, S. The Collagen Family. *Cold Spring Harb. Perspect. Biol.* **2011**. https://doi.org/10.1101/cshperspect.a004978.

(14) Shoulders, M. D.; Raines, R. T. Collagen Structure and Stability. *Annual Review of*

Biochemistry. 2009. https://doi.org/10.1146/annurev.biochem.77.032207.120833.

(15) Khoshnoodi, J.; Pedchenko, V.; Hudson, B. G. Mammalian Collagen IV. *Microscopy Research and Technique*. 2008. https://doi.org/10.1002/jemt.20564.

(16) Janson, I. A.; Putnam, A. J. Extracellular Matrix Elasticity and Topography: Material-Based Cues That Affect Cell Function via Conserved Mechanisms. *Journal of Biomedical Materials Research - Part A*. 2015. https://doi.org/10.1002/jbm.a.35254.

(17) Kubow, K. E.; Vukmirovic, R.; Zhe, L.; Klotzsch, E.; Smith, M. L.; Gourdon, D.; Luna, S.; Vogel, V. Mechanical Forces Regulate the Interactions of Fibronectin and Collagen i in Extracellular Matrix. *Nat. Commun.* **2015**. https://doi.org/10.1038/ncomms9026.

(18) Nishi, N.; Matsushita, O.; Yuube, K.; Miyanaka, H.; Okabe, A.; Wada, F. Collagen-Binding Growth Factors: Production and Characterization of Functional Fusion Proteins Having a Collagen-Binding Domain. *Proc. Natl. Acad. Sci. U. S. A.* **1998**. https://doi.org/10.1073/pnas.95.12.7018.

(19) Schultz, G. S.; Wysocki, A. Interactions between Extracellular Matrix and Growth Factors in Wound Healing. *Wound Repair and Regeneration*. 2009. https://doi.org/10.1111/j.1524-475X.2009.00466.x.

(20) Wegst, U. G. K.; Bai, H.; Saiz, E.; Tomsia, A. P.; Ritchie, R. O. Bioinspired Structural Materials. *Nat. Mater.* **2015**. https://doi.org/10.1038/nmat4089.

(21) CLERK-MAXWELL, J. O Ver de Continuiteit van Den Gas- En Vloeistofiocstand Academisch Proefschrift. *Nature* **1874**. https://doi.org/10.1038/010477a0.

(22) Latimer, W. M.; Rodebush, W. H. Polarity and Ionization from the Standpoint of the Lewis Theory of Valence. *J. Am. Chem. Soc.* **1920**. https://doi.org/10.1021/ja01452a015.

(23) Franklin, R. E.; Gosling, R. G. The Structure of Sodium Thymonucleate Fibres. I. The Influence of Water Content. *Acta Crystallogr.* **1953**. https://doi.org/10.1107/s0365110x53001939.

(24) Watson, J. D.; Crick, F. H. C. Molecular Structure of Nucleic Acids: A Structure for Deoxyribose Nucleic Acid. *Nature* **1953**. https://doi.org/10.1038/171737a0.

(25) Lehn, J. M. Cryptates: The Chemistry of Macropolycyclic Inclusion Complexes. *Acc. Chem. Res.* **1978**. https://doi.org/10.1021/ar50122a001.

(26) Israelachvili, J. *Intermolecular and Surface Forces*; 2011. https://doi.org/10.1016/C2009-0-21560-1.

(27) Chandler, D. Interfaces and the Driving Force of Hydrophobic Assembly. *Nature*. 2005. https://doi.org/10.1038/nature04162.

(28) Harayama, T.; Riezman, H. Understanding the Diversity of Membrane Lipid Composition. *Nature Reviews Molecular Cell Biology*. 2018. https://doi.org/10.1038/nrm.2017.138.

(29) Israelachvili, J. N.; Mitchell, D. J.; Ninham, B. W. Theory of Self-Assembly of Hydrocarbon Amphiphiles into Micelles and Bilayers. *Journal of the Chemical Society,*

Faraday Transactions 2: Molecular and Chemical Physics. 1976. https://doi.org/10.1039/F29767201525.

(30) Helfrich, W. Elastic Properties of Lipid Bilayers: Theory and Possible Experiments. *Zeitschrift fur Naturforsch. - Sect. C J. Biosci.* **1973**. https://doi.org/10.1515/znc-1973-11-1209.

(31) Helfrich, W.; Prost, J. Intrinsic Bending Force in Anisotropic Membranes Made of Chiral Molecules. *Phys. Rev. A* **1988**. https://doi.org/10.1103/PhysRevA.38.3065.

(32) Selinger, J. V.; Schnur, J. M. Theory of Chiral Lipid Tubules. *Phys. Rev. Lett.* **1993**. https://doi.org/10.1103/PhysRevLett.71.4091.

(33) Lombardo, D.; Kiselev, M. A.; Magazù, S.; Calandra, P. Amphiphiles Self-Assembly: Basic Concepts and Future Perspectives of Supramolecular Approaches. *Advances in Condensed Matter Physics*. 2015. https://doi.org/10.1155/2015/151683.

(34) Selinger, R. L. B.; Selinger, J. V.; Malanoski, A. P.; Schnur, J. M. Shape Selection in Chiral Self-Assembly. *Phys. Rev. Lett.* **2004**. https://doi.org/10.1103/PhysRevLett.93.158103.

(35) Armon, S.; Efrati, E.; Kupferman, R.; Sharon, E. Geometry and Mechanics in the Opening of Chiral Seed Pods. *Science (80-.).* **2011**. https://doi.org/10.1126/science.1203874.

(36) Armon, S.; Aharoni, H.; Moshe, M.; Sharon, E. Shape Selection in Chiral Ribbons: From Seed Pods to Supramolecular Assemblies. *Soft Matter* **2014**. https://doi.org/10.1039/c3sm52313f.

(37) Zhang, M.; Grossman, D.; Danino, D.; Sharon, E. Shape and Fluctuations of Frustrated Self-Assembled Nano Ribbons. *Nat. Commun.* **2019**. https://doi.org/10.1038/s41467-019-11473-6.

(38) Dill, K. A.; MacCallum, J. L. The Protein-Folding Problem, 50 Years On. *Science*. 2012. https://doi.org/10.1126/science.1219021.

(39) Cheng, P. N.; Pham, J. D.; Nowick, J. S. The Supramolecular Chemistry of β-Sheets. *Journal of the American Chemical Society*. 2013. https://doi.org/10.1021/ja3088407.

(40) Chothia, C. Conformation of Twisted β-Pleated Sheets in Proteins. *J. Mol. Biol.* **1973**. https://doi.org/10.1016/0022-2836(73)90022-3.

(41) Weatherford, D. W.; Salemme, F. R. Conformations of Twisted Parallel Beta-Sheets and the Origin of Chirality in Protein Structures. *Proc. Natl. Acad. Sci. U. S. A.* **1979**. https://doi.org/10.1073/pnas.76.1.19.

(42) Ho, B. K.; Curmi, P. M. G. Twist and Shear in β-Sheets and β-Ribbons. *J. Mol. Biol.* **2002**. https://doi.org/10.1006/jmbi.2001.5385.

(43) Liberta, F.; Loerch, S.; Rennegarbe, M.; Schierhorn, A.; Westermark, P.; Westermark, G. T.; Hazenberg, B. P. C.; Grigorieff, N.; Fändrich, M.; Schmidt, M. Cryo-EM Fibril Structures from Systemic AA Amyloidosis Reveal the Species Complementarity of Pathological Amyloids. *Nat. Commun.* **2019**. https://doi.org/10.1038/s41467-019-09033-z.

(44) Kollmer, M.; Close, W.; Funk, L.; Rasmussen, J.; Bsoul, A.; Schierhorn, A.; Schmidt, M.; Sigurdson, C. J.; Jucker, M.; Fändrich, M. Cryo-EM Structure and Polymorphism of Aβ Amyloid Fibrils Purified from Alzheimer's Brain Tissue. *Nat. Commun.* **2019**. https://doi.org/10.1038/s41467-019-12683-8.

(45) Levin, A.; Hakala, T. A.; Schnaider, L.; Bernardes, G. J. L.; Gazit, E.; Knowles, T. P. J. Biomimetic Peptide Self-Assembly for Functional Materials. *Nat. Rev. Chem.* **2020**, *45* (Supplement), S-102. https://doi.org/10.1038/s41570-020-0215-y.

(46) Iadanza, M. G.; Jackson, M. P.; Hewitt, E. W.; Ranson, N. A.; Radford, S. E. A New Era for Understanding Amyloid Structures and Disease. *Nature Reviews Molecular Cell Biology*. 2018. https://doi.org/10.1038/s41580-018-0060-8.

(47) Yarger, J. L.; Cherry, B. R.; Van Der Vaart, A. Uncovering the Structure-Function Relationship in Spider Silk. *Nature Reviews Materials*. 2018. https://doi.org/10.1038/natrevmats2018.8.

(48) Webber, M. J.; Appel, E. A.; Meijer, E. W.; Langer, R. Supramolecular Biomaterials. *Nature Materials*. 2015. https://doi.org/10.1038/nmat4474.

(49) Berndt, P.; Fields, G. B.; Tirrell, M. Synthetic Lipidation of Peptides and Amino Acids: Monolayer Structure and Properties. *J. Am. Chem. Soc.* **1995**. https://doi.org/10.1021/ja00142a019.

(50) Hartgerink, J. D.; Beniash, E.; Stupp, S. I. Self-Assembly and Mineralization of Peptide-Amphiphile Nanofibers. *Science (80-.).* **2001**. https://doi.org/10.1126/science.1063187.

(51) Hendricks, M. P.; Sato, K.; Palmer, L. C.; Stupp, S. I. Supramolecular Assembly of Peptide Amphiphiles. *Acc. Chem. Res.* **2017**. https://doi.org/10.1021/acs.accounts.7b00297.

(52) Tantakitti, F.; Boekhoven, J.; Wang, X.; Kazantsev, R. V.; Yu, T.; Li, J.; Zhuang, E.; Zandi, R.; Ortony, J. H.; Newcomb, C. J.; Palmer, L. C.; Shekhawat, G. S.; De La Cruz, M. O.; Schatz, G. C.; Stupp, S. I. Energy Landscapes and Functions of Supramolecular Systems. *Nat. Mater.* **2016**. https://doi.org/10.1038/nmat4538.

(53) Pashuck, E. T.; Cui, H.; Stupp, S. I. Tuning Supramolecular Rigidity of Peptide Fibers through Molecular Structure. *J. Am. Chem. Soc.* **2010**. https://doi.org/10.1021/ja908560n.

(54) Cui, H.; Muraoka, T.; Cheetham, A. G.; Stupp, S. I. Self-Assembly of Giant Peptide Nanobelts. *Nano Lett.* **2009**. https://doi.org/10.1021/nl802813f.

(55) Lai, C. T.; Rosi, N. L.; Schatz, G. C. All-Atom Molecular Dynamics Simulations of Peptide Amphiphile Assemblies That Spontaneously Form Twisted and Helical Ribbon Structures. *J. Phys. Chem. Lett.* **2017**. https://doi.org/10.1021/acs.jpclett.7b00745.

(56) Sato, K.; Hendricks, M. P.; Palmer, L. C.; Stupp, S. I. Peptide Supramolecular Materials for Therapeutics. *Chemical Society Reviews*. 2018. https://doi.org/10.1039/c7cs00735c.

(57) Stawikowski, M.; Fields, G. B. Introduction to Peptide Synthesis. *Curr. Protoc. Protein Sci.* **2012**. https://doi.org/10.1002/0471140864.ps1801s69.

(58) Acar, H.; Srivastava, S.; Chung, E. J.; Schnorenberg, M. R.; Barrett, J. C.; LaBelle, J. L.;

Tirrell, M. Self-Assembling Peptide-Based Building Blocks in Medical Applications. *Advanced Drug Delivery Reviews*. 2017. https://doi.org/10.1016/j.addr.2016.08.006.

(59) Missirlis, D.; Krogstad, D. V.; Tirrell, M. Internalization of P5314-29 Peptide Amphiphiles and Subsequent Endosomal Disruption Results in SJSA-1 Cell Death. *Mol. Pharm.* **2010**. https://doi.org/10.1021/mp100193h.

(60) Missirlis, D.; Teesalu, T.; Black, M.; Tirrell, M. The Non-Peptidic Part Determines the Internalization Mechanism and Intracellular Trafficking of Peptide Amphiphiles. *PLoS One* **2013**. https://doi.org/10.1371/journal.pone.0054611.

(61) Chin, S. Control of Hierarchical Order and Development of Stimuli-Responsive Self-Assembled Materials Across Multiple Length Scales, Northwestern Unviersity, 2019.

(62) Korevaar, P. A.; Newcomb, C. J.; Meijer, E. W.; Stupp, S. I. Pathway Selection in Peptide Amphiphile Assembly. *J. Am. Chem. Soc.* **2014**. https://doi.org/10.1021/ja503882s.

(63) Zhang, S.; Greenfield, M. A.; Mata, A.; Palmer, L. C.; Bitton, R.; Mantei, J. R.; Aparicio, C.; De La Cruz, M. O.; Stupp, S. I. A Self-Assembly Pathway to Aligned Monodomain Gels. *Nat. Mater.* **2010**. https://doi.org/10.1038/nmat2778.

(64) Sleep, E.; Cosgrove, B. D.; McClendon, M. T.; Preslar, A. T.; Chen, C. H.; Sangji, M. H.; Pérez, C. M. R.; Haynes, R. D.; Meade, T. J.; Blau, H. M.; Stupp, S. I. Injectable Biomimetic Liquid Crystalline Scaffolds Enhance Muscle Stem Cell Transplantation. *Proc. Natl. Acad. Sci. U. S. A.* **2017**. https://doi.org/10.1073/pnas.1708142114.

(65) Freeman, R.; Han, M.; Álvarez, Z.; Lewis, J. A.; Wester, J. R.; Stephanopoulos, N.; McClendon, M. T.; Lynsky, C.; Godbe, J. M.; Sangji, H.; Luijten, E.; Stupp, S. I. Reversible Self-Assembly of Superstructured Networks. *Science (80-.).* **2018**. https://doi.org/10.1126/science.aat6141.

(66) Redondo-Gómez, C.; Abdouni, Y.; Becer, C. R.; Mata, A. Self-Assembling Hydrogels Based on a Complementary Host-Guest Peptide Amphiphile Pair. *Biomacromolecules* **2019**. https://doi.org/10.1021/acs.biomac.9b00224.

(67) Webber, M. J.; Tongers, J.; Renault, M. A.; Roncalli, J. G.; Losordo, D. W.; Stupp, S. I. Development of Bioactive Peptide Amphiphiles for Therapeutic Cell Delivery. *Acta Biomater.* **2010**. https://doi.org/10.1016/j.actbio.2009.07.031.

(68) Silva, G. A.; Czeisler, C.; Niece, K. L.; Beniash, E.; Harrington, D. A.; Kessler, J. A.; Stupp, S. I. Selective Differentiation of Neural Progenitor Cells by High-Epitope Density Nanofibers. *Science (80-.).* **2004**. https://doi.org/10.1126/science.1093783.

(69) Edelbrock, A. N.; Àlvarez, Z.; Simkin, D.; Fyrner, T.; Chin, S. M.; Sato, K.; Kiskinis, E.; Stupp, S. I. Supramolecular Nanostructure Activates TrkB Receptor Signaling of Neuronal Cells by Mimicking Brain-Derived Neurotrophic Factor. *Nano Lett.* **2018**. https://doi.org/10.1021/acs.nanolett.8b02317.

(70) Rubert Pérez, C. M.; Álvarez, Z.; Chen, F.; Aytun, T.; Stupp, S. I. Mimicking the Bioactivity of Fibroblast Growth Factor-2 Using Supramolecular Nanoribbons. *ACS Biomater. Sci. Eng.* **2017**. https://doi.org/10.1021/acsbiomaterials.7b00347.

(71) Berns, E. J.; Álvarez, Z.; Goldberger, J. E.; Boekhoven, J.; Kessler, J. A.; Kuhn, H. G.; Stupp, S. I. A Tenascin-C Mimetic Peptide Amphiphile Nanofiber Gel Promotes Neurite Outgrowth and Cell Migration of Neurosphere-Derived Cells. *Acta Biomater.* **2016**. https://doi.org/10.1016/j.actbio.2016.04.010.

(72) Lee, S. S.; Huang, B. J.; Kaltz, S. R.; Sur, S.; Newcomb, C. J.; Stock, S. R.; Shah, R. N.; Stupp, S. I. Bone Regeneration with Low Dose BMP-2 Amplified by Biomimetic Supramolecular Nanofibers within Collagen Scaffolds. *Biomaterials* **2013**. https://doi.org/10.1016/j.biomaterials.2012.10.005.

(73) Shah, R. N.; Shah, N. A.; Lim, M. M. D. R.; Hsieh, C.; Nuber, G.; Stupp, S. I. Supramolecular Design of Self-Assembling Nanofibers for Cartilage Regeneration. *Proc. Natl. Acad. Sci. U. S. A.* **2010**. https://doi.org/10.1073/pnas.0906501107.

(74) Moyer, T. J.; Kassam, H. A.; Bahnson, E. S. M.; Morgan, C. E.; Tantakitti, F.; Chew, T. L.; Kibbe, M. R.; Stupp, S. I. Shape-Dependent Targeting of Injured Blood Vessels by Peptide Amphiphile Supramolecular Nanostructures. *Small* **2015**. https://doi.org/10.1002/smll.201403429.

(75) Sweeney, S. M.; Guy, C. A.; Fields, G. B.; San Antonio, J. D. Defining the Domains of Type I Collagen Involved in Heparin-Binding and Endothelial Tube Formation. *Proc. Natl. Acad. Sci. U. S. A.* **1998**. https://doi.org/10.1073/pnas.95.13.7275.

(76) Aumailley, M. The Laminin Family. *Cell Adhesion and Migration*. 2013. https://doi.org/10.4161/cam.22826.

(77) Safont-Sempere, M. M.; Fernández, G.; Würthner, F. Self-Sorting Phenomena in Complex Supramolecular Systems. *Chemical Reviews*. 2011. https://doi.org/10.1021/cr100357h.

(78) Shigemitsu, H.; Fujisaku, T.; Tanaka, W.; Kubota, R.; Minami, S.; Urayama, K.; Hamachi, I. An Adaptive Supramolecular Hydrogel Comprising Self-Sorting Double Nanofibre Networks. *Nat. Nanotechnol.* **2018**. https://doi.org/10.1038/s41565-017-0026-6.

(79) Kramer, R.; Lehn, J. M.; Marquis-Rigault, A. Self-Recognition in Helicate Self-Assembly: Spontaneous Formation of Helical Metal Complexes from Mixtures of Ligands and Metal Ions. *Proc. Natl. Acad. Sci. U. S. A.* **1993**. https://doi.org/10.1073/pnas.90.12.5394.

(80) Kreger, S. T.; Voytik-Harbin, S. L. Hyaluronan Concentration within a 3D Collagen Matrix Modulates Matrix Viscoelasticity, but Not Fibroblast Response. *Matrix Biol.* **2009**. https://doi.org/10.1016/j.matbio.2009.05.001.

(81) Ou, K. L.; Hosseinkhani, H. Development of 3D in Vitro Technology for Medical Applications. *International Journal of Molecular Sciences*. 2014. https://doi.org/10.3390/ijms151017938.

(82) Broedersz, C. P.; Mackintosh, F. C. Modeling Semiflexible Polymer Networks. *Rev. Mod. Phys.* **2014**. https://doi.org/10.1103/RevModPhys.86.995.

(83) Gittes, F.; Mickey, B.; Nettleton, J.; Howard, J. Flexural Rigidity of Microtubules and Actin Filaments Measured from Thermal Fluctuations in Shape. *J. Cell Biol.* **1993**. https://doi.org/10.1083/jcb.120.4.923.

(84) Adamcik, J.; Jung, J. M.; Flakowski, J.; De Los Rios, P.; Dietler, G.; Mezzenga, R. Understanding Amyloid Aggregation by Statistical Analysis of Atomic Force Microscopy Images. *Nat. Nanotechnol.* **2010**. https://doi.org/10.1038/nnano.2010.59.

(85) Dadonaite, B.; Vijayakrishnan, S.; Fodor, E.; Bhella, D.; Hutchinson, E. C. Filamentous Influenza Viruses. *Journal of General Virology*. 2016. https://doi.org/10.1099/jgv.0.000535.

(86) Usov, I.; Mezzenga, R. FiberApp: An Open-Source Software for Tracking and Analyzing Polymers, Filaments, Biomacromolecules, and Fibrous Objects. *Macromolecules* **2015**. https://doi.org/10.1021/ma502264c.

(87) Kroy, K. Dynamics of Wormlike and Glassy Wormlike Chains. *Soft Matter* **2008**. https://doi.org/10.1039/b807018k.

(88) Kroy, K.; Glaser, J. The Glassy Wormlike Chain. *New J. Phys.* **2007**. https://doi.org/10.1088/1367-2630/9/11/416.

(89) Stein, A. M.; Vader, D. A.; Weitz, D. A.; Sander, L. M. The Micromechanics of Three-Dimensional Collagen-I Gels. *Complexity* **2011**. https://doi.org/10.1002/cplx.20332.

(90) Nam, S.; Hu, K. H.; Butte, M. J.; Chaudhuri, O. Strain-Enhanced Stress Relaxation Impacts Nonlinear Elasticity in Collagen Gels. *Proc. Natl. Acad. Sci. U. S. A.* **2016**. https://doi.org/10.1073/pnas.1523906113.

(91) Engler, A. J.; Sen, S.; Sweeney, H. L.; Discher, D. E. Matrix Elasticity Directs Stem Cell Lineage Specification. *Cell* **2006**. https://doi.org/10.1016/j.cell.2006.06.044.

(92) Discher, D. E.; Janmey, P.; Wang, Y. L. Tissue Cells Feel and Respond to the Stiffness of Their Substrate. *Science*. 2005. https://doi.org/10.1126/science.1116995.

(93) Panzetta, V.; Fusco, S.; Netti, P. A. Cell Mechanosensing Is Regulated by Substrate Strain Energy Rather than Stiffness. *Proc. Natl. Acad. Sci. U. S. A.* **2019**. https://doi.org/10.1073/pnas.1904660116.

(94) Yeh, Y. C.; Ling, J. Y.; Chen, W. C.; Lin, H. H.; Tang, M. J. Mechanotransduction of Matrix Stiffness in Regulation of Focal Adhesion Size and Number: Reciprocal Regulation of Caveolin-1 and B1 Integrin. *Sci. Rep.* **2017**. https://doi.org/10.1038/s41598-017-14932-6.

(95) Chaudhuri, O.; Gu, L.; Darnell, M.; Klumpers, D.; Bencherif, S. A.; Weaver, J. C.; Huebsch, N.; Mooney, D. J. Substrate Stress Relaxation Regulates Cell Spreading. *Nat. Commun.* **2015**. https://doi.org/10.1038/ncomms7365.

(96) Chaudhuri, O.; Gu, L.; Klumpers, D.; Darnell, M.; Bencherif, S. A.; Weaver, J. C.; Huebsch, N.; Lee, H. P.; Lippens, E.; Duda, G. N.; Mooney, D. J. Hydrogels with Tunable Stress Relaxation Regulate Stem Cell Fate and Activity. *Nat. Mater.* **2016**. https://doi.org/10.1038/nmat4489.

(97) Rosales, A. M.; Anseth, K. S. The Design of Reversible Hydrogels to Capture Extracellular Matrix Dynamics. *Nature Reviews Materials*. 2016. https://doi.org/10.1038/natrevmats.2015.12.

(98) Page-McCaw, A.; Ewald, A. J.; Werb, Z. Matrix Metalloproteinases and the Regulation of Tissue Remodelling. *Nature Reviews Molecular Cell Biology*. 2007. https://doi.org/10.1038/nrm2125.

(99) Han, Y. L.; Ronceray, P.; Xu, G.; Malandrino, A.; Kamm, R. D.; Lenz, M.; Broedersz, C. P.; Guo, M. Cell Contraction Induces Long-Ranged Stress Stiffening in the Extracellular Matrix. *Proc. Natl. Acad. Sci. U. S. A.* **2018**. https://doi.org/10.1073/pnas.1722619115.

(100) Bonnans, C.; Chou, J.; Werb, Z. Remodelling the Extracellular Matrix in Development and Disease. *Nature Reviews Molecular Cell Biology*. 2014. https://doi.org/10.1038/nrm3904.

(101) Madl, C. M.; Lesavage, B. L.; Dewi, R. E.; Dinh, C. B.; Stowers, R. S.; Khariton, M.; Lampe, K. J.; Nguyen, D.; Chaudhuri, O.; Enejder, A.; Heilshorn, S. C. Maintenance of Neural Progenitor Cell Stemness in 3D Hydrogels Requires Matrix Remodelling. *Nat. Mater.* **2017**. https://doi.org/10.1038/nmat5020.

(102) Trappmann, B.; Baker, B. M.; Polacheck, W. J.; Choi, C. K.; Burdick, J. A.; Chen, C. S. Matrix Degradability Controls Multicellularity of 3D Cell Migration. *Nat. Commun.* **2017**. https://doi.org/10.1038/s41467-017-00418-6.

(103) Loebel, C.; Mauck, R. L.; Burdick, J. A. Local Nascent Protein Deposition and Remodelling Guide Mesenchymal Stromal Cell Mechanosensing and Fate in Three-Dimensional Hydrogels. *Nat. Mater.* **2019**. https://doi.org/10.1038/s41563-019-0307-6.

(104) Radiom, M. Characterization of Single Polymer Molecules. In *Atomic-force Microscopy and Its Applications*; 2019. https://doi.org/10.5772/intechopen.77999.

(105) Sharma, S.; Grintsevich, E. E.; Phillips, M. L.; Reisler, E.; Gimzewski, J. K. Atomic Force Microscopy Reveals Drebrin Induced Remodeling of F-Actin with Subnanometer Resolution. *Nano Lett.* **2011**. https://doi.org/10.1021/nl104159v.

(106) JPK instruments. *Collagen: Levels of Structure and Alignment*.

(107) Sis, M. J.; Webber, M. J. Drug Delivery with Designed Peptide Assemblies. *Trends in Pharmacological Sciences*. 2019. https://doi.org/10.1016/j.tips.2019.08.003.

(108) Gao, C.; Kewalramani, S.; Valencia, D. M.; Li, H.; McCourt, J. M.; De La Cruz, M. O.; Bedzyk, M. J. Electrostatic Shape Control of a Charged Molecular Membrane from Ribbon to Scroll. *Proc. Natl. Acad. Sci. U. S. A.* **2019**. https://doi.org/10.1073/pnas.1913632116.

(109) Moyer, T. J.; Cui, H.; Stupp, S. I. Tuning Nanostructure Dimensions with Supramolecular Twisting. *J. Phys. Chem. B* **2013**. https://doi.org/10.1021/jp3087978.

(110) Gao, C.; Li, H.; Li, Y.; Kewalramani, S.; Palmer, L. C.; Dravid, V. P.; Stupp, S. I.; Olvera De La Cruz, M.; Bedzyk, M. J. Electrostatic Control of Polymorphism in Charged Amphiphile Assemblies. *J. Phys. Chem. B* **2017**. https://doi.org/10.1021/acs.jpcb.6b11602.

(111) Tsoras, A. N.; Champion, J. A. Protein and Peptide Biomaterials for Engineered Subunit Vaccines and Immunotherapeutic Applications. *Annual Review of Chemical and Biomolecular Engineering*. 2019. https://doi.org/10.1146/annurev-chembioeng-060718-030347.

(112) Moyer, T. J.; Finbloom, J. A.; Chen, F.; Toft, D. J.; Cryns, V. L.; Stupp, S. I. PH and Amphiphilic Structure Direct Supramolecular Behavior in Biofunctional Assemblies. *J. Am. Chem. Soc.* **2014**. https://doi.org/10.1021/ja5042429.

(113) Aggeli, A.; Nyrkova, I. A.; Bell, M.; Harding, R.; Carrick, L.; McLeish, T. C. B.; Semenov, A. N.; Boden, N. Hierarchical Self-Assembly of Chiral Rod-like Molecules as a Model for Peptide β-Sheet Tapes, Ribbons, Fibrils, and Fibers. *Proc. Natl. Acad. Sci. U. S. A.* **2001**. https://doi.org/10.1073/pnas.191250198.

(114) Nyrkova, I. A.; Semenov, A. N.; Aggeli, A.; Boden, N. Fibril Stability in Solutions of Twisted β-Sheet Peptides: A New Kind of Micellization in Chiral Systems. *Eur. Phys. J. B* **2000**. https://doi.org/10.1007/s100510070127.

(115) Rüter, A.; Kuczera, S.; Pochan, D. J.; Olsson, U. Twisted Ribbon Aggregates in a Model Peptide System. *Langmuir* **2019**. https://doi.org/10.1021/acs.langmuir.8b03886.

(116) Fishwick, C. W. G.; Beevers, A. J.; Carrick, L. M.; Whitehouse, C. D.; Aggeli, A.; Boden, N. Structures of Helical β-Tapes and Twisted Ribbons: The Role of Side-Chain Interactions on Twist and Bend Behavior. *Nano Lett.* **2003**. https://doi.org/10.1021/nl034095p.

(117) Adamcik, J.; Castelletto, V.; Bolisetty, S.; Hamley, I. W.; Mezzenga, R. Direct Observation of Time-Resolved Polymorphic States in the Self-Assembly of End-Capped Heptapeptides. *Angew. Chemie - Int. Ed.* **2011**. https://doi.org/10.1002/anie.201100807.

(118) Newcomb, C. J.; Moyer, T. J.; Lee, S. S.; Stupp, S. I. Advances in Cryogenic Transmission Electron Microscopy for the Characterization of Dynamic Self-Assembling Nanostructures. *Current Opinion in Colloid and Interface Science*. 2012. https://doi.org/10.1016/j.cocis.2012.09.004.

(119) Adamcik, J.; Mezzenga, R. Study of Amyloid Fibrils via Atomic Force Microscopy. *Current Opinion in Colloid and Interface Science*. 2012. https://doi.org/10.1016/j.cocis.2012.08.001.

(120) Manning, G. S. Counterion Condensation on Charged Spheres, Cylinders, and Planes. In *Journal of Physical Chemistry B*; 2007. https://doi.org/10.1021/jp0670844.

(121) Tanford, C. Theory of Micelle Formation in Aqueous Solutions. *J. Phys. Chem.* **1974**. https://doi.org/10.1021/j100617a012.

(122) Nagarajan, R. *Structure-Performance Relationships in Surfactants*; Esumi, K., Ueno, M., Eds.; CRC Press, 2003. https://doi.org/10.1201/9780203911518.

(123) Liu, M.; Zhang, L.; Wang, T. Supramolecular Chirality in Self-Assembled Systems. *Chemical Reviews*. 2015. https://doi.org/10.1021/cr500671p.

(124) Rubin, N.; Perugia, E.; Goldschmidt, M.; Fridkin, M.; Addadi, L. Chirality of Amyloid Suprastructures. *J. Am. Chem. Soc.* **2008**. https://doi.org/10.1021/ja800328y.

(125) Rubin, N.; Perugla, E.; Wolf, S. G.; Klein, E.; Mátl, F.; Addadi, L. Relation between Serum Amyloid A Truncated Peptides and Their Suprastructure Chirality. *J. Am. Chem. Soc.* **2010**. https://doi.org/10.1021/ja909345p.

(126) Reynolds, N. P.; Adamcik, J.; Berryman, J. T.; Handschin, S.; Zanjani, A. A. H.; Li, W.; Liu, K.; Zhang, A.; Mezzenga, R. Competition between Crystal and Fibril Formation in Molecular Mutations of Amyloidogenic Peptides. *Nat. Commun.* **2017**. https://doi.org/10.1038/s41467-017-01424-4.

(127) Kurouski, D.; Lombardi, R. A.; Dukor, R. K.; Lednev, I. K.; Nafie, L. A. Direct Observation and PH Control of Reversed Supramolecular Chirality in Insulin Fibrils by Vibrational Circular Dichroism. *Chem. Commun.* **2010**. https://doi.org/10.1039/c0cc02423f.

(128) Ting, D.; Wang, G.; Shapovalov, M.; Mitra, R.; Jordan, M. I.; Dunbrack, R. L. Neighbor-Dependent Ramachandran Probability Distributions of Amino Acids Developed from a Hierarchical Dirichlet Process Model. *PLoS Comput. Biol.* **2010**. https://doi.org/10.1371/journal.pcbi.1000763.

(129) Shapovalov, M. V.; Dunbrack, R. L. A Smoothed Backbone-Dependent Rotamer Library for Proteins Derived from Adaptive Kernel Density Estimates and Regressions. *Structure* **2011**. https://doi.org/10.1016/j.str.2011.03.019.

(130) Micsonai, A.; Wien, F.; Kernya, L.; Lee, Y. H.; Goto, Y.; Réfrégiers, M.; Kardos, J. Accurate Secondary Structure Prediction and Fold Recognition for Circular Dichroism Spectroscopy. *Proc. Natl. Acad. Sci. U. S. A.* **2015**. https://doi.org/10.1073/pnas.1500851112.

(131) Feigin, L. A.; Svergun, D. I. *Structure Analysis by Small-Angle X-Ray and Neutron Scattering*; 1987. https://doi.org/10.1007/978-1-4757-6624-0.

(132) Weigand, S. J.; Keane, D. T. DND-CATs New Triple Area Detector System for Simultaneous Data Collection at Multiple Length Scales. In *Nuclear Instruments and Methods in Physics Research, Section A: Accelerators, Spectrometers, Detectors and Associated Equipment*; 2011. https://doi.org/10.1016/j.nima.2010.12.045.

(133) Toby, B. H.; Von Dreele, R. B. GSAS-II: The Genesis of a Modern Open-Source All Purpose Crystallography Software Package. *J. Appl. Crystallogr.* **2013**, *46* (2), 544–549. https://doi.org/10.1107/S0021889813003531.

(134) Chen, C. H.; Palmer, L. C.; Stupp, S. I. Self-Repair of Structure and Bioactivity in a Supramolecular Nanostructure. *Nano Lett.* **2018**. https://doi.org/10.1021/acs.nanolett.8b02709.

(135) Selinger, J. V.; Spector, M. S.; Schnur, J. M. Theory of Self-Assembled Tubules and Helical Ribbons. *J. Phys. Chem. B* **2001**. https://doi.org/10.1021/jp010452d.

(136) Wei, G.; Su, Z.; Reynolds, N. P.; Arosio, P.; Hamley, I. W.; Gazit, E.; Mezzenga, R. Self-Assembling Peptide and Protein Amyloids: From Structure to Tailored Function in Nanotechnology. *Chemical Society Reviews*. 2017. https://doi.org/10.1039/c6cs00542j.

(137) Gremer, L.; Schölzel, D.; Schenk, C.; Reinartz, E.; Labahn, J.; Ravelli, R. B. G.; Tusche, M.; Lopez-Iglesias, C.; Hoyer, W.; Heise, H.; Willbold, D.; Schröder, G. F. Fibril Structure of Amyloid-β(1–42) by Cryo–Electron Microscopy. *Science (80-.).* **2017**. https://doi.org/10.1126/science.aao2825.

(138) Sachse, C.; Fändrich, M.; Grigorieff, N. Paired β-Sheet Structure of an Aβ(1-40) Amyloid Fibril Revealed by Electron Microscopy. *Proc. Natl. Acad. Sci. U. S. A.* **2008**. https://doi.org/10.1073/pnas.0712290105.

(139) Ferrari, A.; Hoerndli, F.; Baechi, T.; Nitsch, R. M.; Götz, J. β-Amyloid Induces Paired Helical Filament-like Tau Filaments in Tissue Culture. *J. Biol. Chem.* **2003**. https://doi.org/10.1074/jbc.M308243200.

(140) Mandelkow, E.; Von Bergen, M.; Biernat, J.; Mandelkow, E. M. Structural Principles of Tau and the Paired Helical Filaments of Alzheimer's Disease. In *Brain Pathology*; 2007. https://doi.org/10.1111/j.1750-3639.2007.00053.x.

(141) Fitzpatrick, A. W. P.; Falcon, B.; He, S.; Murzin, A. G.; Murshudov, G.; Garringer, H. J.; Crowther, R. A.; Ghetti, B.; Goedert, M.; Scheres, S. H. W. Cryo-EM Structures of Tau Filaments from Alzheimer's Disease. *Nature* **2017**. https://doi.org/10.1038/nature23002.

(142) Guerrero-Ferreira, R.; Taylor, N. M. I.; Mona, D.; Ringler, P.; Lauer, M. E.; Riek, R.; Britschgi, M.; Stahlberg, H. Cryo-EM Structure of Alpha-Synuclein Fibrils. *Elife* **2018**. https://doi.org/10.7554/eLife.36402.

(143) Li, B.; Ge, P.; Murray, K. A.; Sheth, P.; Zhang, M.; Nair, G.; Sawaya, M. R.; Shin, W. S.; Boyer, D. R.; Ye, S.; Eisenberg, D. S.; Zhou, Z. H.; Jiang, L. Cryo-EM of Full-Length α-Synuclein Reveals Fibril Polymorphs with a Common Structural Kernel. *Nat. Commun.* **2018**. https://doi.org/10.1038/s41467-018-05971-2.

(144) Lara, C.; Adamcik, J.; Jordens, S.; Mezzenga, R. General Self-Assembly Mechanism Converting Hydrolyzed Globular Proteins into Giant Multistranded Amyloid Ribbons. *Biomacromolecules* **2011**. https://doi.org/10.1021/bm200216u.

(145) Samanta, A.; Liu, Z.; Nalluri, S. K. M.; Zhang, Y.; Schatz, G. C.; Stoddart, J. F. Supramolecular Double-Helix Formation by Diastereoisomeric Conformations of Configurationally Enantiomeric Macrocycles. *J. Am. Chem. Soc.* **2016**. https://doi.org/10.1021/jacs.6b09258.

(146) Konda, M.; Ghosh, T.; Mobin, S. M.; Das, A. K. Intertwined Gababutin-Based Supramolecular Double Helix. *New J. Chem.* **2019**, *43* (12), 4830–4834. https://doi.org/10.1039/c8nj05009k.

(147) Lafleur, R. P. M.; Herziger, S.; Schoenmakers, S. M. C.; Keizer, A. D. A.; Jahzerah, J.; Thota, B. N. S.; Su, L.; Bomans, P. H. H.; Sommerdijk, N. A. J. M.; Palmans, A. R. A.; Haag, R.; Friedrich, H.; Böttcher, C.; Meijer, E. W. Supramolecular Double Helices from Small C 3 -Symmetrical Molecules Aggregated in Water . *J. Am. Chem. Soc.* **2020**. https://doi.org/10.1021/jacs.0c08179.

(148) Provenzano, P. P.; Eliceiri, K. W.; Campbell, J. M.; Inman, D. R.; White, J. G.; Keely, P. J. Collagen Reorganization at the Tumor-Stromal Interface Facilitates Local Invasion. *BMC Med.* **2006**. https://doi.org/10.1186/1741-7015-4-38.

(149) Li, L.; Eyckmans, J.; Chen, C. S. Designer Biomaterials for Mechanobiology. *Nature Materials*. 2017. https://doi.org/10.1038/nmat5049.

(150) Hall, M. S.; Alisafaei, F.; Ban, E.; Feng, X.; Hui, C. Y.; Shenoy, V. B.; Wu, M. Fibrous Nonlinear Elasticity Enables Positive Mechanical Feedback between Cells and ECMs. *Proc. Natl. Acad. Sci. U. S. A.* **2016**. https://doi.org/10.1073/pnas.1613058113.

(151) Cui, H.; Webber, M. J.; Stupp, S. I. Self-Assembly of Peptide Amphiphiles: From Molecules to Nanostructures to Biomaterials. *Biopolymers*. 2010. https://doi.org/10.1002/bip.21328.

(152) Goldberger, J. E.; Berns, E. J.; Bitton, R.; Newcomb, C. J.; Stupp, S. I. Electrostatic Control of Bioactivity. *Angew. Chemie - Int. Ed.* **2011**. https://doi.org/10.1002/anie.201100202.

(153) Pashuck, E. T.; Stupp, S. I. Direct Observation of Morphological Tranformation from Twisted Ribbons into Helical Ribbons. *J. Am. Chem. Soc.* **2010**, *132* (26), 8819–8821. https://doi.org/10.1021/ja100613w.

(154) Cui, H.; Cheetham, A. G.; Pashuck, E. T.; Stupp, S. I. Amino Acid Sequence in Constitutionally Isomeric Tetrapeptide Amphiphiles Dictates Architecture of One-Dimensional Nanostructures. *J. Am. Chem. Soc.* **2014**. https://doi.org/10.1021/ja507051w.

(155) Zhang, S.; Andreasen, M.; Nielsen, J. T.; Liu, L.; Nielsen, E. H.; Song, J.; Ji, G.; Sun, F.; Skrydstrup, T.; Besenbacher, F.; Nielsen, N. C.; Otzen, D. E.; Dong, M. Coexistence of Ribbon and Helical Fibrils Originating from HIAPP 20-29 Revealed by Quantitative Nanomechanical Atomic Force Microscopy. *Proc. Natl. Acad. Sci. U. S. A.* **2013**. https://doi.org/10.1073/pnas.1209955110.

(156) Ziserman, L.; Mor, A.; Harries, D.; Danino, D. Curvature Instability in a Chiral Amphiphile Self-Assembly. *Phys. Rev. Lett.* **2011**. https://doi.org/10.1103/PhysRevLett.106.238105.

(157) Crick, F. H. C. The Fourier Transform of a Coiled-Coil. *Acta Crystallogr.* **1953**. https://doi.org/10.1107/s0365110x53001952.

(158) Dokukin, M. E.; Sokolov, I. Quantitative Mapping of the Elastic Modulus of Soft Materials with HarmoniX and PeakForce QNM AFM Modes. *Langmuir* **2012**. https://doi.org/10.1021/la302706b.

(159) Young, T. J.; Monclus, M. A.; Burnett, T. L.; Broughton, W. R.; Ogin, S. L.; Smith, P. A. The Use of the PeakForceTM Quantitative Nanomechanical Mapping AFM-Based Method for High-Resolution Young's Modulus Measurement of Polymers. *Meas. Sci. Technol.* **2011**. https://doi.org/10.1088/0957-0233/22/12/125703.

(160) Sweers, K. K. M.; Van Der Werf, K. O.; Bennink, M. L.; Subramaniam, V. Atomic Force Microscopy under Controlled Conditions Reveals Structure of C-Terminal Region of α-Synuclein in Amyloid Fibrils. *ACS Nano* **2012**. https://doi.org/10.1021/nn300863n.

(161) Missirlis, D.; Khant, H.; Tirrell, M. Mechanisms of Peptide Amphiphile Internalization by SJSA-1 Cells in Vitro. *Biochemistry* **2009**. https://doi.org/10.1021/bi802356k.

(162) Attwood, S. J.; Choi, Y.; Leonenko, Z. Preparation of DOPC and DPPC Supported Planar Lipid Bilayers for Atomic Force Microscopy and Atomic Force Spectroscopy. *Int. J. Mol. Sci.* **2013**. https://doi.org/10.3390/ijms14023514.

(163) Svitkina, T. The Actin Cytoskeleton and Actin-Based Motility. *Cold Spring Harb. Perspect.*

Biol. **2018**. https://doi.org/10.1101/cshperspect.a018267.

(164) Pulokas, J.; Suloway, C.; Fellmann, D.; Zhu, Y.; Cheng, A.; Quispe, J.; Guerra, F.; Stagg, S.; Potter, C. S.; Carragher, B. High Throughput Image Acquisition Using the Leginon System. *Microsc. Microanal.* **2005**. https://doi.org/10.1017/s1431927605508766.

(165) Golde, T.; Huster, C.; Glaser, M.; Händler, T.; Herrmann, H.; Käs, J. A.; Schnauß, J. Glassy Dynamics in Composite Biopolymer Networks. *Soft Matter* **2018**. https://doi.org/10.1039/C8SM01061G.

(166) Flory, P. J. Thermodynamics of High Polymer Solutions. *The Journal of Chemical Physics*. 1941. https://doi.org/10.1063/1.1750971.

(167) Huggins, M. L. Some Properties of Solutions of Long-Chain Compounds. *J. Phys. Chem.* **1942**. https://doi.org/10.1021/j150415a018.

(168) Wu, A.; Isaacs, L. Self-Sorting: The Exception or the Rule? *J. Am. Chem. Soc.* **2003**. https://doi.org/10.1021/ja028913b.

(169) Mukhopadhyay, P.; Wu, A.; Isaacs, L. Social Self-Sorting in Aqueous Solution. *J. Org. Chem.* **2004**. https://doi.org/10.1021/jo049976a.

(170) Jolliffe, K. A.; Timmerman, P.; Reinhoudt, D. N. Noncovalent Assembly of a Fifteen-Component Hydrogen-Bonded Nanostructure. *Angew. Chemie - Int. Ed.* **1999**. https://doi.org/10.1002/(SICI)1521-3773(19990401)38:7<933::AID-ANIE933>3.0.CO;2-3.

(171) Ligthart, G. B. W. L.; Ohkawa, H.; Sijbesma, R. P.; Meijer, E. W. Complementary Quadruple Hydrogen Bonding in Supramolecular Copolymers. *J. Am. Chem. Soc.* **2005**. https://doi.org/10.1021/ja043555t.

(172) Ji, W.; Álvarez, Z.; Edelbrock, A. N.; Sato, K.; Stupp, S. I. Bioactive Nanofibers Induce Neural Transdifferentiation of Human Bone Marrow Mesenchymal Stem Cells. *ACS Appl. Mater. Interfaces* **2018**. https://doi.org/10.1021/acsami.8b13653.

(173) Chen, C. H.; Hsu, E. L.; Stupp, S. I. Supramolecular Self-Assembling Peptides to Deliver Bone Morphogenetic Proteins for Skeletal Regeneration. *Bone*. 2020. https://doi.org/10.1016/j.bone.2020.115565.

(174) Onogi, S.; Shigemitsu, H.; Yoshii, T.; Tanida, T.; Ikeda, M.; Kubota, R.; Hamachi, I. In Situ Real-Time Imaging of Self-Sorted Supramolecular Nanofibres. *Nat. Chem.* **2016**. https://doi.org/10.1038/nchem.2526.

(175) Da Silva, R. M. P.; Van Der Zwaag, D.; Albertazzi, L.; Lee, S. S.; Meijer, E. W.; Stupp, S. I. Super-Resolution Microscopy Reveals Structural Diversity in Molecular Exchange among Peptide Amphiphile Nanofibres. *Nat. Commun.* **2016**. https://doi.org/10.1038/ncomms11561.

(176) Van Gestel, J.; Palmans, A. R. A.; Titulaer, B.; Vekemans, J. A. J. M.; Meijer, E. W. "Majority-Rules" Operative in Chiral Columnar Stacks of C 3-Symmetrical Molecules. *J. Am. Chem. Soc.* **2005**. https://doi.org/10.1021/ja0501666.

(177) Guler, M. O.; Soukasene, S.; Hulvat, J. F.; Stupp, S. I. Presentation and Recognition of Biotin on Nanofibers Formed by Branched Peptide Amphiphiles. *Nano Lett.* **2005**. https://doi.org/10.1021/nl048238z.

(178) Dundas, C. M.; Demonte, D.; Park, S. Streptavidin-Biotin Technology: Improvements and Innovations in Chemical and Biological Applications. *Appl. Microbiol. Biotechnol.* **2013**. https://doi.org/10.1007/s00253-013-5232-z.

(179) Alborzinia, H.; Schmidt-Glenewinkel, H.; Ilkavets, I.; Breitkopf-Heinlein, K.; Cheng, X.; Hortschansky, P.; Dooley, S.; Wölfl, S. Quantitative Kinetics Analysis of BMP2 Uptake into Cells and Its Modulation by BMP Antagonists. *J. Cell Sci.* **2013**. https://doi.org/10.1242/jcs.109777.

(180) Smyth, M. S.; Martin, J. H. J. X Ray Crystallography. *Journal of Clinical Pathology - Molecular Pathology*. 2000. https://doi.org/10.1136/mp.53.1.8.

(181) Unwin, P. N. T.; Henderson, R. Molecular Structure Determination by Electron Microscopy of Unstained Crystalline Specimens. *J. Mol. Biol.* **1975**. https://doi.org/10.1016/0022-2836(75)90212-0.

(182) Kong, J.; Yu, S. Fourier Transform Infrared Spectroscopic Analysis of Protein Secondary Structures. *Acta Biochim. Biophys. Sin. (Shanghai).* **2007**. https://doi.org/10.1111/j.1745-7270.2007.00320.x.

(183) Greenfield, N. J. Using Circular Dichroism Spectra to Estimate Protein Secondary Structure. *Nat. Protoc.* **2007**. https://doi.org/10.1038/nprot.2006.202.

(184) Cavalli, A.; Salvatella, X.; Dobson, C. M.; Vendruscolo, M. Protein Structure Determination from NMR Chemical Shifts. *Proc. Natl. Acad. Sci. U. S. A.* **2007**. https://doi.org/10.1073/pnas.0610313104.

(185) Fischer, T.; Hayn, A.; Mierke, C. T. Fast and Reliable Advanced Two-Step Pore-Size Analysis of Biomimetic 3D Extracellular Matrix Scaffolds. *Sci. Rep.* **2019**. https://doi.org/10.1038/s41598-019-44764-5.

(186) Nam, S.; Lee, J.; Brownfield, D. G.; Chaudhuri, O. Viscoplasticity Enables Mechanical Remodeling of Matrix by Cells. *Biophys. J.* **2016**. https://doi.org/10.1016/j.bpj.2016.10.002.

(187) Jahn, T. R.; Makin, O. S.; Morris, K. L.; Marshall, K. E.; Tian, P.; Sikorski, P.; Serpell, L. C. The Common Architecture of Cross-β Amyloid. *J. Mol. Biol.* **2010**. https://doi.org/10.1016/j.jmb.2009.09.039.

(188) Leung, C. Y.; Palmer, L. C.; Kewalramani, S.; Qiao, B.; Stupp, S. I.; De La Cruz, M. O.; Bedzyk, M. J. Crystalline Polymorphism Induced by Charge Regulation in Ionic Membranes. *Proc. Natl. Acad. Sci. U. S. A.* **2013**. https://doi.org/10.1073/pnas.1316150110.

(189) Crouse, D. T. X-Ray Diffraction and the Discovery of the Structure of DNA. A Tutorial and Historical Account of James Watson and Francis Crick's Use of X-Ray Diffraction in Their Discovery of the Double Helix Structure of DNA. *J. Chem. Educ.* **2007**. https://doi.org/10.1021/ed084p803.

(190) Harutyunyan, B.; Dannenhoffer, A.; Kewalramani, S.; Aytun, T.; Fairfield, D. J.; Stupp, S. I.; Bedzyk, M. J. Molecular Packing of Amphiphilic Nanosheets Resolved by X-Ray Scattering. *J. Phys. Chem. C* **2017**. https://doi.org/10.1021/acs.jpcc.6b11391.

(191) Gabriel, J.; Blochowicz, T.; Stühn, B. Compressed Exponential Decays in Correlation Experiments: The Influence of Temperature Gradients and Convection. *J. Chem. Phys.* **2015**. https://doi.org/10.1063/1.4914092.

(192) Stetefeld, J.; McKenna, S. A.; Patel, T. R. Dynamic Light Scattering: A Practical Guide and Applications in Biomedical Sciences. *Biophysical Reviews*. 2016. https://doi.org/10.1007/s12551-016-0218-6.

(193) Brandão, H. B.; Sangji, H.; Pandžić, E.; Bechstedt, S.; Brouhard, G. J.; Wiseman, P. W. Measuring Ligand-Receptor Binding Kinetics and Dynamics Using k-Space Image Correlation Spectroscopy. *Methods* **2014**. https://doi.org/10.1016/j.ymeth.2013.07.042.

(194) Chen, G.; Deng, C.; Li, Y. P. TGF-β and BMP Signaling in Osteoblast Differentiation and Bone Formation. *International Journal of Biological Sciences*. 2012. https://doi.org/10.7150/ijbs.2929.

(195) Wu, M.; Chen, G.; Li, Y. P. TGF-β and BMP Signaling in Osteoblast, Skeletal Development, and Bone Formation, Homeostasis and Disease. *Bone Res.* **2016**. https://doi.org/10.1038/boneres.2016.9.

M. Hussain Sangji

hussainsangji@u.northwestern.edu | (224) 659-3735

Education

PhD | 2020 | Northwestern University, Evanston, IL
Department: Biomedical Engineering, Group of Prof. Samuel Stupp.
Thesis Project: Self-Assembly of Supramolecular Biomaterials Across Length Scales

MSc | 2015 | McGill University, Montreal, QC
Department: Physics, Group of Prof. Peter Grutter.
Thesis Project: Development of a force sensing device for neurosurgery and neurodegeneration.

BSc | 2013 | McGill University, Montreal, QC
Major: Honours Physics
Minor: Mathematics
First Class Honours (CGPA: 3.6)

Mentorship

(2016-2017) Mentored a master's student in Biomedical Engineering for her research thesis project. Worked closely with her to design a project, plan experiments and discuss results.
(2017 Summer) Mentored an undergraduate student during a summer research internship and was responsible for all aspects of the student's project. Helped the student understand the research topic by assigning readings and discussing literature in an educational manner.

Teaching Experience

Managed discussion sections and taught students during office hours.
Winter 2018 Teaching Assistant, Northwestern University, Thermodynamics
Fall 2014 Teaching Assistant, McGill University, Electricity and Magnetism
Winter 2013 Teaching Assistant, McGill University, Measurements Lab
Fall 2013 Teaching Assistant, McGill University, Modern Physics Lab

Leadership Experience

Leadership Fellow – Northwestern Center for Leadership **Jan 2019-June 2019**
Researched the challenges faced by organizations to implement diversity initiatives and harness the value of diverse teams to create impact, and ran a workshop for ~20 graduate students.

McCormick Graduate Leadership Council (MGLC) **Sept 2016-Aug 2018**
President (2017-2018), and Professional Development Chair. Managed professional development and social programs for graduate students in the McCormick School of Engineering.
Oversaw a team of 8 members who organized events for graduate students, and collaborated with University faculty, staff and alumni.

Developed new programs for graduate students including an entrepreneurship event series, and an Alumni mentorship program.

Advisory Committee on Investment Responsibility (ACIR) Sept 2018-May 2020
Graduate student representative (elected position). Represent the interests of the graduate student community on questions of Ethical and Social policies in the management of the Northwestern endowment.
Worked closely with a university committee consisting of faculty, staff, alumni, and undergraduate students to assess investment policy proposals, and advise the Northwestern endowment committee.

Graduate Student Association (GSA) Sept 2018- Aug 2019
Social Chair. Work with team of graduate students from departments across Northwestern to create social events for students.

Publications

Anthonisen, Madeleine, Yuning Zhang, M. Hussain Sangji, and Peter Grütter. "Quantifying bio-filament morphology below the diffraction limit of an optical microscope using out-of-focus images." *Applied Optics* 59, no. 9 (2020): 2914-2923.

Yi, Sijia, Xiaohan Zhang, M. Hussain Sangji, Yugang Liu, Sean D. Allen, Baixue Xiao, Sharan Bobbala et al. "Surface engineered polymersomes for enhanced modulation of dendritic cells during cardiovascular immunotherapy." *Advanced Functional Materials* 29, no. 42 (2019): 1904399.

Anthonisen, Madeleine, Matthew Rigby, M. Hussain Sangji, Xue Ying Chua, and Peter Grütter. "Response of mechanically-created neurites to extension." *Journal of the mechanical behavior of biomedical materials* 98 (2019): 121-130.

Freeman, R.; Han, M.; Álvarez, Z.; Lewis, J. A.; Wester, J. R.; Stephanopoulos, N.; McClendon, M. T.; Lynsky, C.; Godbe, J. M.; Sangji, H.; Luijten E.; Stupp, S. I. "Reversible Self-Assembly of Superstructured Networks" *Science* 362(6416), (2018) 808-813.

Sleep, E.; Cosgrove, B. D.; McClendon, M. T.; Preslar, A. T.; Chen, C. H.; Sangji, M. H.; Rubert Pérez, C. M.; Haynes, R. D.; Meade, T. J.; Blau, H. M.; Stupp, S. I. “Injectable Biomimetic Liquid Crystalline Scaffolds Enhance Muscle Stem Cell Transplantation” *Proc. Natl. Acad. Sci*. 114(38), (2017) E7919-E7928. PMCID: PMC5617293

Brandao, Hugo B., M Hussain Sangji, Elvis Pandžić, Susanne Bechstedt, Gary J. Brouhard, and Paul W. Wiseman. "Measuring ligand–receptor binding kinetics and dynamics using k-space image correlation spectroscopy." *Methods* 66 (2014): 273-282.

Tripathy, Umakanta, Maxime Giguère-Bisson, M Hussain Sangji, Marie-Josée Bellemare, D. Scott Bohle, Elias Georges, and Paul W. Wiseman. "Optimization of malaria detection based on third

harmonic generation imaging of hemozoin." *Analytical and bioanalytical chemistry* 405, no. 16 (2013): 5431-5440.

Fellowships and awards

2015 Professional development scholarship (Northwestern, $2000)
2015 Graduate Excellence Award (McGill, $5000)
2014 GREAT Travel Award (McGill, $1000)
2014 NSERC-CREATE Neuroengineering Graduate Fellowship (McGill, $17000)
2013 NSERC-CREATE Neuroengineering Graduate Fellowship (McGill, $17000)
2013 NSERC-CREATE Neuroengineering Undergraduate Fellowship May (McGill, $6500)